Development of a large RF plasma source for non-linear microwave-plasma interactions

PhD Thesis

Kieran James Wilson

Atoms Beams and Plasmas

Physics

University of Strathclyde, Glasgow

March 1, 2024

March 1, 2024

This thesis is the result of the author's original research. It has been composed by the author and has not been previously submitted for examination which has led to the award of a degree.

Signed:

Date: March 1, 2024

When this seemed an impossible task,
you made me believe.
When I was snowed under,
you dug me out.
When I ran out of steam,
you dragged me over the finish line.
My dearest Jade,
I could not have done this without you.

Thank you.

Abstract

A critical aspect of modern fusion research is the open question of how to efficiently couple energy into fusion plasmas. In magnetically confined schemes, particularly high density spherical aspect tokamaks, it is difficult to reach plasma resonances with injected microwave beams, as the usual targets, like the first or second harmonic of the electron cyclotron resonance and lower hybrid are cut off due to the high plasma frequencies. In inertial confinement schemes non-linear wave-plasma interactions at optical frequencies cause fast electrons that preheat the fuel (SRS) and reduce implosion performance or cause back-scattered signals (SBS) that can damage laser systems. These environments are either difficult to access or too harsh for detailed probe diagnostics. Thus, a large, low density, low temperature plasma source in the form of a helicon has been developed to enable the study of parametric and other beat-wave type interactions at microwave frequencies. In this parameter space experiments can be conducted on longer length and timescales in a long lived continuous operation plasma that will not destroy probe diagnostics. This thesis presents the design and commissioning of the apparatus, including characterisation measurements and the development of a numerical model of the plasma source. The device operated in the HF band at powers up to 200 W. Noble gas plasmas in either helium or argon can be generated, with neutral gas pressures ranging from 0.8 Pa to 6.8 Pa. Peak $n_e \approx 3 \times 10^{15}$ m^{-3} and T_e 1 - 2 eV have been measured for helium in the inductively coupled mode while argon plasmas with $n_e \approx 1\times 10^{15}$ m^{-3} and T_e between 0.5 eV and 1 eV have been achieved. The device has been successfully operated in the helicon mode in helium at an RF power of 200 W at 14 MHz, with evidence of enhanced confinement and altered radial profile. A fluid numerical model of the source has also been developed that has low computation cost. The model over-estimates the densities by a factor of 3 - 4 and the temperatures by a factor of 2. This model is lacking the capacitive coupling that may be present in the apparatus and should provide better predictive capability in future high power operation. The model looks capable of calculating the helicon mode, showing wave structures that match the dispersion relation and profiles predicted by helicon wave theory in the literature.

Acknowledgements

First and foremost, I would like to acknowledge the unwavering support and dedication of Prof. K. Ronald, without whom I could never have completed this work. I am forever grateful.

There are many others who have been instrumental in this work: Dr. C. Whyte for his direction and expertise and constructing the apparatus, Mr. L. Selman for his work 'in the trenches' with me over the last 4 years, Dr. B. Eliasson for his contributions to interpretation of results and numerical modelling as well as helping with feedback on this thesis. Prof. A. D. R. Phelps for his continued support in all aspects of this work, from experimental guidance to thesis feedback; which continued despite his retirement during this work. I would like to extend a particular thanks to Prof. M. Koepke for sharing his expertise in Langmuir probe. Prof. R. Bingham and Prof. A. Cairns have been instrumental in guiding the project.

I would also like to thank other members of the group for their support over the last several years; Dr. P. MacInnes, Dr. D. Speirs, Dr. C. Robertson, Dr. C. Donaldson and Dr. L. Zhang. I would also like to thank Mr. D. Barclay for fabricating various components for the apparatus. Although not directly related to the work, I would also like to thank Dr. A. Young for our interesting conversations in the office over the years. A particular thanks is in order for both Dr. D. Woodward and Dr. L Walker; who were senior PhD students who made me feel welcome when I started my PhD and were instrumental in building my

confidence in those early days. Lastly, but by no means least, I would like to pay tribute to Prof. A. Cross, our group lead. We lost Prof. Cross suddenly during this work and he has left shoes that will be impossible to fill. Prof. Cross was well respected in his field and was particularly welcoming and encouraging to me. His expertise and kind attitude set an example for us all.

Outwith academia, I would like to thank my Mum, who sowed the seeds of my intellectual curiosity and my passion for learning. My Dad, who instilled in me a willingness to apply that curiosity to the world around me, a skill that I have come to realise does not come hand-in-hand with intellectual ability. I would like to thank my little sister, for her support and cheer, for reminding me of my achievements when I can't see the forest for the trees. I would also like to acknowledge my parents in-law; who's love and support over these last few years have been an important contribution to my work. The self-confidence they have imparted to me have been a vital quality in completing this thesis. Lastly I would like to acknowledge all of my wider family and friends for their support and their investment in my progress.

Maybe I would have gotten here eventually, but I would be in much worse shape for it; thank you all.

List of Symbols

Greek Alphabet

α, β	Spring index
α	Spatial decay constant
δ	Skin depth
δ_c	Wave frequency normalised to cyclotron frequency
δ_m	Propagated scale and measurement uncertainty
δ_r	Random uncertainty
δ_T	Total combined uncertainty
δ_ξ	Collisional skin depth
ϵ	Electric permittivity
ϵ_r	Relative permittivity of medium
η	Beat wave current drive efficiency
Γ	Flux
Γ	Gamma function
γ	Numerical factor for reaction rate constant
γ_i	Instability growth rate
Γ_t	Thermal emission flux
Γ_V	Voltage reflection coefficient
γ_0	Instability growth rate, without damping
γ_{EM}	Damping rate of electromagnetic wave
γ_{ES}	Damping rate of electrostatic wave
γ_{iota}	Secondary emission coefficient for species ι
$\hat{\phi}_k, \hat{\phi}_l$	Basis functions associated with nodes k and l, respectively
κ	Plasma dielectric constant
Λ	Energy loss rate
λ_1	Mean free path, collisional regime
λ_2	Mean free path, collisionless regime
λ_D	Debye length
λ_{Ds}	Debye length at the sheath edge
λ_{mfp}	Mean free path
λ_{pump}	Pump beam wavelength
μ	Material permeability
μ	Mobility
ν	Collision Frequency
ν_e	Electron collision frequency
ν_r	Fast electron collisional slowing rate
ν_{ei}	Electron-ion collision frequency

Ω	Cyclotron frequency
Ω	Inner product domain
ω	Angular frequency of electromagnetic wave
ω_0	Pump wave angular frequency
ω_p	Plasma frequency
ω_s	Scattered wave angular frequency
ω_{ek}	Electrostatic wave angular frequency
ω_{ik}	Ion wave angular frequency
ω_{RF}	RF drive angular frequency
Φ	(Vector) of nodal unknowns
ϕ	Wave phase
ϕ^e	Element interpolation function
ρ	Charge density
$\sigma(\varepsilon)$	Reaction cross section
σ	Conductivity
θ_1	Angle between pump wave and background magnetic field
ε	Energy
ε_i	Ion energy gained across sheath potential
ε_x	Energy loss for reaction x
$\varepsilon_{p,i}$	Mean thermal energy of an emitted particle from species i
ε_t	Mean thermal energy of an emitted electron

Latin Alphabet

$\bar{T_e}$	Mean electron temperature
$\bar{V_p}$	Plasma potential, DC part
$\bar{x}$	mean of all data points in a measurement set
$\mathcal{D}$	Permittivity difference term
$\mathcal{L}$	Permittivity for a left circularly polarised wave
$\mathcal{P}$	Permittivity parallel to field
$\mathcal{R}$	Permittivity for a right circularly polarised wave
$\mathcal{S}$	Permittivity sum term
$\tilde{I_L}$	Current at the load
$\tilde{I}$	Complex amplitude of the current on a transmission line
$\tilde{V_L}$	Voltage at the load
$\tilde{V_p}$	Plasma potential, AC part
$\tilde{V}$	Complex amplitude of the voltage on a transmission line
$\vec{A}$	Vector potential
$\vec{n}$	Surface normal vector
$\vec{p_0}$	Initial momentum
$\vec{v_0}$	Initial velocity
$\vec{v_{0,i}}$	Initial velocity of species i
A	Amplitude
A	Area
a	Waveguide wide dimension
A_0	Initial vector potential
A_p	Langmuir probe collecting area
a_0	Quiver velocity normalised to the speed of light

A_{coil}	Antenna coil area
B	Magnetic Field
B	Magnetic flux density (Magnetic flux density)
B	Susceptance
b	Waveguide short dimension
B_0	Bias magnetic field
B_r	Magnetic flux density, r component
B_z	Magnetic flux density, z component
B_θ	Magnetic flux density, θ component
B_{crit}	Critical Magnetic Field
C'	Distributed capacitance
C	Capacitance
C	Inter-element continuity vector
C_n	Wave magnetic field amplitude
c_n^S	Molar concentration of species n with stoichiometry exponent S
D	Diffusivity
d_{node}	Displacement at spring 'node'
E	Electric field
E_m	Inductive electric field
E_s	Electrostatic field
$f(\epsilon)$	Energy distribution function
f	Frequency
f^e	Element force vector
F_i	Force acting on species i
f_Δ	Maximum allowable detuning
f_{ce}	Electron cyclotron frequency
f_{ci}	Ion cyclotron frequency
f_c	Waveguide cutoff frequency
f_{LH}	Lower hybrid frequency
F_{node}	Force at spring 'node'
f_p	Plasma frequency
f_{RF}	RF drive frequency
$F_{X(\alpha)}$	For Greek symbol: Force at node X due to all forces on spring α
$F_{X(Y)}$	For Latin symbol: Force at node X due to the displacement of node Y
G'	Distributed conductance
G	Conductance
G_0	Transmission line characteristic conductance
G_L	Load conductance
I	Current
i	Coil domain index
i	current on a transmission line
I_0	Pump beam intensity
I_0^+	Forward current wave amplitude
I_0^-	Backward current wave amplitude
I_i	Langmuir probe current, ion contribution
I_m	Magnet coil current
I_{coil}	Current flowing in RF antenna
I_{esat}	Electron saturation current
I_e	Langmuir probe current, electron contribution
I_{isat}	Ion saturation current

I_{probe}	Langmuir probe current, as collected by an ammeter
I_{sat}	Saturation current
J	Current density
J_e	External current density
J_s	Space charge limited current density
J_{ind}	Induced current density
K	Spring stiffness constant
k	Total wavenumber
k^e	Stiffness matrix
k_0	Pump wave wavenumber
k_d	Damping part of wavenumber
k_i	Rate constant for reaction i
k_s	Skin number
k_w	Whistler wavenumber
k_z	Axial wavenumber
$k_\perp$	Perpendicular wavenumber
k_{ck}	Electrostatic wave wavenumber
k_{sc}	Scattered wave wavenumber
L'	Distributed inductance
l, m, n	Spring node index
L	1D element length
L	Inductance
l	length
l_p	Probe collecting tip length
m	Azimuthal mode number of helicon wave
m	Linear regression analysis gradient
m	Waveguide wide dimension mode number
N	Basis function order
N	Number of measurements
n	Electron Density
n	Summation index
n	Waveguide short dimension mode number
n_0	Equilibrium plasma density
n_j	Density of species j
n_j^0	Equilibrium density of species j
n_s	Ion density at the sheath edge
n_t	Solenoid turn density
n_c	Critical density
$n_{e,0}$	Initial electron density
P	Power
p	Pressure
P_{coil}	RMS power dissipated by RF antenna
P_{RF}	RF power
Q	Point representing the approximate solution
Q	Quality factor
q	Charge
q_j	Charge of species j
q_η	Quantum efficiency
Q_ε	Energy production rate
R'	Distributed resistance
$R(x)$	Galerkin method residuals
R	Resistance

r	Radial position
R_0	Transmission line characteristic resistance
R_a	Relative action transfer
r_c	Reaction rate
R_e	Electron production rate
r_e	Wall reflection coefficient
r_i	Reaction rate for reaction i
R_L	Load resistance
R_n	Source term for species n
r_p	Probe radius
R_s	Series resistance
R_V	Virtual resistance
r_v	Vessel radius
r_x	Reaction rate for reaction x
r_{maj}	Tokamak major radius
r_{sheath}	Sheath radius
$r_{solenoid}$	Solenoid radius
r_{vessel}	Vessel radius
S	Stoichiometry exponent
s	Sheath thickness
s	Species index
S_{11}	Scattering parameter, input port voltage reflection coefficient (Γ)
S_{12}	Scattering parameter, reverse voltage gain
S_{21}	Scattering parameter, forward voltage gain
S_{22}	Scattering parameter, output port voltage reflection coefficient (Γ)
S_{coil}	Antenna coil surface
T	Point representing the true solution
t	time
t_c	Mean time between collisions
T_e	Electron Temperature
T_e^δ	Absolute uncertainty, electron temperature
T_g	Neutral gas temperature
T_j	Temperature of species j
$t_{c,i}$	Mean time between collisions for species i
$T_{e,0}$	Initial electron temperature
u	Drift velocity
V	Electric potential
V	Electrostatic potential
V	Plane representing the solution space for the approximate solution
v	Speed
v	voltage on a transmission line
V_0^+	Forward voltage wave amplitude
V_0^-	Backward voltage wave amplitude
V_f	Floating potential
v_f	Fluid velocity
V_f^δ	Absolute uncertainty, floating potential
V_i	Voltage across coil domain i
v_i	Ion speed
V_P	Plasma potential with respect to laboratory ground
V_p^δ	Absolute uncertainty, plasma potential
V_s	Sheath potential drop

v_s	Ion velocity at the sheath edge
V_W	Wall potential relative to laboratory ground
V_Δ	Potential difference between probe and plasma
v_∞	Ion speed in bulk plasma
V_B	Langmuir probe DC bias voltage
v_B	Bohm speed
V_{coil}	Total voltage across RF antenna
$v_{e,th}$	Electron thermal speed
v_{f0}	Particle velocity at the probe surface, radial component
$v_{f\theta}$	Particle velocity at the probe surface, θ component
v_{os}	Electron quiver velocity
v_{r0}	Particle velocity at the sheath edge, radial component
$v_{r\theta}$	Particle velocity at the sheath edge, θ component
V_{RF}	Plasma potential, AC part
v_{th}	Particle thermal velocity
V_{TOT}	Plasma volume
X	Reactance
x	Mesh fitting independent variable
X_c	Capacitor reactance
x_i	A data point in a measurement set
x_k, x_l	Coordinates of nodes k and l, respectively
$y(x)$	Galerkin method exact solution
Y	Admittance
Y_{IN}	Input admittance
Z	Impedance
Z_0	Characteristic impedance of a transmission line
Z_L	Impedance of a load connected to a transmission line
Z_X	Impedance of reactive component
$Z_{33\mu\mathrm{H}}$	Impedance of 33 μH inductor
$Z_{66\mu\mathrm{H}}$	Impedance of 66 μH inductor
Z_{choke}	Impedance of RF chokes
Z_{IN}	Input impedance
Z_s	Sheath impedance
Z_T	Total choke impedance
VSWR	Voltage standing wave ratio

Mathematical Operators

$< X >$	Average value of X
β	Distribution function gamma expression
$\delta(\vec{r})$	Dirac-delta function
$\forall$	‘for all values of’
$\hat{\phi}_n$	Galerkin method basis function
$\hat{\theta}$	Azimuthal unit vector
$\hat{i}, \hat{j}, \hat{k}$	Cartesian 3D unit vectors
$\hat{z}$	Unit vector, z direction
∇	Del, vector differential operator
$\phi(x)$	Galerkin method approximate solution

Φ_k, Φ_l	Interpolation function values at nodes k and l, respectively
θ	Azimuthal coordinate
I	Unit tensor
i	Imaginary unit
j	Imaginary unit, used to separate from the current symbol i
J_n	Bessel function of the first kind, order n
x	1D cartesian x-coordinate
z	Axial position coordinate

Physical Constants

ϵ_0	Permittivity, vacuum
μ_0	Magnetic permeability, vacuum
c	Speed of light
e	Elementary charge
F	Faraday constant
k_B	Boltzmann constant
m_e	Electron mass
m_i	Ion mass
N_A	Avogadro's number

Modifying Signs

$\|, \perp$	Parallel, perpendicular (component)
ε	Energy
e, i	Electron, ion
p, s	Parallel, series (connection)
r, θ, z	Components along cylindrical coordinate axes
x, y, z	Components along rectangular coordinate axes

List of Figures

List of Tables

Contents

Chapter 1

Introduction

Plasmas can support a great variety of waves and the development of the theory of wave propagation has been important in understanding these interactions. Cold plasma wave theory provides the starting point for the analysis and predicts many different types of plasma wave, both electrostatic and electromagnetic, while warm plasma wave theory provides an extension for hot plasmas [1]. Plasma wave theory provides insight on the propagation behaviour of waves in a plasma, while collisional and collisionless [2] damping mechanisms allow for prediction of how the energy of such wave is absorbed by a plasma. This understanding has been critical in the development of fusion devices over the last 7 decades as very high densities and temperatures are required for a plasma to reach the 'ignition' [3] condition, where self heating due to the production of energetic fusion α particles outstrips the system losses and the reaction becomes self sustaining. Getting to such a condition is no easy task and thus the scientific community is split on the best approach: magnetic or inertial confinement. In the magnetic confinement approach [4] the plasma is contained by a magnetic field; the 2 prominent examples are tokamaks and stellarators. In this approach Ohmic heating, neutral beam heating or RF heating are employed to steadily ramp the temperature and density of a deuterium-tritium (D-T) plasma until ignition is reached, at which point the external heating systems can be turned off[1]. The other mainstream approach is inertial confinement [5] by imploding a pellet of D-T ice under the action of intense laser light; the hope being the compression caused by ablation of the outer layer of the pellet will provide enough heat and confinement to ignite the resulting dense plasma. Both schemes have recently shown promise with the Joint European Torus (JET) setting a new record for the most fusion energy released in one shot [6] and the National Ignition Facility (NIF) announcing break-even in a recent experiment [7]. The question of how best to heat a tokamak is an open one and needs resolution if upcoming machines are to be effective, while non-linearities in wave-plasma interactions still plague the inertial regime. With that in mind, this thesis presents the design, construction, commissioning, characterisation and modelling of a new, large RF plasma source in the form of a helicon. This device operates at longer length scales and provides flexibility with regards to B-field variability and density profiling. It will serve as a test-bed for the study of intense, non-linear microwave interactions to inform and corroborate theoretical and modelling developments for a variety of processes relevant to these important areas of research.

1.1 Electromagnetic waves in fusion plasmas

1.1.1 Heating and current drive

Historically, the initial source of heating for a tokamak comes from the Ohmic dissipation of the plasma currents that are driven by the startup solenoid [4]. However, this process is self defeating as the Ohmic power dissipation is inversely proportional to the electron temperature. Thus there comes a maximum temperature for a given tokamak where the plasma losses are balanced by the Ohmic dissipation; further heating becomes very inefficient. In spherical tokamaks, where

---

[1] However, auxiliary systems for profile control will still consume a large amount of power.

the minor radius is small the solenoid is competing for space with many other critical systems. Indeed, some experiments aim to try and eliminate this central solenoid altogether by use of the bootstrap current [8]. For this reason, a variety of systems have been developed for plasma heating and current drive. Each has its own benefits and pitfalls and while each can provide significant heating no combination of heating systems has yet been able to push an experiment beyond ‘break even’.

Neutral Beam Injection

This type of heating system [9] is a little outwith the RF and microwave themes of the present thesis. However, it would be remiss of any description of tokamak heating to gloss over this very important system. In this heating strategy, beams of energetic neutrals (10s of keV) are injected into the plasma where they are ionised and collisionally transfer energy to the bulk population. Since they are initially neutral, they are unaffected by the magnetic field and can be calibrated to deposit their energy at almost arbitrary depths within the plasma. In this system, ions are generated outside the tokamak and passed through an accelerating field, after which they are passed through a gas target to recombine and form a neutral beam through charge exchange. The penetration depth of the neutral beam is broadly proportional to the beam energy and so core penetration on large tokamaks requires high beam energies. However, in a neutral beam injector system, the neutralising charge exchange process is competing with the cross section for ionising collisions. The fraction of the beam that leaves the injector as a neutral is inversely proportional to the beam energy and thus the efficiency drops off with higher energy [4].

RF Systems: ICRF

‘ICRF’ stands for the ‘ion cyclotron range of frequencies’ [10], describing a category of techniques for heating the plasma ions that utilises frequencies near, or equal to the ion cyclotron frequency. In the late 1950s and early 1960s, the first attempts at cyclotron heating focused on launching a shear Alfvén wave (also known as the slow magnetosonic wave). This wave would be injected in a high magnetic field region and made to propagate into a region of lower magnetic field, thus causing the wave to meet its resonance condition at $\omega \approx \Omega_i$ and this idea was met with some success in earlier fusion devices like the B-66 stellarator [11]. However, it became apparent for larger scale tokamaks that this mode could not propagate through to the core of the plasma due to mode conversion near the edge [10]. Later, a scheme for ion heating was developed that utilised the compressional Alfvén wave (fast magnetosonic wave). It was found that this wave can couple to a minority second ion species and thus be absorbed, while any remaining energy converts to the ‘ion-Bernstein’ wave (IBW) and Landau damps, transferring energy to the electrons [12, 13]. The main problem with this method is that the ion cyclotron frequency is well below the electron plasma frequency for a typical tokamak, meaning the wave must tunnel through an evanescent layer to reach the resonance, lowering the efficiency; in addition, the long wavelength has no vacuum solution within the confines of a tokamak, adding to the evanescent gap. This also forces the antenna to be close to the resonance layer, straining the engineering and material sciences requirements due to the aggressively hot plasma.

RF Systems: Lower Hybrid

Lower hybrid heating schemes utilise frequencies between the ion and electron cyclotron frequencies and were first discussed by Golant [14]. Again, this range of frequencies are forbidden in a typical fusion plasma, thus the launch antennas for these must also rely on tunnelling through an evanescent layer as in the ion cyclotron resonance heating (ICRH) case. Experiments injecting below the resonance frequency were plagued with parametric instabilities near the plasma edge [15]. However injecting above the resonance allowed for efficient heating of electrons through Landau damping. Lower hybrid current drive was identified as a method for generating large plasma currents at tokamak parameters [16] and subsequent experiments showed promising results, even at ITER conditions [17]. It has even been found that lower hybrid waves could substitute for the central solenoid of a tokamak by providing the necessary startup current [18].

RF Systems: ECRH

‘Electron Cyclotron Resonance Heating’ or, ECRH utilises resonant absorption at the electron cyclotron frequency. For typical tokamaks this is the frequency range of 10s of GHz to over 100 GHz. Most devices (ASDEX-UPGRADE, DIII-D & ITER to give examples) utilise the 2^{nd} or 3^{rd} harmonic, although ITER should also be able to access the fundamental resonance. This heating and current drive technique has the overt advantage that if the resonance is above the plasma frequency, there is no tunnelling through evanescent layers; the higher frequency means there is also a valid vacuum solution and thus the antenna for such a system can be placed far from the plasma. However, spherical tokamaks such as MAST-U (Mega Ampère Spherical Tokamak Upgrade) have a higher density and lower cyclotron frequency, presenting a challenge for the implementation of this scheme, although some alternatives like electron Bernstein wave mode conversion have been identified as a replacement [19]. A thorough review of electron cyclotron absorption was given by Bornaticci et al [20] in 1983, although experiments were taking place earlier than this [21] (1976). This scheme relies on direct heating of the electrons, which then thermalise with the ions to provide bulk heating.

1.1.2 Inertially confined schemes

The interaction of plasma with electromagnetic waves also plays a vital role in the inertial confinement scheme, in the form of parametric instabilities. In the inertial confinement scheme a solid fuel pellet composed of deuterium and tritium is impinged with intense laser beams, the energy from these beams ablate the surface layer of the fuel pellet, due to Newton's third law the inner part of the pellet experiences an inward force and compresses. The fuel is then compressed to[2] 100s of g cm^{-3} and temperatures of the order of 10 keV by a shock wave travelling in at 100s of km s^{-1}. The interactions of the laser light with the coronal plasma play a crucial role in the coupling of the laser energy[3]. One of the major issues facing ICF experiments is understanding instabilities; some are moderated by electron plasma waves, some by ion-acoustic waves.

Hot electrons and preheating

In ICF implosions, the compression achieved is the overarching factor in whether a shot can reach ignition. In many experiments it has been found that 'anomalous' hot electrons raise the temperature of the coronal plasma and reduce the compression, and thus neutron yield. This electron 'pre-heating' was predicted early on by some of Kruer's numerical work [22] in which it is found that EM waves with large amplitude propagating near the plasma frequency can excite both ion and electron oscillations in a 1D simulation. 'Strong anomalous heating' is predicted. This heating was subsequently observed in an experiment where a laser ablated a foil target [23]. The plasma temperature was inferred by measuring x-ray emission and energetic x-rays at a few tens of keV were observed and it was suggested that a plasma instability may be producing a hot tail in the electron distribution. It is possible to reduce preheating by including a high Z material

---

[2] Iron: 7.9 g cm^{-3}, Lead: 11.3 g cm^{-3}

[3] Kruer [22] is a popular reference for this area.

in the fuel pellet, between the ablator shell and the D-T ice layer and Kidder determined, for contemporary lasers and ‘reasonable parameters‘ that, given a sufficiently thick shield layer, the energy requirement for a $\approx 1\mu$m laser is over 1 MJ to achieve energy gain from the fuel [24]. Although it was pointed out that a reduction in the wavelength leads to significant reductions in the preheating due to instabilities; 9-fold if the wavelength were halved, 34-fold if the wavelength were cut to 1/3. Indeed, NIF’s laser delivers light in the 300 nm range at ≈ 2 MJ.

NIF utilises ‘indirect drive’ [25], where the fuel pellet is placed inside a high conductivity capsule called a Holhraum. The lasers are directed through apertures in this Holhraum and allowed to impinge on the inner walls as opposed to the target itself. The inner metallic surface then radiates a ‘bath’ of x-rays symmetrically about the fuel pellet, thereby improving implosion symmetry. Another approach, however, is to use ‘direct drive’ [26] where the lasers impinge directly on the fuel pellet. Although managing asymmetry is more difficult, the benefit is reduced loss of the laser beam energy. One such apparatus developing this approach is the OMEGA facility, although OMEGA’s laser is much less powerful at 26 kJ, the coupling is ≈ 4 times more efficient [27]. It is hoped that, if the issues surrounding non-uniform target illumination are solved, that a NIF equivalent laser could yield significantly more fusion energy output. These predictions rely on the accuracy of ‘hydrodynamic scaling’ codes [28]. However, these codes do not take into account the instabilities and non-linearity that will inevitably occur when the experimental work is scaled up and there has been evidence of the two plasmon decay (TPD) in direct drive experiments [29].

The shock ignition scheme [30] may ultimately use laser plasma instabilities to its benefit, it has been shown that the two plasmon decay observed at OMEGA reaches a saturation for this method and subsequently become negligible at the high pressures obtained [31] and stimulated Raman scattering (SRS) takes over which, Weber argues, could benefit compression without preheating the fuel. Experimental observations of X ray emissions indicate the presence of supra-thermal electrons due to SRS in implosion experiments using the OMEGA laser [32]. Although it has subsequently been shown that the interplay between TPD and SRS is a matter of optimisation of the fuel pellet structure; falling on the wrong side of parameter space can lead to the hot electrons degrading the compression due to preheating [33].

Ions in laser plasmas

Instabilities are not solely the domain of the extremely hot electrons in these extreme laser plasmas. The ions are also incredibly energetic and under the action of intense laser fields. Problems arise in the form of Brillouin scattering, where electromagnetic waves couple to an ion-acoustic wave and cause back-scattering that can damage laser systems; this was identified as early as the 1970s [34]. Kruer later provided theory and numerical modelling relevant to indirect drive ICF [35], explaining that smoothing techniques like the four-colour scheme are responsible for setting up Brillouin scattering. In the four-colour scheme the laser beam is composed of 4 separate frequencies with small offsets and thus the parametric instability can take hold as it is a beat wave phenomenon. This has the effect of transferring some of the back-scattered energy between the incident laser beams in the Holhraum. Indeed, this effect was observed in short order in the laboratory [36]. This so-called ‘cross beam energy transfer’, or CBET is now used to control implosion symmetry on indirect drive experiments [37]. The direct drive approach does not benefit from this process, the energy transfer between the beams results in a loss in energy coupled to the pellet, as much as 20% [38]. Although modelling efforts are underway to understand this instability in the context of direct drive [39], there is still a long way to go for this scheme.

1.2 RF discharges

1.2.1 Inductively coupled plasmas

An RF plasma source is used as the basis for the apparatus as they have shown to be (relatively) simple, cost effective and scalable. The source can operate in two modes, as a helicon when operating with its solenoidal magnet coils; or as an inductively coupled plasma (ICP) without the magnets. These sources are also sometimes referred to as 'Transformer Coupled Plasmas' (TCP) or 'RF Inductive Plasmas' (RFI) [40, Chapter 12] and have become an area of great interest as a way of energising plasma in reactors for plasma materials processing [41,42] and as a scientific tool for atomic emission spectroscopy [43] as well as mass spectrometry [44]. The spectroscopy context is quite far removed from the present apparatus, typically taking the form of the 'plasma torch', a high pressure jet of gas flowing through a solenoidal coil and becoming ionised. However, the materials processing context is much closer to the apparatus of this thesis, typically employing gas pressures less than 100 Pa [41]. There are 3 main categories of inductively coupled plasma; the helical source of Hittorf [45], the flat spiral antenna and the immersed antenna [41,46]. A 4th, slightly more unusual ICP is the 'transformer' source [47], where an evacuated glass tube wraps around the 'primary' of a transformer and allows the plasma to act as the secondary.

The helical inductively coupled plasma source is highly scalable [40], from materials processing pressures < 10 Pa such as in [48] and [49], to the atmospheric jets employed in the aforementioned spectroscopy diagnostics. Since the first inductive plasmas were of the helical type, much more theoretical treatment has been given to the problem of the coupling and operation of these devices. In an ICP the discharge is sustained (when the density is high) by the action of the so-called 'inductive' part of the electric field, where currents are generated through Faraday's law. The larger body of evidence and theory supporting the helical sources make an introduction from this perspective more complete than if one were to begin with the flat spiral of interest in this apparatus. In principle the flat spiral employs the same physics, but in a more difficult geometry since the cylindrical symmetry and better coupling of the helical type is no longer applicable.

The first reported experiments involving a plasma generated by an induction coil were reported in 1883 by the aforementioned Hittorf in a paper titled 'On the electrical conduction of the gases'[4], with a follow up experiment conducted a few years later by J.J. Thomson [50]. Thomson described an experimental setup where Leyden jars are rapidly charged and discharged through a wire wound around an evacuated glass tube that had been back-filled with a small amount of various gas samples. This early work is the first reference to the 'ring discharge' as these inductive sources had been found to exhibit a ring-like structure in their optical emission. Many fascinating observations are to be found in this study, such as the separation of the plasma into 2 parts by use of an electromagnet, as well as an early example of enhancing confinement using a magnetic field. However even in this early work, which precedes Thomson's own discovery of the electron (1897), an important aspect of how the RF power is coupled to the plasma is acknowledged. This being the distinction between electrostatic and 'electromotive' (inductive) coupling. The electrostatic contributions are that part of the electric field from Gauss' law, while the so-called 'inductive electric field' ('electromotive') is that part from Faraday's law. Such a distinction is important for understanding the apparatus presented in this thesis as most of the experiments have been carried out in the regime where electrostatic coupling dominates, owing to its low density aligning with the overall objectives of microwave scattering studies. This mode of operation is now commonly referred to as the low density 'E-mode', in contrast with the high density 'H-mode' and a source operating in the E-mode is,

---

[4] The original paper in German is titled 'Ueber die Electricitätsleitung der Gase'.

strictly speaking, a capacitively coupled plasma. However, the present apparatus is referred to as an ICP when the field coils are off so as to not confuse it with the style of discharge where parallel plates are used to provide the oscillating electromagnetic field; in that scheme the plates are often in direct contact with the plasma. In a modern setting it is now known that both coupling mechanisms play a role in any ICP.

In an attempt to isolate the inductive influence, Thomson installed a Faraday screen between the induction coil and the glass tube, thereby blocking the electrostatic field and allowing the discharge to be analysed solely from the perspective of the inductive electric field. Many years later, Thomson presented his mathematical theory of electrodeless discharges in which all currents sustaining the plasma are taken to be from the magnetic forces of the induction coil surrounding the vessel [51]. He showed that a direct capacitive plasma, where parallel plates are in contact with the gas, requires only half the electric field to sustain it compared to the induction coil. Already observed experimentally, he showed theoretically that there is an optimum pressure at which these discharges operate; that is, the pressure at which the mean free path for an electron is equal to the distance traversed in one RF period:

$$\lambda_{mfp} = \frac{v}{\nu}. \tag{1.1}$$

Thomson also described the two competing mechanisms governing the role of the neutral gas pressure in the coupling of AC power. At high pressures, Thomson found that the minimum magnetic field $\vec{B}$ required to sustain the discharge is proportional to the gas pressure:

$$B_{crit} = \frac{v_{\perp}^2 m_e}{r_v e \lambda_1 f}, \tag{1.2}$$

where

f is the frequency,
λ_1 is the gyro arc length
$v_\perp$ is the electron's tangential velocity,
m is the electron mass
r_v is the discharge radius and
e is the electron charge

Where the derivation has taken into account that at high pressures the scale length λ_1 is moderated by electrons colliding with the gas before reaching a sufficient kinetic energy for impact ionisation. At low pressure the mean free path is much greater and the scale length parameter changes to describe the arc length traced by the electron during a half period of the AC; the minimum field strength becomes:

$$B_{crit} = \frac{\lambda_2 f m_e}{r_v e}. \tag{1.3}$$

This is to say that, in high pressure gasses, the limiting factor in plasma production is the electrons being unable to receive the all the energy available from the fields. In AC fields the charges attain a maximum velocity twice in one period; for each half period the electron is accelerating. If the electron's excursion is blocked by a gas particle it will not be able to reach its maximum, decreasing the coupling efficiency. Thus, as the pressure increases, it becomes more and more difficult to ionise the gas. This is in contrast to the low pressure regime, where the mitigating factor is electrons colliding with the gas less than twice in a period. Then the typical electron is able to go past its maximum energy and experience the reverse part of the oscillation. When this electron does eventually collide it will be less than its maximum, decreasing the efficiency. Thus as the pressure gets lower, and the mean free path larger, it gets more and more difficult to ionise the gas.

Later, Townsend disagreed with the purely inductive theory [52], claiming the electrostatic potential across the driving solenoid is the driving factor for this kind of discharge. Using a simple LC circuit model, the fields inside the solenoid can be determined; first the electrostatic field, simply given as,

$$E_s = \frac{V}{l} = \frac{L}{l}\frac{dI}{dt}, \tag{1.4}$$

where

V is the voltage drop across the coil

l is the length of the solenoid,

L is the solenoid self inductance and

I is the solenoid current

Then the 'inductive field' at a point r inside the discharge is found in terms of the magnetic field B as

$$E_m = \frac{r}{2}\frac{dB}{dt}, \tag{1.5}$$

finding that the ratio of E_s/E_m is

$$\frac{E_s}{E_m} = \frac{2\pi n_t r_{sol}^2}{r}, \tag{1.6}$$

where

n_t is the turn density (m^{-1}) and

r_{sol} is the solenoid radius.

Consider a 'typical' turn density of 100 m^{-1} and a radius of 5 cm. The lowest value of the ratio eq. (1.6) will occur when $r \approx a$ and the resulting value is around 30. Thus, Townsend argued the main contribution to the discharge must be the electrostatic field and not, as Thomson proposed, the inductive field. This simple circuit analysis neglects the parasitic capacitance of the solenoid and does not hold if such effects are comparable to the capacitance of the 'condenser' in the driving circuit. Townsend was aware of this limitation and conducted several experiments to directly measure both fields in an inductive discharge; he found the ratios to be ≈ 40 in that particular apparatus; not too far from the value for negligible parasitic effects.

In response to this debate, MacKinnon [53] conducted a systematic study of iodine and mercury discharges, owing to their sharp optical transitions under certain conditions. It was found that these discharges can operate in 2 modes, one electrostatically dominated and one inductively dominated. The electrostatic mode of the discharges occurred at 'low excitation' and exhibited a diffuse 'glow' from the walls of the glass tube while the inductive mode took the form of a bright ring. To show the electrostatic nature of the glow discharge, the apparatus was calibrated so that the ring discharge was present. A fraction of the glass cylinder was then covered in a conducting foil and the resulting discharge exhibited rings in the portions of the vessel not covered by foil, while the glow mode was mostly unaffected. In another demonstration, MacKinnon showed that for fields large enough to excite the ring mode with the tube, one may move the tube outside of the solenoid and find the ring discharge will not be produced. However, a glow discharge will be possible. This is due to there being no inductive field outside of a solenoid, while the electrostatic portion remains finite.

It was subsequently shown by Kunz [54] that the discharges coexist in many experiments. By extending the theory of Thomson, it was predicted that there is a shift in the resonant frequency of the circuit when the ring discharge occurs; this shift is positive valued and grows slowly with the plasma conductivity. However, it is pointed out that Tykociner found, experimentally, that the resonant frequency downshifted in practice [55]. Thus, Kunz explored the frequency shift that ought to be caused by an electrostatic glow discharge in the weak excitation regime, finding that its resonant frequency is ‘small’ compared with the RLC circuit’s resonant frequency before the presence of the discharge. Thus, these discharges have significant coupling in both the electrostatic and electromagnetic sense.

On the closing of the question on whether these discharges are electrostatic or electromagnetic, the interest in these discharges declined [56]. Recently, some renewed interest has spurred measurements with more modern techniques. Amorim [48] describes a small bench sized discharge a few cm in diameter and about 25 cm long, operating in argon at powers up to 400 W. The transition between the E-mode and H-mode is observed to occur at $\approx$ 250 W in a discharge of pressure $\approx$ 20 Pa, while at $\approx$ 9 Pa the transition occurs at just under 400 W. It is observed that at lower pressures under 4 Pa the sharp jump in density with increasing RF power is not observed. The authors claim that the transition is now a smooth one; although it may just be the transition was out of reach for the RF equipment.

In a different pressure regime and slightly larger vessel [46], Suzuki et al. provides analytic expressions for the ‘power transfer efficiency’ of an inductively coupled plasma. In this 50 cm diameter by 50 cm long vessel employing a variety of loop antennas, both external and immersed, it is shown that the E-mode to H-mode jump occurs in plasmas in a pressure range 0.01 to 1 Pa. It is found experimentally that an inductive antenna immersed in a plasma provides better electrostatic coupling than an external one of identical geometry. It is also found that the immersed antenna provides a smoother transition between the capacitive and inductive modes. Here the inductive mode is again represented as an equivalent circuit where the RF antenna is the primary coil of a transformer and the plasma taken to be the secondary. The total power dissipated in the plasma is eventually shown to be proportional to the plasma inductance. An important detail is that the plasma inductance is modelled as two distinct inductors in series; one inductor represents the inductance due to the overall geometry of the plasma and the other representing ‘electron inertia’ or ‘kinetic inductance’. This kinetic inductance represents the finite time taken to accelerate charges under the action of an electric field due to their inertia, which results in a phase ‘lag’ of the resulting fields. The resulting behaviour is identical to the back-EMF due to the self inductance of a conductor. Both the ‘geometry’ inductance and ‘kinetic’ inductance are of similar order and both must be taken into account to get an accurate representation of the inductive coupling efficiency. Overall this turns out to be proportional to the plasma density for typical laboratory plasmas. The capacitive mode follows an almost identical pattern for the power dissipated, except the equivalent circuit gives the plasma as a branch in parallel with the antenna instead of a transformer coupling. Now, the plasma is decomposed into 2 capacitive components in series, being given as the capacitance of the dielectric window and the capacitance of the sheath adjacent to the window. For a typical apparatus the sheath capacitance dwarfs the dielectric’s and thus the total can be found from just the dielectric capacitance. The coupling efficiency then becomes inversely proportional to the electron density. This is an important development as it shows the sharp transitions and unbalanced coupling arise due to the disparity in the capacitance of the dielectric and the discharge. Were commonly available glasses to have much higher dielectric constants the behaviour of these discharges would be significantly different. This is seen to small effect in the aforementioned immersed antenna, the disparity between sheath and dielectric capacitance is much reduced due the geometry.

Lastly, Lee and Chung [57] provide some insight into the stability requirements of each of the ICP modes in terms of power and pressure. The analysis is based on the helical configuration since the symmetry makes the problem more tractable. As well as a sudden jump in density, the transition from E-mode to H-mode in an

ICP is accompanied by a hysteresis effect. The difference in the critical power has been reported to be as much as 20 W and is related to the non linear relationship between the power coupling and the plasma density. It was already known that the change to the H-mode was related to the skin depth becoming comparable with the dimensions of the vacuum vessel [58] but a more rigorous relationship between critical density and power with properties such as pressure and vessel size are possible. This is achieved by solving Maxwell's equations for the given geometry and calculating the Poynting vector directly. The Maxwell equations are given as:

$$\vec{\nabla} \cdot \vec{E} = 0 \text{ (quasi-neutrality)}, \tag{1.7}$$

$$\vec{\nabla} \cdot \vec{B} = 0, \tag{1.8}$$

$$\vec{\nabla} \times \vec{E} = -i\omega\vec{B}, \tag{1.9}$$

$$\vec{\nabla} \times \vec{B} = \mu_0\vec{J} + i\omega\epsilon\mu_0\vec{E}, \tag{1.10}$$

where

ω is the drive frequency

$\vec{J}$ is the conduction current,

The time derivatives have already been taken, assuming a frequency ω. The second term on the RHS in eq. (1.10) is the displacement current. This set of equations are separately solved in the case of the electrostatic and inductive ($\partial E/\partial t \equiv 0$ in eq. (1.10)) mode. Upon finding the electric and magnetic fields the power is found in the usual way:

$$P = \mathrm{Re}(\frac{1}{2}\int \left(\vec{E} \times \vec{B^*}\right) d\vec{A}) \tag{1.11}$$

Both the capacitive and inductive power deposition are found to be parabolic as a function of density with the capacitive mode having a maximum at a significantly lower electron density. The total power is then simply taken to be the sum. This EM field power has to be balanced with the power dissipated by the plasma and Lieberman's [40] expression is linked to the plasma density and is balanced against the drive EM fields controlled by the antenna current. Thus for a given antenna current the resulting plasma density can be found. However, if at such a point the power in the fields is growing faster (with density) than the plasma dissipation, any small fluctuation that increases the electron density will cause a power imbalance in favour of increasing ionisation, causing a runaway growth in the electron population. This is eventually stopped by the plasma becoming too dense and acting to screen some of the EM power, a stable balance is reestablished and the discharge is now in the H-mode. It is then shown the transition point is marked by the collision frequency and field frequency being equal. In the collisionless regime the skin depth is not a function of pressure and so the critical density is nearly independent of pressure. In the collisional regime the critical density begins to increase rapidly with pressure. Thus for a low pressure laboratory plasma it is expected the critical density should be reasonably static for a range of parameters, while an application such as a plasma torch at atmospheric pressure will have a critical density that is a strong function of the pressure.

1.2.2 Helicon sources

A natural extension of the ICP is to confine the discharge with a magnetic field. When these discharges have a strong, external, static, bias magnetic field parallel to the axis a plasma wave mode known as a helicon wave [59] (as given by [60]) is enabled that enhances the RF coupling and produces a much higher density and temperature discharge. A recent and very thorough review by Chen [60] provides excellent detail on the landmark works in theory, computations and experimental work and therein lies a more expansive introduction. However, some key highlights bear relevance to the present apparatus.

Lehane and Thonemann [61] made the first experimental measurements of helicon waves and discharge properties. Their apparatus was able to excite both the $m = 0$ and $m = 1$ wave modes (discussed later), identifying that these waves exist between the ion and electron cyclotron frequencies as the bounded solution to low frequency whistler waves. Measurements of the attenuation of the wave and their amplitudes were made in both modes, giving good agreement with the previously established theory [62]. Using Langmuir probes and interferometry, typical average electron densities of 10^{19} m^{-3} were achieved in a discharge tube 10 cm in diameter and 1 m in length using Xenon at pressures of a few Pa. The mode number m of a helicon wave determines its structure and is related to the antenna used to excite the plasma. Chen [63] gives the solutions for the electromagnetic fields as well as the field patterns for both modes.

The $m = 0$ mode is excited by a flat spiral antenna in most cases, the geometry being similar to that of many material processing ICPs. The fields in this mode are azimuthally symmetric and Chen's solution for the electric field gives an idea of their behaviour:

$$E_r = A\omega \left(\frac{k}{k_z}\right) J_1\left(Tr\right)\sin(\phi), \tag{1.12}$$

$$E_\theta = A\omega J_1\left(Tr\right)\cos(\phi), \tag{1.13}$$

where

E_r is the radial component

E_θ is the azimuthal component

A is the amplitude,

ω is the wave angular frequency,

k is a total wavenumber for the helicon,

k_z is the axial (propagation) wavenumber,

J_1 denotes a Bessel function of the first kind,

T is the transverse wavenumber,

ϕ is the wave phase.

The important feature of this solution is the lack of dependence on the angular coordinate θ, indicating this mode is azimuthally symmetric. Because the radial and azimuthal components are phase shifted by $\pi/2$, the total pattern moves between fully radial (electrostatic/ capacitive) and fully azimuthal (electromagnetic/ inductive) during an RF cycle. The electrostatic and inductive coupling discussion regarding ICPs is of great significance to these discharges. Note, the parameter k in eq. (1.12) is inversely proportional to the B-field, thus the electrostatic coupling becomes less dominant as the axial B-field is increased. Indeed, the density jumps concordant with the transition between the E-mode and H-mode are observed in helicon sources. The results of Chi et al [64] from their investigation using a helicon source with a saddle antenna (discussed shortly), reveal 5 distinct modes for the discharge, each characterised by its own density jump. The lowest 2 modes are found to be the usual E and H modes from the simple ICP. A 3$^{\text{rd}}$ mode appears when the helicon wave is able to satisfy a cavity resonance within the confines of the vessel. A further 2 mode jumps can occur, corresponding to higher order modes for the cavity resonance. Surprisingly, the last 2 modes are dominated by the propagation of the azimuthally symmetric $m = 0$ mode, in spite of the source of the discharge being the $m = \pm 1$ saddle antenna fig. 1.1. Chi claims this to be the first observation of a saddle antenna exciting the $m = 0$ helicon mode.

It is also known that a second plasma wave mode exists in these devices, the Trivelpiece-Gould mode. Early treatments by Klozenberg make the assumption that the plasma is highly collisional, noticing that this simplifies the Bessel equa-

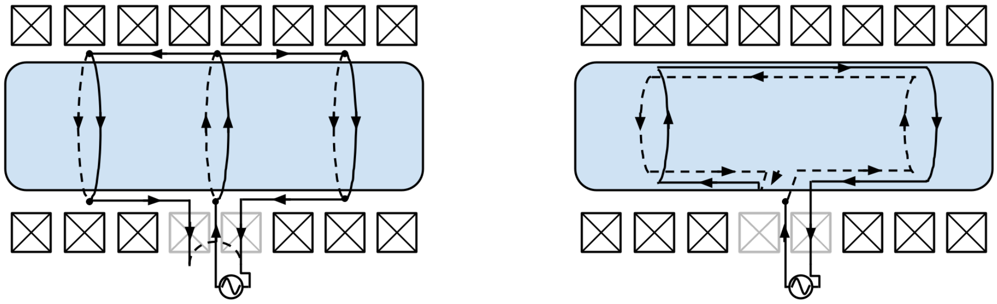

((a)) Nagoya type III ((b)) Boswell saddle

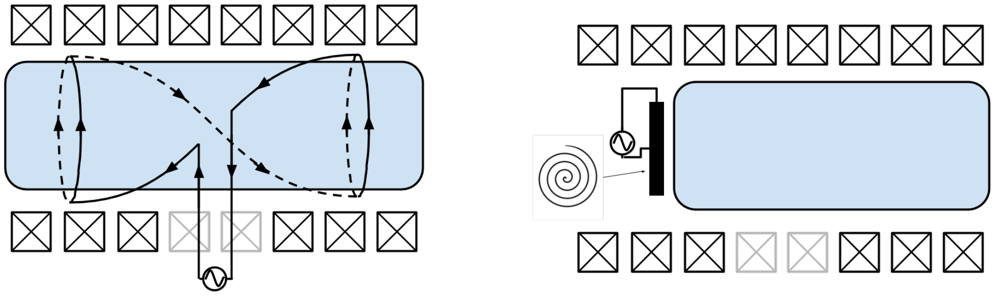

((c)) Twisted helix ((d)) Flat spiral

Figure 1.1: Common helicon antennas

tions. This simplification implies the plasma dielectric constant has been made entirely real, thus the impedance is entirely real. Boswell recognised that including a mode with such an effect would lead to increased damping and power deposition which motivates the derivation of the dispersion relations for this radially propagating mode [65]. This has since become known as the ‘Trivelpiece-Gould’ mode. Chen and Arnush later provide a ‘generalised’ theory where both modes are included in the solution [66, 67].

The exciting antennas for a helicon have several designs (fig. 1.1). The $m = 0$ antenna is usually a spiral [68] or a single loop [69]. However, the $m = 1$ antennas have a more complicated geometry. The Nagoya type III antenna of Watari et al [70] employs the splitting of a conductor around the centre of the discharge tube, then further splitting the current, sending it parallel with the axis of the tube before again forming a ring at the end. At the bottom of this ring the current is then fed back to the entry point. This design has the effect of having opposing currents above and below the axis as well as an asymmetry in the directions of the ring currents around the tube. This leads to a buildup of charge and a large amplification of the electrostatic fields. A useful development by Boswell is the saddle antenna that achieves much the same mechanism but has a split, allowing it to be more easily attached and removed from a vessel [71]. Lastly, the helical antenna [72], that most closely resembles the solenoid seen in the helical ICPs. This antenna resembles the Nagoya antenna but is twisted into a helix and has the electrical path similar to 2 solenoids twisted with anti parallel axes, with each of those currents exciting the $m = \pm 1$ waves. Each of the 3 antennas in fig. 1.1(a) - fig. 1.1(c) can be used to excite helicon discharges along the entire length of a dielectric vessel, or around a spool to be used as an ionization chamber that feeds into a larger stainless steel expansion chamber, allowing for easier experimental access.

The apparatus presented in this thesis operates with a spiral antenna in the $m = 0$ helicon mode (provided the axial magnetic field is present), although the apparatus could be converted to use an $m = 1$ antenna by the addition of a glass spool, the simpler implementation and field symmetry of the spiral is preferred; this aids both construction and computations. Shinohara is a key figure in helicon research involving $m = 0$ sources and has built several machines over the last 30 years. The earliest report [68], where Shinohara claims to have the first experimental evidence of launching the $m = 0$ mode using a flat spiral antenna, describes a vessel 1.7 m long with a diameter of 46 cm. The antenna at one end of the vessel is a 4 turn copper spiral with a diameter of 18 cm (similar to the antenna presented in chapter 3) and is mounted to an 8 mm thick quartz window. As with ICPs, the dielectric constant plays a key role in the mechanisms behind the mode transitions and density jump and this material is different from the borosilicate plate used in the present apparatus. Using 7 MHz RF with typical powers of 2kW and an axial B-field of 3.6 mT, an argon plasma of $n_e \approx 10^{18}$ m^{-3}

and $T_e = 2$ eV is produced for pressures at a few 10s of Pa. Helicon waves are expected since the drive frequency lies between the lower hybrid (on the order of a few 100s of kHz at 3.6 mT) and the electron cyclotron frequency (≈ 100 MHz). This is confirmed by measurements of the magnetic field across the radius of the antenna which show the fields following the correct shape of Bessel function associated with the $m = 0$ mode number. In the helicon mode the introduction of a Faraday screen, like those in ICP experiments, reduces the power transfer efficiency of the antenna; this indicates a significant electrostatic component of the helicon and TG waves. Later [73], the axial field variation is measured and found to follow the predicted dispersion relation, although the waves are damped much more aggressively than expected, with Shinohara commenting that Landau damping would be expected to have a characteristic length on the order of a few metres for this plasma, in contrast to the ≈ 30 cm measured here.

Another interesting investigation on this particular apparatus involves a radical departure from the usual antenna configuration, where the axially aligned spiral antenna is replaced by an antenna mounted on the side of the chamber (i.e. launching across the radius) [74]. The helicon wave is still easily coupled and dense (6×10^{16} m^{-3}) plasma of $T_e = 3$ eV is still produced. It should be noted that it appears a higher axial field is used here (100 mT compared to 3.6 mT), for a less dense plasma. However it does show that it is not a requirement that the antenna must be axially mounted. Several antenna designs are tested and Shinohara finds that so-called ‘ladder’ antennas are less efficient than loop antennas or spirals, suggesting that any antenna geometry which allows for anti parallel currents to flow near each other will reduce the overall effective coupling of the antenna. It is also shown that an internal antenna can also excite the helicon wave effectively.

In the axial spiral antenna regime, an investigation of the effects that conducting obstacles have on the plasma profile is carried out [75]. Electrodes with a variety of geometries are placed downstream of the exciting spiral antenna and their effect on the plasma radial profile measured as a function of their DC bias voltage. The first electrode is a small flat disk with its surface parallel to the $r - z$ plane (perpendicular to the antenna plane). It is found that biasing the electrode positive slightly increased the peak density on the axis of the system, which already had a parabolic profile to begin with; biasing negative had no effect. The behaviour was similar for an electrode constructed of concentric thin cylinders (axis aligned with that of the vessel and spiral antenna), but the change in peak density was significantly higher. These electrode configurations share a similarity in that their surfaces are perpendicular to the plane of the exciting antenna. Therefore, 2 other electrodes were tested, this time with surfaces parallel to the plane of the helicon antenna. First, an annular electrode at positive bias was found to behave in the same way as before, causing an increase in the peak density. However at negative voltages this electrode caused a flattening of the plasma profile such that its radial profile has a plateau shape with a width on the order of the biasing electrode. Lastly, a simple disk with surface parallel to the antenna plane was placed in the discharge. It was found that without any bias applied, the presence of the electrode caused a reduction in the peak density and the profile across the diameter had a ‘hollow’ in the centre. A positive bias caused this valley to deepen, while negative potentials caused the usual peaked parabolic profile to return. In a further exploration [76], the biasing electrode takes the form of concentric rings parallel to the antenna plane. It is shown how the profiles are altered when different rings can be independently biased. For a 3 ring setup it was shown that when no bias is applied on any ring the aforementioned ‘valley’ profile is present. However, biasing the 2 outer rings to a positive potential returned the peaked profile The explanation given is that the positive electrodes draw electron current parallel to the background field and so reduce the density at that region. While when the outer electrodes are negatively biased the relatively positive inner ring depletes the electron density and deepens the valley in the radial profile. A study with a 10 ring electrode showcases the incredibly fine control of the plasma profile that is possible with this kind of setup. Also observed is a rotation of the plasma in the azimuthal direction, downstream of the electrode, which looks to be caused by the $\vec{E} \times \vec{B}$ drift set up by the electrode field and axial B-field.

In a different discharge using loop antennas to excite $m = 0$ helicon waves [77], Shinohara investigates mode jumps in helicons and finds the method of power balance similar to that used for ICPs [57] predicts mode jumps reasonably well. A model for predicting the plasma impedance also appears to be corroborated by experiment and could allow for analysis of these discharges as an equivalent circuit model. A few years later, Shinohara reports on a new ‘very large’ helicon source [78], again driven by the flat spiral antenna in the $m = 0$ mode. To date this is the largest demonstration of a helicon plasma, with a diameter of 75 cm and a length of 4.86 m, giving a volume of 2.1 m^3. Although other apparatus have similar [79] or greater [80] volumes, they rely on diffusion chambers and do not fill the entire volume with dense plasma. This apparatus is lined with 14 magnet coils that typically run with a current of 50 A, providing an axial B-field of 14 mT along most of the vessel. Typical operating pressures are 0.03 Pa to 0.3 Pa in argon and the device shows very low threshold powers of less than 1 W at 7 MHz, which is claimed to be due to the good capacitive coupling at low powers. Helium is usually more difficult to ionise than argon due to its higher ionisation potential but Shinohara demonstrates the ease with which this apparatus creates a helium discharge at just 10 W of RF power when the B-field is at 14 mT with a pressure of 0.3 Pa. The helium discharge becomes much more difficult to start at the bottom of the pressure range and Shinohara advises the use of a hot tungsten wire to provide a small seed population of free electrons to help startup in this regime. Lastly, modest control of the radial profile of the plasma is demonstrated by simply adjusting the current in some of the field coils near the antenna, showing once more the great versatility of these devices and their promise as both a fundamental physics tool and potentially as a processing plasma.

A plasma processing helicon was developed by Tynan et al [81] in the form of the MORI reactor. This reactor is similar to that of some flat spiral ICPs, a set of permanent magnets provide the axial B-field and the antenna and matching circuit are built into the machine. It operates in the $m = 0$ helicon mode. This reactor makes use of some of the radial profiling techniques discussed to provide a uniform density ($10^{17} - 10^{18}\mathrm{m}^{-3}$) and temperature ($T_e = 3 - 4$ eV) across most of the diameter of the device, giving more uniform etch rates for the substrate at the bottom of the reactor. Another helicon source, the 'controlled shear decorrelation experiment' (CDCX) has been used to support investigations of sheared flows that are significant to cross-scale turbulence mixing and suppression in tokamaks. This experiment [82] makes use of annular electrodes downstream of the antenna to create the azimuthal plasma flow, allowing investigation of this phenomenon in an environment that is less harsh for diagnostics compared to tokamaks. Helicons have also found interest for thrusters, as a way to generate plasma for a new generation of hall effect thrusters [83] and in the VASIMR concept [84] wherein a helicon provides a helium discharge that flows downstream to an ICRH antenna that accelerates ions and provides thrust. Shinohara has also worked on miniaturisation of helicons for extremely small satellites. In a recent review [85], mm sized discharges are described, with the smallest being the 0.5 mm diameter 'small helicon device' (SHD) [86] with $n_e > 10^{16}\mathrm{m}^{-3}$.

1.3 RF Plasma Requirements

Modern tokamaks, as outlined, present difficulties to microwave heating and current drive techniques [87]; while laser fusion experiments are hampered by parametric instabilities such as Raman and Brillouin scattering [27, 88]. The prevalence of these processes in inertial confinement literature means these are a pragmatic starting point as the present apparatus is only rescaling from optical to microwave frequencies. Thus, the initial campaign will focus on these unmagnetised modes, establishing the proof of concept at these scale lengths in a simplified regime while providing additional insights relevant to laser-plasma interactions. The next campaign will then build on this understanding by confining the plasma with a magnetic field to investigate the dynamics of these beat wave couplings when the modes are magnetised. The modes involved in this scenario are expected to be oscillations at the electron cyclotron or upper hybrid resonant frequencies which are useful for heating and current drive in tokamaks [89] and previous work in this area has shown it would be possible to couple energy to these modes via non-linear beat wave couplings [90]. The ultimate goal in this investigation would be to demonstrate controlled and targeted non-linear excitation of plasma resonances using microwaves at the necessary normalised intensities.

Raman scattering theory is covered in more detail in the next chapter; but there is a critical plasma density below which the instability cannot occur, that being $2\omega_{pe}$. Since the available microwave amplifiers are operating at $f \approx 10$GHz, this limits the plasma frequency to 5 GHz and implies a maximum electron density of 3×10^{17} m^{-3}. Inductively coupled plasmas and helicons powered by RF sources in the range of 100s of W to a few kW can provide these densities of $10^{15} - 10^{18}$ m^{-3}. The maximum density achieved in this thesis is $n_e \approx 3 \times 10^{15}$ m^{-3} [41,60]. For context, the plasma densities reported in the Mega Ampere Spherical Tokamak Upgrade (MASTU) can reach $n_e \approx 10^{20}$ m^{-3} [91], corresponding to a plasma frequency of 90 GHz, requiring greater than 180 GHz microwave sources to trigger Raman scattering. A beat-wave driven electron cyclotron wave, on the other hand, would exist in a 0.5 T magnetic field on MASTU which implies a cyclotron resonance frequency $\Omega_e = 14$ GHz. Thus a beat wave drive would require two signals greater than 90 GHz and differing by 14 GHz. In the present apparatus the magnet coils are estimated to be capable of providing fields up to 87.5 mT when all 8 coils are fitted, corresponding to a cyclotron frequency of 2.4 GHz.

Aside from satisfying the theoretical constraints for wave propagation and coupling imposed by the frequency of the available high power microwave sources, the experiment intends to provide an environment that enables the use of insertion diagnostics, normally not possible for either type of fusion plasma. Inertial confinement experiments are too small in both length and time scales to implement Langmuir probes. Although magnetic confinement experiments are large enough to host probes, the central part of the plasma is far too hot and temperatures of several keV will destroy Langmuir probes. This apparatus operates at a much lower temperature, < 2 eV in the inductive mode while $T_e < 10$ eV is expected in the helicon mode. Thus Langmuir probe diagnostics can be a main feature of the diagnosis. Additionally the continuous wave operation of the source eliminates any ‘shot to shot variability’ concerns.

Chapter 2

Background theory

2.1 Parametric wave coupling and wave mixing

2.1.1 Raman scattering

Raman scattering is an instability in which an incident transverse electromagnetic wave couples into a growing electrostatic Langmuir oscillation and a scattered light wave [88]. The condition for conservation of energy and momentum in this process is given by

$$\omega_0 = \omega_s + \omega_{ek}, \tag{2.1}$$

$$\vec{k_0} = \vec{k_{sc}} + \vec{k_{ek}} \tag{2.2}$$

where ω_0 is the incident EM wave frequency, ω_s is the frequency of the scattered EM wave, and w_{ek} is the electron plasma wave frequency. The minimum incident frequency that will cause this scattering will be $\omega_0 > 2\omega_{pe}$ which, in terms of the plasma density is the requirement $n_e < \frac{1}{4}n_c$, n_e being the electron density and n_c being the critical density. The instability occurs when an incident EM wave meets a longitudinal density perturbation caused by an electrostatic Langmuir wave. The transverse polarisation of the EM wave will cause electrons to oscillate in the transverse direction, with the resulting current producing a new EM wave in the plasma. This will beat with the incident EM wave with a spatial structure matched to the electron plasma wave, the wave pressure associated with the anti-nodes will enhance the plasma modulation. A feedback loop will occur as long as the growth rate of the instability overcomes the damping rates of the electron wave and the scattered EM wave. The growth rate with damping γ is given by

$$(\gamma_i + \gamma_{ES})(\gamma_i + \gamma_{EM}) = \gamma_0^2. \tag{2.3}$$

With a threshold condition that the damping of the electrostatic and electromagnetic oscillations must be overcome such that

$$\gamma_0 > \sqrt{\gamma_{ES}\gamma_{EM}} \tag{2.4}$$

where γ_{ES}, γ_{EM} are the damping rates of the electron wave and the scattered wave respectively and γ_0 is the growth rate when damping is neglected. The growth rate can be expressed in terms of the plasma and wave properties as

$$\gamma_0 = \frac{1}{4} k_{sc} v_{os} \sqrt{\frac{\omega_{pe}^2}{\omega_{ek}\omega_s}}, \tag{2.5}$$

with v_{os} being the oscillation speed of the electrons in the electric field of the pump wave and ω_{ek} is the frequency of the electron plasma wave ($\omega_{pe} \approx \omega_{ek}$). Kruer finds that equation (2.4) can be expressed as [92]

$$\gamma_0 > \frac{\nu_{ei}}{2} \frac{\omega_{pe}}{\omega_s}, \tag{2.6}$$

where ν_{ei} is the collision frequency of electrons with ions. Substitution of (2.6) into (2.5) gives, upon adopting the normalised quiver velocity (in the classical limit) for the electron $a_0 = \frac{v_{os}}{c}$,

$$\frac{1}{4}a_0 k_{sc} c\sqrt{\frac{\omega_{pe}}{\omega_s}} > \frac{\nu_{ei}}{2}\frac{\omega_{pe}}{\omega_e} \tag{2.7}$$

$$a_0 > \frac{2\nu_{ei}}{kc}\sqrt{\frac{\omega_{pe}}{\omega_s}}. \tag{2.8}$$

2.1.2 Brillouin scattering

The Brillouin instability is broadly similar to Raman scattering but the incident EM wave now couples into a scattered light wave and an electrostatic ion oscillation. The frequency and wavenumber matching conditions are similar, though this instability is not as restricted in parameter space since the ion-acoustic frequency $\omega_{ik} << \omega_0 \approx \omega_s$. In inertial confinement fusion experiments it can prevent efficient absorption of the incident laser energy, with one particular case observing absorption being reduced by 20 - 50% [93]. When the scattered light wave is resonantly absorbed, the growth rate of the instability is at a maximum and is given by

$$\gamma_i = \frac{1}{2\sqrt{2}}\frac{a_0\omega_{pi}}{\sqrt{\frac{c_s}{c}}}, \tag{2.9}$$

where c_s is the ion acoustic speed, c is the speed of light and ω_{pi} is the ion plasma frequency. The threshold intensity for this instability to take place is

$$a_0 > \frac{\sqrt{2}\nu_{ei}}{\omega_{pi}}\frac{n_e}{n_c}\sqrt{\frac{c_s}{c}}, \tag{2.10}$$

with ν_{ei} being the electron-ion collision frequency.

This a_0 value can be calculated for a given microwave beam and is given by:

$$a_0 = \frac{\sqrt{2I_0}e\lambda_{pump}}{2\pi c^2 m_e}\sqrt[4]{\frac{\mu_0}{\epsilon_0}}, \tag{2.11}$$

where

I_0 is the intensity of the beam and

λ_{pump} is the wavelength of the microwave beam

since this normalised intensity scales with the beam wavelength, microwaves are much more perturbative than optical lasers for a given intensity. Of course, microwave technology cannot match overall laser intensities, but the increased wavelength does mean they can match the a_0 values of some modern laser-plasma experiments and trigger the same instabilities.

2.1.3 Beat-wave heating and current drive

The non-linear beating of two high frequency EM waves in a magnetically confined plasma can produce longitudinal Langmuir oscillations or obliquely propagating upper hybrid waves [90], the damping of which leads to current drive and heating. The former case can be achieved by injecting two EM waves into a plasma, where the second differs from the first by the electron plasma frequency ω_{pe} and the waves conform to matching conditions similar to those of the scattering processes. Amin and Cairns deduce that the most efficient configuration for maximising the energy of the beat wave is when the pump waves propagate anti-parallel to one another, they also derive an expression for the current drive efficiency in [90]. They define the current drive efficiency η_{bw} to be

$$\eta = \left| \frac{\text{toroidal electron current}}{\text{total input power}} \right|, \tag{2.12}$$

where

$$\eta = \frac{e\, q_\eta R_a \cos\theta_1}{2\pi r_{maj}\, m_e \nu_r v_{||}}. \tag{2.13}$$

R_a is the "relative action transfer" and describes the ratio of energy or momentum transferred to the beat wave, q_η is the "quantum efficiency", e is the electronic charge, θ_1 is the angle pump wave 1 makes with the magnetic field, r_{maj} is the major radius of the tokamak, $v_{||}$ is the resonant electron velocity, m_e is the electron mass and ν_r is the collisional slowing rate of the fast electrons. They calculate the portion of incident power transferred to the beat wave, in 2D in the context of tokamaks to be approximately 29% for JET (Joint European Torus, Culham) and 32% for MTX (Microwave Tokamak Experiment, Livermore).

2.2 Helicons

2.2.1 Dispersion relation

It is argued in [66] that the dispersion relation for helicons can be found from extending the cold plasma theory. Indeed, the helicon mode is just the bounded whistler wave solution to the cold plasma dispersion relation, plotted in fig. 2.1. The cold plasma dielectric tensor is [1], [appendix A]

$$\vec{\vec{\epsilon}}_r = \begin{bmatrix} \mathcal{S} & -i\mathcal{D} & 0 \\ i\mathcal{D} & \mathcal{S} & 0 \\ 0 & 0 & \mathcal{P} \end{bmatrix}, \tag{2.14}$$

assuming the fields vary as $e^{(-i\omega t)}$, taking the direction of the bias magnetic field to define the z axis and the conductivity tensor to be $\vec{\vec{\sigma}} = \frac{\omega\epsilon_0}{i}(\vec{\vec{\epsilon}}_r - \vec{\vec{I}})$ [94], where $\vec{\vec{I}}$ is the unit tensor and $\vec{\vec{\epsilon}}$ is the dielectric tensor. Definitions for the components are in appendix A. With the tensor form for the conductivity and permittivity, Maxwell's equations can be simplified, e.g.:

$$\begin{aligned} \nabla \times \vec{B} &= \mu_0 \vec{J} + \mu_0 \epsilon_0 \frac{\partial \vec{E}}{\partial t} \\ &= \mu_0 \vec{J} - i\omega\mu_0\epsilon_0\vec{E} \\ &= \mu_0 \vec{\vec{\sigma}} \cdot \vec{E} - i\omega\mu_0\epsilon_0\vec{E} \\ &= \mu_0 \left(i\omega\epsilon_0 \vec{\vec{I}} - i\omega\epsilon_0\vec{\vec{\epsilon}} \right) \cdot \vec{E} - i\omega\mu_0\epsilon_0\vec{E} \end{aligned}$$

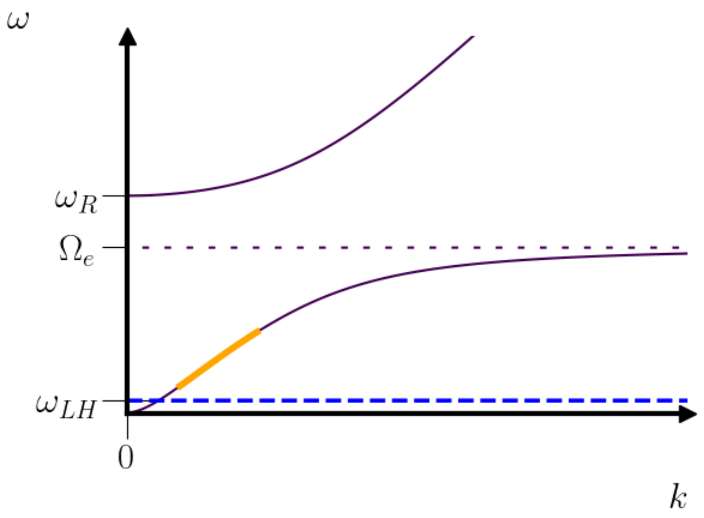

Figure 2.1: Dispersion of the parallel propagating R mode in a magnetised plasma. Highlighted in orange is the whistler branch below the cyclotron resonance Ω_e but above the lower hybrid resonance ω_{LH}. When bounded in a plasma vessel this orange branch is the helicon wave.

$$\therefore \nabla \times \vec{B} = -i\omega\mu_0\epsilon_0\vec{\vec{\epsilon}} \cdot \vec{E}. \tag{2.15}$$

The total current can be written in terms of the dielectric tensor

$$\vec{J} - i\omega\epsilon_0\vec{E} = -i\omega\epsilon_0\vec{\vec{\epsilon}}\vec{E}. \tag{2.16}$$

Combining the conduction and displacement currents into a total plasma current $\vec{J}$ gives

$$\vec{J} = -i\omega\epsilon_0 \begin{bmatrix} \mathcal{S} & -i\mathcal{D} & 0 \\ i\mathcal{D} & \mathcal{S} & 0 \\ 0 & 0 & \mathcal{P} \end{bmatrix} \cdot \begin{bmatrix} E_x \\ E_y \\ E_z \end{bmatrix}. \tag{2.17}$$

From here it is possible to solve for $\vec{E}$ to get the plasma electric field [66]

$$\vec{E} = -\frac{\Omega_e}{\epsilon_0\omega_p^2}\left(i\delta_c\vec{J} + \hat{z} \times \vec{J}\right). \tag{2.18}$$

where Ω_e is the electron cyclotron frequency, ω_p is the plasma frequency, $\delta_c = \frac{\omega}{\Omega_e}$ and ω is the wave frequency while $\vec{J}$ is the conduction current. Chen and Arnush in [66] find a wave equation for $\vec{B}$ using (2.18) and a reduced form of Maxwell-Ampère (neglecting displacement currents) to get

$$\delta_c \nabla \times \left(\nabla \times \vec{B}\right) - k_z \nabla \times \vec{B} + k_w^2 \vec{B} = 0. \tag{2.19}$$

Where

$$k_w^2 = \delta_c k_{sc}^2, \qquad k_{sc} = \frac{\omega_{pe}}{c}, \tag{2.20}$$

with k_w the wavenumber of a whistler wave and k_{sc} the skin number. Making an auxiliary equation for (2.19) gives

$$\delta_c k^2 - k_z k + k_w^2 = 0, \tag{2.21}$$

the roots of which are

$$k = \frac{k_z}{2\delta_c}\left\{1 \mp \sqrt{1 - \frac{4\delta_c k_w^2}{k_z^2}}\right\}. \tag{2.22}$$

Assuming $k_w << k_z$, a MacLaurin expansion can be taken to give

$$k \approx \frac{k_z}{2\delta_c}\left\{1 \mp \left(1 - \frac{2\delta_c k_w^2}{k_z^2}\right)\right\} = \begin{cases} \frac{k_w^2}{k_z} \\ \frac{k_z}{\delta_c} \end{cases} ; \tag{2.23}$$

the first case gives the helicon propagation wave vector

$$k = \frac{k_w^2}{k_z} = \frac{\omega}{k}\frac{n_0 e \mu_0}{B_0}, \tag{2.24}$$

which is the helicon dispersion relation derived by Chen [63] while the second case is the dispersion relation for the Trivelpiece-Gould (TG) mode. When this mode can exist it is usually responsible for much of the energy that sustains a discharge. however it is not present for all of parameter space and Boswell gave parameter ranges over which the TG mode could be expected to exist [65], when $\omega_{RF} < \Omega_e$ and $\omega_{RF} \gg \nu, \Omega_i$.

2.2.2 Field patterns

In [63] Chen gives the field patterns of the helicon mode. Taking the current in the plasma to be due to the drift of the guiding centre, the electric field can be expressed as

$$\vec{E} = \frac{\vec{J} \times \vec{B_0}}{en_0} \tag{2.25}$$

along with Maxwell's equations (ignoring displacement current),

$$\nabla \times \vec{E} = -\frac{\partial \vec{B}}{\partial t}, \tag{2.26}$$

$$\nabla \times \vec{B} = \mu_0 \vec{J}. \tag{2.27}$$

Using (2.25) in (2.26) gives

$$\nabla \times \vec{E} = \nabla \times \left(\frac{\vec{J} \times \vec{B_0}}{en_0} \right) \tag{2.28}$$

$$\implies \nabla \times \left(\frac{\vec{J} \times \vec{B_0}}{en_0} \right) = -\frac{\partial \vec{B}}{\partial t} \tag{2.29}$$

$$\implies i\omega \vec{B} = \frac{\left(\vec{B_0} \cdot \nabla \right) \vec{J}}{en_0} \tag{2.30}$$

$$\implies \vec{B} = \frac{kB_0}{\omega en_0} \vec{J} \tag{2.31}$$

$$\implies \vec{B} = \frac{kB_0}{\mu_0 \omega en_0} \left(\nabla \times \vec{B} \right). \tag{2.32}$$

Now let

$$k = \frac{\mu_0 \omega e n_0}{k_z B_0} \tag{2.33}$$

so that

$$\nabla \times \vec{B} = k\vec{B}. \tag{2.34}$$

Taking the curl of (2.34) in cylindrical coordinates and separating components gives Bessel's equation for B_z

$$r^2 \frac{\partial^2 B_z}{\partial r^2} + r\frac{\partial B_z}{\partial r} + \left(k_\perp^2 r^2 - m^2\right) B_z = 0, \tag{2.35}$$

with $k_\perp$ being the transverse wavenumber defined by

$$k_\perp^2 = k^2 - k_z^2. \tag{2.36}$$

The solution to (2.35) is given by the Bessel functions:

$$B_z = C_3 J_m(k_\perp r_v) \tag{2.37}$$

In a similar fashion the other components are given by

$$B_r = C_1 J_{m-1} + C_2 J_{m+1}, \tag{2.38}$$

$$B_\theta = i\left(C_1 J_{m-1} - C_2 J_{m+1}\right); \tag{2.39}$$

where

$$C_1 = \left(k + k_z\right) A, \qquad C_2 = \left(k - k_z\right) A,\ C_3 = -2ik_\perp A, \qquad A = \frac{iC_3}{2k_\perp}. \tag{2.40}$$

Then by (2.26)

$$E_r = i\frac{\omega}{k_z}\left(C_1 J_{m-1} - C_2 J_{m+1}\right), \tag{2.41}$$

$$E_\theta = -\frac{\omega}{k_z}\left(C_1 J_{m-1} + C_2 J_{m+1}\right), \tag{2.42}$$

$$E_z = 0. \tag{2.43}$$

Selecting m in these relations gives the mode patterns in a helicon wave, which for the $m = 0$ mode are

$$B_r = -Ak_z J_1(k_\perp r_v)\cos(\psi)\,, \qquad E_r = A\omega\frac{k}{k_z}J_1(k_\perp r_v)\sin(\psi)\,\psi, \tag{2.44}$$

$$B_\theta = Ak_z J_1(k_\perp r_v)\sin(\psi)\,, \qquad E_\theta = A\omega J_1(k_\perp r_v)\cos(\psi)\,, \tag{2.45}$$

$$B_z = Ak_\perp J_0(k_\perp r_v)\sin(\psi)\,\psi, \qquad E_z = 0. \tag{2.46}$$

The electric field in fig. 2.2 switches between purely radial and purely azimuthal every quarter cycle, while the magnetic field does the same but $\frac{\pi}{2}$ out of phase. Consider the case where $k >> k_z$, the electric field will be mostly dominated by the radial component, making the pattern look like it is switching between the two signs of the radial pattern every half cycle. The patterns for the $m = \pm 1$ are slightly more complicated [63] and rotate in different directions depending on the sign since the m = +1 mode is coupled to the electrons and the m = -1 mode is coupled to the ions (meaning it is less efficient at sustaining a discharge). Indeed, Blackwell and Chen were able to observe this experimentally [95].

2.3 Transmission lines

An overview of transmission line theory is important for understanding the operation and design choices for the RF drive system that sustains the plasma source. The source must be connected to the drive antenna by such a transmission line and this line must satisfy certain electrical requirements for maximum power transfer to the plasma (which also minimises harmful reflections back to the transmitter). Since the frequency range of the transmitter is the 'amateur'

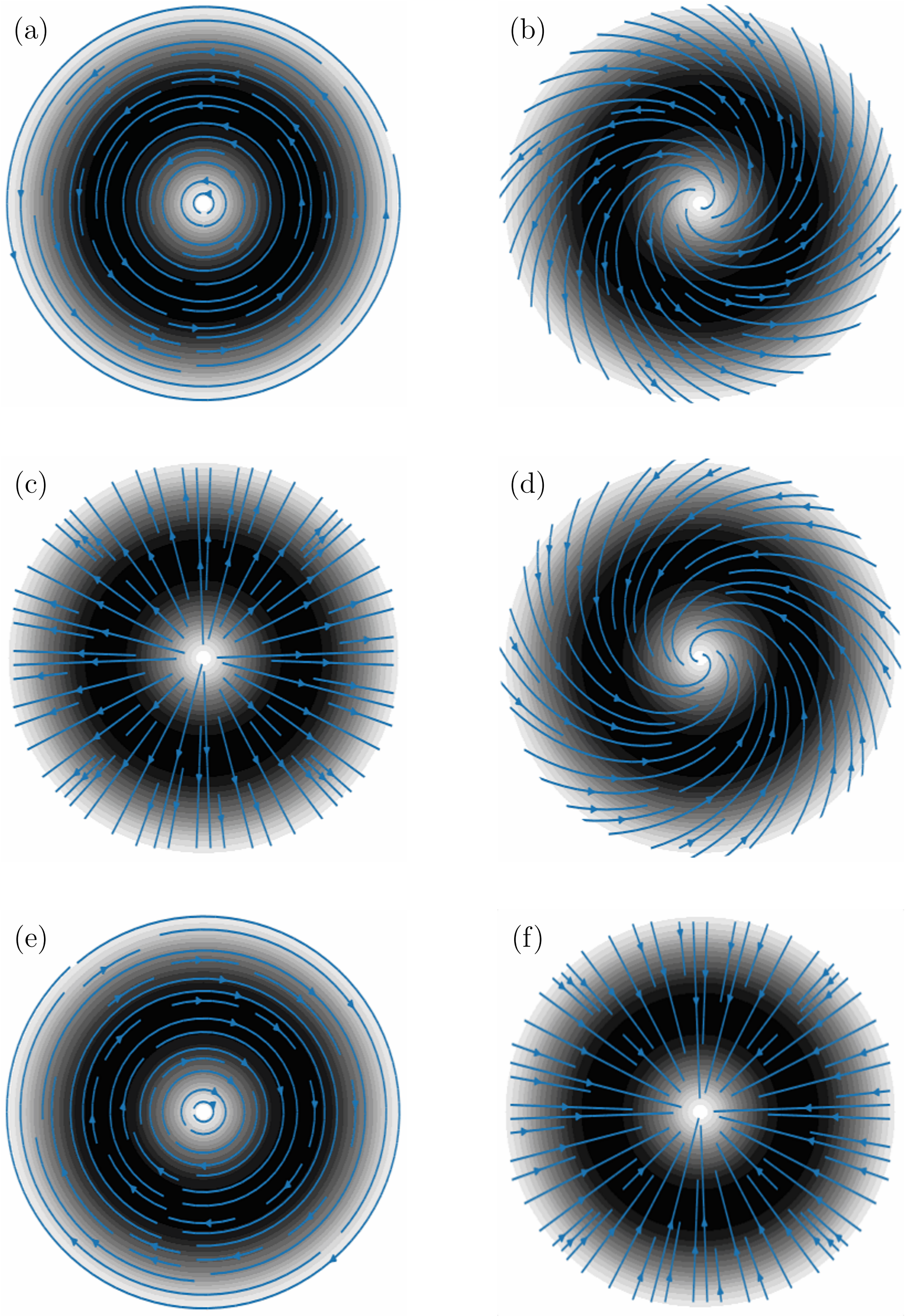

Figure 2.2: Electric field patterns of the $m = 0$ mode for various phases: (a) $\psi \approx 0$, (b) $\psi \approx \pi/4$, (c) $\psi \approx \pi/2$, (d)$\psi \approx 3\pi/4$, (e) $\psi \approx \pi$, (f) $\psi \approx 3\pi/2$. Shading indicates the magnitude of the field.

HF band ($3 \leq f \leq 30$ MHz), the use of rectangular wave-guide as a transmission line is impractical. The cut-off frequency for a rectangular wave-guide is given by the transverse wave-number of the mode with the least number of nodes in its transverse structure, the $TE_{0,1}$ mode. This wavenumber $k_\perp$ is given by [96]:

$$k_\perp = \sqrt{\left(\frac{n\pi}{a}\right)^2 + \left(\frac{m\pi}{b}\right)^2} \tag{2.47}$$

where m and n are the shorter and longer dimension mode numbers respectively, while a and b are the dimension values respectively. Using $m = 0$ and $n = 1$ gives the lowest possible value, so

$$k_\perp = \frac{\pi}{b}. \tag{2.48}$$

The frequency associated with the mode is

$$\nu = \frac{ck_\perp}{2\pi} \tag{2.49}$$

So the waveguide large dimension that will have cutoff at the bottom of the band is

$$b = \frac{cn}{\nu} \tag{2.50}$$

The lowest frequency of the HF band is $\nu = 3$ MHz, giving $b = 100$ m. Typically a waveguide has an aspect ratio of ≈ 2, so a waveguide on the order of 100 m wide by 50 m tall would be required. Co-axial cables are much better suited as they have no cutoff frequency and operate in the TEM mode, although it is important to note that they do have an upper ‘cut-off’ frequency specified. This is just a performance metric and notes the point at which higher order modes appear, which leads to increased difficulty in matching to the source or load.

The propagation of EM waves on a transmission line cannot be adequately captured by simple circuit theory (usually only applied when the wavelength of the signal is much larger than the electrical length of the circuit). Thus a model

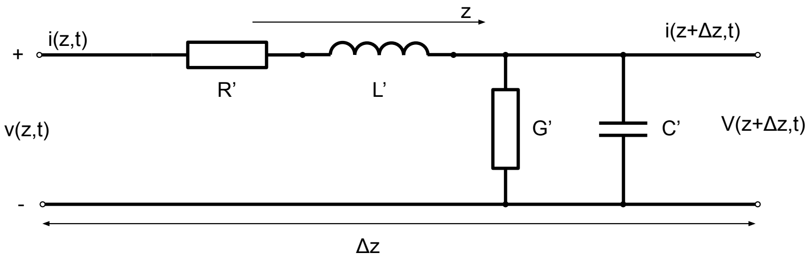

Figure 2.3: An elemental length of transmission line as a lumped element model.

for the transmission line that captures the distributed dissipation and storage of electrical energy is needed. The analysis begins by describing these properties as series and parallel lumped elements on the line:

- $R^{'}$ the Ohmic dissipation (Ω m^{-1}) in the conductors that make up the line. This is modelled as a series resistance.
- $L^{'}$ the inductance of the structure (H m^{-1}) which is related to the energy stored in the magnetic field. This is modelled in series.
- $G^{'}$ the conductance of the dielectric structure (S m^{-1}), this is the leakage between the driven and return conductors. This is taken to be a parallel resistance.
- $C^{'}$ the capacitance of the structure (F m^{-1}), which is related to the energy stored in the electric field. It is modelled in parallel.

The schematic for this model is shown in fig. 2.3, the voltage across and current through the structure is taken to be a function of z, the position along the line and time t. Kirchhoff's current and voltage laws give:

$$v(z,t) - i(z,t)R'\Delta z - \frac{\partial}{\partial t} i(z,t)L'\Delta z = v(z+\Delta z,t) \tag{2.51}$$

$$i(z,t) - v(z+\Delta z,t)G'\Delta z - \frac{\partial}{\partial t} v(z+\Delta z,t)C'\Delta z = i(z+\Delta z,t) \tag{2.52}$$

These can be cast in terms of the first derivative with respect to position by gathering the first and last terms before dividing by Δz and taking the limit as $\Delta z \to 0$:

$$\frac{\partial}{\partial z} v(z,t) = -\left(i(z,t) R' + \frac{\partial}{\partial t} i(z,t) L' \right) \tag{2.53}$$

$$\frac{\partial}{\partial z} i(z,t) = -\left(v(z,t) G' + \frac{\partial}{\partial t} v(z,t) G' \right) \tag{2.54}$$

These are known as the time domain telegrapher's equations and they describe the variation of current and voltage on a transmission line in terms of its resistance, leakage, inductance and capacitance. Typically the frequency domain telegrapher's equations are of more use and can be found by defining the signals to have a (complex) amplitude that is a function of position only, with a sinusoidal part describing the time variation:

$$v(z,t) = \tilde{V}(z) e^{-j\omega t} \tag{2.55}$$

$$i(z,t) = \tilde{I}(z) e^{-j\omega t} \tag{2.56}$$

Substitution of this into eq. (2.53) and eq. (2.54) yields equations where the exponential terms cancel leaving:

$$\frac{\partial}{\partial z} \tilde{V}(z) = -\left(R' + j\omega L' \right) \tilde{I}(z) \tag{2.57}$$

$$\frac{\partial}{\partial z} \tilde{I}(z) = -\left(G' + j\omega C' \right) \tilde{V}(z) \tag{2.58}$$

With this result the wave equation for a transmission line can be derived. Differentiating eq. (2.57) with respect to z and substituting eq. (2.58) into the result yields:

$$-\frac{\partial^2}{\partial z^2} \tilde{V}(z) - \left(R' + j\omega L' \right) \left(G' + j\omega C' \right) \tilde{V}(z) = 0. \tag{2.59}$$

The expression scaling the second term is the propagation constant,

$$k = \sqrt{(R' + j\omega L')\,(G' + j\omega C')}, \tag{2.60}$$

so that the wave equations are now (after following the analogous procedure for the current on the line):

$$-\frac{\partial^2}{\partial z^2}\tilde{V}(z) - k^2\tilde{V}(z) = 0, \tag{2.61}$$

$$-\frac{\partial^2}{\partial z^2}\tilde{I}(z) - k^2\tilde{I}(z) = 0. \tag{2.62}$$

Wave equations have a general solution of the form

$$\tilde{V}(z) = V_0^+ e^{-kz} + V_0^- e^{+kz} \tag{2.63}$$

$$\tilde{I}(z) = I_0^+ e^{-kz} + I_0^- e^{+kz}. \tag{2.64}$$

The components of this solution represent a forward and backward wave travelling on the transmission line. Choosing the solution for current, the telegrapher's equation becomes eq. (2.58):

$$\tilde{V}(z) = \frac{k\left(I_0^+ e^{-kz} - I_0^- e^{+kz}\right)}{G' + j\omega C'}, \tag{2.65}$$

which can then be substituted into the general solution to yield:

$$V_0^+ = \frac{k}{G' + j\omega C'} I_0^+ \tag{2.66}$$

$$V_0^- = \frac{-k}{G' + j\omega C'} I_0^-; \tag{2.67}$$

Ohm's law for each of the travelling waves. Thus the 'characteristic impedance' of the transmission line is

$$Z_0 \equiv \frac{V_0^+}{I_0^+} = -\frac{V_0^-}{I_0^-}. \tag{2.68}$$

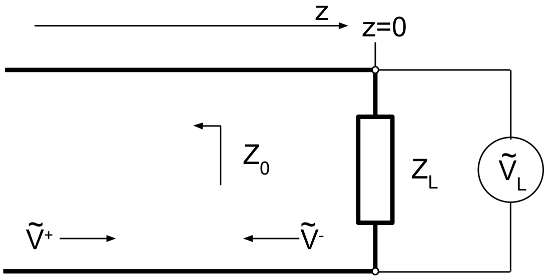

Figure 2.4: A typical load terminating a transmission line.

This relates the current and voltage associated with each individual wave, not the resulting superposition. This value is determined by the dimensions and dielectric materials and structure of the transmission line and is independent of its length. It is crucial that this value is known as transmission lines that terminate with some load that differs from this impedance will see some of the incident energy reflected. For this reason the characteristic impedance of transmission lines as well as ports on sources and laboratory equipment such as oscilloscopes or network analysers are typically standardised to $Z_0 = 50 + 0\,i\Omega$ or 1 MΩ. The purely real impedance is desired since the imaginary components of impedance represent the tendency of a component or structure to store energy in the electric (capacitance) and magnetic (inductance) fields, which can lead to matching difficulties.

For some applications it is impractical or impossible to ensure the line terminates with a component having an impedance of Z_0, so significant reflections usually need to be dealt with. A typical schematic for a terminated transmission line is shown in fig. 2.4 and is represented as a resistor (even if it is a complex load with a non-zero reactance). The forward and backward travelling components of the voltage wave solution eq. (2.63) are:

$$\tilde{V}^+(z) = V_0^+ e^{-kz} \tag{2.69}$$

$$\tilde{V}^-(z) = V_0^- e^{+kz} \tag{2.70}$$

which when evaluated at the $z = 0$ point in fig. 2.4 gives:

$$\tilde{V}^{+}(0) = V_0^{+} \tag{2.71}$$

$$\tilde{V}^{-}(0) = V_0^{-} \tag{2.72}$$

At the load there must be continuity in the potential and current at the point where the load is connected:

$$\tilde{V}^{+}(0) + \tilde{V}^{-}(0) = \tilde{V}_L \tag{2.73}$$

$$\tilde{I}^{+}(0) + \tilde{I}^{-}(0) = \tilde{I}_L \tag{2.74}$$

Since the current in the load can be linked to the line potential by using the characteristic impedance;

$$\frac{\tilde{V}^{+}(0)}{Z_0} - \frac{\tilde{V}^{-}(0)}{Z_0} = \tilde{I}_L, \tag{2.75}$$

and upon substitution of eq. (2.71) and eq. (2.72) into eq. (2.73) and eq. (2.75) respectively this becomes

$$V_0^{+} + V_0^{-} = \tilde{V}_L \tag{2.76}$$

$$\frac{V_0^{+}}{Z_0} - \frac{V_0^{-}}{Z_0} = \tilde{I}_L. \tag{2.77}$$

Using eq. (2.76) and eq. (2.77) in Ohm's law the amplitude of the reflected signal becomes a simple ratio of the forward signal:

$$Z_L = \frac{\tilde{V}_L}{\tilde{I}_L} \tag{2.78}$$

$$Z_L = \frac{V_0^{+} + V_0^{-}}{\frac{V_0^{+}}{Z_0} - \frac{V_0^{-}}{Z_0}} \tag{2.79}$$

$$\frac{V_0^{-}}{V_0^{+}} = \Gamma_V, \tag{2.80}$$

where

$$\Gamma_V = \frac{Z_L - Z_0}{Z_L + Z_0}. \tag{2.81}$$

The ratio Γ_V is known as the voltage reflection coefficient and gives the ratio of the reflected wave's amplitude to the forward wave's amplitude. It is bound to the limits $-1 \leq \Gamma_V < 1$.

In transmission line circuits where $Z_L \neq Z_0$, Γ_V is non-zero, thus both forward and reverse travelling waves exist. These waves constructively and destructively interfere, causing a standing wave pattern to develop along the line. This can significantly impact a system as any point of constructive interference increases the power dissipated in the transmission line at that point, leading to localised failures from intense heat generated at the anti-nodes. The reflected wave can also carry a significant fraction of the transmitted power back to the source and cause significant damage.

To see the behaviour of these standing waves eq. (2.80) can be rearranged for V_0^-, which can then be eliminated in eq. (2.63),

$$\tilde{V}(z) = V_0^+ \left(e^{-jkz} + \Gamma_V e^{+jkz}\right). \tag{2.82}$$

The absolute value of the real part of the voltage on the line is then the square root of the voltage multiplied by its complex conjugate:

$$\begin{aligned}
\left|\tilde{V}(z)\right| &= \sqrt{\tilde{V}(z)\tilde{V}^*(z)} && (2.83)\\
&= \sqrt{{V_0^+}^2 \left(e^{-jkz} + \Gamma_V e^{+jkz}\right)\left(e^{-jkz} + \Gamma_V e^{+jkz}\right)^*} && (2.84)\\
&= \sqrt{{V_0^+}^2 \left(e^{-jkz} + \Gamma_V e^{+jkz}\right)\left(e^{+jkz} + \Gamma_V^* e^{-jkz}\right)} && (2.85)\\
&= \sqrt{{V_0^+}^2 \left(1 + \Gamma_V^* e^{-2jkz} + \Gamma_V e^{2jkz} + \Gamma_V^2\right)} && (2.86)
\end{aligned}$$

Defining Γ_V as a complex phasor gives:

$$\Gamma_V = |\Gamma_V|\, e^{j\phi}. \tag{2.87}$$

Substituting this form of Γ_V and simplifying the exponential terms by use of Euler's identity:

$$\left|\tilde{V}(z)\right| = V_0^+ \sqrt{1 + |\Gamma_V|^2 + 2\,|\Gamma_V| \cos(2kz + \phi)} \tag{2.88}$$

The current on the line is similarly evaluated:

$$\left|\tilde{I}(z)\right| = \frac{V_0^+}{Z_0} \sqrt{1 + |\Gamma_V|^2 - 2\,|\Gamma_V| \cos(2kz + \phi)}. \tag{2.89}$$

The reflection coefficient Γ_V is one of the most important metrics when working with transmission lines. However, it is frequently recast in another form; the Voltage Standing Wave Ratio (VSWR). This is defined as the ratio of the maximum voltage amplitude on the line to the minimum. The maximum occurs when the $\cos(2kz + \phi)$ term is 1:

$$\left|\tilde{V}(z)\right|_{MAX} = V_0^+ \sqrt{1 + |\Gamma_V|^2 + 2\,|\Gamma_V|}. \tag{2.90}$$

While the minimum is $\cos(2kz + \phi) = -1$:

$$\left|\tilde{V}(z)\right|_{MIN} = V_0^+ \sqrt{1 + |\Gamma_V|^2 - 2\,|\Gamma_V|}, \tag{2.91}$$

then;

$$VSWR = \frac{V_0^+ \sqrt{1 + |\Gamma_V|^2 + 2\,|\Gamma_V|}}{V_0^+ \sqrt{1 + |\Gamma_V|^2 - 2\,|\Gamma_V|}}, \tag{2.92}$$

$$VSWR = \frac{1 + |\Gamma_V|}{1 - |\Gamma_V|} \tag{2.93}$$

This VSWR is the metric an operator usually works with when matching a circuit. It is a little more convenient than working with the reflection coefficient as it describes the 'goodness' of the match and treats both short and open-circuits equally. The VSWR is bound by the limits $1 \leq VSWR < \infty$. With 1 representing a perfect match ($\Gamma_V = 0$, $Z_L = Z_0$) and both open and short circuits $\rightarrow \infty$. Typical systems and RF sources aim for $VSWR < 2$ which represents $< 33\%$ reflected power. A $VSWR = 3$ means 50% reflected power, while a small reflection of $< 1\%$ reflected power would imply a $VSWR < 1.02$.

2.4 Plasma sheaths

Plasmas are characterised in part by their electrical neutrality and ability to self-screen external electrostatic fields (and indeed any oscillating signal with frequency lower than the plasma frequency). This phenomenon is known as Debye screening and originated from a derivation by Debye concerning the extent of influence of the electrostatic potential of charges in an ionic solution [97]. In a plasma this effect is mimicked and free charges can move to screen any potential gradients. To see how this could arise, consider a snapshot of the position of all free charges in a plasma. Assume that in this picture the free electrons and ions are all equally spaced, resulting in a potential $V = 0$. Placing a test charge into this arrangement will cause some perturbation in the potential, take a positive charge as an example; the electrons from all directions will move towards this charge and the plasma ions will move away. The net result is a test charge that gets screened by a cloud of opposite charges, the length scale over which the potential disturbance from the test charge can permeate the surrounding plasma is known as the Debye length. Poisson's equation can be used to determine the electrostatic behaviour;

$$\nabla^2 V = -\frac{\rho}{\epsilon_0}, \tag{2.94}$$

where (2.95)

V is the electrostatic potential,

ρ is the charge density and

ϵ_0 is the permittivity of free space.

Thermodynamic equilibrium is assumed and thus a Boltzmann distribution is applicable for the charged species

$$n_j = n_j^0 e^{-\frac{q_j V}{k_B T}}, \tag{2.96}$$

where (2.97)

j is the species index,

n is the number density for the species,

q is the charge of the species,

k_B is the Boltzmann constant and

T is the plasma temperature.

(2.98)

Before substitution into the Poisson equation it is common to take a Taylor expansion (imposing $qV << k_B T$) of the exponential term in the Boltzmann equation:

$$n_j = n_j^0 \left(1 - \frac{q_j V}{k_B T}\right) \tag{2.99}$$

The charge density ρ is the sum over all plasma charges plus a contribution due to the test charge:

$$\begin{aligned}
&\rho = \rho_{plasma} + \rho_{test} \\
\Longrightarrow\ &\rho = \sum_{j=1}^{N} q_j n_j + \rho_{test} \\
\Longrightarrow\ &\rho = \sum_{j=1}^{N} q_j n_j^0 \left(1 - \frac{q_j V}{k_B T}\right) + \rho_{test} \\
\Longrightarrow\ &\rho = \sum_{j=1}^{N} q_j n_j^0 - \sum_{j=1}^{N} q_j n_j^0 \frac{q_j V}{k_B T} + \rho_{test} \text{ and quasi-neutrality applies,} \\
\Longrightarrow\ &\rho = -\sum_{j=1}^{N} q_j n_j^0 \frac{q_j V}{k_B T} + \rho_{test} \qquad (2.100)
\end{aligned}$$

With this simplification the Poisson equation now reads,

$$\begin{aligned}
\nabla^2 V - \sum_{j=1}^{N} \frac{q_j^2 n_j^0}{\epsilon_0 k_B T} V + \frac{\rho_{test}}{\epsilon_0} &= 0\ , \\
\nabla^2 V - \frac{1}{\lambda_D^2} V + \frac{\rho_{test}}{\epsilon_0} &= 0 \text{ and} \\
\nabla^2 V - \frac{1}{\lambda_D^2} V + \frac{q_{test}\delta(\vec{r})}{\epsilon_0} &= 0 \qquad (2.101)
\end{aligned}$$

Where in the last step the test charge is taken to be a point charge using the Dirac-delta function $\delta(\vec{r})$, the solution to the differential equation eq. (2.101) then gives the potential in the plasma as a function of radial distance from the point test charge:

$$V(\vec{r}) = \frac{q_{test}}{4\pi\epsilon_0 r} e^{-\frac{r}{\lambda_D}}. \qquad (2.102)$$

Therefore, an electrostatic disturbance in a plasma drops off exponentially from the source of the disturbance with a characteristic $1/e$ folding distance of λ_D, in addition to the $1/r$ decrease of the Coulomb force. This length scaling is known as the Debye length:

$$\lambda_D^2 = \sum_{j=1}^{N} \frac{\epsilon_0 k_B T_j}{q_j^2 n_j^0} \tag{2.103}$$

but usually the ions are cold compared to the electrons and so the electron Debye length contribution usually dominates giving the potential length scale as

$$\lambda_D^2 = \frac{\epsilon_0 k_B T_e}{e^2 n_e}. \tag{2.104}$$

Consider now the situation where there is no perturbing test charge, but a metal boundary. This boundary will quickly attain a negative charge as the more mobile electrons will suffer more frequent collisions and therefore the wall will attain a negative charge. The result is a plasma touching a boundary with a negative potential and this boundary provides an electrostatic disturbance like before. This time however, the charges can stream towards the source of the potential and be lost from the plasma. It is a source of potential and a sink for charge. A significant reduction in particle density occurs in an unbalanced manner and a non-neutral region develops 'protecting' the bulk plasma from being further perturbed by the boundary. This layer at the plasma edge is known as a 'plasma sheath' and arises from considering ions that are not frozen.

Consider an ion as it moves outward from the bulk plasma towards the negative potential presented by a boundary like that shown schematically fig. 2.5. The ion kinetic energy at any point x will consist of its initial kinetic energy plus any energy gained by moving through the electric field set up by the potential at the wall;

$$\frac{1}{2} m_i v_i(x)^2 = \frac{1}{2} m_i v_\infty(x)^2 - eV(x), \tag{2.105}$$

where m_i is the ion mass,

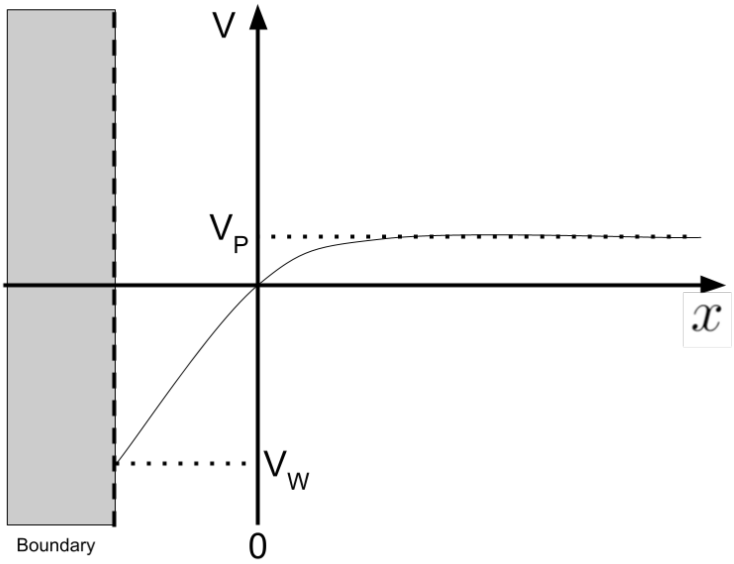

Figure 2.5: A schematic of the potential drop between a plasma and a metal wall

$v_i(x)$ is the ion speed at position x and

v_∞ is the ion ‘starting’ velocity in the bulk plasma.

For the streaming ions the flux must conserved and so the flux at the sheath edge can be related to the flux at any other point.

$$n_i(x)v_i(x) = n_s v_s, \tag{2.106}$$

which, when solving for $n_i(x)$ and substituting the velocity $v_i(x)$ as given by eq. (2.105) reveals the ion density to be a function of the sheath edge density:

$$n_i(x) = n_s \left(1 - \frac{2eV(x)}{m_i v_s^2}\right)^{-1/2}. \tag{2.107}$$

Thus the ion density varies across the sheath region, while the electron variation is still governed by the Boltzmann relation eq. (2.96).

The Poisson equation now becomes

$$\nabla^2 V(x) = \frac{en_s}{\epsilon_0}\left(e^{\frac{V(x)}{T_e}} - \left(1 - \frac{V(x)}{\varepsilon_i}\right)^{-1/2}\right). \tag{2.108}$$

Where :

$$\varepsilon_i = \frac{m_i v_s^2}{2e}. \tag{2.109}$$

This cannot be linearised with a Taylor expansion as $V(x)$ is not negligible compared to the temperature. However, the electric field can be obtained by multiplying by dV/dx and then integrating with respect to x:

$$\int_0^V \frac{dV}{dx}\frac{d^2V(x)}{dx^2} = \int_0^V \frac{en_s}{\epsilon_0}\left(e^{\frac{V(x)}{T_e}} - \left(1 - \frac{V(x)}{\varepsilon_i}\right)^{-1/2}\right)\frac{dV}{dx}dx \tag{2.110}$$

Where integration by parts simplifies the LHS and the integration with respect to V on the right hand side gives:

$$\frac{1}{2}\left(\frac{dV}{dx}\right)^2 = \frac{en_s}{\epsilon_0}\left(T_e e^{\frac{V(x)}{T_e}} - T_e + 2\varepsilon_i\left(1 - \frac{V(x)}{\varepsilon_i}\right)^{1/2} + 2\varepsilon_i\right) \tag{2.111}$$

Although this requires a numerical routine to solve, some limits on the plasma parameters can be deduced by noticing the charge density and thus the electric field must be real valued; so the RHS must be positive. Using a Taylor expansion to first order gives a trivial result that $V < 0$; a given for the choice of reference. Taking a second order Taylor expansion reduces the RHS to

$$\frac{V^2}{2T_e} - \frac{V^2}{4\varepsilon_i} \geq 0 \tag{2.112}$$

Cancelling V and substituting the ion energy in terms of the sound speed at the sheath edge:

$$\varepsilon_i \geq \frac{T_e}{2}. \tag{2.113}$$

Thus ions enter the sheath with energy at least half that of the electron thermal energy. The implication is that the ions gain all of this energy on the transit from the bulk plasma to the sheath edge, through a so-called ‘pre-sheath’ where the plasma neutrality still holds but a small electric field exists that starts off the drift motion towards the boundary. Taking one more step and substituting eq. (2.113) shows that ions enter the sheath with a velocity [98]

$$v_s \geq \sqrt{\frac{T_e}{2m_i}}. \tag{2.114}$$

The well known Bohm criterion for the minimum speed of ions entering a plasma sheath, useful to know when one wishes to convert an ion flux to a current density being drawn by a metallic surface in contact with a plasma.

The sheath can be taken to be a diode-like structure consisting of the probe surface and the plasma. The current in a diode is given by the well known Child law of space charge limited current:

$$J_s = \frac{4}{9}\epsilon_0\sqrt{\frac{2e}{m_i}}\frac{V^{3/2}}{s^2}, \tag{2.115}$$

where

V is the potential across the surfaces and

s is the sheath thickness

This current density is also given by:

$$J_s = en_s v_s. \tag{2.116}$$

Rearranging for the sheath thickness:

$$s = \frac{\sqrt{2}}{3}\lambda_{Ds}\left(\frac{2V}{T_e}\right)^{3/4} \tag{2.117}$$

Thus the sheath surrounding a metallic object in a plasma will grow with the applied potential, this has an important bearing on the interpretation of Langmuir probe results.

Chapter 3

Experimental methods

3.1 Plasma source

3.1.1 Vacuum chamber

The vacuum chamber for the plasma source is a cylindrical, stainless steel vessel in 4 sections. In total the vacuum envelope is 2.84 m long with a diameter of 1 m. Each of the 4 sections is 0.74 m long and they are connected by circumferential flanges holding an o-ring. A sketch of the vessel can be seen in fig. 3.1 & fig. 3.2. The borosilicate plate at $z = 0$ has a diameter of 0.5 m and is approximately 25 mm thick; mounted to this plate on the air side is the RF antenna for launching helicon waves or for ionisation by inductive coupling. This antenna is surrounded by a Faraday 'cage' comprised of another vacuum vessel section that has been left at atmospheric pressure. The system is pumped through a port at $z \approx 2.8$ m, neutral gasses can be fed in via a manifold system incorporating needle valves located on the end-plate at $z = 2.84$ m.

Pumps, control and pressure measurement

The vacuum line consists of three separate pumps with various bypasses for efficient use of pumps in their optimum pressure ranges and a schematic is shown

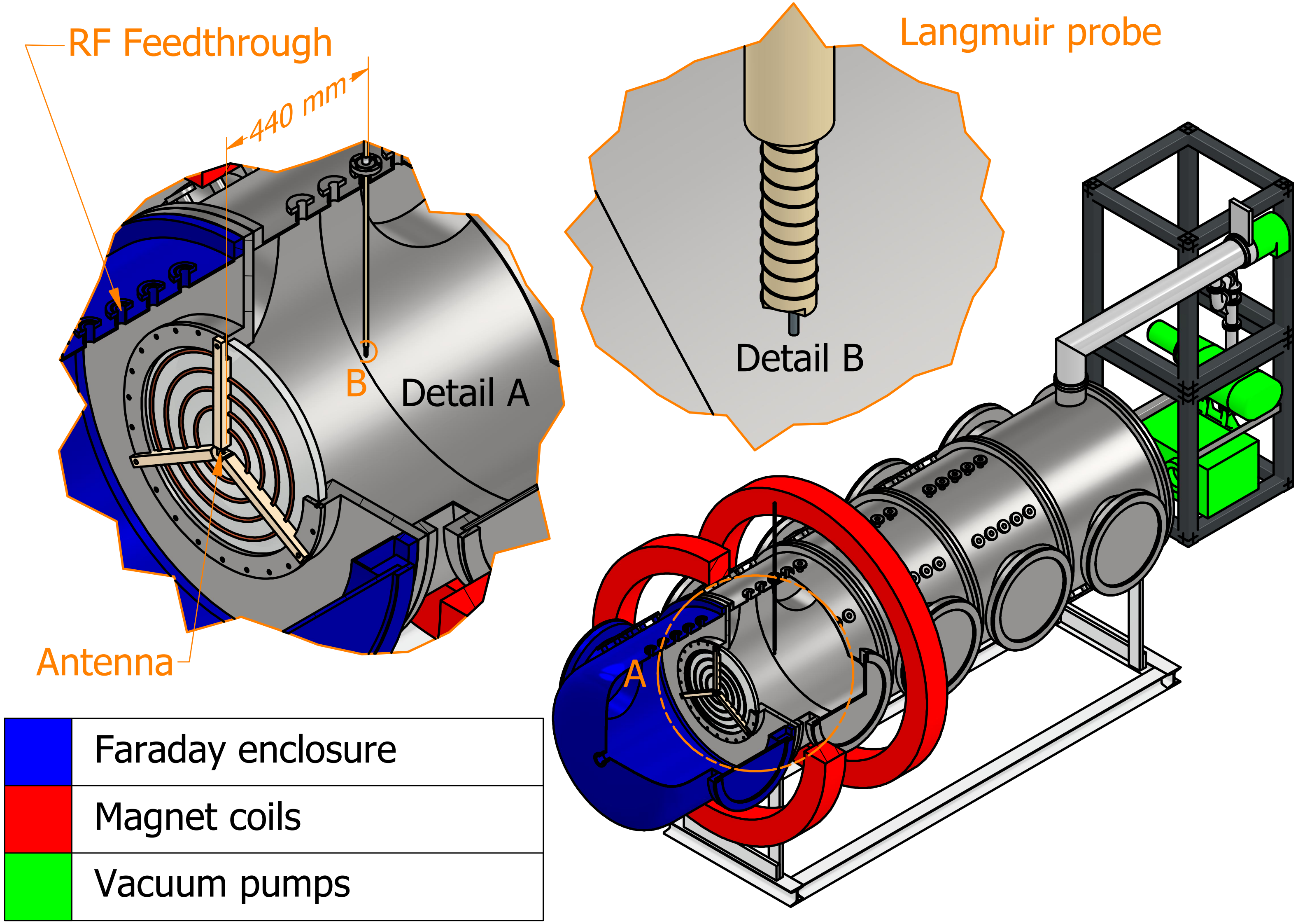

Figure 3.1: 3D CAD drawing of the apparatus, showing the relative positioning of the spiral antenna, Langmuir probe and vacuum pumping arrangement.

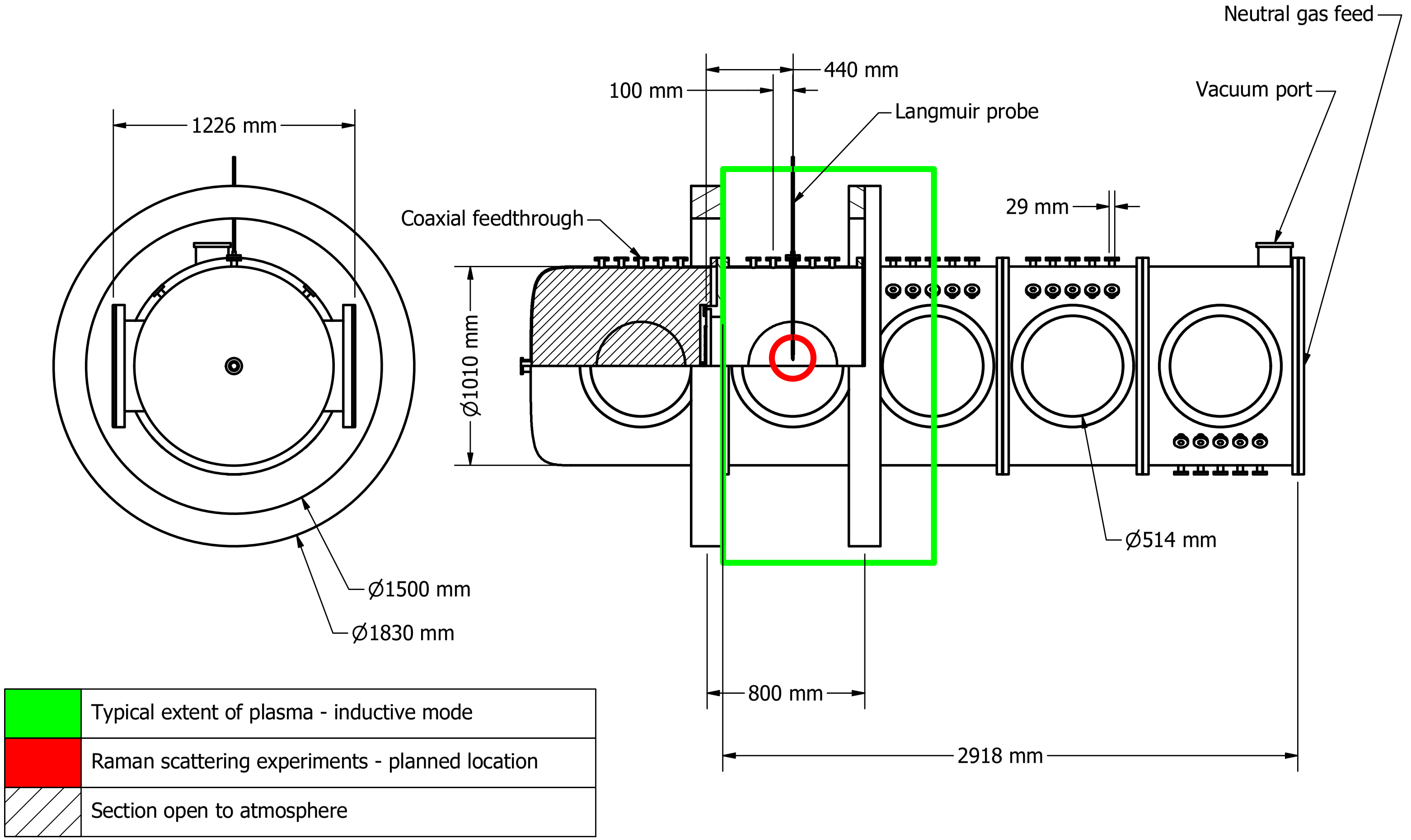

Figure 3.2: 2D elevation sketch of the vessel and key dimensions, the green box identifies the typical extent of a plasma in the inductively coupled mode of operation.

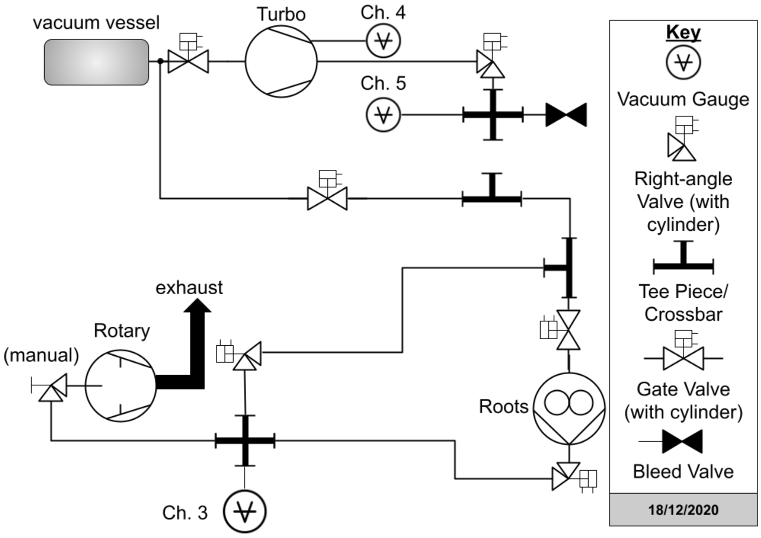

Figure 3.3: Vacuum Circuit

in fig. 3.3. Starting from the atmosphere point in the circuit, the first pump is a rotary vane primary pump which also provides the low foreline pressure required for the other 2 pumps, this is also the pump that is used to start the vessel evacuation if the apparatus has been raised to atmospheric pressure. Next in the circuit is a roots pump which operates when the vessel pressure $p < 80$ mbar. This stage does not affect the ultimate pressure of the vacuum but does accelerate the process of pumping from atmosphere to High Vacuum (HV). The rotary vane and roots pump provide a foreline pressure < 1 mbar for the final stage turbomolecular drag pump that achieves an ultimate vacuum of $2{\times}10^{-5}$ mbar, or 2% of the usual minimum experimental pressure of 10^{-3} mbar. A turbomolecular drag pump would ordinarily be connected to a vacuum vessel by bolting directly to a high vacuum port. However in this case some distance is required to protect the pump from the B-field generated by the electromagnets. This long pipe ultimately lowers the conductance of the pump circuit; there is also a bend in this pipe which, in the molecular flow limit where this device operates, only introduces a minor impedance to the flow [99].

These pressures are measured by several pressure gauges, both in the foreline and inside the vacuum vessel. In the foreline Pirani gauges are used as there is no requirement for accurate measurement at low pressures, only an indication of order of magnitude for safe pump operation. Inside the vacuum vessel 4 different gauges are used for cross-calibration of the base pressure and the neutral gas pressure during source operation. The most important of these gauges is the '10^{-1}' range capacitance manometer[1], an absolute pressure device that provides a measurement that is independent of the gas species and operates on the principle of a thin capacitive film buckling slightly under a pressure difference between the measurement cavity and a reference cavity held at Ultra High Vacuum (UHV) of $\approx 10^{-10}$ mbar. Complementing these are 2 ionisation gauges that create an ionising electron current via a hot cathode. The resulting ionisation by the energetic electrons produces a current on an anode. This current depends on the gas pressure and species, so an extra conversion factor must be applied to find the correct pressure for different gas species. These are mainly used as a cross calibration check for the manometer. This is particularly useful as the zero-point calibration on a manometer can drift over short periods (several days) where the ionisation gauges are not prone to substantial drifts in their calibration. Lastly, another Pirani and 'atmosphere range' manometer gauge are used in the vessel for tracking high pressures during venting to atmosphere.

Control of the pump system is achieved through a pneumatic circuit controlled by a DC switchboard. The position of each vacuum valve in fig. 3.3 is controlled by a pneumatically actuated cylinder. The pressurised airflow is toggled by a bank of solenoid actuated, spring return 5/2 pneumatic control valves, with the high signal for the solenoid being provided by a switchboard. In the interests of operator convenience and to minimise the risk of misconfiguration, the switchboard provides red and green lamps as indications of valve position (closed and

---

[1] A capacitance manometer is generally labelled by its 'range', meaning its maximum rated measurement pressure. In this instance the manometer is a '4 decade' unit that can measure from 10^{-5} mbar to 10^{-1} mbar

open respectively). The position indicators use reed switches to actively detect both the open and closed positions of the cylinder to provide positive indication that a valve is not stuck between states.

Gas back-fill is achieved by means of a line connected to the flange at the opposite end of the vessel from the antenna. A high pressure gas cylinder is throttled by a 2 stage regulator. The output from this regulator splits in two; one line feeds a fine needle valve while the other feeds a 10 sccm MKS ‘Flometer’. The needle valve allows for coarse manual adjustment while the MKS flow controller maintains the pressure via a ‘proportional–integral–derivative controller (PID)’ algorithm to achieve pressure stability over long periods of time. An additional line with large aperture valves is used to vent the vessel to a pressure slightly greater than atmospheric pressure using nitrogen, preventing contamination of inner surfaces during maintenance and upgrade activities. The pump control and pressure measurements are vital in this scenario as one must ensure the high vacuum pumps are not exposed to sudden, large changes in pressure or pressures that exceed their maximum rated inlet or exhaust pressures. If a valve were to open with the main chamber several orders of magnitude above the fore line the pumps could be irreparably damaged. The atmosphere range capacitance manometer is vital to ensure that equilibrium is approached gradually so as to not rupture the various Mylar windows on the apparatus. Various overpressure relief valves provide an extra layer of protection. One is placed on the vacuum vessel and is a pressure relief valve that is kept closed by a spring. The spring is calibrated such that a pressure of slightly greater than atmosphere will open the valve. Thus, the vacuum chamber can never achieve a pressure significantly above atmosphere. Another valve that is attached to the nitrogen line opens progressively as atmospheric pressure is reached and thus the rate of change in the chamber pressure is self-limiting as equilibrium is approached.

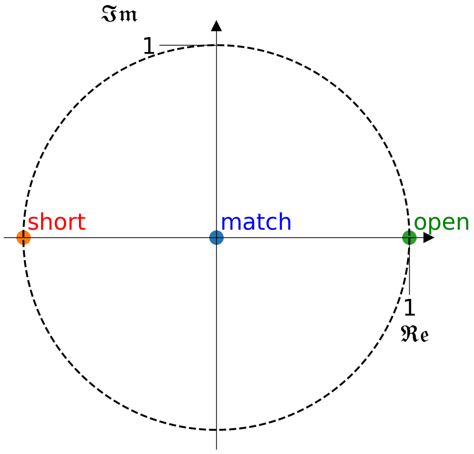

Figure 3.4: An Argand diagram showing the bounds of all permissible reflection coefficients.

3.1.2 RF system

The Smith Chart

Matching the antenna to the RF supply is vital for safe and efficient operation of the RF system. Any discussion of matching is greatly helped by understanding the Smith chart, a tool for visualising how an RF network's reflection behaviour changes as components are added. As will be seen in the next section on matching networks; the algebra, although straightforward becomes laborious and obfuscates the physical intuitions governing the different topologies. Thus, Phillip H. Smith of Bell Laboratories invented the "Transmission Line Calculator", which became widely known by his name, to aid in these "laborious calculations" [100, 101]. The Smith chart is primarily a plot of the complex reflection coefficient Γ, with impedance curves added to visualise changes to Γ as components are added to a circuit. The first step in building the Smith chart is to start with the complex locus in fig. 3.4 that defines the limits of Γ $(0 < \Gamma \leq 1)$. Consider a length of transmission line terminated in a load such as in fig. 2.4. It is convenient

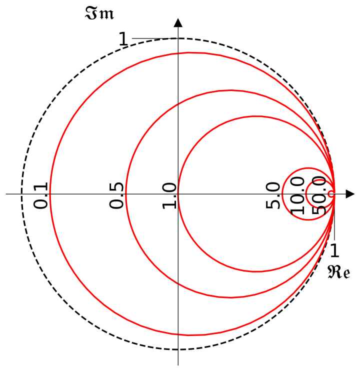

Figure 3.5: Circles of constant resistance on the Smith chart.

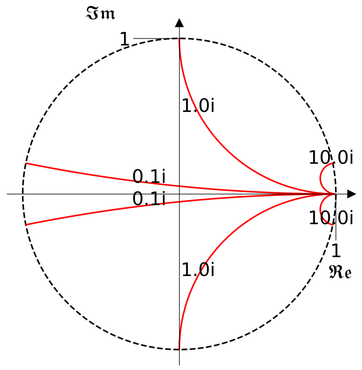

Figure 3.6: Circles of constant reactance on the Smith chart.

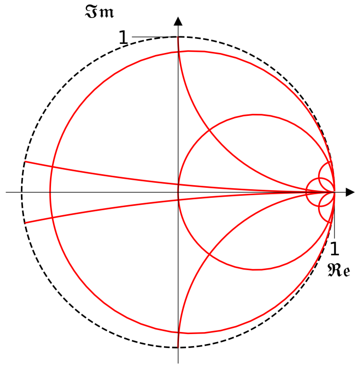

Figure 3.7: The Smith chart as an impedance view.

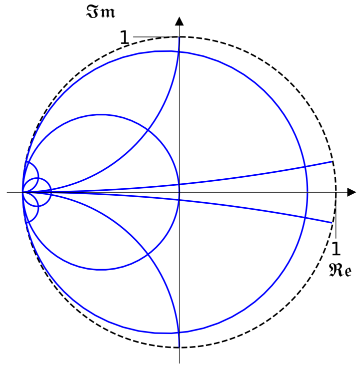

Figure 3.8: Admittance Smith chart for working with shunt elements.

introduce the normalised impedance $\bar{Z}_L$:

$$\bar{Z}_L = \frac{Z_L}{Z_0} \tag{3.1}$$

As would be expected from eq. (2.81) a real input should give a real valued Γ and so any pure resistance will appear on the real axis of the Smith chart. There are 3 particularly important points on the real line, $\bar{Z}_L = 0$ (short circuit), 1 (perfect match) & $\to \infty$ (open circuit) corresponding to $\Gamma = -1$, 0 & 1 respectively.

Matching Techniques

Since the load in the antenna system is complex, non-linear and unknowable a-priori when plasma is present, it must include variable components in order to adjust the impedance to match the 50Ω output port on the generator. Typically any added components are then considered to be a part of the load impedance Z_L and the aim is to have this value be $50 + 0i\Omega$ 'looking from the source'. This is a phrase commonly used in transmission line analysis; 'looking from **X** ' or 'as viewed from **X**' describes the point on the transmission line schematic and which direction of flow to consider. This is hinted at in fig. 2.4 by the right-angled arrow next to Z_0 which means 'looking back down the transmission line the impedance is Z_0'. If the arrow points to the right the value would then be Z_L.

Matching of an RF circuit is usually achieved using a 'matching network' that consists of variable inductors and capacitors. This matching network can typically be purchased as a 'black-box' component that is installed between the RF source and the load. Some units are computer controlled while others are manual (of course in this case user understanding is required). Typical HF commercial units with automatic matching capability are unsuitable for this type of load as a 'static' electrical load is assumed. That is; a typical radio antenna has a fixed impedance regardless of air pressure and power applied. For this reason, the algorithm used to find the correct match or 'tune' simply tries all combinations and then chooses the one resulting in the minimum $VSWR$. Since moving the match parameters too far from ideal means less forward coupled power, the plasma is usually lost during the automatic unit's parameter scan. Therefore the matching network is manually operated.

Reactive series elements

A reactive element placed in series with a load can transform its impedance and this transformation can be viewed on a Smith chart to gain insight into the physics

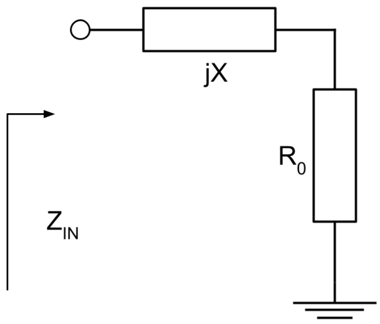

Figure 3.9: Layout for a reactance in series with the load

underpinning the network. The schematic in fig. 3.9 shows a generic imaginary impedance jX connected in series with a load. It is useful to examine both the impedance Z and admittance Y of such networks at each stage of analysis:

$$Z = R + jX \tag{3.2}$$

$$Y = G + jB \tag{3.3}$$

$$Z = \frac{1}{Y} \tag{3.4}$$

It is also worth noting that for a purely resistive load:

$$R = \frac{1}{G} \tag{3.5}$$

and for a purely reactive load:

$$X = -\frac{1}{B} \tag{3.6}$$

Where R is the resistance, X is the reactance (both in Ohms); while G is the conductance and B the susceptance (in Siemens). If the purely resistive load has $R_L = 50\ \Omega$ then the load impedance is simply 50Ω. The conductance is then simply $1/50\ \Omega$ and hence the admittance is $1/50\ \Omega$. If the impedance of the reactive element is similarly $50j\Omega$ then the admittance is $(1/50)j\ \Omega$. The series connection gives a simple addition in impedance space:

$$Z_{IN} = Z_L + Z_{\mathrm{X}} = R_L + jX\Omega \tag{3.7}$$

and the admittance can be found by the reciprocal sum or by taking the inverse of the impedance:

$$\begin{aligned} Y_{IN} &= \frac{1}{Z_{IN}} && (3.8) \\ &= \frac{1}{R_L + jX} && (3.9) \\ &= \frac{R_L - jX}{R_L^2 + X^2} && (3.10) \end{aligned}$$

The conductance of the circuit has thus changed:

$$\frac{1}{R_L} \to \frac{R_L}{R_L^2 + X^2}. \tag{3.11}$$

The key point to note is that the network's conductance has been altered without changing its resistance.

Parallel reactive elements

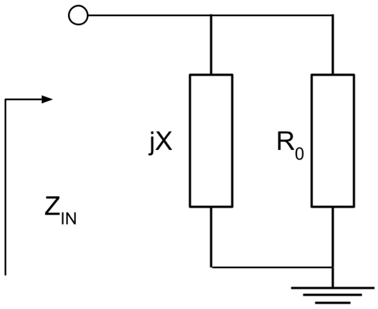

Figure 3.10: Layout for reactance in parallel with the load

If the reactive element is placed in parallel as in fig. 3.10, the admittance is:

$$Y_{IN} = G_L = \frac{1}{R_L}. \tag{3.12}$$

Thus adding a parallel component changes the admittance to:

$$Y_{IN} = G_L + jB_p = \frac{1}{R_L} - j\frac{1}{X_p} \tag{3.13}$$

and the impedance is then:

$$\begin{aligned} Z_{IN} &= \frac{1}{Y_{IN}} && (3.14)\\ &= \frac{1}{G_L + jB_p} && (3.15)\\ &= \frac{G_L - jB_p}{G_L^2 + B_p^2}. && (3.16) \end{aligned}$$

and the resistance is now

$$R = \frac{G_L}{G_L^2 + B_p^2} = \frac{\frac{1}{R_L}}{\frac{1}{R_L^2} + \frac{1}{X_p^2}}. \tag{3.17}$$

Thus, a parallel reactive element does not affect the apparent conductance of the load, but does change its apparent resistance. The Smith chart then displays how these transformations manifest in reflection space for a transmission line terminated by such a network. Reactive series components transform along the circle of constant resistance in an impedance chart, the direction is given by the type of component; since capacitors have a negative reactance they will transform in a counter-clockwise direction, while the opposite is true of an inductor. Reactive components added in parallel behave similarly, they transform along the lines of constant conductance in an admittance chart; with capacitors moving clockwise since they have a positive susceptance, while inductors in parallel transform counter-clockwise. When matching with the aid of a Smith chart, the objective is to transform the load impedance toward the centre of the chart. This can usually be done in 2 steps, by choosing a series(parallel) component to transform along a constant resistance(conductance) circle, then choosing a parallel(series) component to transform along the constant conductance(resistance) circle. With this understanding of a Smith chart laid out, a discussion of matching networks becomes much more intuitive.

The L-network

The simplest topology for an RF matching network is the L-network, so-called because the circuit diagram is L shaped. There are 8 different L-network topologies, since there are 2 components and 4 options for each. The general operation is for the first component to alter the resistance or conductance to match the source or transmission line before using a second component to cancel the reactance that is introduced by the first component. They are shown in fig. 3.11. The top-level grouping for these come from their tendency to pass or block signals. The topologies in fig. 3.11(a) to fig. 3.11(d) are termed 'high-pass' since the series capacitor conducts AC (and blocks DC) while fig. 3.11(e) through fig. 3.11(h) are 'low-pass' since the parallel capacitor shorts AC (and passes DC). Since the design problem calls for maximum transmission of AC power the low pass networks need no discussion. With 4 networks eliminated as a design choice, the remaining 4 must be analysed to determine their coverage of the Smith chart:

1: Consider the 2$^{\text{nd}}$ (furthest from load) element.

2: Note which view will be most useful; impedance or admittance. A series element will transform on an impedance curve while a parallel element will transform along an admittance curve.

3: Then consider which direction the element will move along the curve. An inductor has a positive signed reactance, therefore on the impedance view it

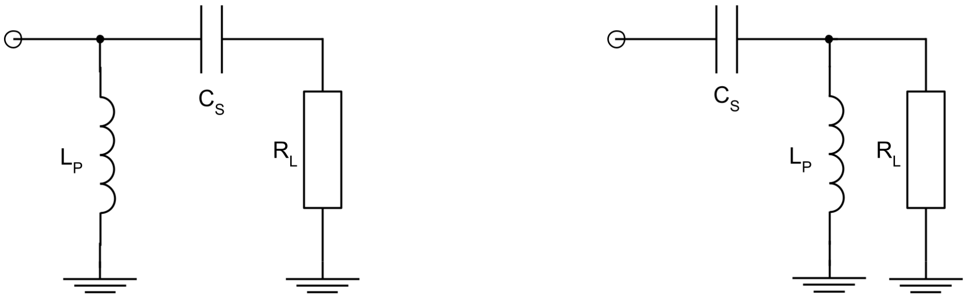

((a)) $X > 0$ & $\bar{R}_L < 1$, $X < 0$ & $\bar{G}_L > 1$ ((b)) $X > 0$ & $\bar{R}_L > 1$, $X < 0$ & $\bar{G}_L < 1$

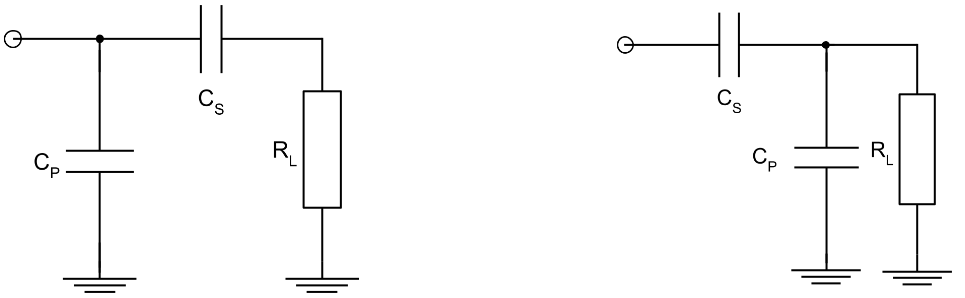

((c)) $X > 0$ & $\bar{R}_L, \bar{G}_L < 1$ ((d)) $X > 0$ & $\bar{R}_L, \bar{G}_L < 1$

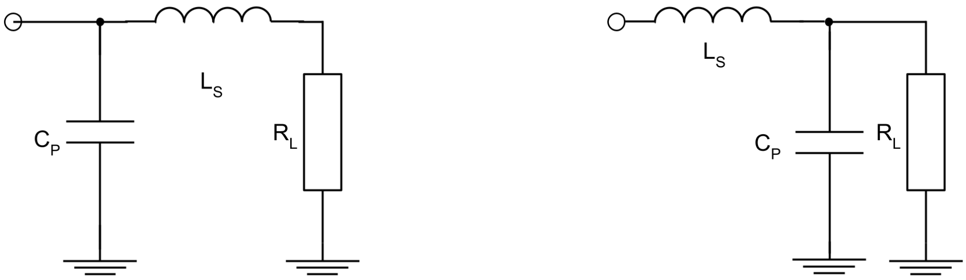

((e)) $X > 0$ & $\bar{G}_L > 1$, $X < 0$ & $\bar{R}_L < 1$ ((f)) $X > 0$ & $\bar{G}_L < 1$, $X < 0$ & $\bar{R}_L > 1$

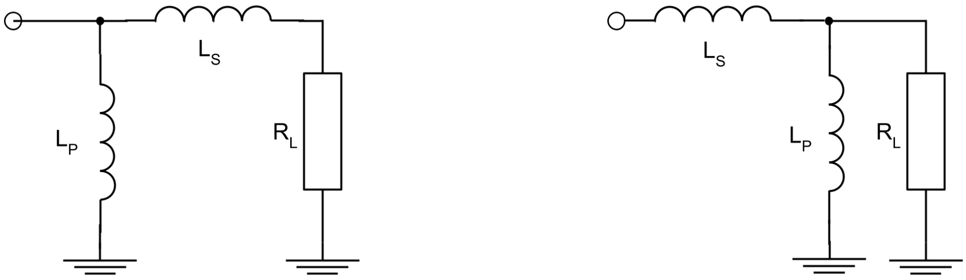

((g)) $X < 0$ $\bar{R}_L, \bar{G}_L < 1$ ((h)) $X < 0$ $\bar{R}_L, \bar{G}_L < 1$

Figure 3.11: All possible L-branch matching networks

will transform clockwise on a constant-resistance curve towards the ‘open’ singularity. On the admittance view it will transform counter-clockwise towards the ‘short’ singularity since it will have a negative-signed susceptance. A capacitor has a negative signed reactance and thus moves in the opposite direction to an inductor.

4: With an understanding of the allowed transformation, deduce which curve; unit resistance or unit conductance would allow for that transformation to reach the origin. It will be the goal of the first element to transform onto this curve.

5: Then consider the first element and the points on the plane that are reachable by means of its impedance transformation.

This covers the graphical method of matching using the Smith chart and reflection coefficient transformations, which aids in choosing a topology. There are also ‘design’ equations for L-networks in order to assign values to the components for a given load at a given frequency. These design equations introduce the concept of the quality factor Q for a resonant electrical circuit, revealing a significant drawback of simple L-networks. The 2 networks used in the apparatus are given by (fig. 3.11(a) and fig. 3.11(b)); the high pass networks with an inductor in parallel. The Q for a circuit formed of a resistance and one reactive element is:

$$Q = \frac{X}{R} \tag{3.18}$$

for an element where the reactance is in series with the resistive component and

$$Q = \frac{R}{X} \tag{3.19}$$

when that reactance is in parallel. Now consider the circuit in fig. 3.11(a), the series combination of the load resistance and the capacitor can be taken as a single component with $Q_L = X_c/R_L$, the aim in this topology is for the capacitor to change the conductance to the required value. Comparing eq. (3.3) to eq. (3.10) gives the conductance as

$$G = \frac{R_L}{R_L^2 + X_c^2}. \tag{3.20}$$

The characteristic impedance of the line is denoted by $Z_0 = R_0 = 1/G_0$:

$$\frac{1}{R_0} = \frac{R_L}{R_L^2 + X_L^2} \tag{3.21}$$

$$X_c = -\sqrt{R_L\left(R_0 - R_L\right)} \tag{3.22}$$

the negative solution is taken since the component is to be a capacitor. Substitution of Q provides:

$$Q^2 = \frac{R_0}{R_L} - 1. \tag{3.23}$$

This result reveals that Q, which represents the damping of the resonant circuit, as well as its bandwidth, is fixed for a given design problem. That is, if only an L-network is available, the discrepancy between source and load fixes the bandwidth. A similar result can be found for the other high pass network in fig. 3.11(b):

$$Q^2 = \frac{R_L}{R_0} - 1 \tag{3.24}$$

This motivates a discussion on broadband matching and the circuit topologies that are used in a variable tuner unit.

Broadband matching: Pi and T networks

In order to make Q a controllable value in these problems the matching is done in 2 stages; the load is first matched to an arbitrary ‘virtual’ resistor that replaces the line resistance in eq. (3.23) and eq. (3.24) via an L network; this allows the Q to be chosen since R_L can be ‘chosen’. The line or source is then matched to this virtual resistance R_V via a second L network. Consider the circuit on the right

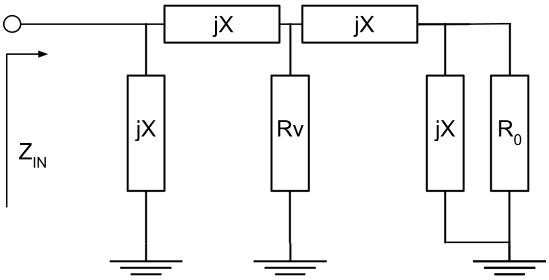

Figure 3.12: A schematic of a 2 stage matching circuit

hand side of fig. 3.12. A topology is first chosen to reflect the high or low pass required for the application. In this case high pass is desirable. Next, Q can be approximated [102] as:

$$Q = \sqrt{\frac{max(R_s, R_L)}{R_v} - 1}. \tag{3.25}$$

Where R_s is the resistance of the voltage source. Thus the desired Q can be

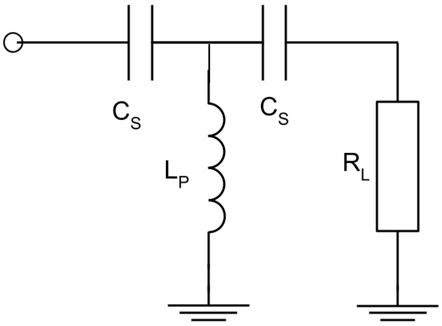

Figure 3.13: Schematic of the HF matching network.

chosen and the appropriate virtual resistance determined. With the virtual resistance known, the values for the inductor and capacitor can be determined from eq. (3.18) and eq. (3.19) for both the left and right hand circuits. The virtual resistor is then omitted from the schematic and the inner reactances combined to formed a single lumped element. These circuits are named 'pi' or 'T' networks depending on where the parallel components are placed since they resemble the letters Π and T when the middle elements are merged.

Matching Unit

The matching unit used to transfer maximum power to the plasma is based on the 'T-network' topology in high pass form. With 2 variable rotating vane air capacitors connected in series and a ceramic core roller inductor in parallel. This allows for the 200 W HF generator to transfer maximum power to the load-tuner circuit by raising the parallel equivalent resistance and tuning out any stray reactance. It also helps to protect the generator from harmful reflections from any mismatch. It is imperative that the components are variable as the complex impedance of the antenna-plasma system is multi-variate; depending on the frequency of operation, power, gas species and pressure as well as cable lengths. It is impossible to fix these variables since the coupled power and electron density must by definition be altered to ionise the neutral gas. Indeed, the operator must continually monitor the reflections from the system and adjust accordingly during plasma startup. The reflections must also be monitored during experiments as small excursions in neutral gas pressure or thermal expansion of coaxial cables can cause a loss of optimum matching. In extreme cases this can result in the increased reflection shutting off the generator via a safety interlock. A schematic of the matching network can be seen in fig. 3.13.

RF diagnostics

The suite of RF diagnostics has two main purposes; to protect the generator from harmful reflections and to provide a phenomenological characterisation of the plasma. That is, the RF parameters recorded do not necessarily give a prediction of plasma parameters, but they do inform the operator that the plasma is stable, in a known condition and as a quick diagnostic for system errors. Diagnosis of system faults in this way are possible since the RF parameters are unchanging between plasma runs providing all other parameters are the same; for example a surge or drop in the neutral gas pressure causes a mismatch, or a contaminant such as air will cause the match settings to be different. The performance of the HF network is monitored via directional couplers functioning as VSWR meters, they sample both the forward and reflected power and display the standing wave ratio. The aim of the operator is to minimise the VSWR on the output of the RF generator; thereby minimising damaging reflections and conversely maximising the forward power transmitted to the rest of the circuit. This does not necessarily maximise the power absorbed by the plasma (and by proxy the plasma density), this only provides maximum transfer to the coupled circuit consisting of the matching network, antenna and plasma; as well as safety for the generator. The next task is to analyse the match settings and the circulating power trapped in the 'RF cavity'; a match setting contradicting previous data usually indicates a fault, however if both the match settings and total circulating power are 'correct' then the plasma is operating under its calibrated conditions.

3.1.3 Helicon antenna design and testing

The flat, spiral shaped helicon antenna is an integral part of the apparatus and an enabling feature of the project; it is simple and cost effective. Copper, 'micro-bore' pipe ≈ 7 mm in diameter was used in the construction of the antenna as copper's high conductivity and ductility make it efficient electrically and easy to shape. The copper is softened with heat and wound onto a template to form a continuous spiral, with the ends of the pipe bent perpendicular to the plane of the winding to connect to a coaxial adapter. When a DC signal is applied the antenna presents a short circuit on the transmission line. The antenna makes 4 turns across its radius, keeping to designs seen in the literature [68]. Since the antenna needs to be future-proofed for up to several kW of RF power; it has been fitted to a water cooling system. Shown in fig. 3.14 is the helicon antenna before mounting to the apparatus. Before installation the transmission properties of the antenna were measured to check compatibility with the HF band. A vector

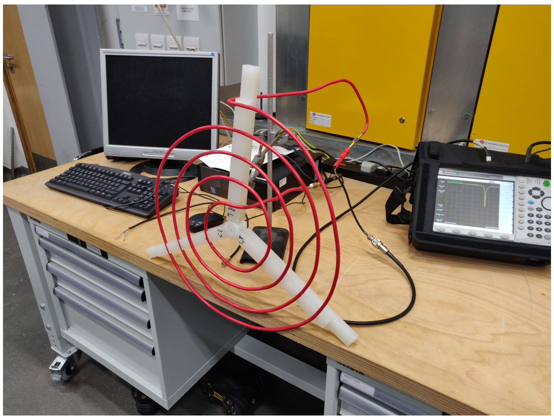

Figure 3.14: Bench testing of the helicon antenna .

network analyser (VNA) can be used to pass a test signal and determine the reflection coefficient Γ, since this is simply given by the S_{11} scattering parameter from either a 1-port or 2-port network measurement. The VNA used for the measurements has a reference impedance of 50 Ω, therefore $|S_{11}|=|\Gamma|=0$ means a load impedance of 50 Ω. When $|S_{11}|=1$ the real and imaginary parts must be examined to reveal the behaviour; for $\mathrm{Re}(S_{11}) \to -1$ the load becomes a short circuit while $\mathrm{Re}(S_{11}) \to +1$ is an open circuit. Any non-zero imaginary part implies a reactive behaviour. Substituting $\Gamma = S_{11}$ in eq. (2.81) and rearranging for the load impedance Z_L gives

$$Z_L = Z_0 \frac{1+S_{11}}{1-S_{11}}. \tag{3.26}$$

The reflection coefficient and complex impedance as a function of frequency over the HF band is shown in fig. 3.15 and fig. 3.16. The maximum in S_{11} at $f \approx 10$ MHz is a purely real reflection implying the antenna is presenting as an open circuit at this frequency. Calculating the complex impedance shows this open circuit behaviour is occurring at the self resonant frequency of the antenna and this frequency should be avoided. This 'self resonance' occurs as the parasitic capacitance of the antenna starts to resonate with the inductance, specifically the frequency at which the susceptance contributions due to the inductive component

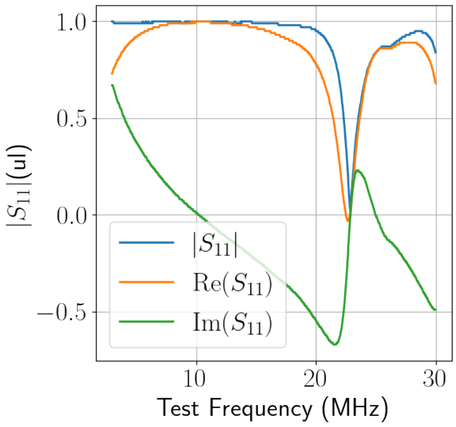

Figure 3.15: Reflection measurement using a 1-port calibration on the VNA

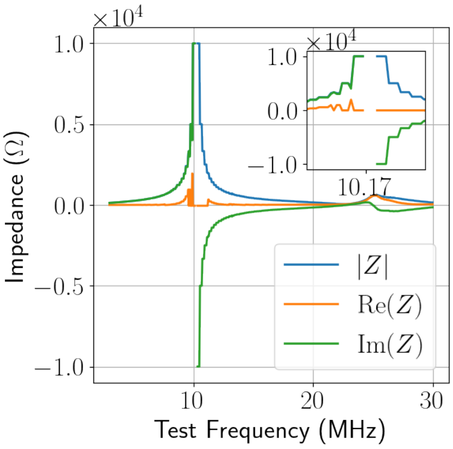

Figure 3.16: Impedance values derived from S_{11}

(the windings) and the capacitive component (coupling between the windings) cancel. Operation at this frequency is not possible as the antenna acts as a choke at this point. Below the self resonant frequency the antenna behaves inductively, while above it behaves capacitively. These measurements are highly variable depending on the orientation of the antenna; as can be seen by the results of the setup shown in fig. 3.17. This antenna would not be considered to be truly in free space in either of the two test scenarios shown as the shortest wavelength tested is 10 m, the entire room and the receiving antenna are thus in the near field.

This can be seen in fig. 3.18 & fig. 3.19 where the maximum reflection occurs at a slightly different frequency, thus the self-resonant frequency has changed. This result emphasises the importance of parasitic effects in the behaviour of such antennas. It is also important to note that the higher frequency dip in S_{11} corresponds with a maximum in S_{21}, reinforcing that the higher frequency features are not self-resonance effects. In light of the sensitivity to nearby objects, a third characterisation is in order; after the antenna has been mounted to the dielectric window and enclosed in a Faraday cage. In this instance the effect on the self-resonant behaviour is more pronounced. The self resonant frequency now appears to have moved to near the bottom of the HF band (≈ 4.3 MHz). The

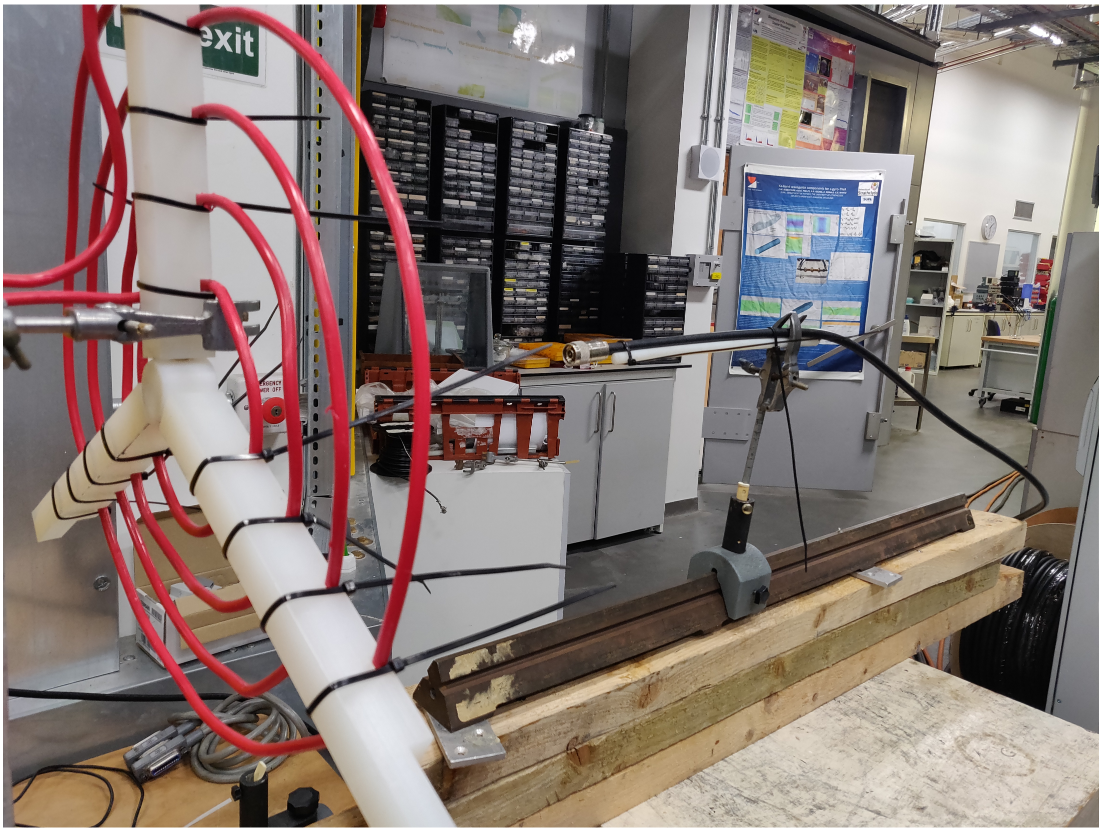

Figure 3.17: Transmission measurement setup for the helicon antenna, various antenna were connected to the coaxial line

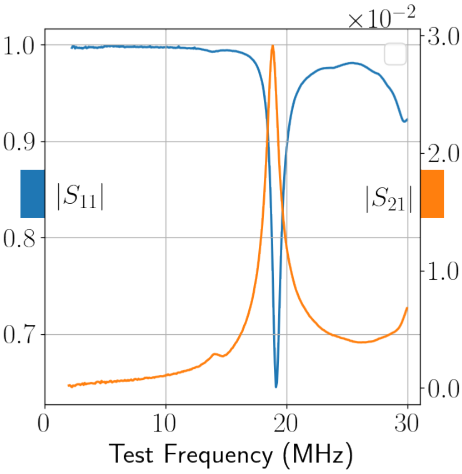

Figure 3.18: Reflection and transmission measurements as detected by a '900 MHz' dipole antenna

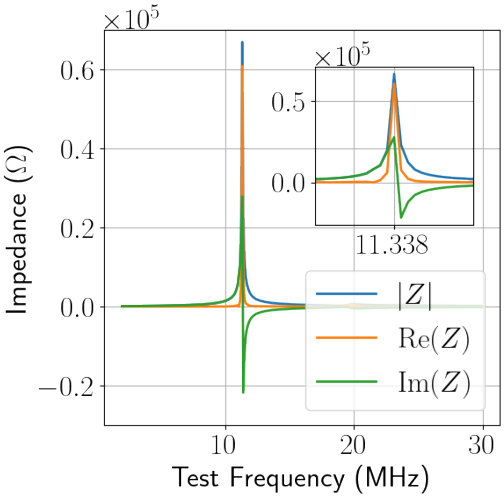

Figure 3.19: Impedance values derived from S_{11}

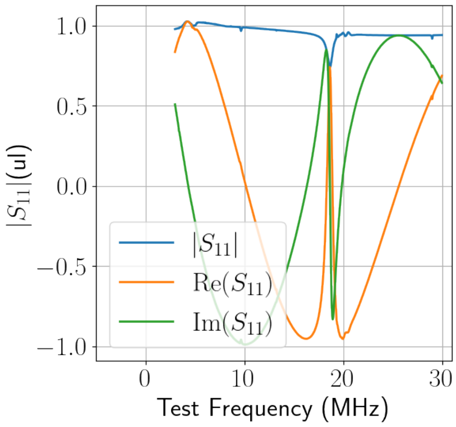

Figure 3.20: Reflection measurements of the helicon antenna after mounting to the vessel.

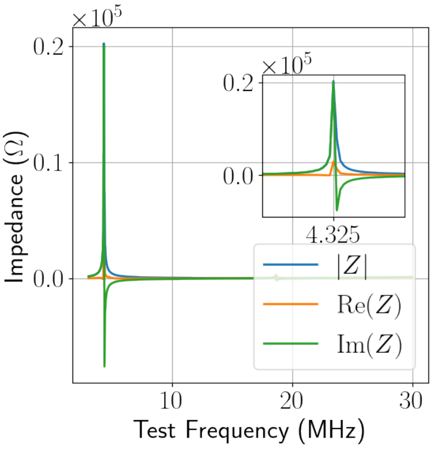

Figure 3.21: Impedance values derived from S_{11}

same behaviour appears as in fig. 3.15, with $|S_{11}| \approx 1$. The real part is also 1 and positive, with no imaginary component. Note, however the behaviour as the frequency approaches the minimum in S_{11} that is concordant with the 'closest match'. The real part of the reflection coefficient becomes purely real, but with $\mathrm{Re}(S_{11}) \approx$ -1, revealing that at approximately 16 MHz the antenna presents a short circuit. The minimum in S_{11} occurs at $\approx$ 18.6 MHz and coincides with the antenna behaving as a purely resistive element ($\mathrm{Im}(S_{11}) = 0$), although not quite 50 Ω.

3.2 RF-compensated Langmuir probe

The primary diagnostic used in this apparatus is the frequency-compensated Langmuir probe, a variation on the now ubiquitous electric probe introduced by Harold Mott-Smith and Irving Langmuir in the 1920s [103]. The Langmuir probe technique consists of immersing a conductor in the plasma and applying a DC bias voltage; the measurement of the current as a function of this bias voltage gives a non-linear relationship known as the 'IV characteristic'. From this characteristic the plasma electron density and temperature can be determined. With extra care the ion densities can also be determined. The theory and analysis can be fairly straightforward for ‘textbook’ cases where the probe is infinitely thin, has no magnetic field, no noise and; in stark contrast to this apparatus, a plasma potential that is not varying. In the case of RF plasmas the plasma potential oscillates at the RF drive frequency [40] and needs further analysis to extract the required information.

3.2.1 Probe diagnostics

As seen earlier (chapter 2), a metallic object in contact with a plasma is shrouded in a sheath that ‘protects’ the plasma from the perturbation, yet not completely shielding the exchange of charge with the plasma. A Langmuir probe takes advantage of this limited disturbance and allows in-situ measurements of plasma parameters by studying how the charge collection (current collection) varies with an applied bias voltage. This measurement is typically known as an ‘IV characteristic’. Interpreting these characteristic traces to extract the plasma conditions can present many challenges; however the analysis is always underpinned by understanding sheath potential, geometry and current density passing through said sheath.

As a first approximation consider a plane collector that extends infinitely in all directions, the total current collected by such a conductor is naturally separated by plasma species as

$$I_{probe}(V) = I_e(V) + I_i(V), \tag{3.27}$$

where the sheath edge will be taken to be the collection surface as any particle crossing this boundary is lost from the plasma. For the ions the total current to the probe will be given by

$$I_i(V) = q_i n_i v_i A_{probe} \tag{3.28}$$

ignoring sheath expansion effects q_i and A are fixed quantities; v_i is not fixed but the ion drift velocity at the sheath edge is given by the Bohm velocity v_B. To obtain the ion density at the sheath edge, a Boltzmann relation is imposed as no charge separation has occurred yet and so thermodynamic equilibrium applies:

$$n_s = n_o e^{-\frac{eV}{T_e}}. \tag{3.29}$$

The energy gained in the transit through the pre-sheath is given by eq. (2.113), thus using $E_i = eV = T_e/2$ gives the ion density at the sheath edge (read 'collecting surface') as

$$n_s = n_0 e^{-\frac{T_e}{2T_e}} = n_0 e^{-\frac{1}{2}} \approx 0.61 n_0, \tag{3.30}$$

revealing the ion density at the sheath edge is a fixed fraction of the bulk density regardless of the wall or plasma potential. This then gives a fairly straightforward expression for the ion current to a planar probe as

$$I_i \approx 0.61 n_o q_i v_B A. \tag{3.31}$$

This value is often referred to as the Bohm current.

The electron density at the probe is a little more involved and requires integrating the velocity distribution function over the velocity space $v_{min} < v < \infty$ where v_{min} is the minimum velocity required to overcome a given retarding field from the probe. The result of that analysis is:

$$I_e \approx -n_0 e A \frac{v_{th}}{4} e^{\frac{eV_\Delta}{T_e}}. \tag{3.32}$$

where V_Δ is the potential difference between the probe and plasma. This is a piece-wise definition and only holds for $V_\Delta < 0$, above 0 the electron current holds at

$$I_{esat} \approx -n_0 e A \frac{v_{th}}{4}, \tag{3.33}$$

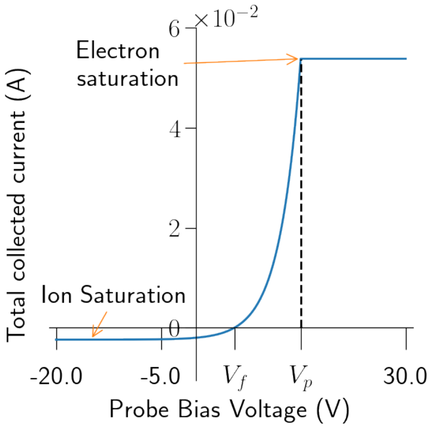

Figure 3.22: A plot of the 'ideal' planar probe characteristic.

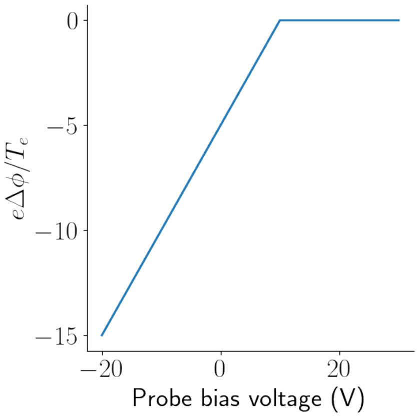

Figure 3.23: A plot of the constant slope showing the temperature.

an important parameter known as the electron saturation current. In the case of a true planar probe of infinite dimensions the collected current would cease to be a function of V_Δ above 0 and hold at this value, which is not true in the majority of realistic geometries.

Although this description of probe theory is incomplete with respect to the implemented probe geometry, this simplified theory for the current collection is an ideal place to introduce a 'textbook' example of a probe IV trace fig. 3.22 and annotate some key features that are used to determine various plasma parameters. In the negative probe bias region the ion saturation limit occurs, where the potential of the probe is sufficient to repel all electrons and leave behind just the Bohm current. In principle this can be used to determine the ion density. Knowledge of the electron temperature would be required in order to calculate the Bohm velocity in eq. (3.28); in reality this is of no help as the magnitude of the ion currents are small enough that experimental errors and system noise make any estimate quite inaccurate. Moving up in bias voltage the next important point is the floating potential. At this point the probe has become slightly less negative with respect to the plasma and a small population of higher energy electrons are able to cross to the sheath edge; enough to cancel out the ion current, resulting in no net current. The region between the floating potential and the plasma potential is a region of exponentially varying electron collection. This is commonly referred to as the retarding field portion of the trace as the probe is still slightly negative with respect to the plasma. At the plasma potential the probe is now collecting the thermal flux of both electrons and ions, since the electrons are much lighter and hotter they represent a much higher current density (in typical RF plasmas). In this simplified description the current then decouples from the probe bias voltage and electron saturation is reached. In reality, finite geometries introduce sheath expansion effects that produce a growth in the collection area A as a function of the potential.

The retarding field region of these traces is particularly important as they can indicate the electron temperature. In order to find the temperature the electron current must be isolated by subtracting the ion saturation current, thereby lifting the entire trace above the axis. The natural logarithm of the electron current then produces a straight line that has a slope of $1/T_e$. Before a logarithm can be taken the current must be normalised to the electron saturation current for good housekeeping of physical dimensions. The traces in fig. 3.22 and fig. 3.23 were constructed with the so far derived theory using a hydrogen plasma with $n = 1 \times 10^{18}$ m^{-3}, $T_e = 2$ eV and a probe collection area of 2×10^{-6} m ^{2}. It is evident from the log plot that the slope of the straight line is 1/2, thus the reciprocal gives an electron temperature of 2 eV. Another method for obtaining the electron temperature that becomes useful in real experiments where much noise is present in the data is to use the difference between the floating and plasma potentials since this difference only depends on the Bohm speed and electron thermal speed. The only other knowledge required is the gas species for the mass in the expression for the Bohm criterion.

An extension to this theory to account for cylindrical geometry effects was introduced by Langmuir and Tonks [104] and uses the ‘orbital motion limited collection' approach to correct the ion current collection. In this approach the ions are considered to have 2 velocity components in the polar coordinate system centred in the probe. The radial component is mostly as before but the potential of the probe acts as a centripetal force to trap ions with certain tangential velocities. Much like a satellite in orbit, too high a tangential velocity and the particle will 'fly past' the probe and not be collected. The starting point is as before; conservation of energy is imposed but now includes radial and tangential velocity, as well as a statement conserving angular momentum:

$$\frac{1}{2}m_i\left(v_{r0}^2+v_{\theta 0}^2\right)+eV_\Delta=\frac{1}{2}m_i\left(v_{rf}^2+v_{\theta f}^2\right), \tag{3.34}$$

$$sv_{\theta 0}=Rv_{\theta f}, \tag{3.35}$$

where

v_{r0} is the radial velocity at the sheath edge,

$v_{\theta 0}$ is the tangential velocity at the sheath edge,

v_{rf} is the radial velocity at the probe surface,

$v_{\theta f}$ is the tangential velocity at the probe surface and

V_Δ is the potential difference between the probe and plasma

By asserting that an ion must have radial velocity $v_{r0}>0$ at the sheath edge to enter the sheath and that the final radial component must be purely real upon impact with the probe ($v_{rf}^2>0$), the range of tangential velocities the probe can then capture are:

$$-\frac{2eV_\Delta}{m_i}\sqrt{\frac{r_p^2}{s^2-r_p^2}\left(1+\frac{m_i}{2eV_\Delta}\right)} < v_{\theta 0} < \frac{2eV_\Delta}{m_i}\sqrt{\frac{r_p^2}{s^2-r_p^2}\left(1+\frac{m_i}{2eV_\Delta}\right)}. \tag{3.36}$$

The ion flux is then integrated over an isotropic distribution function to get the collected ion current as:

$$I = 2enr_s l_p\sqrt{\frac{2e\left|V_\Delta\right|}{m_i}} \tag{3.37}$$

Note that unlike the planar theory, the ion current is now dependent on the probe potential. This extension mostly affects the result for the ion current, the previously derived expression for the electron current to a planar collector still provides a good approximation for the cylindrical probe.

The full expression for ion collection

It is important to note that certain assumptions are made in the derivation of the ion current eq. (3.37), namely that the voltages on the probe are large compared to the plasma potential. The full analytic expression can be obtained without these assumptions and Langmuir and Mott-Smith derive these in their seminal work on probe theory. The full derivation is rather involved but gives the end result for the ion current in terms of error functions.

$$I = I_{sat}\left(\frac{r_s}{r_p}\left(1-erf\sqrt{\frac{r_p^2V_\Delta^2}{r_s^2-r_p^2}}\right)+erf\sqrt{\frac{r_s^2V_\Delta^2}{r_s^2-r_p^2}}\right), \tag{3.38}$$

where V_Δ is the DC bias on the probe with respect to the plasma,

I_{sat} is the ion saturation current,

r_p is the probe radius and

r_s is the sheath radius.

With an understanding of the principles behind Langmuir probes, sheaths and the currents they collect one is well placed to begin analysing probe traces. Of course real world traces do not look like that of fig. 3.22, but nonetheless the theory holds when the task is approached with care and a knowledge of the limitations and assumptions used in the derivation of the theory.

RF Compensation

The probe theory until now assumes a DC generated plasma with a time invariant plasma potential, meaning any DC probe bias is constant relative to the plasma. In an RF generated plasma this is not the case as the plasma potential oscillates at the RF drive frequency [40]. This has an averaging effect on the probe trace and standard analysis techniques can subsequently overestimate the temperature as the exponential region takes on a shallower slope [105]. While revised analysis techniques [106] are available, the presented approach utilises a probe in such a way as to compensate for the oscillation in V_p [107], allowing for more standard interpretations.

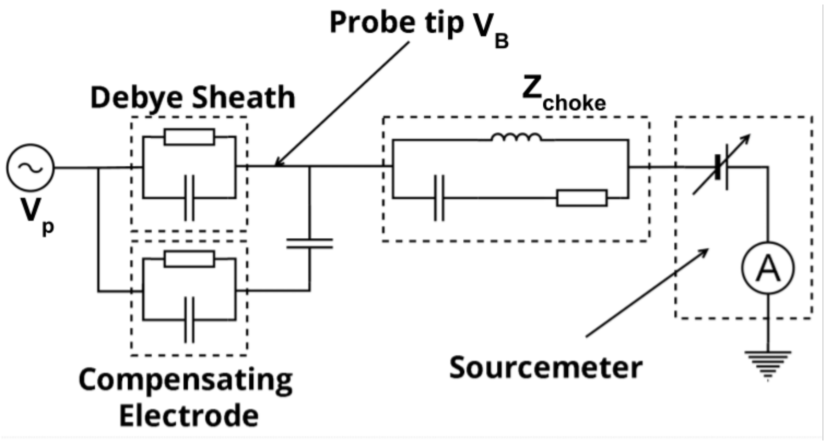

Figure 3.24: RF compensated probe-plasma equivalent circuit

Consider the equivalent circuit of the probe-plasma system in fig. 3.24, the plasma potential is considered as an AC source with frequency equal to the RF drive frequency, while the point denoted by V_B is the DC bias produced by the source-meter. The RF chokes denoted by Z_{choke} are in series with the probe tip and are chosen to resonate at the RF drive frequency to attenuate any oscillating signals at both the fundamental and second harmonic of the RF. However, this does not solve the problem of the oscillating potential difference V_{Δ} between probe and plasma, this is achieved by the larger area compensating electrode that samples the oscillating signal and feeds it back to the probe tip. Thus, everything 'plasma side' of the chokes is free to oscillate with the plasma. Lastly, a large (nF) capacitor is placed in series with the compensating electrode to block the potentially large DC ion and electron currents on the compensating electrode from feeding back into the measurement circuit; the result is the probe tip is the only source of DC for the ammeter to measure.

The primary constraint is the ratio of the voltage divider formed by the series connection of the chokes and plasma. The amplitude of the signal passed to the ammeter is:

$$V_B = \frac{Z_c}{Z_s + Z_c} V_p, \tag{3.39}$$

where (3.40)

V_B is the DC bias on the probe with respect to ground,

Z_c is the impedance of the RF chokes and

Z_s is the impedance of the plasma sheath.

In an RF device the plasma potential will be a superposition of a 'true' DC potential plus a component oscillating at the RF frequency:

$$V_p = \bar{V_p} + \tilde{V_p}. \tag{3.41}$$

For the probe traces to be analysed in the usual way the oscillating component should not cause an excursion in V_Δ of more than $\approx kT/e$, or saturation regime currents will be mixed with the retarding field regime current, making it difficult to determine the electron temperature. The signal measured at the output of this voltage divider should then satisfy, for the oscillating part;

$$\frac{Z_c}{Z_c + Z_s}\tilde{V}_p \ll \frac{k_b T_e}{e}, \tag{3.42}$$

which can be rearranged to give a requirement for the choke impedance as

$$Z_c \gg \left(\frac{e\left|\tilde{V}_p\right|}{k_b T_e} - 1 \right) Z_s. \tag{3.43}$$

Unfortunately it can be difficult to satisfy this by choosing a choke with a large impedance as these are typically too physically large for most Langmuir probes. This is where the compensating electrode provides the balance for the potential divider; by coupling to the plasma impedance in parallel with a large capacitance Z_s can be reduced greatly, thus opening up more options for small inductors that may have a lower impedance.

3.2.2 Probe design, construction and testing

The RF compensation method provides the basis for the Langmuir probe design. The primary probe in use for characterisation experiments uses the circuit in fig. 3.24. The RF chokes and coupling capacitor are ‘Surface Mount Devices’ (SMD) on a printed-circuit-board (PCB), while the compensating electrode takes the form of a tungsten coil wrapped around the last few centimetres of the probe body, concentric with the main collecting tip. This primary electrode is also tungsten to provide robustness in a potentially extreme environment.

The main body of the probe is constructed from ‘Alumina’ (Aluminium Oxide,

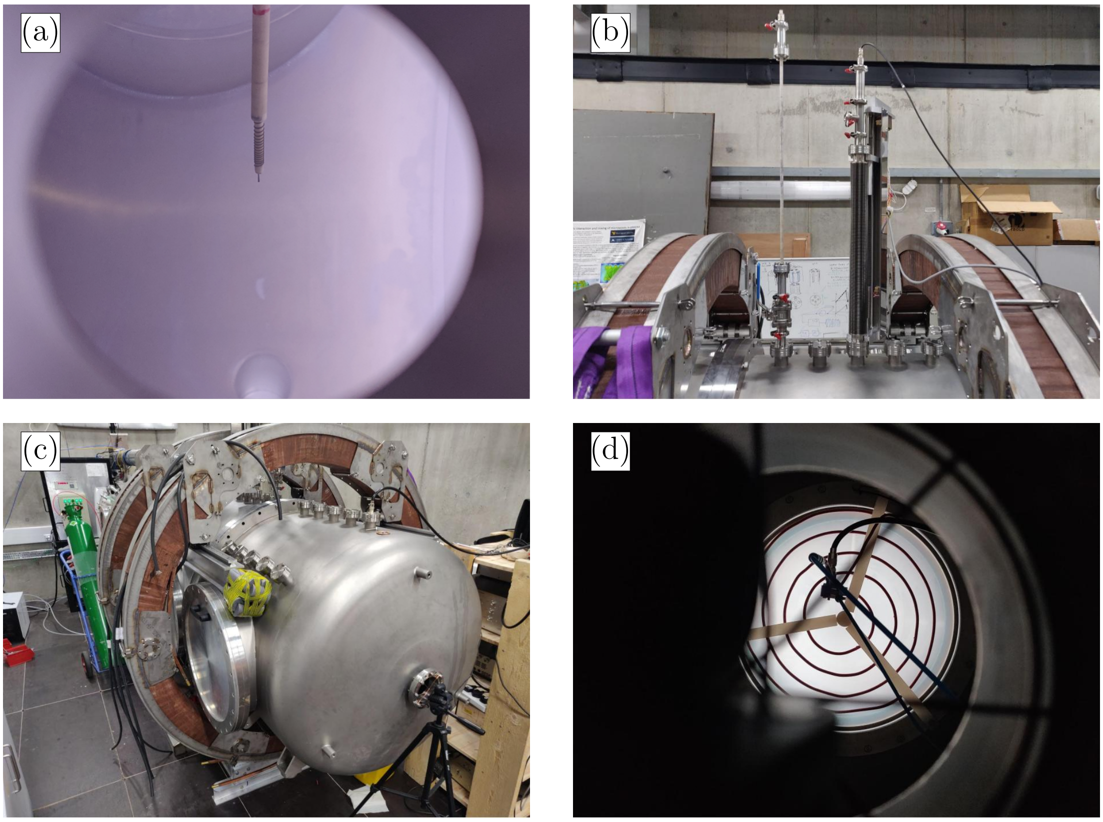

Figure 3.25:
(a) The probe immersed in the glow of a plasma.
(b) Left, manually translating probe with most of the alumina visible; right, the translation stage housing a second probe.
(c) Overview of the apparatus, with the Helmholtz pair mounted.
(d) The spiral RF antenna back-lit by the glow of a helium plasma.

Al_2O_3) tube for its excellent electrical insulation and high melting point [108] (2072 °C). This material is most commonly used in heavy industry where heat resistance is important, such as furnace linings. Alumina has also found a use on the present apparatus more than once, serving as the insulating material between the windings of the electromagnets surrounding the vessel as it can serve its insulator function even as a thin layer a few μm thick. The alumina body comprises 2 sections, a long tube 1 m long and 10 mm in diameter that serves as a conduit for the test lead to reach the vacuum feed-through without exposure to the plasma, while at the probe end a smaller piece of alumina 8 mm in diameter is mounted concentrically in the main housing, this piece of 'twin bore' can be seen in fig. 3.25(a) and fig. 3.27(b) and serves to hold the main collecting tip while acting as a support for the compensating electrode.

Just behind this twin-bore, a small PCB holds the circuitry [107] that couples the main collector and compensating electrode. This circuit is quite simple and consists of 4 RF chokes and a parallel capacitor, with 2 connection points for the electrodes and 1 connection point for the lead to the feed-through. The design frequency for this probe is 14 MHz and so the series chokes consist of 2 inductors with a self-resonant frequency of 14 MHz and 2 with a self resonant frequency of 28 MHz as it is sometimes found the 2nd harmonic of the RF drive can be important in driving the plasma potential oscillations [107]. The effectiveness of this circuit rests on the ability of the chokes to satisfy eq. (3.43).

Using $|V_{RF}| = 100$ V [107] and $T_e = 5$ eV in eq. (3.43) gives (approximately) the requirement $Z_{choke} \gg 730 \times Z_s$. The impedance of the sheath is [109]:

$$Z_s = \frac{2\lambda_D^2}{\epsilon_0 A v_B}. \tag{3.44}$$

Where A is the probe surface area, for this probe $A \approx 2.5 \times 10^{-5}$ m^2, while for a helium plasma with $T_e = 5$ eV the Bohm speed v_B is 11,000 ms^{-1}. Taking a typical electron density from the literature of $n_e \approx 10^{18}$ m^{-3} [60]. These parameters give $Z_s \approx 230\,\Omega$. This means the choke impedance should satisfy $Z_{choke} \gg 4.3\,\mathrm{k}\Omega$. A 50 kΩ impedance should easily satisfy this design requirement. The inductors chosen to act as the chokes are SMD wire-wound inductors chosen for their suitability for soldering to a PCB and their small size (2 mm x 1.6 mm x 0.9 mm) which allows the probe body to remain narrow. For 14 MHz filtering a Murata LQH2MCN680K02 68µH inductor is used with a declared self-resonant frequency of 14 MHz. In reality the maximum impedance presented by this inductor is actually at a frequency of 20 MHz, where the magnitude of the impedance reaches 50 kΩ, while at 14 MHz the impedance reaches just 10 kΩ. The 28 MHz choke is from the same series, an LQH2MCN330K02 unit with an inductance of 33 µH, while the claimed self-resonant frequency of 28 MHz presents an impedance of 19.6 kΩ, the true maximum occurs at 31 MHz (30 kΩ). The total impedance presented at each of the design frequencies is the following sum:

$$Z_T(f) = Z_{66\mu H}(f) * 2 + Z_{\,33\mu H}(f) * 2. \tag{3.45}$$

However, it is common to be in a situation where the requirement eq. (3.43) is not adequately exceeded and this leads to the purpose of the compensating electrode. Since it is difficult to achieve a high value on the LHS, the RHS is lowered by ensuring the compensating electrode in parallel has a much lower impedance by using a conductor with a larger surface area. In this case, the coil winding has a length of approximately 400 mm and a diameter $\approx$ 0.3 mm giving a total surface area of 4.3×10^{-4} m^{-2}, $\approx$ 20 times greater than the main collector, thus relaxing the impedance requirement on the chokes by a factor of 20 down to 200Ω. This compensating electrode is pulling down the resistance with its larger surface area but also serving as a more efficient pickup for the oscillating RF signal and coupling this back to the main probe tip via a (relatively) large capacitor to ensure the probe is always locked with a constant V_Δ with respect to the plasma. This ensures the DC bias applied by the sourcemeter is the true, time-invariant DC bias. Lastly, this capacitor has the added benefit of blocking extra plasma current sampling, which is a DC signal. Thus the precise area of this electrode need not be known as it does not contribute to the IV trace. The DC applied to the probe is provided by a Keithley 2400 sourcemeter that can provide a bias of -200 V $\leq \mathrm{V_B} \leq +200$ V, while being able to record collected currents into the nA range. Since most RF plasmas have plasma potentials of a few V to a few 10s of V [40], the voltage range is more than adequate. While nA of collected current correspond to ion densities of 10^{11} m^{-3} in an argon plasma at $T_e \approx 5$ eV. A density that does not satisfy the definition of a plasma within the confines of the vessel. This sourcemeter is operated under computer control, in tandem with the computer controlled translation stage for the probe.

3.2.3 Langmuir probe system

Physical implementation

The translation stage for the Langmuir probe is a key feature of the apparatus as it allows automation and precise positioning of the probe, without breaking the vacuum. It consists of a flexible bellows pipe with > 0.5 m excursion allowing the probe to scan positions from the outboard edge to the centre of the vessel, with a minimum step ≈ 0.1 mm. The translation stage allows for a small over-excursion past the vessel centre of up to 100 mm to allow testing of the assumption of azimuthal symmetry. The design of the probe feed-through (fig. 3.27(a)) on the bottom of the translation stage shows a soft dielectric insert. This is an important feature that stops the alumina from scratching surfaces inside the vacuum as well as preventing the probe body from acquiring conductive material; alumina is harder than stainless steel, thus some metal is transferred to the probe in the event of any contact during translation. The choke circuitry is placed close to

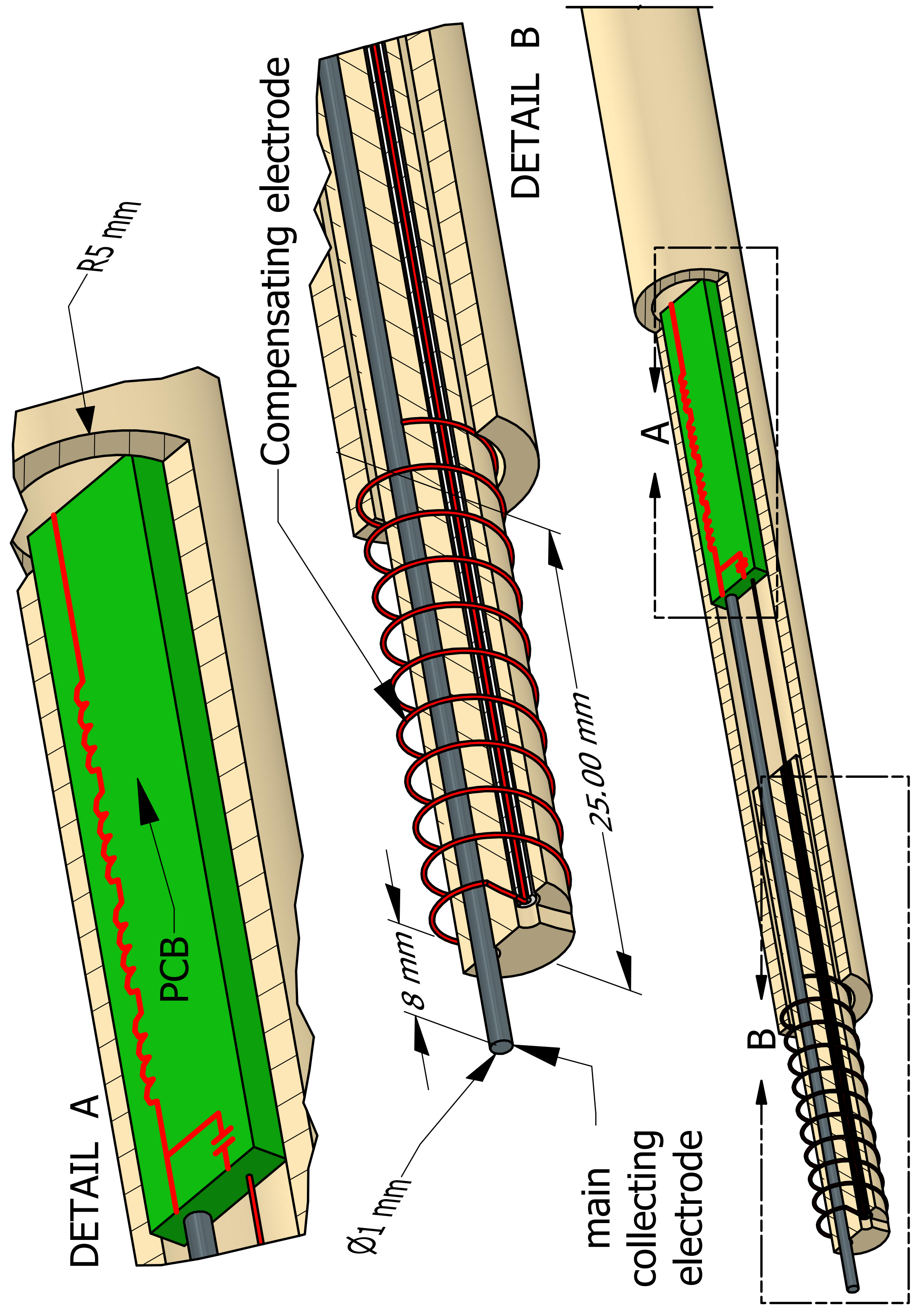

Figure 3.26: Detailed 3D CAD drawing of the Langmuir probe tip assembly.

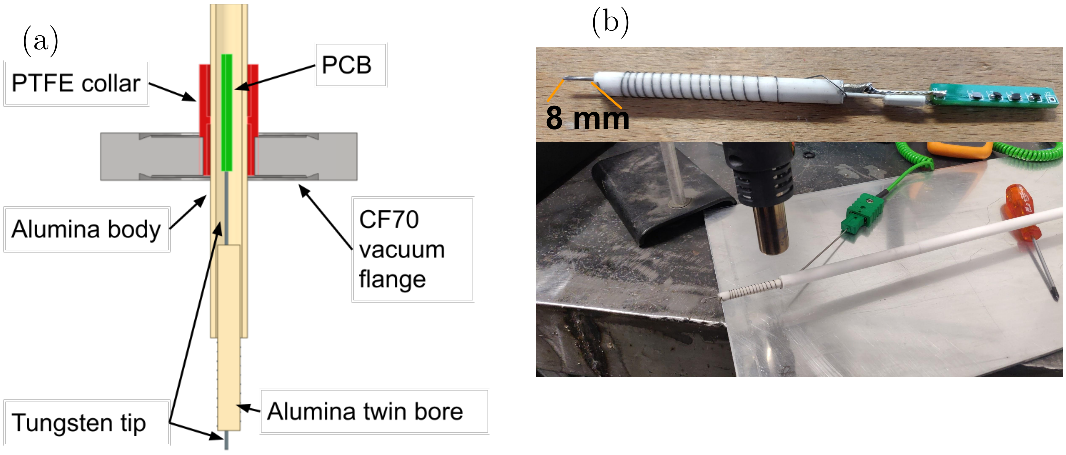

Figure 3.27: (a); CAD drawing of the probe tip and feed-through and (b); construction of the probe tip assembly.

the probe tip and the PCB terminates on a copper wire that carries the signal to a coaxial feed-through at the top of the bellows, where the vacuum seal is made. Currently there is no such apparatus for axial measurements and a vacuum intervention is required, with the entire translation stage being uncoupled and transferred to a new port at a different axial position.

Analysis Routine

Although a Langmuir probe can be simple in its implementation, the detail can become quite involved. Real Langmuir probe data is noisy and there are large uncertainties introduced during analysis. This is partly due to the noisy nature of the plasma medium and partly the large number of mathematical processing steps required to transform from the raw probe data to plasma parameters such as density and temperature. Prior to presenting the probe characterisation data in chapter 5, the method for a probe measurement and the subsequent analysis routines are shown by discussing, step-by-step a single example trace taken by the probe.

The probe system is controlled via a custom python routine which automates the stepping of the translation stage as well as recording the data from the sourcemeter. These results are then passed off to an automated routine that analyses the raw data to produce the plasma parameters and profiles described in chapter 5. The routine returns 5 parameters; the floating potential V_f, the plasma potential V_p. the electron temperature T_e, the electron density n_e and the ion density n_i.

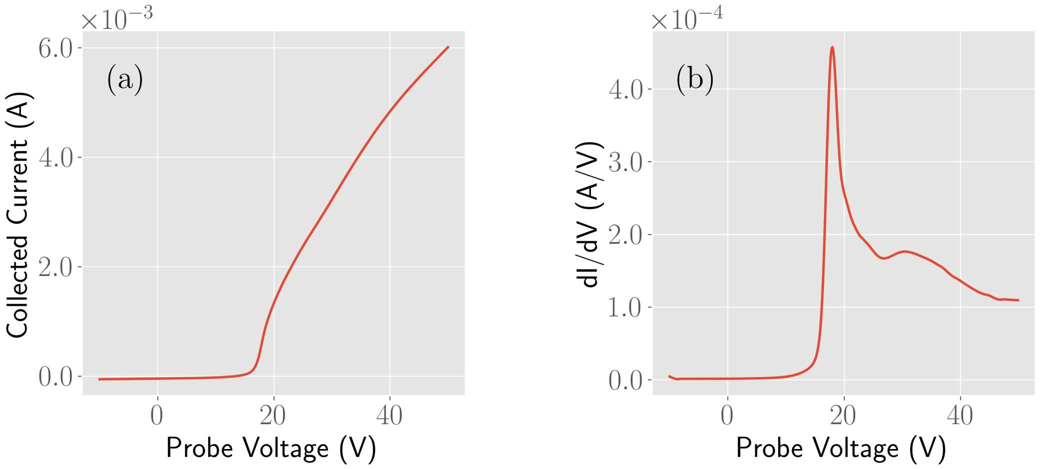

Figure 3.28: Helium ICP at 1.8 Pa, 200 W at $r = 0$, $z = 0.44$ m; (a), an example IV trace and (b), its first derivative.

The floating potential is a simple parameter to estimate, simply where the IV trace goes from negative to positive. The floating potential is then assigned to the data point closest to the interpolated zero-crossing. The plasma potential is a more involved process requiring several steps. In essence the strategy is to find the point in the IV trace where the exponential growth ends. Spotting this point in the ideal 'textbook' trace of fig. 3.22 is rather straightforward. However, in real probe traces there are 2 factors that make the plasma potential difficult to spot by eye. The first is a rounding of the 'knee' that occurs at the plasma potential due to statistical noise and fluctuations in the plasma potential. The second is the lack of saturation of the electron current. Where the ideal trace takes on a constant value, in reality the sheath around the probe grows with the potential as in eq. (2.117). In some cases this current can grow aggressively and, although not exponentially, it can be difficult to spot the changeover point. The analysis routine uses the first derivative of the IV trace to find this point as electron saturation marks the point where exponential growth of the current with voltage ceases. Therefore, the first derivative should reach a maximum at this point. An example of this procedure is shown in fig. 3.28. The sampling resolution in this case is 0.1 V. The first derivative is taken using a central difference scheme, the first and last points on the curve are calculated by forward and backward schemes respectively. The results of the numerical differentiation are then passed through a rolling average filter function utilising a narrow window on the order of 1 volt. This is a pragmatic step; the numerical differentiation enhances any noise in the trace and can cause spurious peaks that do not represent the true extrema of the curve. If all the measured traces were perfectly smooth this step would not be required. The python ‘SciPy’ library is then used to find the local maxima in the curve via the ‘argrelextrema’ function.

With V_f and V_p known, a simple algebraic expression can be used to obtain the electron temperature [110]:

$$T_e = \frac{V_f - V_p}{\ln\left(0.6\sqrt{\frac{2\pi m_e}{m_i}}\right)} \tag{3.46}$$

Next is the electron density n_e, which requires knowledge of the electron saturation current. In the ideal case this would simply be the value of the IV trace at the plasma potential. However, as seen in fig. 3.28(a) the ‘knee’ can become rounded due to noise and averaging effects. Thus, the underlying IV characteristic must be extrapolated into this region. This can be achieved by taking the natural logarithm of the IV trace and since the retarding field region is an exponential function, the natural logarithm will be a straight line. A window is used that is centred between V_f and V_p and no wider than the magnitude of T_e (this region has a width at least a few times the electron temperature). A simple linear regression analysis is performed using this window and the resulting straight line extrapolated to the plasma potential. This point in the ln trace is then converted back to a saturation current in A. The electron density is then calculated using eq. (3.33).

Lastly, the ion densities are estimated separately by using a curve fitting routine employing a least squares strategy. The expression in eq. (3.38) is used, with the Bohm current eq. (3.28) used for I_{sat} and a Child law sheath thickness eq. (2.117) used for a, where $a = s + r$. The only free parameters given are the ion density and the electron temperature. The resulting density that produces the best fit in the ion saturation region is taken to be the ion density.

Uncertainties

Accompanying much of the probe data in this thesis are error bars. These error bars represent a combination of the statistical error from repeat measurements as well as resolution errors. Some of these scale errors are propagated through several algebra steps, leading to fairly large uncertainties. This is difficult to mitigate as the parameters of interest are separated from the measured quantity (current) by plasma sheath theory.

The statistical or random uncertainty δ_r is taken to be the standard deviation:

$$\delta_r = \sqrt{\frac{\sum_{\iota}^{N} (x_{\iota} - \bar{x})^2}{N}} \tag{3.47}$$

while the total uncertainty is taken to be the quadrature sum of the scale and propagated uncertainties δ_m:

$$\delta_T = \sqrt{\delta_r^2 + \delta_m^2} \tag{3.48}$$

The scale uncertainty in the floating potential is simply taken as the resolution $V_f^\delta = \pm 0.1$ V, since the floating potential is not interpolated but 'snapped' to the nearest measurement point. The plasma potential is taken to have an uncertainty of $V_p^\delta = \pm 0.3$V since the second derivative must be evaluated to find a peak in the first derivative. A central difference scheme requires points on either side to evaluate a point and it is this window that is used (see appendix D). The uncertainty in the electron temperature is then taken to be the quadrature sum of the floating and plasma potential:

$$T_e^\delta = \frac{\sqrt{\delta^2 V_p + \delta^2 V_f}}{\ln\left(0.6\sqrt{\frac{2\pi m_e}{m_i}}\right)} \tag{3.49}$$

This result is intuitive in that a voltage resolution on the order of the width of the exponential region will naturally lead to > 100% errors.

The error in the electron density will stem from the error associated with the thermal speed (T_e^δ), the uncertainty in the area of the probe (scale error from digital verniers) and the error in the saturation current. The uncertainty in the saturation current is the largest contribution since this straddles a region of exponential growth. The uncertainty in a logarithm is given as [84]:

$$\delta \ln(X) = \frac{\delta X}{X} \tag{3.50}$$

The linear regression analysis gives that:

$$\ln(I) = mV + C \tag{3.51}$$

and so

$$\ln(I_{esat}) = mV_p + C \tag{3.52}$$

$$\implies \delta \ln(I_{esat}) = mV_p^{\delta} = \frac{\delta I_{esat}}{I_{esat}} \tag{3.53}$$

$$\implies \delta I_{esat} = I_{esat} * m * V_p^{\delta} \tag{3.54}$$

The error in the probe area is 3%, the error in the electron density can now be estimated as

$$\delta n_e = \sqrt{\frac{T_e^{\delta}}{T_e}^2 + \frac{\delta I_{esat}}{I_{esat}}^2 + \frac{\delta A_p}{A_p}^2}\, n_e \tag{3.55}$$

Lastly, the uncertainty in the ion density is estimated by evaluating the ion saturation current at both the estimated V_p and at the maximum excursion $V_p - V_p^{\delta}$. This change is taken to be the error in the saturation current I_{isat}. The uncertainty in the ion density is then estimated as:

$$\delta n_i = \sqrt{\frac{T_e^{\delta}}{T_e}^2 + \frac{\delta I_{isat}}{I_{isat}}^2 + \frac{\delta A_p}{A_p}^2}\, n_i \tag{3.56}$$

Chapter 4

Numerical methods

An important aspect of developing a new experimental apparatus is the ability to predict its behaviour when key parameters are varied. This allows for; prediction of plasma characteristics, revealing system faults, revealing a misunderstanding of the important physics or even revealing new physics that may be difficult to observe first hand. Moreover, if a calculation is accurate, the experimental characterisation can be narrowed to the correct parameter space for the intended physics. To this end, a predictive model of the inductively coupled discharge is desirable, one that supports extension to the magnetically confined helicon mode. Such a model must accurately predict the plasma density, temperature and profiles; taking into account the geometry of the system, the RF drive parameters, confining magnetic field and gas species.

A fluid approach is appropriate since the macroscopic features of interest vary slowly over the length scales relevant to the plasma dynamics. The distribution functions are also expected to be Maxwellian and to not change form at any point in the plasma evolution. The fluid approach also has the added benefit of reduced computation time as the volume is approximately 2.8 m^3 the particle in cell (PiC) method would be too demanding of current desktop workstations. Thus, the fluid model employed by COMSOL Multiphysics to describe inductively coupled discharges was chosen because of its capabilities for easily coupling the fluid plasma equations, plasma chemistry and electromagnetic field solvers. The code solves for the model equations on an efficient spatial grid and a blending of frequency and time domain to improve compute times. Although some details of the microscopic plasma behaviour are lost in this model, the speed with which 'global' questions about the plasma can be answered makes this approach appealing for the apparatus development.

4.1 The finite element method

COMSOL employs the finite element method for solving a given system of equations. Generally, the finite element method (FEM) is used to solve systems of partial differential equations, usually in complex geometries where using a rectangular grid would require too many nodes for a timely solution. This method was originally developed for solving structural engineering problems such as stress, strain and deflection on beams where complex geometries rendered analytic approaches intractable [111]. These types of problems are a good place to start as they are well understood and can be cast as a simple algebra exercise, helping to separate this method from the calculus of variations, which is vital for implementing the FEM but obfuscates some of the core concepts. Broadly speaking, the 'system' of a finite element solver can be broken down into 4 'subsystems':

1. Meshing
2. Creation of the 'stiffness matrix'
3. The solver
4. Post processing

The heart of the finite element method lies in 1 and 2.

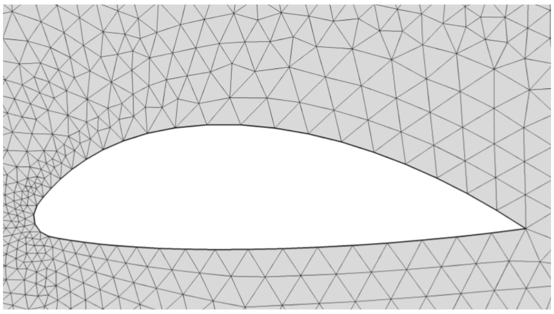

Figure 4.1: A typical tetrahedral mesh around a wing in a fluid dynamics calculation.

4.1.1 Meshing

Meshing of the domain refers to a discretisation method whereby complex geometries are subdivided into discrete ‘elements’ that are typically tetrahedral, but can in principle be any shape. Many modern FEM routines can employ multiple element geometries and varying element size to allow for efficient sampling of irregular shapes. The equations are then solved at the vertices of the elements (the ‘nodes’) and interpolation functions are used to estimate the value of the solution in the intra-node spaces.

4.1.2 The stiffness matrix

To understand the stiffness matrix an analysis of a simple system involving multiple springs connected together is worked through in the following manner:

1. Define the problem (implement equations and draw geometries, set boundary conditions etc.)

2. Recast the problem in its simplest form, involving just two points in 1 dimension (e.g. in heat flow problem, a 1D bar where the only two points on the grid are the end points)

3. Determine a system of equations in terms of these 2 points

4. Build a ‘global’ matrix containing all elements of the system

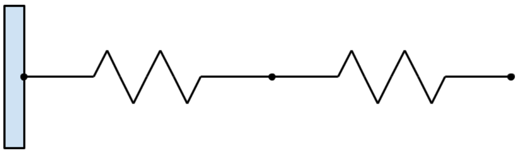

Figure 4.2: The equations governing this simple spring system can be easily determined from a simple balancing of forces.

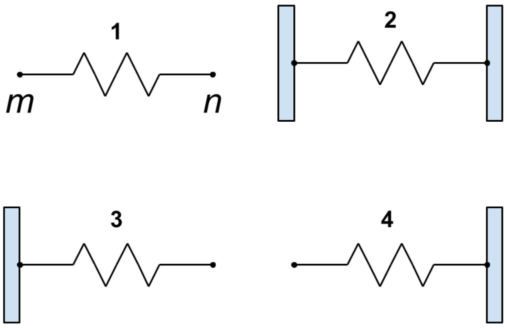

Figure 4.3: The first step is to consider the system of equations for an isolated spring.

Consider a simple system of 2 springs as in fig. 4.2 connected to each other, with 1 end tied to a rigid wall and the other end free to move. The first step is to determine a system of equations from a first principles analysis; for a) a single spring and b) the 2 spring system. A matrix and vector approach that makes the transition from a) to b) trivial will then be demonstrated, which allows for an algorithm to easily build an arbitrarily complex system of equations based on a prototype. Taking the single spring system drawn in fig. 4.3 which has 2 'nodes' m and n, the aim is to create a system of equations describing the forces at each node as a function of that nodes displacement from its rest position. Forces and displacements to the right are positive by convention, converse for the left. This spring has associated with it:

- a stiffness constant K in N/m
- 2 nodes, that each have associated with them:
    - a force F_{node} in N

  - a displacement d_{node} in m
    - $d_{node} = 0 \implies$ rest position

The force at each node will be a superposition of the forces in all possible configurations. These are 1) both ends free, 2) both ends fixed 3) m fixed and n free, 4) m free and n fixed. 1) and 2) are trivial (not really springs) but including them for completeness shows they do not affect the system. For 1) a force applied at either node will obviously cause the entire system to move, therefore no nodal displacement can occur in the reference frame of the spring, $\implies d_m = d_n = 0$ at all times. Therefore (in the reference frame of the spring):

$$F_m = 0$$
$$F_n = 0$$

In case 2) no displacement can be achieved since the nodes are fixed, so again:

$$F_m = 0$$
$$F_n = 0$$

In case 3 node n can be displaced, so there is a force at n and a reaction force at the fixed node m. The notation $F_{X(Y)}$ reads "The force at node X due to the displacement of node Y".

$$F_{n(n)} = Kd_n$$
$$F_{m(n)} = -F_{n(n)} = -Kd_n$$

Finally, in case 4:

$$F_{m(m)} \qquad = Kd_m$$

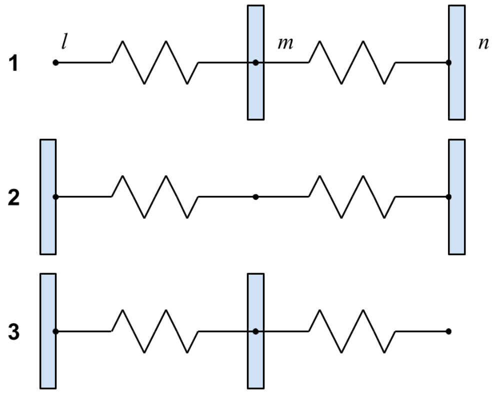

Figure 4.4: The permutations of the 2 spring system

$$F_{n(m)} = -F_{m(m)} \quad = -Kd_m$$

The total force at each node is then

$$\begin{aligned} F_m &= Kd_m - Kd_n \\ F_n &= Kd_n - Kd_m \end{aligned}$$

or

$$\vec{F} = \vec{\vec{K}} \cdot \vec{d} \tag{4.1}$$

$$\begin{bmatrix} F_m \\ F_n \end{bmatrix} = \begin{bmatrix} K & -K \\ -K & K \end{bmatrix} \cdot \begin{bmatrix} d_m \\ d_n \end{bmatrix} \tag{4.2}$$

This can be extended to an arbitrary 2 spring system, the unique and non-trivial permutations are sketched in fig. 4.4. For case 1):

$$\begin{aligned} \text{(trivially) } \underline{F_n = 0} \\ F_l = K_\alpha d_l - K_\alpha d_m \\ \text{since } d_m = 0: \\ \underline{F_l = K_\alpha d_l} \end{aligned}$$

then the reaction force at m is just:

$$\underline{F_m = -F_l = -K_\alpha d_l}$$

For case 2), the notation $F_{m(\alpha)}$ reads "the force at node m due to all forces on spring α":

$$F_m = F_{m(\alpha)} + F_{m(\beta)}$$
$$F_m = -K_\alpha d_l + K_\alpha d_m + K_\beta d_m - K_\beta d_n$$
$$\text{since } d_{l,n} \equiv 0$$
$$\underline{F_m = K_\alpha d_m + K_\beta d_m}$$
$$\text{And the reaction forces are}$$
$$\underline{F_l = K_\alpha d_l - K_\alpha d_m = -K_\alpha d_m}$$
$$\underline{F_n = -K_\beta d_m + K_\beta d_n = -K_\beta d_m}$$

Case 3) is similar to case 1):

$$\underline{F_l = 0}$$
$$F_n = -K_\beta d_m + K_\beta d_n$$
$$\text{since } d_m = 0$$
$$\underline{F_n = K_\beta d_n}$$
$$\text{then the reaction force at } m \text{ is just}$$
$$\underline{F_m = -F_n = -K_\beta d_n}$$

The total forces are then the superposition of all cases:

$$F_l = K_\alpha d_l - K_\alpha d_m$$

$$F_m = -K_\alpha d_l + K_\alpha d_m + K_\beta d_m - K_\beta d_n$$
$$F_n = K_\beta d_n - K_\beta d_m$$

or

$$\vec{F} = \vec{\vec{K}} \cdot \vec{d} \tag{4.3}$$

$$\begin{bmatrix} F_l \\ F_m \\ F_n \end{bmatrix} = \begin{bmatrix} K\alpha & -K_\alpha & 0 \\ -K_\alpha & K_\alpha + k_\beta & -K_\beta \\ 0 & -K_\beta & K_\beta \end{bmatrix} \cdot \begin{bmatrix} d_l \\ d_m \\ d_n \end{bmatrix} \tag{4.4}$$

Suffice it to say, this becomes laborious when the system contains several 'elements'. However, the 'stiffness matrix' in eq. (4.4) can be constructed by addition of the single element prototype matrix in eq. (4.2). Each prototype 2 node matrix is expanded to include empty rows and columns representing the other possible nodes in the system:

$$\begin{bmatrix} K_\alpha & -K_\alpha & 0 \\ -K_\alpha & K_\alpha & 0 \\ 0 & 0 & 0 \end{bmatrix} + \begin{bmatrix} 0 & 0 & 0 \\ 0 & K_\beta & -K_\beta \\ 0 & -K_\beta & K_\beta \end{bmatrix} = \begin{bmatrix} K_\alpha & -K_\alpha & 0 \\ -K_\alpha & K_\alpha + K_\beta & -K_\beta \\ 0 & -K_\beta & K_\beta \end{bmatrix} \tag{4.5}$$

This basic operation represents what is usually called "creating the global stiffness matrix" and amounts to a summation of all the element matrices, with the caveat that each matrix has been cast in terms of the "global" coordinate system. Thus the system is now cast as a tensor equation, usually the interest here would be finding the resulting deflections from applied forces (one can see how this can be easily extended now to a mechanical engineering problem). To do this, the equation eq. (4.4) is rearranged in the intuitive fashion. The resulting matrix cannot be inverted as it is singular, which is remedied by setting the boundary conditions; for example zeroing the first column (equivalent to setting $d_l = 0$, making it fixed) gives an invertible matrix. The rest of the solution comes down to algebra and adds no value for understanding the basic technique.

4.1.3 Weighted residuals and the Galerkin method

The next step in understanding the finite element method comes in studying how a typical physics problem might be approximated and cast in a form in which it might be manipulated as above. Consider a general form of a second order, ordinary differential equation in one dimension:

$$\frac{d^2y(x)}{dx^2} + f(x)y(x) - g(x) = 0 \tag{4.6}$$

By definition, the exact analytic solution $y(x)$ will force the left hand side (LHS) to zero. However, if an approximation $\phi(x) \approx y(x)$ is taken this will become: -

$$\frac{d^2\phi(x)}{dx^2} + f(x)\phi(x) - g(x) \neq 0 \tag{4.7}$$

or, that the LHS is equal to some residual

$$\frac{d^2\phi(x)}{dx^2} + f(x)\phi(x) - g(x) = R(x) \tag{4.8}$$

Let ϕ be a *trial function* that will satisfy

$$R(x) \approx 0 \tag{4.9}$$

This is achieved by taking the inner product of $R(x)$ and a set of basis functions $\hat{\phi}_n$ that define the approximation $\phi(x)$. In a geometry setting the set $\hat{\phi}_n$ would be analogous to $\hat{\imath}$, $\hat{\jmath}$, $\hat{k}$ while $\phi(x)$ would be some vector (position, velocity etc.) in space; in this case the inner product is the dot product. To keep with the

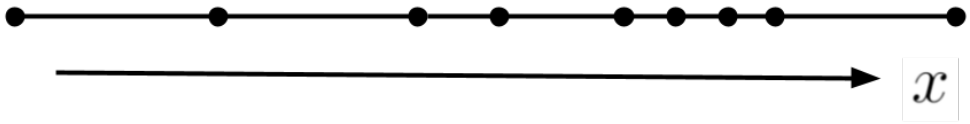

Figure 4.5: A simple discretisation of a 1D domain.

Euclidean analogy, consider a 2D plane V in 3D space and a point T not in this plane. What is the point Q on the plane that V is closest to T? The point Q is at the tip of the vector $Q-T$ that is orthogonal to V. Here T is the true solution $y(x)$, Q is the best guess $\phi(x)$ and V is the space spanned by the basis vectors $\hat{\phi}_n$. To take an example, a common first guess for the approximation $\phi(x)$ would be a polynomial:

$$\phi(x) = \sum_{n=0}^{N} x^n. \tag{4.10}$$

Where $\hat{\phi}_n = x^n$, choosing N = 2:

$$\phi(x) = a + bx + cx^2 \tag{4.11}$$

Where each of the terms can be considered a *basis function* defining a *function space* for $\phi(x)$, the orthogonality constraint is formally given by:

$$< R(x), \hat{\phi}_n > = \int_{\Omega} R(x)\hat{\phi}_n \, d\Omega = 0 \, \forall \, n. \tag{4.12}$$

Which produces a system of equations which can be solved for the missing coefficients a, b & c. Of course, an inner product is only valid over an interval for Ω, this motivates the next key concept for FEM analysis: discretisation.

Consider the 1D domain in fig. 4.5, a solution could be sought for the whole domain but if the solution varies rapidly over this interval the result may be inaccurate. To better approximate the solution, the domain can be divided into a *finite* number of smaller *elements*. These elements need not be uniform and

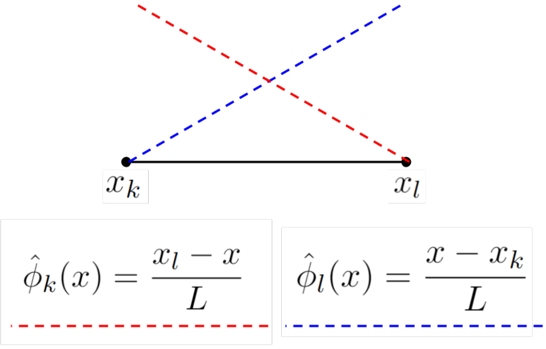

Figure 4.6: A simple, 1D *linear* element with 2 nodes.

nodes can be placed in convenient locations; or can be clustered in regions where the solution is expected to change rapidly (and vice versa) to make computations more efficient. To this end, consider the approximate solution $\phi(x)$ *locally* within in an element. Consider the element in fig. 4.6 which has two nodes (k, l), much like the isolated spring example from fig. 4.2. On this element impose that the local solution on the interval between x_k & x_l is a linear *interpolation function*:

$$\phi^e(x) = a + bx \tag{4.13}$$

At the nodes:

$$\phi(x_k) = a + bx_k = \Phi_k, \tag{4.14}$$

$$\phi(x_l) = a + bx_l = \Phi_l. \tag{4.15}$$

Solving for a and b:

$$a = \frac{\Phi_k x_l - \Phi_l x_k}{L} \tag{4.16}$$

$$b = \frac{\Phi_k - \Phi_l}{L}, \tag{4.17}$$

$$\text{where } L = |x_l - x_k|\,. \tag{4.18}$$

Substitution of eq. (4.16) & eq. (4.17) into eq. (4.13) gives:

$$\phi^e(x) = \hat{\phi}_k(x)\Phi_k + \hat{\phi}_l(x)\Phi_l \tag{4.19}$$

Where

$$\hat{\phi}_k(x) = \frac{x_l - x}{L} \tag{4.20}$$

and

$$\hat{\phi}_l(x) = \frac{x - x_k}{L}. \tag{4.21}$$

Taking a vector form for eq. (4.19):

$$[\phi^e(x)] = [\hat{\phi}][\Phi] \tag{4.22}$$

This is a local approximate solution that has a natural domain Ω, which is the interval $[x_k, x_l]$. This, along with the defined basis vectors $\hat{\phi}$ allows for substitution into eq. (4.12) by using eq. (4.8).

$$\int_{x_k}^{x_l} \hat{\phi}_n \left\{ \frac{d^2\phi^e(x)}{dx^2} + f(x)\phi^e(x) - g(x) \right\} dx \;=\; 0 \tag{4.23}$$

$$\int_{x_k}^{x_l} \hat{\phi}_n \, \frac{d^2\phi^e(x)}{dx^2} \;+ \int_{x_k}^{x_l} \hat{\phi}_n f(x)\phi^e(x) \;- \int_{x_k}^{x_l} \hat{\phi}_n g(x)dx \;=\; 0 \tag{4.24}$$

As is often done in FEM analysis, the constraint on the differentiability of $\phi^e(x)$ is weakened by using integration by parts on the first term in eq. (4.24):

$$\int_{x_k}^{x_l} \hat{\phi}_n \frac{d^2\phi^e(x)}{dx^2} dx = \left[\hat{\phi}_n \frac{d\phi^e(x)}{dx} \right]_{x_k}^{x_l} - \int_{x_k}^{x_l} \frac{d\hat{\phi}_n}{dx}\frac{d\phi^e(x)}{dx} \tag{4.25}$$

and the 2$^{\text{nd}}$ and 3$^{\text{rd}}$ terms are simplified by using average values for $f(x)$ & $g(x)$ respectively:

$$\int_{x_k}^{x_l} f(x)\hat{\phi}_n\phi^e(x)\, dx = \bar{f} \int_{x_k}^{x_l} \hat{\phi}_n\phi^e(x)\, dx \tag{4.26}$$

$$\int_{x_k}^{x_l} g(x)\hat{\phi}_n \, dx = \bar{g}\int_{x_k}^{x_l} \hat{\phi}_n \, dx \tag{4.27}$$

Which gives:

$$\left[\hat{\phi}_n \frac{d\phi^e(x)}{dx}\right]_{x_k}^{x_l} - \int_{x_k}^{x_l} \frac{d\hat{\phi}_n}{dx}\frac{d\phi^e(x)}{dx}\, dx + \bar{f}\int_{x_k}^{x_l} \hat{\phi}_n \phi^e(x)\, dx - \bar{g}\int_{x_k}^{x_l} \hat{\phi}_n \, dx = 0 \tag{4.28}$$

Changing the notation on $\hat{\phi}_n$ to a column vector:

$$\hat{\phi}_n = \begin{bmatrix} \hat{\phi}_k \\ \hat{\phi}_l \end{bmatrix} = \begin{bmatrix} \frac{x_l - x}{L} \\ \frac{x - x_k}{L} \end{bmatrix} \tag{4.29}$$

while noting that

$$\frac{d\hat{\phi}_n}{dx} = \begin{bmatrix} -\frac{1}{L} \\ \frac{1}{L} \end{bmatrix} = \frac{1}{L}\begin{bmatrix} -1 \\ 1 \end{bmatrix} \tag{4.30}$$

and that

$$\hat{\phi}_n\Big|_{x_k} = \begin{bmatrix} 1 \\ 0 \end{bmatrix} = \hat{\imath} \tag{4.31}$$

$$\hat{\phi}_n\Big|_{x_l} = \begin{bmatrix} 0 \\ 1 \end{bmatrix} = \hat{\jmath} \tag{4.32}$$

as well as:

$$\frac{d\phi^e(x)}{dx} = \frac{\Phi_l - \Phi_k}{L} \tag{4.33}$$

Thus the first term in eq. (4.28) becomes:

$$\begin{aligned} &\hat{\phi}_n \frac{d\phi^e(x)}{dx}\bigg|_{x_l} - \hat{\phi}_n \frac{d\phi^e(x)}{dx}\bigg|_{x_k} \\ =&\hat{\jmath}\frac{\Phi_l - \Phi_k}{L} - \hat{\imath}\frac{\Phi_l - \Phi_k}{L} \end{aligned} \tag{4.34}$$

The second term in eq. (4.28) becomes:

$$\begin{aligned}
&\int_{x_k}^{x_l} \left(-\frac{1}{L}\hat{\imath} + \frac{1}{L}\hat{\jmath}\right) \frac{\Phi_l - \Phi_k}{L}\, dx \\
&= \left(-\frac{1}{L}\hat{\imath} + \frac{1}{L}\hat{\jmath}\right) \frac{\Phi_l - \Phi_k}{L} \int_{x_k}^{x_l} dx \\
&= \left(-\frac{1}{L}\hat{\imath} + \frac{1}{L}\hat{\jmath}\right) \frac{\Phi_l - \Phi_k}{L}\, x\big|_{x_k}^{x_l} \\
&= \left(-\frac{1}{L}\hat{\imath} + \frac{1}{L}\hat{\jmath}\right) \frac{\Phi_l - \Phi_k}{L} (x_l - x_k) \\
&= \left(-\frac{1}{L}\hat{\imath} + \frac{1}{L}\hat{\jmath}\right) \frac{\Phi_l - \Phi_k}{L} L \\
&= \frac{\Phi_k - \Phi_l}{L}\hat{\imath} + \frac{\Phi_l - \Phi_k}{L}\hat{\jmath}
\end{aligned} \tag{4.35}$$

The third term:

$$\begin{aligned}
&\bar{f} \int_{x_k}^{x_l} \hat{\phi}_n \phi^e(x) dx \\
&= \bar{f} L \left\{ \left(\frac{\Phi_k}{3} + \frac{\Phi_l}{6}\right)\hat{\imath} + \left(\frac{\Phi_k}{6} + \frac{\Phi_l}{6}\right)\hat{\jmath} \right\}
\end{aligned} \tag{4.36}$$

and the fourth term:

$$\begin{aligned}
&\bar{g} \int_{x_k}^{x_l} \hat{\phi}_n dx \\
&= \frac{\bar{g}L}{2} \left\{ \hat{\imath} + \hat{\jmath} \right\}
\end{aligned} \tag{4.37}$$

substitution of eq. (4.34) through eq. (4.37) into eq. (4.28) yields:

$$\left(\frac{1}{L} - \frac{\bar{f}L}{3}\right)\Phi_k + \left(-\frac{1}{L} - \frac{\bar{f}L}{6}\right)\Phi_l = -\frac{\bar{g}L}{2} - \left.\frac{d\hat{\phi}}{dx}\right|_{x_k} \tag{4.38}$$

$$\left(-\frac{1}{L} - \frac{\bar{f}L}{6}\right)\Phi_k + \left(\frac{1}{L} - \frac{\bar{f}L}{3}\right)\Phi_l = -\frac{\bar{g}L}{2} - \left.\frac{d\hat{\phi}}{dx}\right|_{x_l} \tag{4.39}$$

Where eq. (4.38) corresponds to the $\hat{\imath}$ terms and eq. (4.39) corresponds to the $\hat{\jmath}$

terms. Rearranging this system of equations into matrix form yields an element equation:

$$\begin{bmatrix} \left(\frac{1}{L}-\frac{\bar{f}L}{3}\right) & \left(-\frac{1}{L}-\frac{\bar{f}L}{6}\right) \\ \left(-\frac{1}{L}-\frac{\bar{f}L}{6}\right) & \left(\frac{1}{L}-\frac{\bar{f}L}{3}\right) \end{bmatrix} \begin{bmatrix} \Phi_k \\ \Phi_l \end{bmatrix} = \begin{bmatrix} -\frac{\bar{g}L}{2} \\ -\frac{\bar{g}L}{2} \end{bmatrix} + \begin{bmatrix} \left.\frac{d\hat{\phi}}{dx}\right|_{x_k} \\ \left.\frac{d\hat{\phi}}{dx}\right|_{x_l} \end{bmatrix} \tag{4.40}$$

Or

$$k^e\Phi = f^e + C \tag{4.41}$$

Where k^e is the *element stiffness matrix*, Φ is the vector of *nodal unknowns*, f^e is the *element force vector* and C is the inter-element *continuity requirement.* This element equation can then be used to form a global equation. The continuity terms cancel at shared internal nodes for a given mesh. Thus after constructing the global matrix equation the system becomes:

$$k^e\Phi = f^e \tag{4.42}$$

Where the nodal unknown values for the approximate solution $\phi(x)$ are given by:

$$\Phi = \left(k^e\right)^{-1} f^e \tag{4.43}$$

This has been derived for a linear, 1D element. However, in principle an element can be of any shape and dimension, with as many nodes as needed to suit the problem. These results are for a 1D, linear element and the stiffness matrix was derived for a purely algebraic problem. However, these are the basic techniques that are used by the finite element solver to deconstruct an arbitrary system of differential equations and compute an approximate solution in complex geometries.

4.2 The model

Modelling of the plasma source was carried out using the finite element routine COMSOL Multiphysics using the inductively coupled plasma (ICP) solver. This solver is intended for modelling industrial processing plasmas where a relatively simple model of an inductive antenna ionising a gas stream is sufficient for predicting plasma parameters and profiles. A fluid description of both the ions and electrons as well as their energies are represented on a tetrahedral mesh in a 2D axi-symmetric model.

4.2.1 Governing equations

Plasma evolution

The major set of differential equations being solved for are a set of drift-diffusion equations:

$$\frac{\partial n_{e,i}}{\partial t} + \vec{\nabla} \cdot \vec{\Gamma}_{e,i} = R_e - \left(\vec{v_f} \cdot \vec{\nabla}\right) n_{e,i}, \tag{4.44}$$

$$\vec{\Gamma}_{e,i} = -\left(\vec{\mu}_{e,i} \cdot \vec{E}\right) n_{e,i} - D_{e,i} \cdot \vec{\nabla} n_{e,i} \tag{4.45}$$

$$\frac{\partial n_\varepsilon}{\partial t} + \vec{\nabla} \cdot \vec{\Gamma}_\varepsilon + \vec{E} \cdot \vec{\Gamma}_e = S_{en} - \left(\vec{v_f} \cdot \vec{\nabla}\right) n_\varepsilon + \frac{Q_\varepsilon}{q}, \tag{4.46}$$

$$\vec{\Gamma}_\varepsilon = -\left(\vec{\mu}_{en} \cdot \vec{E}\right) n_\varepsilon - D_{en} \cdot \vec{\nabla} n_\varepsilon \tag{4.47}$$

Where eq. (4.44) describes the density rate of change for the electrons or ions, balancing reaction rates, drift-diffusion and the background velocity of the fluid. Next, in eq. (4.45) $\vec{\Gamma}_{e,i}$ is the flux of particles due to electric field drift and diffusion. Next, eq. (4.46) describes the movement and rate of change of energy associated with a given species, while $\vec{\Gamma}_\varepsilon$ represents the drift-diffusion of the associated energy. In the presented calculations, $\vec{v_f} \equiv 0$, somewhat simplifying the system.

symbol	parameter	unit
$n_{e,i}$	electron/ ion density	$\mathrm{m^{-3}}$
t	time	s
$\vec{v_f}$	fluid velocity	$\mathrm{ms^{-1}}$
$\vec{\mu}_{e,i}$	electron/ ion mobility	$\mathrm{m^2V^{-1}s^{-1}}$
$D_{e,i}$	electron/ ion diffusivity	$\mathrm{m^2s^{-1}}$
$\vec{E}$	electric field	$\mathrm{Vm^{-1}}$
S_{en}	energy loss rate	W
Q_ε	energy deposition rate	W
q	species charge	C

Table 4.1: Parameters involved in the main system of differential equations

The mobility is calculated from a self consistent collision rate ν in the system,

$$\mu = \frac{e}{m_e}\frac{\lambda}{v_e} \tag{4.48}$$

$$\& \; \nu = \frac{v_e}{\lambda} \tag{4.49}$$

$$\implies \mu = \frac{e}{m_e}\frac{1}{\nu} \tag{4.50}$$

This collision rate is given by taking the elastic collision rate of electrons with neutrals, which is the dominant collision loss:

$$\nu = \frac{r_c V_{TOT} N_A}{2} \tag{4.51}$$

Where r_c is the reaction rate in mol/m^{3}s, V_{TOT} is the volume of the plasma in m^3 and N_A is Avogadro's constant. This gives the self consistent mobility as:

$$\mu = \frac{e}{m_e}\frac{2}{r_c V_{TOT} N_A} \tag{4.52}$$

The electron and ion diffusivity are calculated self consistently using Einstein's relations assuming a Maxwellian distribution:

$$D_e = \vec{\vec{\mu}}_e T_e \tag{4.53}$$

$$D_\varepsilon = \vec{\vec{\mu}}_\varepsilon T_e \tag{4.54}$$

$$\text{where } \vec{\vec{\mu}}_\varepsilon = \frac{5}{3}\vec{\vec{\mu}}_e \tag{4.55}$$

The energy loss rate S_{en} describes the rate at which the electron population loses energy to collisions and is given by:

$$S_{en} = F \sum_x r_x \varepsilon_x \tag{4.56}$$

Where x represents a defined plasma chemistry reaction, r_x is the reaction rate in mol/m^{3}s for that reaction, ε_x is the energy lost in the reaction expressed as a potential in V and F is the Faraday constant, 9.65×10^4 sA/mol. Finally, Q_ε is the power deposited by the electromagnetic fields.

Electromagnetic fields

The electromagnetic fields are calculated in the frequency domain using the Ampère-Maxwell law:

$$\vec{\nabla} \times \vec{B} = \mu \vec{J} + \mu\epsilon \frac{\partial \vec{E}}{\partial t} \tag{4.57}$$

The current density includes free currents internal to the simulation under the motion of the fields and an ‘external’ current density that can be defined to represent coils external to the system (such as an RF antenna):

$$\vec{J} = \vec{J}_e + \vec{J}_{ind} = \vec{J}_e + \vec{\vec{\sigma}}\vec{E} + \vec{\vec{\sigma}}\vec{v}_\perp \times \vec{B} \tag{4.58}$$

The $\vec{v} \times \vec{B}$ term arises from including the magnetic field in Ohm's law, which is presented in appendix B

$$\left(i\omega\sigma - \omega^2\epsilon_0\epsilon_r\right)\vec{A} + \vec{\nabla} \times \left(\frac{1}{\mu_0\mu_r}\vec{B}\right) = \vec{J_e} \tag{4.59}$$

The fields are defined as:

$$\vec{B} = \vec{\nabla} \times \vec{A} \tag{4.60}$$

$$\vec{E} = \vec{\nabla}\phi - \frac{d\vec{A}}{dt} \tag{4.61}$$

Field Sources (RF Antenna)

The external current density $\vec{J_e}$ is defined by the current in a coil with specified dimension and material properties. This can be achieved by defining the current in the coil, the voltage across the coil or the total power dissipated in the coil-plasma system. In this model the dissipated power is used as the control parameter to provide a comparison with measurable experimental parameters. One drawback of this method is the problem becomes non-linear when defining a dissipated power as the current and voltage are not uniquely defined for a given problem. The solver must try different current values until a convergent solution is found. For a given target current I, the current density in the coil is solved for via:

$$\int_{A_{coil}} \vec{J_e} \cdot \hat{\theta} dS = I \tag{4.62}$$

where $\hat{\theta}$ is the position vector in the azimuthal direction (defining all current to be flowing azimuthally) and S is the surface slice of the coil. With the current density defined, the voltage across the coil is determined using the microscopic form of Ohm's law:

$$\vec{J_e} = \sigma\vec{E} \tag{4.63}$$

Where $\vec{E}$ is taken to be azimuthal and simply the potential divided by the circumference of the coil, thus:

$$\vec{J}_e = \sigma \frac{V_\iota}{2\pi r}\hat{\theta} \tag{4.64}$$

Where the subscript ι denotes the domain or 'coil'. For example, in a calculation for a set of solenoidal electromagnets connected in series, the domain ι represents a single coil. This leads to a summation over all ι (read 'over all coils') for the total potential drop (Kirchhoff's voltage law):

$$V_{coil} = \sum_{\iota} V_\iota \tag{4.65}$$

The current and resulting voltage across the coil must then satisfy:

$$P_{coil} = \frac{1}{2} I_{coil} V_{coil} \tag{4.66}$$

Where P_{coil} is the total power dissipated in the antenna-plasma system.

Plasma Chemistry

Ionisation processes are captured by the tracking of a variety of plasma 'reactions' between neutrals, electrons, ions and metastables. Cross-section data for each reaction are loaded from an external source. This data is then used to compute a rate for each reaction [112]:

$$r_\iota = k_\iota \prod_{n=1}^{N} c_n^S \tag{4.67}$$

$$k_\iota = \gamma \int_0^{\epsilon_\iota} \bar{\epsilon}\sigma(\epsilon) f(\epsilon) d\epsilon \tag{4.68}$$

Where ϵ is the particle energy in eV, $f(\epsilon)$ is the electron energy distribution function (EEDF) in $\text{eV}^{-3/2}$ and $\sigma(\epsilon)$ is the collision cross section for reaction ι in m^2. The parameter k_ι is the rate coefficient for reaction ι in $\text{m}^3\text{s}^{-1}\text{mol}^{-1}$, c_n

is the molar concentration (mol m^{-3}) of reactant n for reaction ι and S is the relevant entry from the stoichiometry matrix that holds coefficients for the entire set of reactions. Gamma is a factor defined as:

$$\gamma = \sqrt{\frac{2e}{m_e}} \tag{4.69}$$

The factor e is the unitless magnitude of the elementary charge and thus γ has units of kg$^{-1/2}$. For a given species, the rate coefficients are summed to give the 'source' R_n for that species:

$$R_n = N_A \sum_{\iota=1}^{N} r_\iota \tag{4.70}$$

Where ι is a reaction involving species n and N_A is Avogadro's number, therefore R_n has units of m^{-3} s $^{-1}$ and is a number density rate and is used directly in eq. (4.44) for electrons and ions. It is worth noting that the 'energy source term' given by eq. (4.56) uses the rate given in eq. (4.67).

Of course, the cross section $\sigma(\epsilon)$ and distribution function $f(\epsilon)$ must be known ($\bar{\epsilon}$ initial value is given and is then updated via eq. (4.46)). The distribution function is found by assuming a Maxwell-Boltzmann distribution defined in terms of mean energies and incomplete gamma functions:

$$f(\epsilon) = \bar{\epsilon}^{-\frac{3}{2}} \beta_1 e^{-\frac{\epsilon \beta_2}{\bar{\epsilon}}} \tag{4.71}$$

where β_x holds the gamma functions Γ:

$$\beta_1 = \Gamma(5/2)^{\frac{3}{2}} \Gamma(3/2)^{-\frac{5}{2}} \tag{4.72}$$

$$\beta_2 = \Gamma(5/2) \Gamma(3/2)^{-1} \tag{4.73}$$

The cross section $\sigma(\epsilon)$ is then defined for each reaction included in the model using a lookup table. If no lookup tables are available the rate constant can be

equation	reaction	$\Delta\epsilon$ (eV)	method
$e^- + He \rightarrow e^- + He$	elastic scattering	0	table
$e^- + He \rightarrow e^- + He^*$	metastable excitation	19.8	table
$e^- + He \rightarrow 2e^- + He^+$	impact ionisation of neutral	24.6	table
$e^- + He^* \rightarrow 2e^- + He^+$	impact ionisation of metastable	4.78	constant

Table 4.2: Helium plasma chemistry and associated energies.

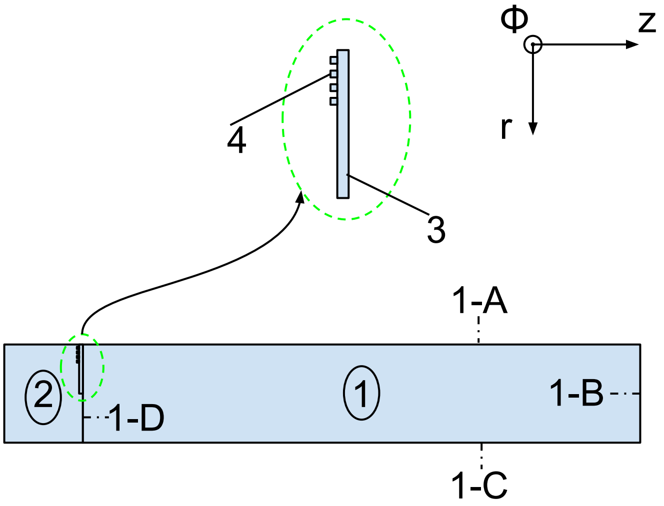

Figure 4.7: The 2D cylindrical geometry of the plasma source model.

defined directly for substitution into eq. (4.68).

With the kinetics in place, the reaction set can now be defined. In the case of helium plasma calculations the chemistry consists of 4 reactions pertaining to elastic scattering, inelastic excitation of a metastable state, impact ionisation of a neutral and impact ionisation of a metastable. These are listed in table 4.2.

4.2.2 Geometry

The plasma volume is modelled in a 2D ‘axi-symmetric’ scheme; a cylindrical coordinate system where half of the rz plane is used. The z-axis forms one boundary of the plane geometry, the other 3 boundaries are then defined arbitrarily. The justification for this scheme is the azimuthally symmetric inductive mode and the $m = 0$ helicon mode can be captured by only the r-z dependence of the fields and plasma. The calculation domain can be split into 4 subdomains defined primarily by the 'material' associated with that subdomain and secondarily by which equations are being solved.

Subdomain 1

Subdomain 1 is the plasma volume. Here, eq. (4.44) to eq. (4.46) are solved for along with the Ampère-Maxwell law eq. (4.57), the plasma chemistry kinetics and tensor conductivity. Initial conditions required for the system of equations are the initial electron density $n_{e,0}$, initial electron temperature $T_{e,0}$, electric potential V ($\equiv 0$), vector potential A_0 ($\equiv 0$), fluid velocity u ($\equiv 0$), bias magnetic flux density B_0, neutral gas temperature T_g and neutral gas pressure p. Each of the boundaries listed in fig. 4.7 1-A to 1-D have associated to them boundary conditions (BC) for the system of differential equations. The boundary 1-A coincides with the z-axis and imposes a symmetry condition for the axis. For Ampère's law the boundary conditions on the external boundaries 1-B, 1-C and 1-D are that the magnetic vector potential $\vec{A}$ must be normal to that boundary (i.e. the magnetic flux density is tangential):

$$\vec{n} \times \vec{A} = 0 \tag{4.74}$$

Another BC required is for the electric potential, which is set to $V = 0$ on all subdomain 1 boundaries (i.e. the walls of the vessel are grounded). The drift-diffusion BC in subdomain 1 is termed the 'wall' condition and is given as:

$$\vec{n} \cdot \vec{\Gamma}_e = \frac{1 - r_e}{1 + r_e} \left(\frac{1}{2} v_{e,th} n_e \right) - \left(\sum_{\iota} \gamma_{\iota} \left(\vec{\Gamma}_{\iota} \cdot \vec{n} \right) + \vec{\Gamma}_t \cdot \vec{n} \right) \tag{4.75}$$

$$\vec{n} \cdot \vec{\Gamma}_{\varepsilon} = \frac{1 - r_e}{1 + r_e} \left(\frac{5}{6} v_{e,th} n_{\varepsilon} \right) - \left(\sum_{\iota} \gamma_{\iota} \varepsilon_{p,\iota} \left(\vec{\Gamma}_{\iota} \cdot \vec{n} \right) + \varepsilon_t \left(\vec{\Gamma}_t \cdot \vec{n} \right) \right) \tag{4.76}$$

Where r_e is a reflection coefficient and is set to 0, $v_{e,th}$ is the electron thermal velocity, γ_{ι} is the secondary emission coefficient for species ι, $\vec{\Gamma}_{\iota}$ is the species flux, n is the normal vector to the surface and $\vec{\Gamma}_t$ is the thermal emission flux at the wall, $\varepsilon_{p,\iota}$ is the mean energy of species ι emitted from the surface and ε_t is the mean energy of thermally emitted electrons at the surface. Thermal emission is disabled by setting:

$$\vec{\Gamma}_t \cdot \vec{n} = 0 \tag{4.77}$$

$$\varepsilon_t = 0 \tag{4.78}$$

Finally, a 'material' is assigned to the subdomain, attributing bulk properties such as conductivity, density, permittivity and permeability etc. In the plasma volume, a placeholder material is assigned and the properties are then over-ridden and calculated self consistently.

Subdomain 2

In subdomain 2, the fields from the antenna are calculated using eq. (4.57). Boundary 2-A uses the same symmetry condition as 1-A, while 2-C and 2-D use the same magnetic flux density condition eq. (4.74) as 1-B and 1-C to mimic the real Faraday cage in the experiment. The material assigned to this subdomain is air, with the solver only requiring the permittivity, permeability and conductivity for use in Ampère's law.

Subdomain 3

Subdomain 3 represents the glass window and is assigned quartz as an approximation to borosilicate glass, again only Ampère's law is solved for here and the same properties are used as in subdomain 2.

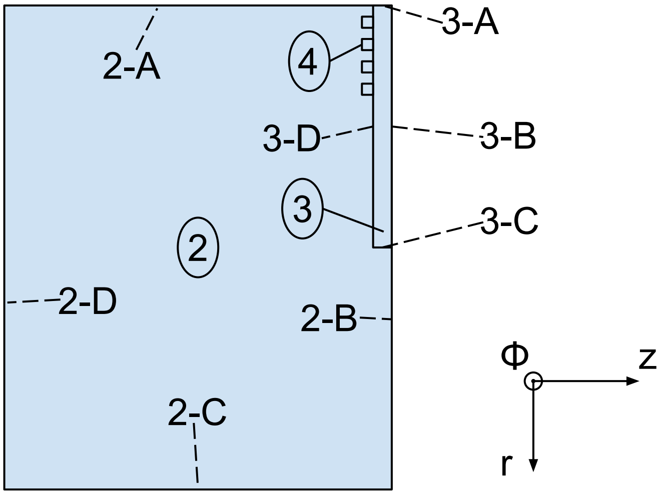

Figure 4.8: Detail view of the Faraday cage and RF antenna geometry.

Subdomain 4

Finally, subdomain 4 represents the antenna coils and approximates the 3D spiral shape by representing the antenna as 4 (physically unconnected) concentric rings that the solver treats as connected in series electrically for the purposes of the power calculation in eq. (4.62) to eq. (4.66). These equations are imposed as well as Ampère's law, again the only material properties needed are those in subdomains 2 and 3. There are no extra boundary conditions in subdomains 2, 3 and 4 as the material properties implicitly define the BC for the solver.

4.3 Convergence testing

When defining a mesh in COMSOL, the user is presented with a multitude of options; the element shape, size, scaling etc. There are many variables that define the size and scaling. Maximum and minimum element sizes, maximum scaling between smallest and largest element and how finely curved regions can be sampled. These must all be simultaneously finely tuned for the algorithm to succeed in generating a mesh; or to run the calculation accurately or efficiently. To

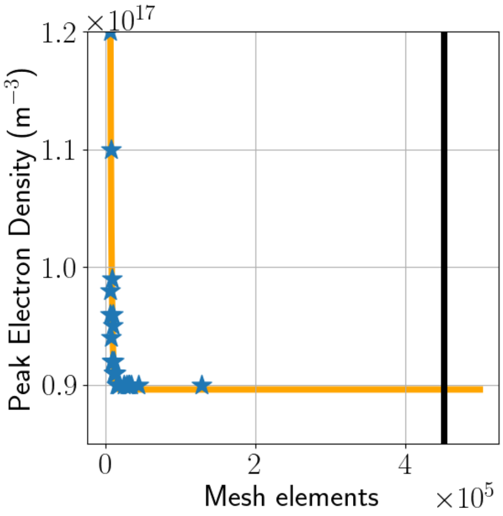

Figure 4.9: Mesh resolution gap in the built in definitions. All possibilities are plotted, the black line represents the densest mesh possible: (fluid: extremely fine), which could not compute. The orange line is an exponential fit.

aid in this, COMSOL comes with a list of pre-defined settings to allow the user to easily generate a mesh for arbitrary geometries. These are split into 4 categories; ‘general physics’, ‘plasma physics’, ‘fluid dynamics’ and ‘semiconductor’. Within each category are several options ranging from ‘extremely coarse’ to ‘extremely fine’. These graduations result in a rapid increase in the mesh density, this can be seen when looking at the total number of mesh elements generated for each of the ‘fluid dynamics’ options in fig. 4.9. The black line represents the densest option providing around 450,000 mesh cells in this case. Triple the next lowest setting; unfortunately the region of stability and convergence seems to lie between these options.

How do the mesh input parameters vary?

For a given mesh size, various parameters are set by COMSOL, table 4.3 shows the difference in settings between all of the ‘fluid dynamics’ meshes. The other categories are ignored since they overlap in resolution and appear to operate under slightly different patterns. Each of the options is assigned a variable x to

Name	Max. size (m)	Min. size (m)	growth rate	C	R_n
Extremely coarse	0.11	0.0035	1.4	1	0.9
Extra coarse	0.065	0.0025	1.3	0.8	1
Coarser	0.0435	0.002	1.25	0.6	1
Coarse	0.0335	0.0015	1.2	0.4	1
Normal	0.0225	0.001	1.15	0.3	1
Fine	0.0175	0.0005	1.13	0.3	1
Finer	0.014	0.0002	1.11	0.25	1
Extra Fine	0.0065	0.000075	1.08	0.25	1
Extremely Fine	0.00335	0.00001	1.05	0.2	1

Table 4.3: Mesh parameters for the fluid dynamics built-in option.

Mesh parameter	equation
Maximum element size	$y = 42(x - 5930)^{-0.778} + 0.001$
Minimum element size	$y = 389(x + 20)^{-1.29} - 2.3 \times 10^{-13}$
Maximum element growth rate	$y = 288(x - 3540)^{-0797} + 1.05$
Curvature factor	$y = 2.4 \times 10^{52}(x + 58500)^{-10.9} + 0.235$

Table 4.4: Equations describing the evolution of the mesh parameters with resolution

substitute as in independent variable to allow curve fitting. Simply assigning 1 to 9 does not reflect the exponential scaling of the options and so the resulting number of mesh elements from each option is used instead. a generic power law is then used as a model curve for each parameter as a function of mesh density:

$$y = A(x - B)^C + D \tag{4.79}$$

The parameter 'resolution of narrow regions' is omitted since it seems to vary only slightly before reaching a maximum value of 1. These fits were obtained using the python module SciPy's 'curve_fit' method which employs a least squares algorithm to fit the model function eq. (4.79) to the data. A graphing calculator was first used to determine approximate values for the constants, this was then passed to the algorithm to narrow the parameter space search to enhance the accuracy of the results. The resulting fits are plotted in fig. 4.10 along with the line equation in table 4.4.

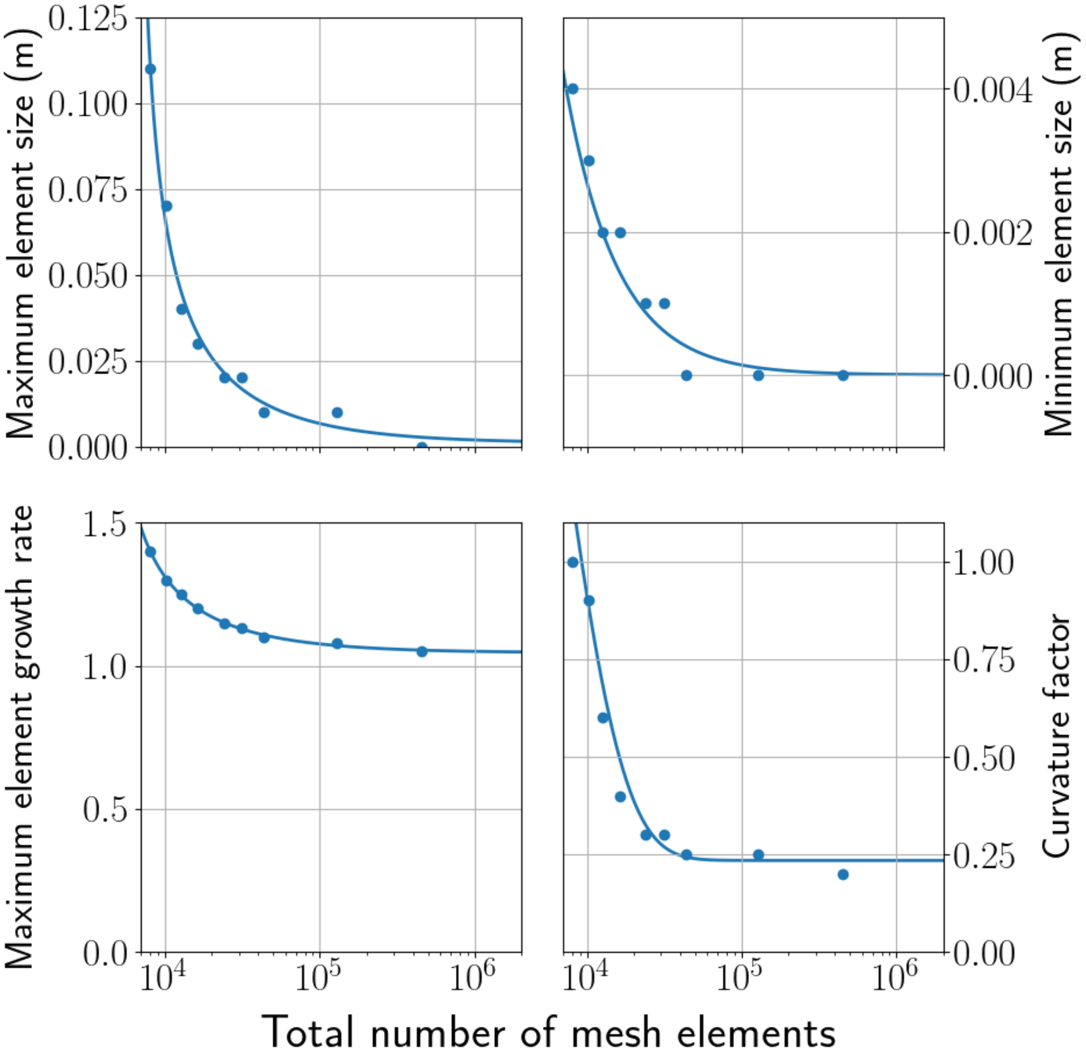

Figure 4.10: Curve fitting results for the fluid mesh options.

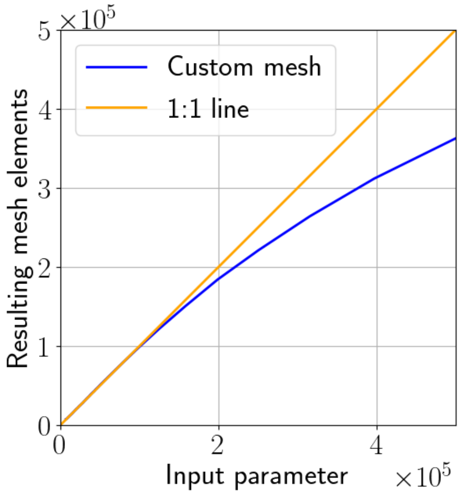

Figure 4.11: The proxy variable diverges above 100,000 but this is not critical to its performance

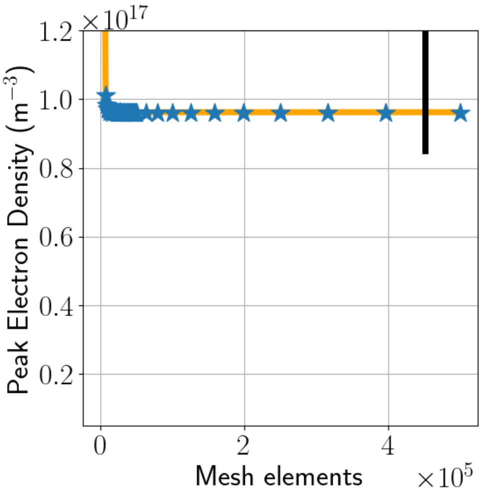

Figure 4.12: The new mesh converges at a different point, but more rapidly

Custom mesh performance

These equations are then used to define a new set of meshes in COMSOL, where x is a proxy for the number of mesh nodes. This proxy for the number of mesh elements is not a good predictor of the final number of elements for $x > 100,000$, as can be seen in fig. 4.11 however this is not the goal. The goal is to create a mesh specification that scales well without numerical errors and in this respect the custom definition for the mesh shows a remarkable improvement. Not only has the gap between 125,000 and 450,000 mesh elements been filled, the new definition is able to provide a mesh that allows for a convergent solution above the previous limit (recall the solver could not find a stable solution at the built in definition for 450,000 elements). It can be seen from fig. 4.12 that the new mesh converges rapidly while extending the upper limit of the calculation's resolution. The final value reached for the peak electron density is slightly different (an increase of 7%), however this mesh is defined slightly differently and the solution will always be a little sensitive to the mesh layout.

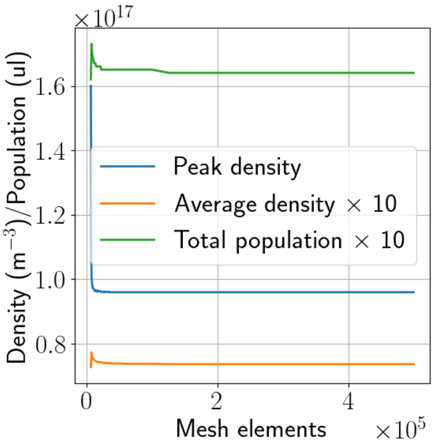

Figure 4.13: Convergence of various parameter types

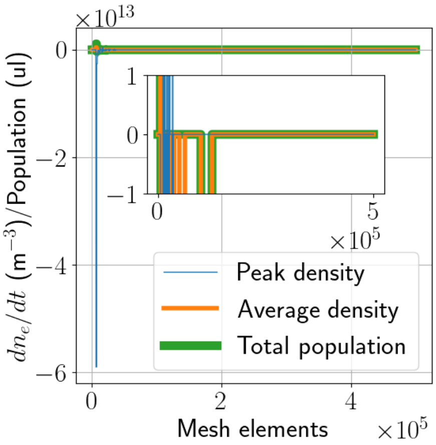

Figure 4.14: First derivatives

Comparing point, average and integrated values

It is important to consider the type of variable used to evaluate the convergence of a calculation as there is a hierarchy to how quickly various outputs converge: point values converge faster than average values which then converge faster than integrated values. The new mesh allows the peak electron density to come within 1% of the asymptote after 11,000 mesh cells and to 0.1% with only 27,000 elements. The results in fig. 4.14 reveal that the average and integrated variables require a higher resolution before they converge fully, however all parameters are still within 1% of the final value for a resolution of 27,000 elements or greater. This resolution is used as standard to benefit from the ≈ 6-fold increase in compute time. The temperature statistics show that the energy balance is also converged as this is the other main differential equation being solved by COMSOL. These are shown in fig. 4.15 and fig. 4.16. It can be seen that the energy content of the calculation is converging in a similar manner to the mass.

The lower resolution's lack of convergence is easily spotted on a contour plot of the electron density in fig. 4.17(a) compared with the converged plot in fig. 4.17(b). The under-resolved calculation clearly shows an impossible plasma

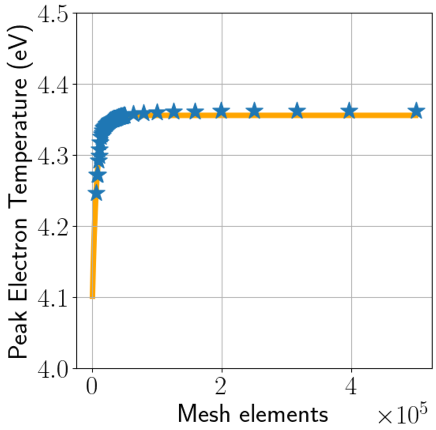

Figure 4.15: Convergence of the peak temperature similar to the density convergence

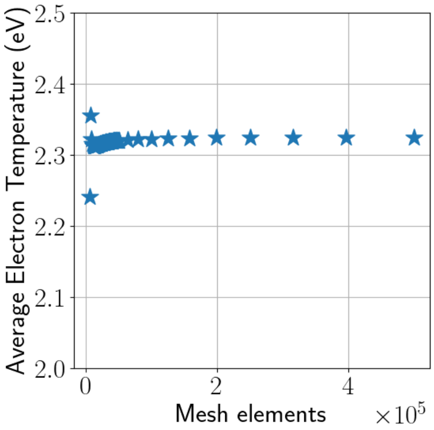

Figure 4.16: The domain average temperature also converges

profile given the parameters and geometry. This necessitates the use of more rigorous analysis for determining convergence. After 10,000 elements the contour maps become indistinguishable from the 250,000 element calculation. The temperature contour plots have no irregular features even at 6000 elements.

Resolving the RF antenna skin depth

An important aspect of the discretisation of this model is resolving the skin depth on the copper RF antenna since this is the region where the currents are flowing. The operation band for the apparatus is $3 < f < 30$ MHz, which when used in the well known expression for the AC skin depth δ in a conductor;

$$\delta = \sqrt{\frac{2}{\omega\sigma\mu}} \tag{4.80}$$

where (4.81)

ω is the AC angular frequency,

σ is the material conductivity and

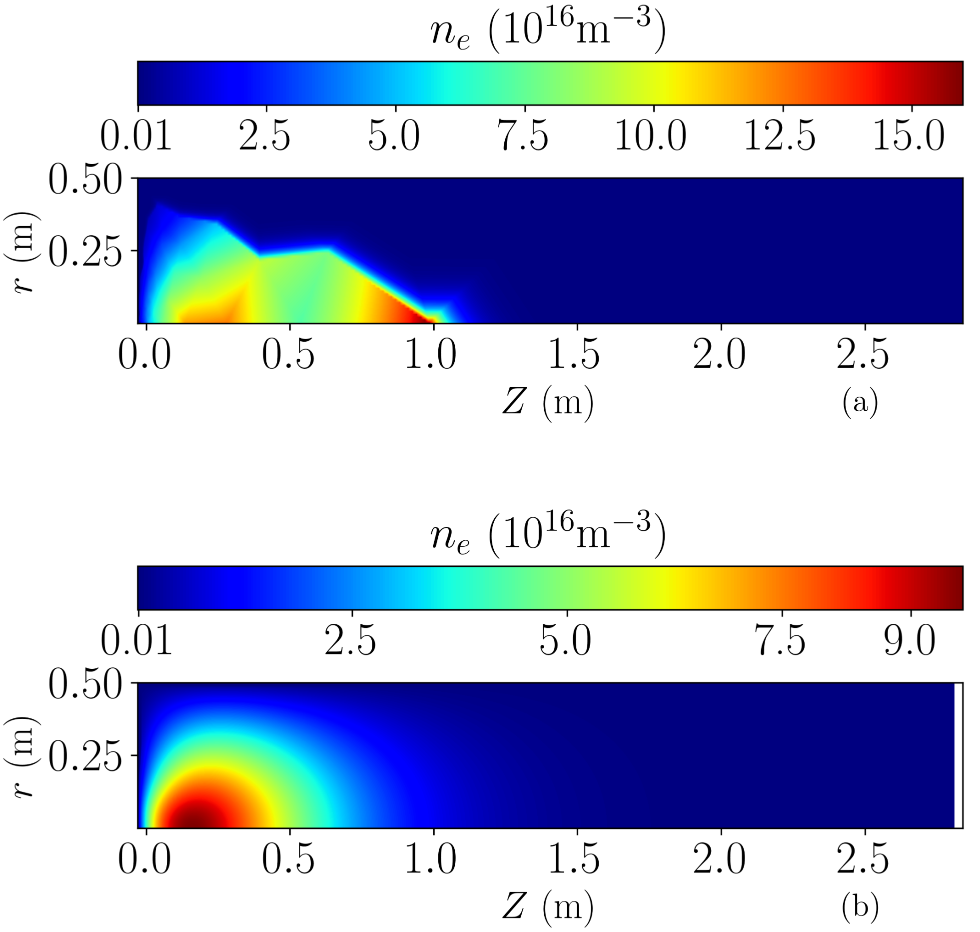

Figure 4.17: Electron density contour maps for; (a) N = 6000, (b) N = 27000

μ is the material permeability.

For the HF band this gives skin depths of $1.2\ \mu\mathrm{m} < \delta < 38\ \mu\mathrm{m}$, therefore the resolution of the antenna coil must provide at least 1 node in this area (ideally several). Specifically, the skin depth describes the $1/e$ folding distance; 3 of which mark the point where the amplitude has decreased to approximately 5% of maximum. A simplifying assumption can be made that all fields are generated by currents flowing in the 3δ thick 'skin' of the conductor. Taking the thinnest skin of 1.2 μm and arbitrarily requiring 10 points in this region implies a mesh spacing of ≈ 100 nm in the antenna coil, or at the very least 0.6 μm

Exploring the effects of the initial conditions on model convergence

It is important to note the behaviour of a model as its initial conditions are changed as these too can affect the final result if the model is under-resolved. The 3 initial conditions required by the solver are; electron density, electron temperature and electric potential. If the model is valid over the range of initial conditions considered, these values should have little effect on the final result providing the calculation is run until steady state. The evolution of the mean electron density shows that the final value converges when the calculation is allowed to run to 1 second. In fig. 4.18 the colouring shows the mean electron density in the plane. The horizontal axis tracks the time in the calculation and the vertical axis tracks a parameter sweep over the initial electron density. For the given parameters in this set of calculations the resulting mean electron density n_e at the end is $\approx 10^{16}\ \mathrm{m}^{-3}$. The plot clearly shows that if n_e starts at the correct value at time $t = 10^{-9}$ s, there is no evolution. The extremes of the parameter sweep show the expected behaviour; at the top of the plot high densities decay over time until the ionization rate due to the RF power is balanced against the losses to the neutral gas and walls. Likewise, the bottom shows low

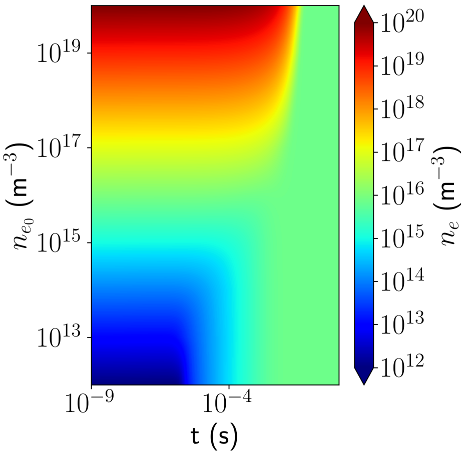

Figure 4.18: X axis shows time, Y axis shows initial electron density, colour axis shows the electron density

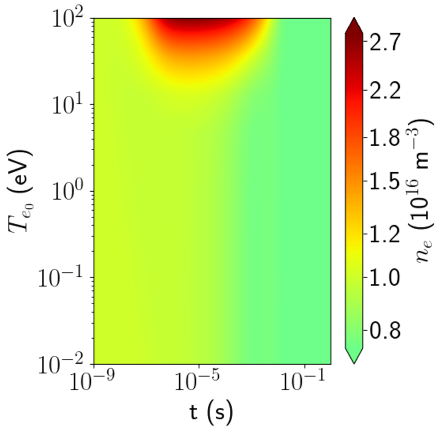

Figure 4.19: X axis shows time, Y axis shows initial electron temperature, colour axis shows the electron density

initial densities increasing until the ionization rate is balanced against losses. In fig. 4.19 the same exercise is repeated with differing initial electron temperatures $T_{e,0}$. Note the final value for T_e is ≈ 3 eV. For the low temperature scenarios the antenna fields raise the temperature and thus the ionisation rate as the calculation progresses. However at very high temperatures there is a burst of ionisation that drops away as the initial 'injection' of energy cannot be replaced by the RF fields. The location of the dense spot in fig. 4.19 coincides with the first ionisation potential for helium ($\approx$ 24V), where close to half of the electron population can directly ionise by the direct route. The evolution of the temperature can also be analysed in a similar manner; in fig. 4.20 the final average electron temperature $\bar{T}_e$ is completely independent of $n_{e,0}$. The variation in the time evolution is to be expected; at low densities the electron population is small and so the energy of the ionising field is spread over a smaller population resulting in a hotter population. The converse is true for the high density initial condition. An interesting feature is seen by following $n_{e,0} = 10^{13}$ m^{-3} across the entire time axis. The temperature approaches the final value in an oscillatory manner, due to the thermal diffusion to the rest of the volume in the wake of the hot spot at $t \approx 5$ µs. The

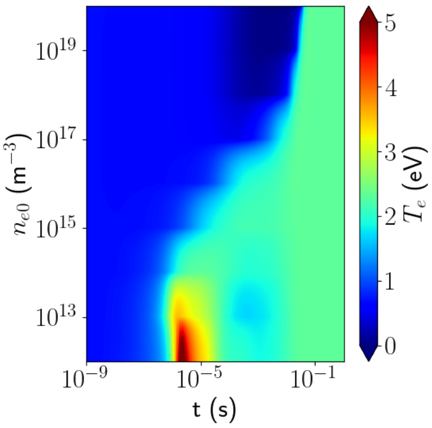

Figure 4.20: X axis shows time, Y axis shows initial electron density, colour axis shows the electron temperature

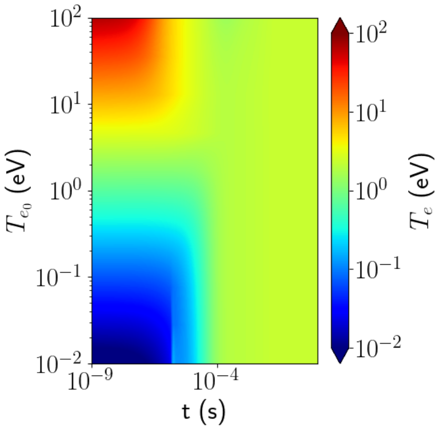

Figure 4.21: X axis shows time, Y axis shows initial electron temperature, colour axis shows the electron temperature

evolution of the temperature in fig. 4.21 mirrors the density behaviour of fig. 4.18 converging slightly quicker since the thermal diffusion will be more rapid than plasma electron/ ion loss due to the latter being entirely moderated by losses to the wall. The initial electric potential has no impact on the calculation.

Chapter 5

Experimental results

The majority of the characterisation work has been carried out in the inductively coupled mode (i.e. with the no bias B-field present). This focus reflects the initial priority of carrying out microwave scattering in the less complicated unmagnetised regime. In order to effectively carry out these investigations the plasma properties and profiles must be known. The lack of a bias magnetic field means the helicon wave cannot propagate and thus its contribution to the electron population via damping is missing. This, combined with the reduced particle confinement and relatively low power, results in a mode of operation with densities much lower than a helicon, where n_e peaks at $\approx 7 \times 10^{15}$ m^{-3}. These densities are suited to scattering experiments in the microwave range as the low electron plasma frequency ($f_{pe} \approx 300$ MHz) means the incident and scattered waves are well above cutoff and so will undergo only weak dispersion prior to any non-linear interaction with the plasma. In addition, this suits the bandwidth available to the X-band equipment as the beat wave frequency must lie within that range. In order to shorten the timescales for ion-coupled parametric instabilities, the choice of gas should be of the lightest that is practical, whilst to lower the threshold for the instabilities the elastic scattering cross section should be minimised. Hydrogen is the lightest element but will complicate the plasma dynamics because of the vast number of pathways for reacting with the vessel, probes, microwave antennas or even contaminants such as water vapour and nitrogen. Moreover, vacuum chambers filled with hydrogen present a serious safety hazard, especially if oxygen were to be accidentally introduced. Thus, helium is chosen as it is the next lightest element and under most laboratory conditions it should remain inert even in the plasma state. Helium is a less popular choice for an RF discharge as its relatively high ionisation potential makes it more difficult to ionise in the standard power range of a few hundred to a few kW that is typical of RF discharges. Indeed, most of the literature concerning inductive and helicon sources discussed in chapter 1 reports on argon experiments. This apparatus has been operated in both gases, since argon provides a simpler environment to commission the source because of its lower ionisation potential; argon is also much less expensive and is not a strategically important resource. The ability to operate in different gases also provides another control parameter in the microwave scattering investigations since the ion timescales and scattering cross sections vary with the gas species.

5.1 Inductive mode

5.1.1 Helium discharge

The plasma densities have been measured over the gas pressure range 0.8 Pa $\leq p \leq$ 6.4 Pa in helium and show smooth profiles that are centred on axis. The choice of gas pressures explored reflect, at the bottom end, limitations of the current design of the Langmuir probe, while on the upper end the consideration is two-fold; the collision frequency should be as low as possible for the scattering experiments and the turbo-drag pump should not be overwhelmed. The radial profiles of the electron density n_e for the helium discharge are presented in fig. 5.1. The axial position is $z = 0.44$ m ($z = 0$ is the vacuum side of the window) and this corresponds with the location of the microwave antenna for the planned paramet-

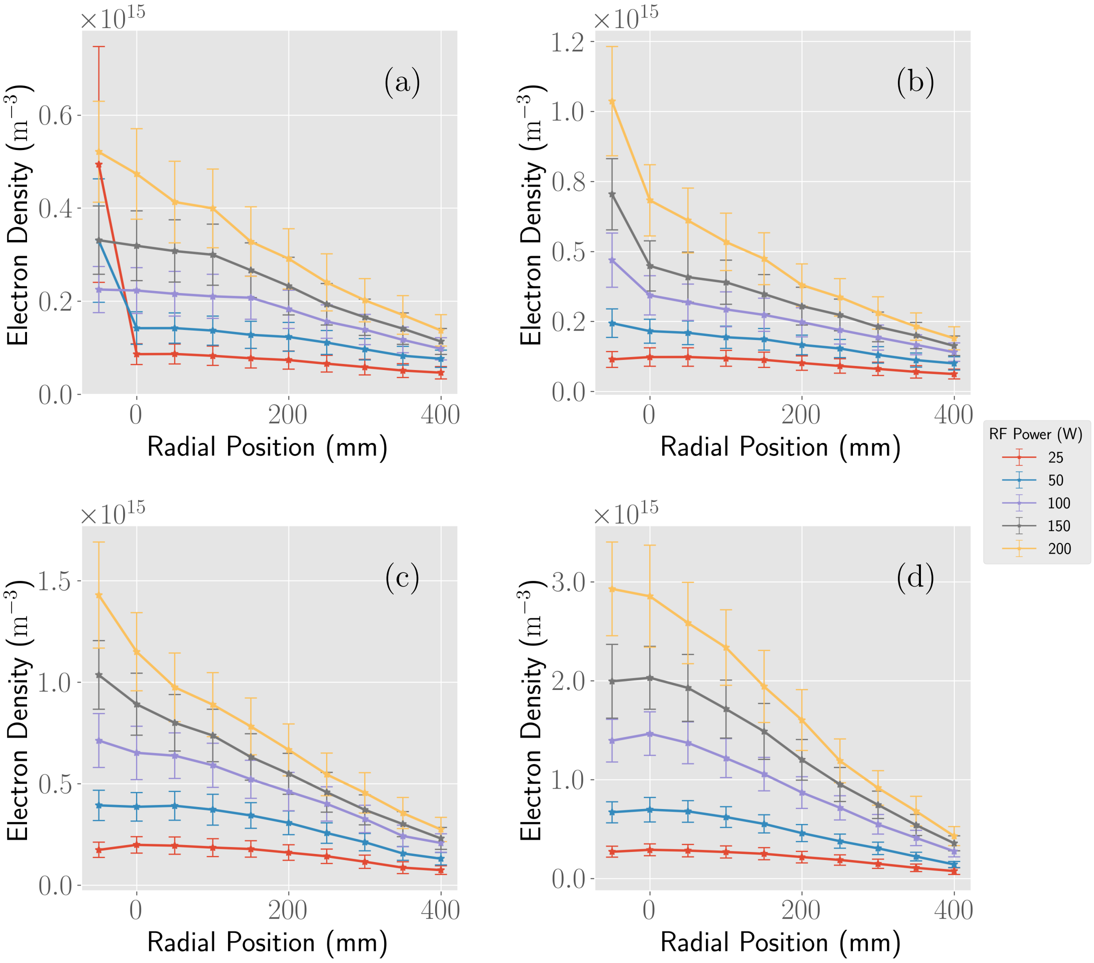

Figure 5.1: Helium n_e profiles over a range of pressures and RF antenna powers; (a) p = 0.8 Pa, (b) p = 1.6 Pa, (c) p = 2.9 Pa, (d) p = 6.4 Pa

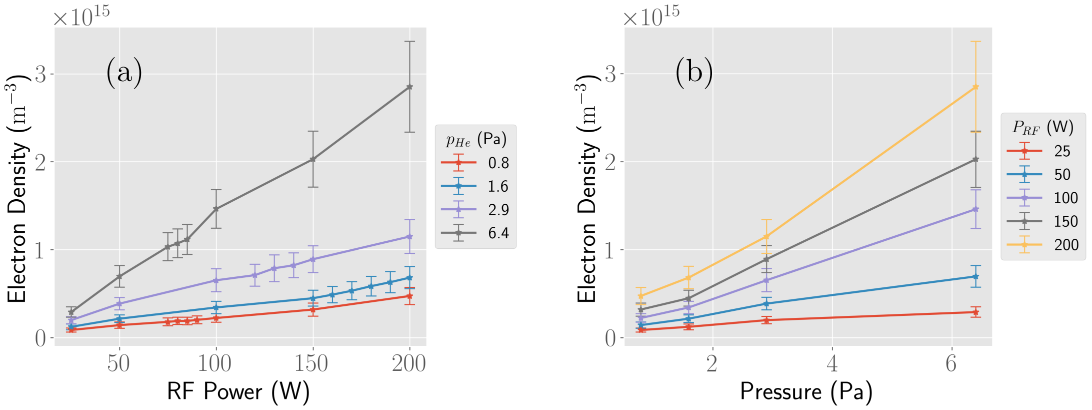

Figure 5.2: Power and pressure dependencies of n_e in helium at $r = 0$, z = 0.44 m

ric scattering experiments. The probe measurements are taken for -50 mm $\leq$ r $\leq$ 400 mm; note the vacuum envelope corresponds to -500 mm $\leq$ r $\leq$ 500 mm. For the range of operating pressures p and RF powers $10 < P_{RF} < 200$ W, fig. 5.1 shows densities in the region 10^{14} m^{-3} to 3×10^{15} m^{-3}. The densities are found to increase with pressure, owing to the lower mean free path producing more ionising collisions, but the profile remains consistent. In the case of the lowest pressure the profile takes on a slight asymmetry. This is not an anomalous reading as the data in fig. 5.1(a) represent the mean value of 3 measurements, this feature is also apparent in the argon plasma, for which axial measurements were taken and this effect is found to worsen with proximity to the antenna. This is discussed later, alongside the argon profiles. From fig. 5.1, the maximum electron plasma frequency is $\approx$ 450 MHz, 2 orders of magnitude less than the frequency of the magnetron to be used for microwave scattering experiments. The evolution of the electron density in the radial centre, at $z = 0.44$ m, is plotted in fig. 5.2 and highlights a change in behaviour for the 6.4 Pa case. It is clear from fig. 5.2(b) that the electron density suddenly grows much faster with P_{RF} after some critical pressure. At this point the skin depth is becoming comparable to the dimensions of the vessel, which is commonly associated with the transition to the higher density inductive mode. This may indicate a jump in density could occur for a slightly higher pressure or density.

In Langmuir probe experiments it can sometimes be difficult to obtain ion information due to the currents being much smaller than the electron contribution. However, the present probe provides clean, repeatable data for the ions and the profile found for the electrons is corroborated by fig. 5.3. For a helium plasma with $n_i \approx 10^{15}$ m^{-3} the ion plasma frequency $f_{pi} \approx 9$ MHz. In a similar trend to the electron profile, the 0.8 Pa case in fig. 5.3(a) shows spurious results at low pressures and densities, further reinforcing the need for a new Langmuir probe to be designed with a larger probe tip.

The ion temperatures are not analysed as the electron current dwarfs the ion contribution in the range of the IV trace where the temperature can be taken. Although not impossible, a very accurate analytic fit for the electron contribution would be required in order to subtract it from the total current and isolate the ion part. The electron temperatures, however, are readily extracted. The radial profiles are plotted in fig. 5.5 and show electron temperatures in the range 1 - 2 eV across most of the parameter range of pressure and RF power. It is surprising, at first, that the electron temperature barely moves when P_{RF} is changed by more than an order of magnitude. However in RF produced plasmas it is a known phenomenon that the bulk electron temperature is a weak function of the input power. Lieberman [40] gives the variation of electron temperatures in RF processing plasmas as a function of the ‘plasma dimension’, a parameter that scales with gas density and the vessel geometry as well as the extent of the sheaths at the walls. From this, temperatures of < 3 eV would be expected for the gas densities in the experiments, indicating the Langmuir probe measurements are in good agreement with RF plasma theory. The radial profile for the temperature shows a slight increase towards the edge of the vessel, this is likely due to the reduced density at the edge of the vessel resulting in an increased skin depth

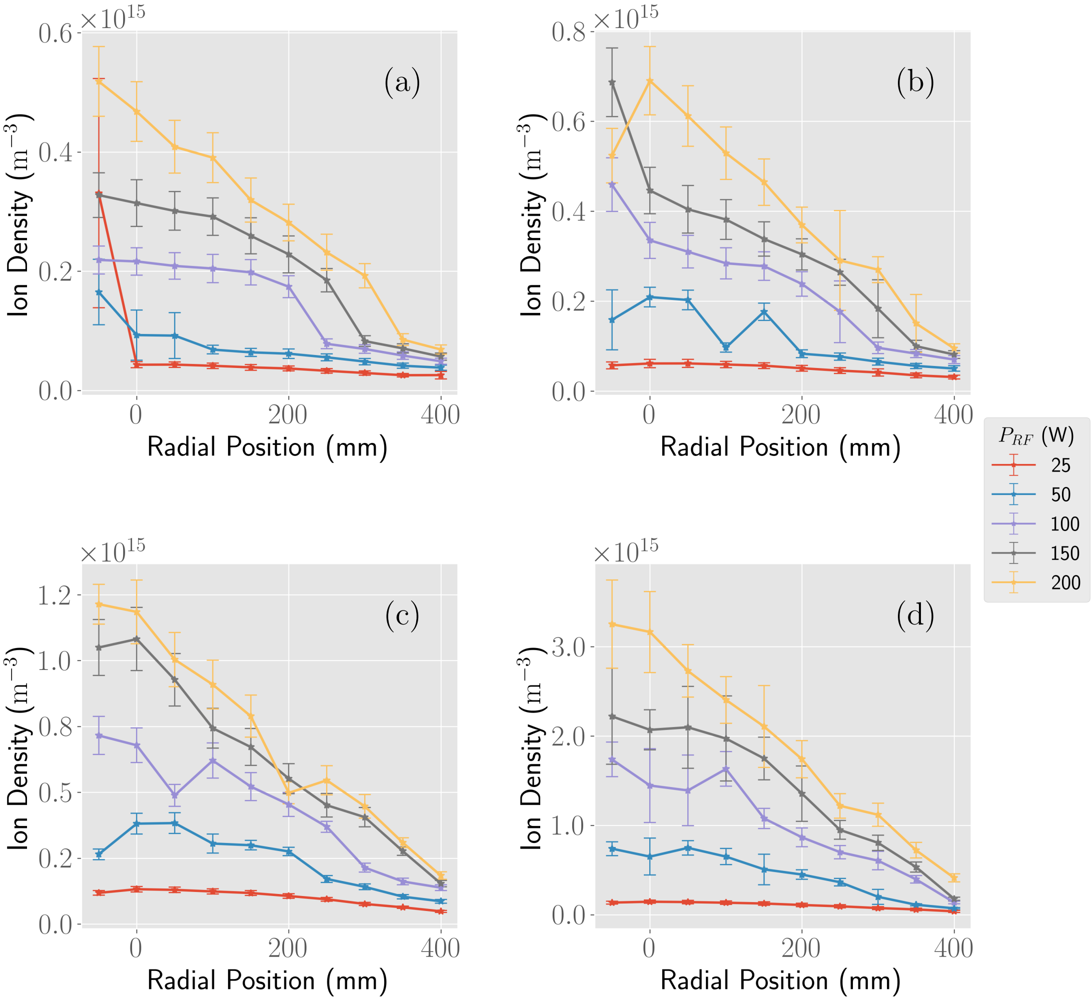

Figure 5.3: Helium n_i profiles over a range of pressures and RF antenna powers; (a) p = 0.8 Pa, (b) p = 1.6 Pa, (c) p = 2.9 Pa, (d) p = 6.4 Pa

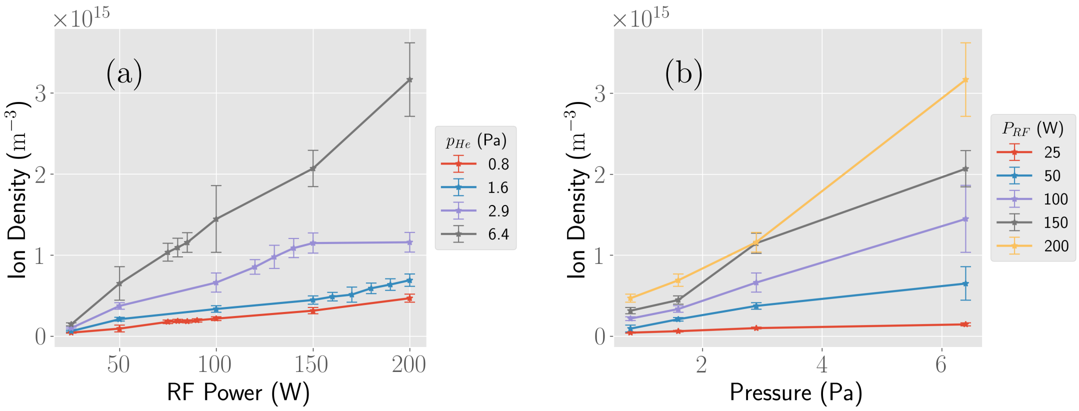

Figure 5.4: Power and pressure dependencies of n_i in helium at $r = 0$, z $=$ 0.44 m

which in turn allows for larger electric fields at this point. The electron temperature tends to decrease with increasing RF power in fig. 5.6(a). It should be noted that the horizontal axis is the forward power set at the HF transmitter and not a measure of power absorbed by the plasma; as the density increases there will be an enhanced screening effect from the electrons. There is an 'optimum' pressure at which maximum heating is observed and this is the collision frequency balancing with the RF frequency. A further increase in the gas pressure results in a reduced mean free path and thus the electrons enter a regime where they collide with gas particles before reaching their maximum momentum in the oscillating fields. Therefore a higher power would be required to maintain the same density and temperature. Low temperatures such as this present a challenge for the implementation of a Langmuir probe diagnostic. As discussed in chapter 3, the oscillation of the plasma potential must be kept to less than the electron temperature in order to have a significant portion of the retarding field section of the IV trace be undisturbed, therefore future work should include probes with higher choke impedances to check that the current probes are adequate.

The floating potential marks the point in the IV trace at which the electron and ion currents are balanced. With respect to the plasma, the floating potential

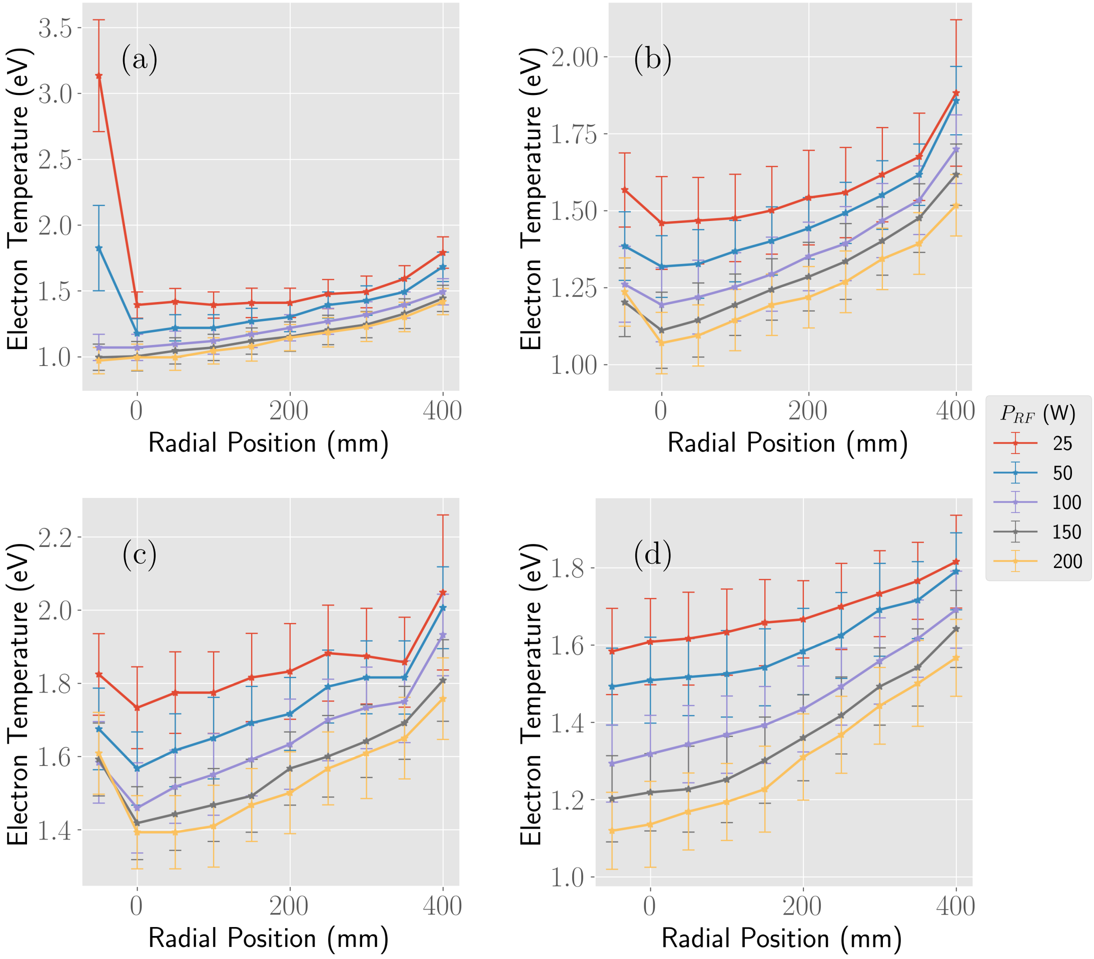

Figure 5.5: Helium T_e profiles over a range of pressures and RF antenna powers; (a) p = 0.8 Pa, (b) p = 1.6 Pa, (c) p = 2.9 Pa, (d) p = 6.4 Pa

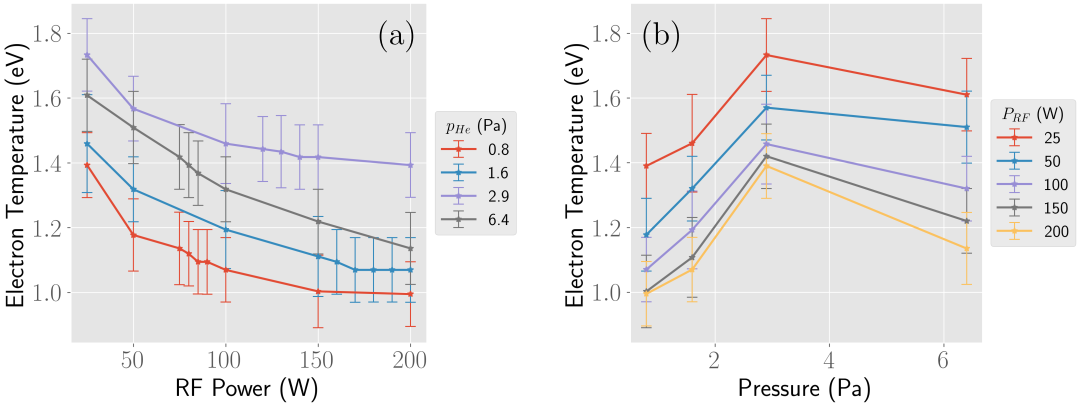

Figure 5.6: Power and pressure dependencies of T_e in helium at $r = 0$, z = 0.44 m

is negative and so most of the low energy electrons are excluded from the probe at this point, while there is a small increase in the (negative) ion current. In broad terms the floating potential is a proxy for the temperature difference between the electrons and ions, where the ions are usually considered to be tied to the gas temperature. The profiles in fig. 5.7 show the floating potential peaks in the centre and falls off towards the edge of the vessel, while fig. 5.8(a) shows the floating potential, as a function of power, reaches a saturation value at low pressures and a peak at 75 W for the highest operating pressure indicating a change in the behaviour of the discharge. The pressure evolution plotted in fig. 5.8(b) shows a weak spike at low pressure before a slight rise in the floating potential.

These values must always be taken in light of the plasma potential, as the horizontal axes of fig. 5.7 & section 5.1.1 are with reference to laboratory ground. The plasma, or space, potential gives the potential of the plasma with respect to laboratory ground and is found at the point where electron saturation occurs on the IV trace (see fig. 3.22). That is, the part where the electron current peaks and does not grow with further increases in probe voltage. This is the point at which the probe is at the same potential as the plasma and all flux of electrons to the collection surface is due to the thermal speed of the electrons. In fig. 5.9 the

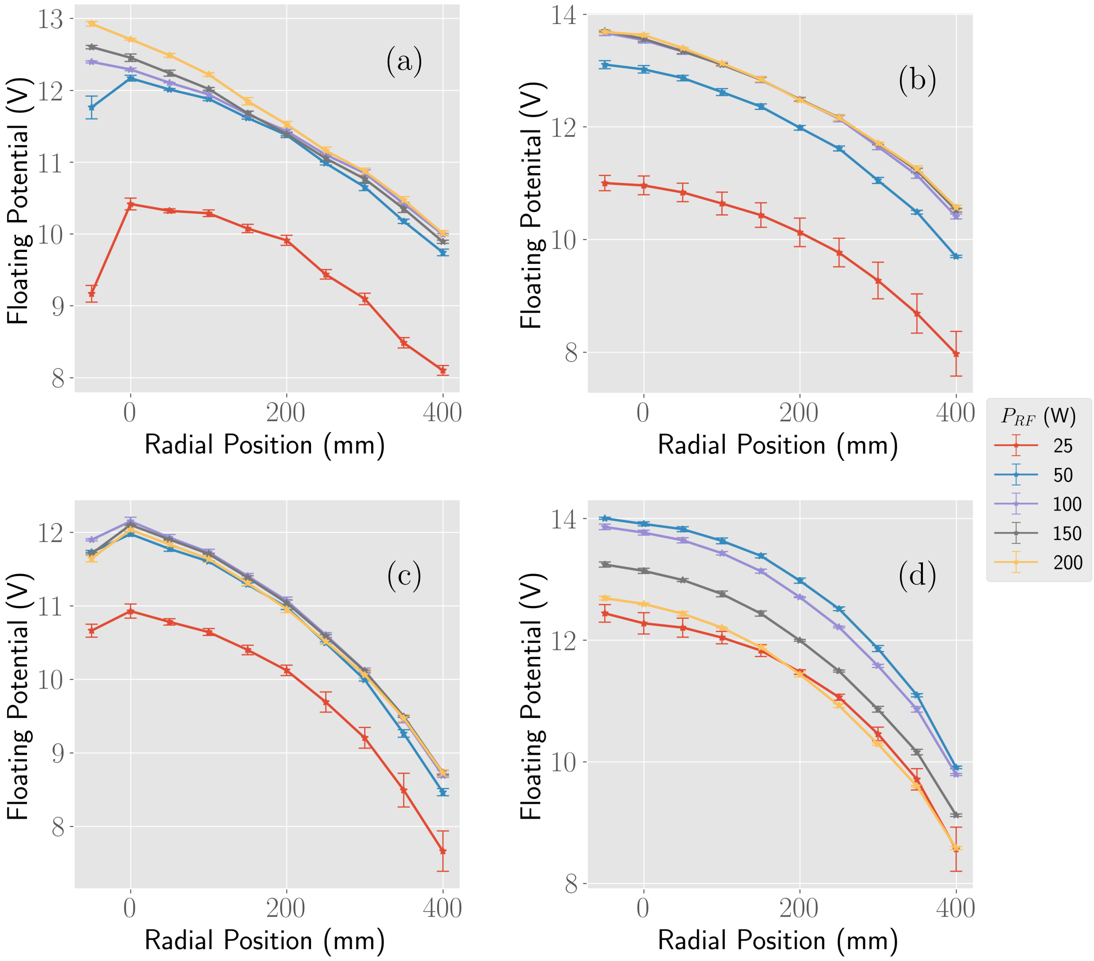

Figure 5.7: Helium V_f profiles over a range of pressures and RF antenna powers; (a) p = 0.8 Pa, (b) p = 1.6 Pa, (c) p = 2.9 Pa, (d) p = 6.4 Pa

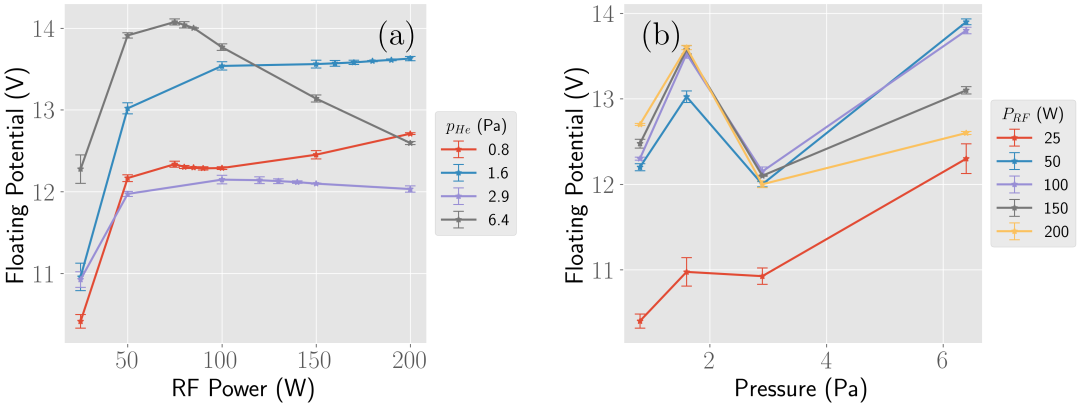

Figure 5.8: Power and pressure dependencies of V_f in helium at $r = 0$, z = 0.44 m

profile of the plasma potential is found to follow the same trend as the floating potential. However, the proportionality is altered from the floating potential as the plasma potential depends on the temperature but also the density, geometry, driving voltage and gas species. Thus, by eq. (3.46), T_e is trending upwards across the radius.

Only radial profiles are presented in the helium case, with the axial profiles left for future work. The first microwave scattering experiments need only information on the radial profiles as the initial campaign is to focus on unmagnetised plasma modes crossing the plasma radially so as to study Raman and Brillouin scattering in a simplified environment. The choice of radial propagation is a practical one; the vessel has large ports diametrically opposed that allow easy access for microwave systems and the Langmuir probe translation stage has enough throw to cover the entire radius of the machine. Thus this region is the most efficient to map and perform initial investigations in.

5.1.2 Argon discharge

The first commissioning experiments for the apparatus were performed using argon. Argon is not ideal for the scattering experiments since its larger radius gives

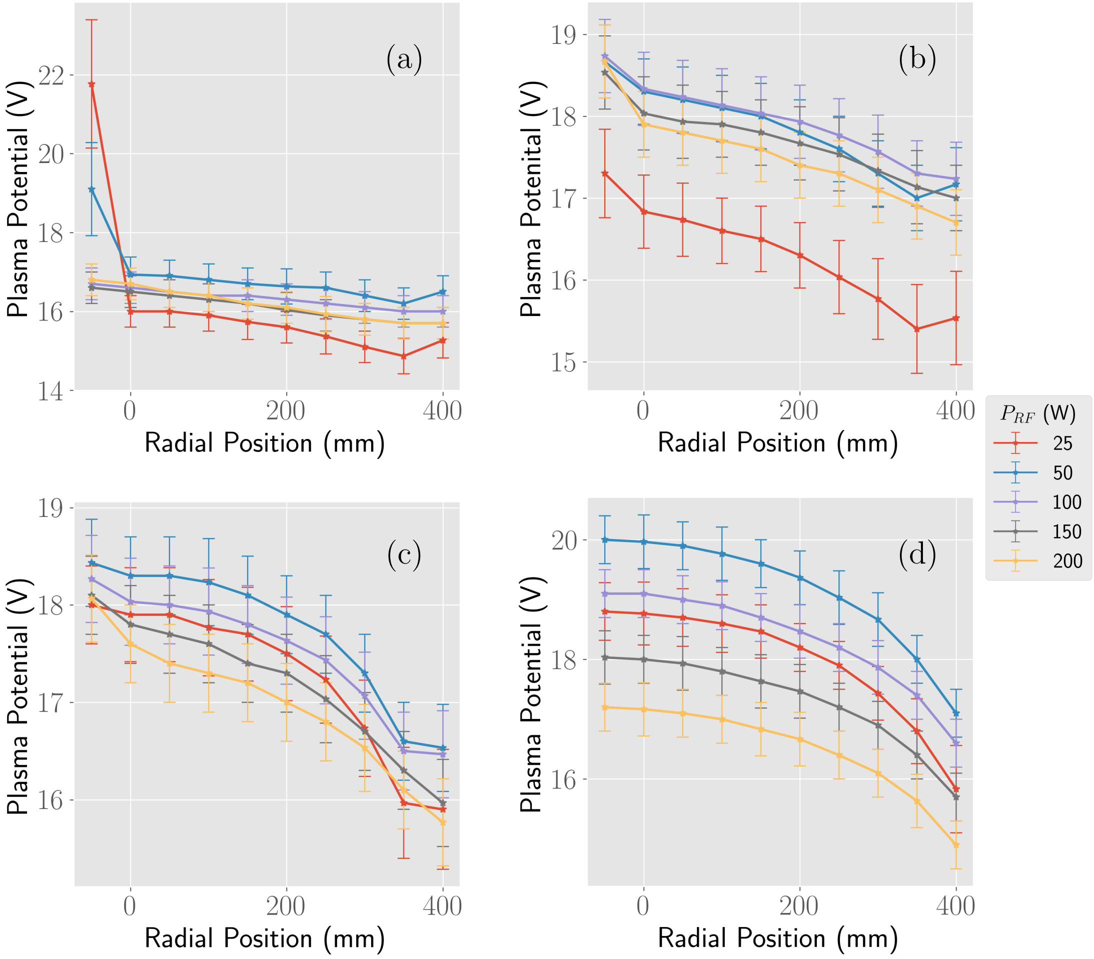

Figure 5.9: Helium V_p profiles over a range of pressures and RF antenna powers; (a) p = 0.8 Pa, (b) p = 1.6 Pa, (c) p = 2.9 Pa, (d) p = 6.4 Pa

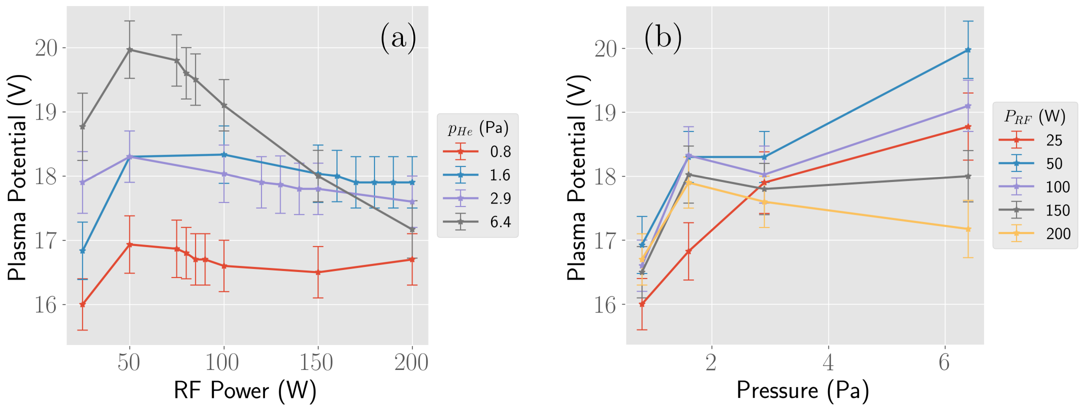

Figure 5.10: Power and pressure dependencies of V_p in helium at $r = 0$, z = 0.44 m

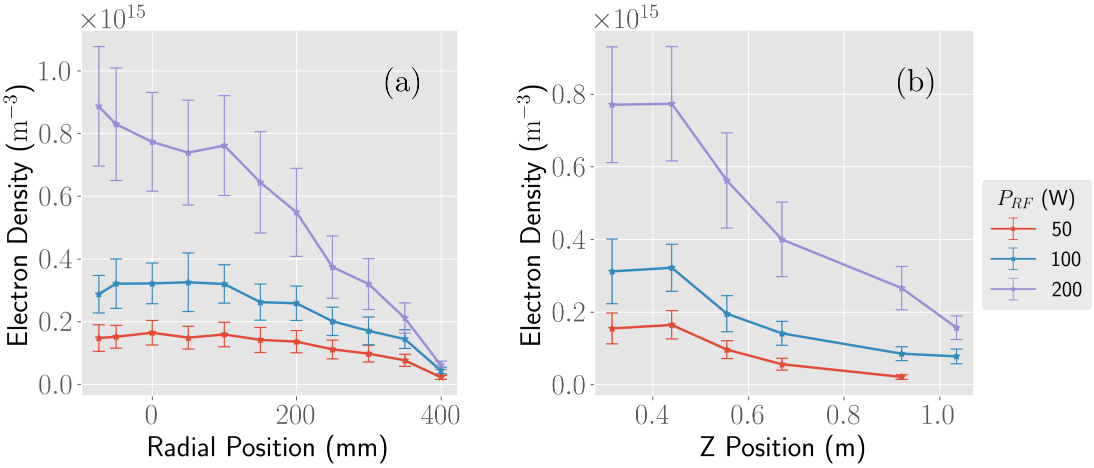

Figure 5.11: Argon n_e profiles at 1 Pa; (a) radial ($z = 0.44$ m), (b) axial ($r = 0$)

rise to a larger cross section for electron-atom collisions and thus more collisional dissipation of both the injected microwave beams and the excited plasma modes; it does, however, have a lower ionisation potential. This makes commissioning more efficient as the matching and input power requirements are relaxed. Since these measurements were only intended as a ‘feet-finding’ exercise, the explored parameter space is less extensive; only 1 Pa has been measured. The radial profiles are similar to those obtained for the helium discharges. The axial profile shows the density declines smoothly but rapidly along z, confirming the RF oscillation is evanescent in the over-dense plasma, with the primary ionisation being localised to the sheath region in front of the antenna. The plasma then diffuses into the rest of the volume. These measurements give an indicator, for future work, of which axial position to choose for radial characterisation if it is found the plasma density must be lowered for the microwave scattering. The ion density also follows the same radial and axial profiles as the electron density. The argon discharge temperatures are not taken to be wholly reliable, but are presented as

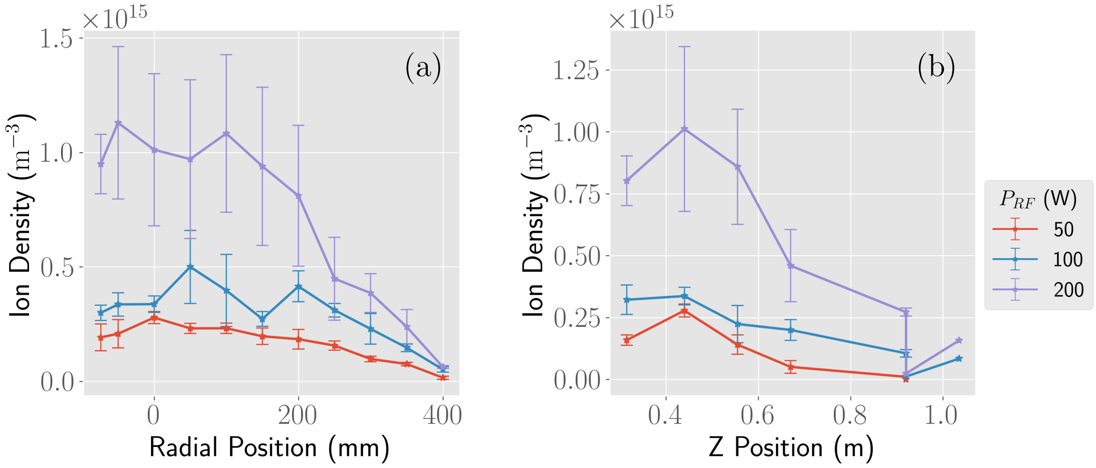

Figure 5.12: Argon n_i profiles at 1 Pa; (a) radial ($z = 0.44$ m), (b) axial ($r = 0$)

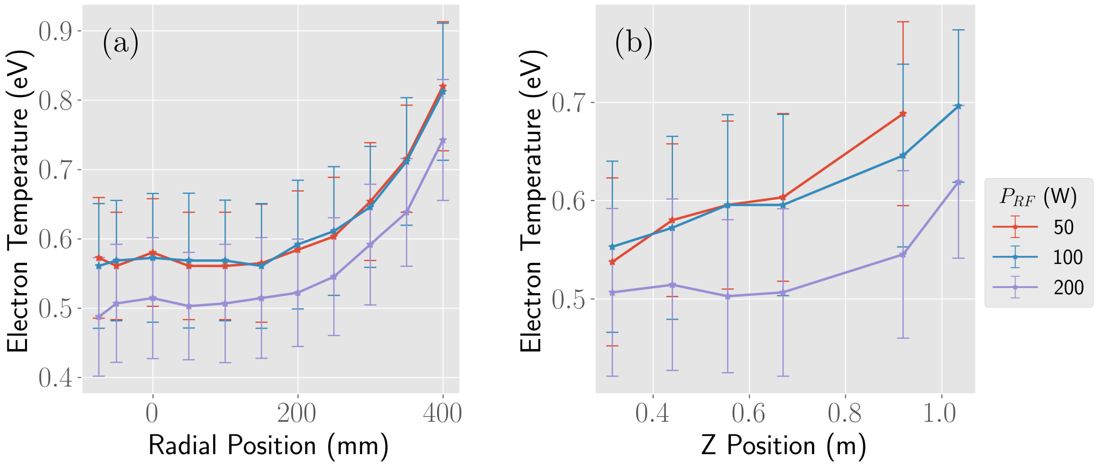

Figure 5.13: Argon T_e profiles at 1 Pa; (a) radial ($z = 0.44$ m), (b) axial ($r = 0$)

a discussion on the limits of validity of the Langmuir probe, and as a motivation for the design of new probes for this apparatus. In fig. 5.13(a) the electron temperatures are very low, < 1 eV, and continue to show the increase at the outer edge that was also evident in the helium discharge. However, the axial profile in fig. 5.13(b) shows an increase out towards the end of the vessel, especially at low RF powers. The relative errors on the electron temperature are significant enough that most of the radial profile could be redrawn as a straight line and still fit between the error bars. The other consideration is the rapid drop off in density, assuming a temperature of 1 eV and a density of 1×10^{13} m^{-3}, the electron Debye length is ≈ 2.4 mm, meaning the sheath radius is at least 5 times the probe radius of 0.5 mm. The sheath can be expected to be a few Debye lengths thick and so the sheath expansion effects will wash out the ‘knee’ associated with the plasma potential. A possible strategy would be to adopt a different probe geometry like a planar probe, where sheath expansion effects are less problematic. This limitation largely lies in the analytic techniques and is not an inherent electrical or physical characteristic of the probe. This is highlighted by comparing the temperature profiles of fig. 5.13 to the floating potential in fig. 5.14 and the plasma potential in fig. 5.15. The floating potential actually follows the expected trend. The floating potential is the simplest point of analysis of an IV trace, merely a recording of the bias voltage where the ammeter reads 0 A. Thus it can be inferred that the electron temperatures are indeed falling, or at the very least the difference in thermal energy between the ions and electrons is reducing. It is unlikely that ions are being heated so far from the RF antenna. The plasma potential is a more subtle feature to spot on an IV trace, and the technique used here is to take the point where the second derivative of the collected current crosses 0. When sheath expansion effects becoming dominant, these techniques become more difficult to apply.

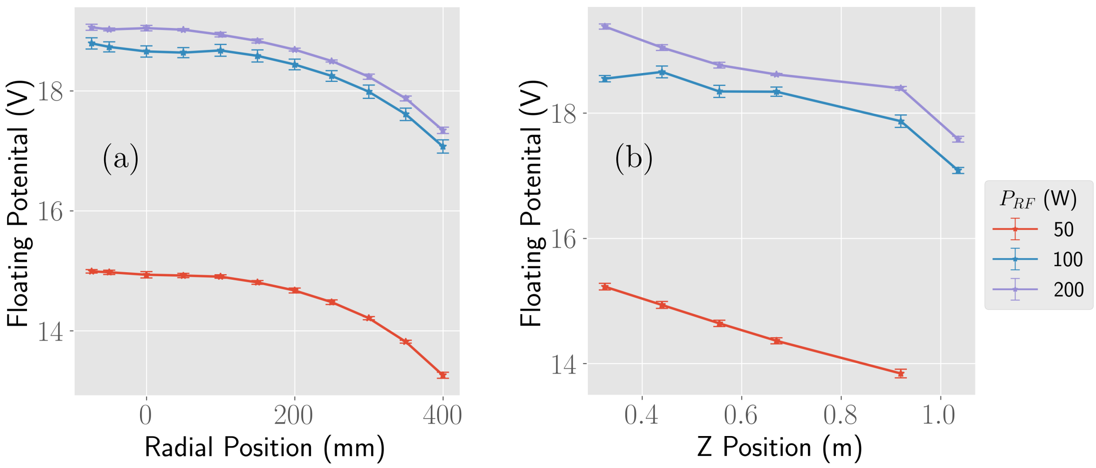

Figure 5.14: Argon V_f profiles at 1 Pa; (a) radial ($z = 0.44$ m), (b) axial ($r = 0$)

5.2 Helicon mode

The electron density is plotted across the vessel radius in fig. 5.16(a) for 3 values of the magnet current I_m. The smallest value of I_m is 0.6 A, which is the lowest setting possible on the power supply. Using the analytic expression for the magnetic field in a Helmholtz pair, it is estimated that $B_0 \approx 10$ μT. For context, the Earth's, surface magnetic field is reported to be on the order of a few tens of μT. In this case the inductively coupled plasma mode is expected, since the electron cyclotron frequency lies below the RF frequency (see chapter 2). The ion density profile is also scarcely affected, as well as the electron temperature, floating and plasma potentials, so this is essentially the field free case. When the magnet current is increased to 12.5 A, the B-field on axis is estimated to be ≈ 2 mT and at this point there is a possibility the helicon mode has been excited. At $B_0 = 2$ mT, $\Omega_e = 55$ MHz and is above the RF frequency (14 MHz). it should be noted, however, that the requirement for the helicon mode is not $f_{RF} < f_{ce}$ but $f_{RF} \ll f_{ce}$ since the wave approaches a resonant condition gradually with increasing frequency as opposed to a cut-off. With the factor $f_{ce}/f_{RF} \approx 4$, it may not be appropriate to categorically label this as the helicon mode. However,

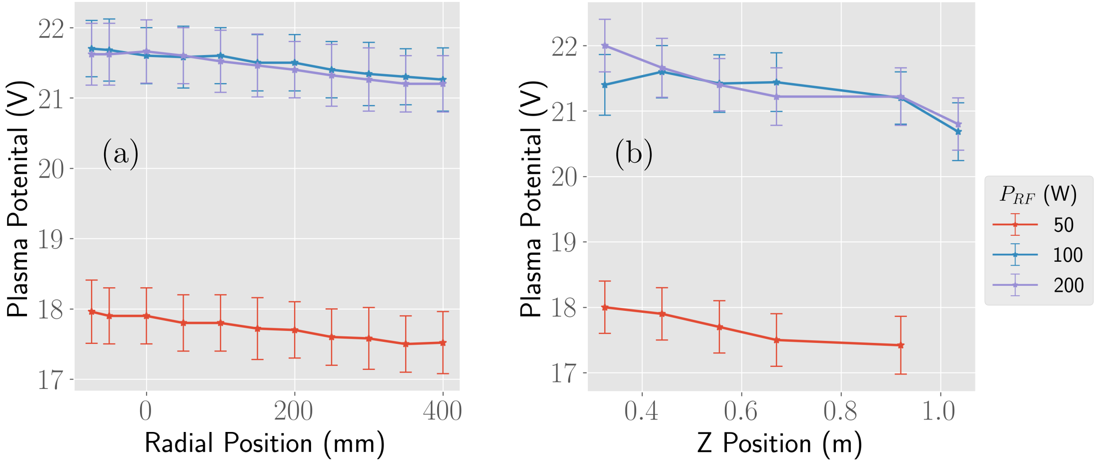

Figure 5.15: Argon V_p profiles at 1 Pa; (a) radial ($z = 0.44$ m), (b) axial ($r = 0$)

the electron densities and temperatures with this B-field appear to have grown compared to the field free case, despite the reduced collection of currents by the probe. The highest magnet current should take the apparatus deep into the parameter space where the helicon wave is expected, with $f_{ce} \approx 220$ MHz. Indeed a hollowed profile is observed in the electron density, characteristic of some helicons for certain experimental conditions (see chapter 1 & [113]), with a sharp rise in the electron temperature on axis where the helicon wave propagates. The temperature has a parabolic profile, coming to a minimum of about 1 eV at the mid-radius of the RF antenna before again rising toward the vessel wall. This has been observed on some RF ICPs and helicons and may be due to an anomalous skin effect [114].

The drive frequency must also be above the lower hybrid frequency and this is not of great concern for the current range of parameters. However, it may become important if the magnetic field and densities are increased in future experiments. The lower hybrid frequency is commonly taken to be:

$$f_{LH} = \sqrt{f_{ce} f_{ci}}. \tag{5.1}$$

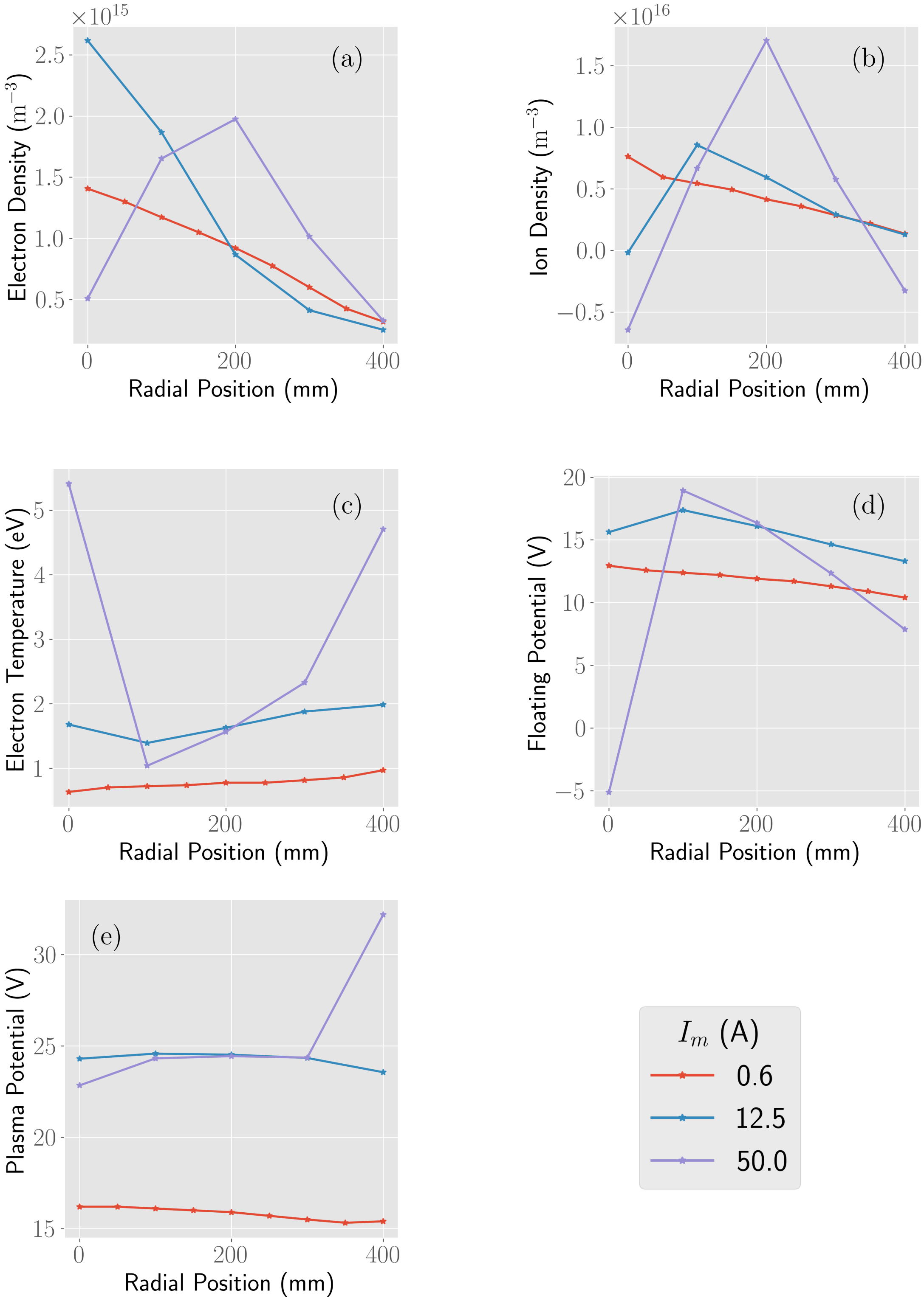

Figure 5.16: Helicon profiles in helium at $P_{RF} = 200$ W, $p = 1$ Pa

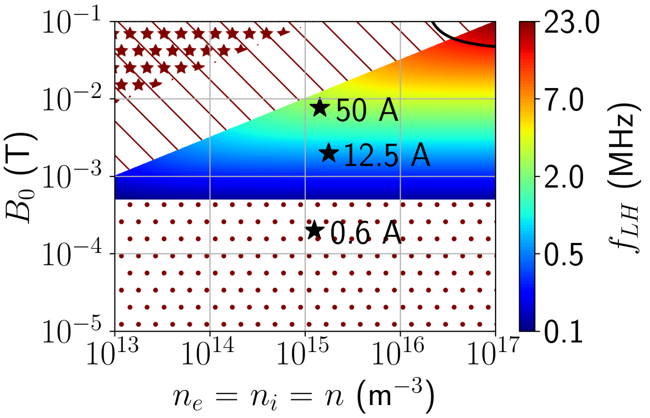

Figure 5.17: Parameter space for operation in the helicon mode

This is an approximation for high densities, usually valid for the high density helicon operation. However, if future scattering experiments require higher magnetic fields while keeping the density low, this expression no longer applies and the lower hybrid frequency becomes a strong function of the density,

$$f_{LH} = \frac{f_{ce} f_{pi}}{\sqrt{f_{pe}^2 + f_{ce}^2}}. \tag{5.2}$$

Which, while not the full expression (see [94] Ch. 6), provides a reasonable approximation for the mid density range. The range of valid parameter space for operation in the helicon mode is plotted in fig. 5.17. The primary feature of this diagram is the coloured region which indicates where the helicon wave can propagate. The colour bar shows the value of the lower hybrid frequency in the n, B parameter space, note the slight curvature in the colour map due to the low density regime. The black line in the top right corner shows the points where $f_{LH} = f_{RF}$, anything 'north-east' of this line is forbidden. The white, patterned regions indicate areas where the helicon mode is expected to be forbidden for reasons other than meeting the lower hybrid resonance. In the bottom of the plot the dotted area shows where $f_{RF} > 0.1 f_{ce}$, while the hatched region in the top left shows where the helicon mode is cutoff due to an extra requirement as per [114], where the plasma density must be high, or $f_{ce} \ll f_{pe}$. Thus this is the region where $f_{ce} > 0.1\ f_{pe}$, meaning the oscillations are only weakly magnetised. Lastly, [114] also proposes that the ion cyclotron frequency should be well below the lower hybrid ($f_{ci} \ll f_{LH}$). However, considering the slightly more stringent requirement, the star covered region represents where $f_{ci} > 0.1 f_{LH}$. This plot is not prescriptive as most of the requirements are based on being far removed from progressive damping and resonance effects. This plot does, however, indicate a possible 'safe space' for further exploration of the helicon mode of this apparatus.

Without more detailed sweeps of input power, magnetic field and gas pressure it is difficult to state definitively if the helicon mode has been achieved. It will be important for future work to fully map this parameter space and perform field measurements with field probes. Experiments in this regime would benefit from this knowledge as, although the presence of the static magnetic field will of course affect any scattering experiments, the presence of the electrostatic helicon and Trivelpiece-Gould waves propagating in the system could further complicate matters. In the short term this is not an issue, since the inductive mode without the magnetic field has waves that are evanescent where no coupling to injected microwave beams would be expected.

Chapter 6

Numerical results

The experiment is restricted to a certain parameter space due to several factors. The input RF power is currently limited to 200 W, as the 4 kW valve amplifier system has not been commissioned. Even with the valve amplifier the tuning unit is only rated to 3500 W. The pressure range is limited for a few reasons. The bottom of the pressure range is determined by the ultimate vacuum of the pumps, which has never been lower than 1×10^{-3} Pa. To keep the neutral gas contaminant free the lowest operating pressure used is 0.1 Pa so that, assuming the background pressure is due to air from the laboratory, purity is at least 99%. The bottom of the pressure range is further raised by the fact that the Langmuir probe begins to present difficulties below 0.5 Pa. The top of the pressure range is governed by pump limitations. It is desirable to use turbomolecular pumps with high flow rates, again to keep the neutral gas contamination low. The turbo pump begins to overheat as $p_g \rightarrow 10$ Pa, thus the maximum pressure used is 6.4 Pa[1]. Further, there are limitations on the frequencies the generator is capable of, since the transmitter is limited to the HF bands due to legal restrictions. It should be noted that even with this limitation this is still a very flexible source in terms of

---

[1] The odd number stems from a cross-calibration. Some initial historic data was taken at '5' Pa, which turned out to be slightly wrong. On re-calibrating the true pressure was 6.4 Pa. Further experiments continued to use this value to provide continuity with historic data.

frequency control. Most systems are limited to the industrial frequency of 13.56 MHz or its second harmonic. Many of these limitations can be overcome through future upgrades to: the pump system, Langmuir probes (design and analysis), the matching network design and the HF equipment. Indeed, many upgrades in this area are planned. Thus, aside from fundamental interest, it is of great utility to develop a numerical model that can predict the characteristics of the plasma over a wider range of parameter space than is available in the current iteration of this apparatus.

6.1 Inductive mode

The work on a numerical model naturally begins with the inductively coupled mode as the lack of a bias magnetic field simplifies the physics. Inductively coupled sources also benefit from a maturity in modelling capability, especially in the COMSOL suite, since the semiconductor processing industry has great interest in being able to model and design ICP sources. These inductive sources can typically be modelled in a regime where azimuthal symmetry is assumed, termed 'axi-symmetric' in the COMSOL solvers. The model provides predictions of steady state profiles at a low computational cost and over a wide domain in parameter space. Although the plasma calculations are 'time dependent', they are only so in the sense that the solver must evolve the plasma in the time domain to move from the arbitrary initial condition to the predicted steady state parameters. Since the initial condition does not correspond to any real laboratory start up procedure, the time evolution has no bearing on reality[2]. Thus, the steady state solutions are all presented at $t = 1$ s; the steady state is typically reached after ≈ 0.1 s. However, since the solver adjusts its time step dynamically based on the rate of change of the plasma with time, the last 0.9 seconds only accounts for a

---

[2] Of course, the time evolution remains of interest as the evolution should still follow all of the relevant physics, even if the initial condition is infeasible in a laboratory.

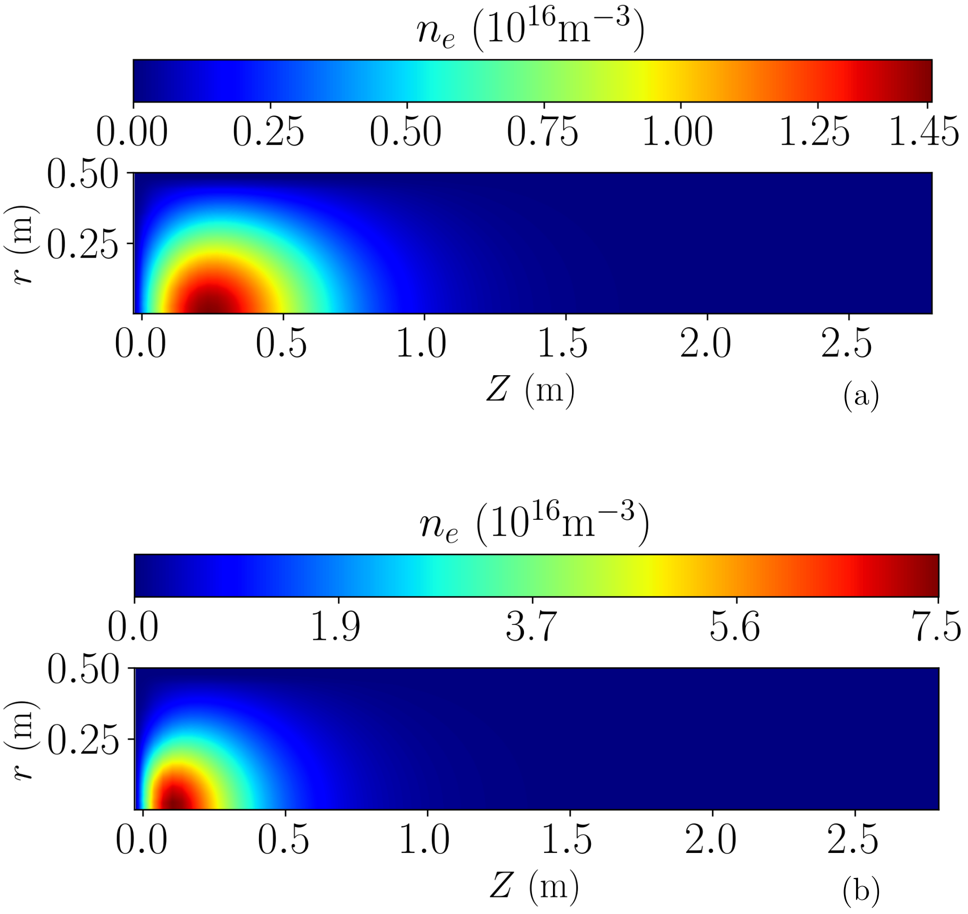

Figure 6.1: Helium ICP contour maps for n_e; (a) 1.8 Pa, (b) 6.5 Pa

few % of the total run time. Thus, one can be an order of magnitude away from where steady state occurs, with little computational expense.

6.1.1 Profiles

The plasma density profiles are shown as contour maps for 2 experimentally relevant cases in fig. 6.1. The frequency $f_{RF} = 14$ MHz, while the gas species is helium and $P_{RF} = 180$ W, which is the closest value to 200 W in the set of parameter sweeps this data is taken from. The magnitude of the density is overestimated compared to the Langmuir probe data, which will be a theme throughout the numerical results and is discussed in chapter 7. For the 1.8 Pa case the peak density of $n_e = 1.45 \times 10^{16}$ m^{-3} occurs on the z-axis at $z = 0.26$ m while in the higher pressure case the density has risen to $n_e = 7.5 \times 10^{16}$ m^{-3} and is closer to the antenna at $z = 0.16$ m. The overall profile of the plasma is slightly more constricted in the high pressure case. This behaviour is to be expected; the greater gas pressure will cause an increase in the electron-neutral collision frequency and this in turn increases the skin depth. However, the coupling efficiency of the inductive mode increases with the gas pressure resulting in an increase in the electron density [46] and the collisional skin depth scales as $\sqrt{\nu/n_e}$ [40]. If the increase in the density outstrips the increase in collisionality the skin depth will decrease. Indeed, COMSOL estimates the collision frequency to be 99 MHz in the high pressure case and 31 MHz for the lower pressure. While the density averaged over the same volume is 4.6×10^{16} m^{-3} and 9.9×10^{15} m^{-3} respectively. Thus going from the low pressure case to the high pressure case, the skin depth would be expected to decrease by a factor:

$$\sqrt{\frac{46/9.9}{99/31}} \approx 1.2 \tag{6.1}$$

The location of the maximum density along the z-axis varies by $0.26/0.16 \approx 1.6$, showing the plasma dimensions are tracking the evolution of the skin depth in a consistent manner. The contour maps for the electron temperatures T_e in the same parameter range are plotted in fig. 6.2. Like the density, the electron temperatures are overestimated, with the low pressure case showing a peak $T_e \approx 4.6$ eV at the surface of the dielectric window, while in the 6.5 Pa case the temperature is again peaked at the window surface but has fallen to ≈ 3 eV. The peak value for the temperature is not expected to be a strong function of power or pressure. This is because the electromagnetic field from the antenna is not effectively screened in the sheath and thus the hottest electrons are expected to

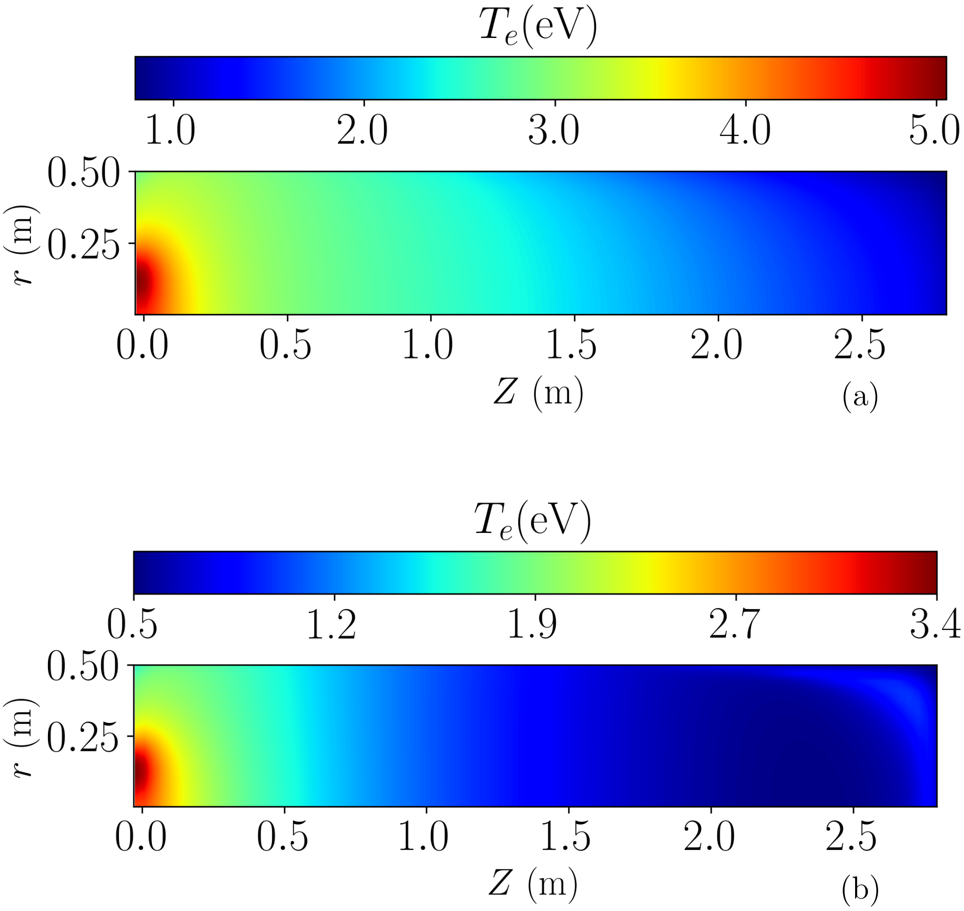

Figure 6.2: Helium ICP contour maps for T_e; (a) 1.8 Pa, (b) 6.5 Pa

be found in proximity to the antenna, unlike the densities, which are expected to fall in a sheath (see chapter 3). One can, however see that the decay constant follows the correct ratio. The collisional skin depth $\delta_\xi \equiv 1/\alpha$, where α is the spatial decay constant of the evanescent electromagnetic wave's amplitude in the plasma. An examination of the rate of change of the electron temperature in the bulk plasma shows the spatial decay of the electron temperature along z is approximately twice the rate for the high pressure case compared to the low pressure.

In order to make the axi-symmetric approximation, some components of the

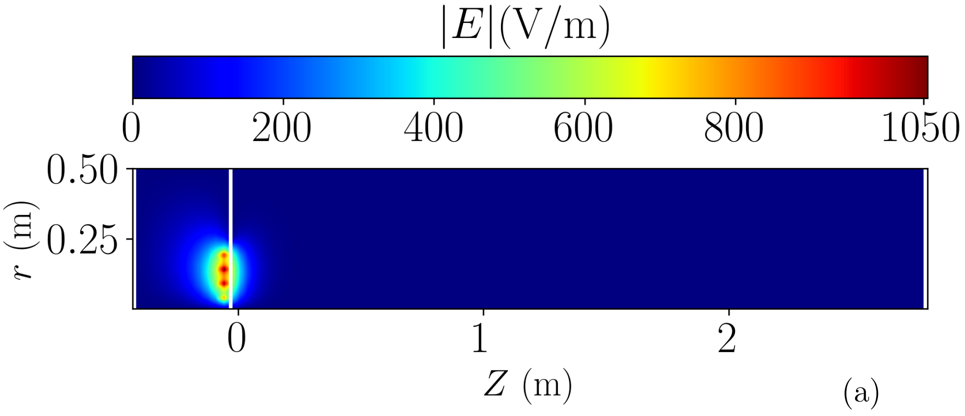

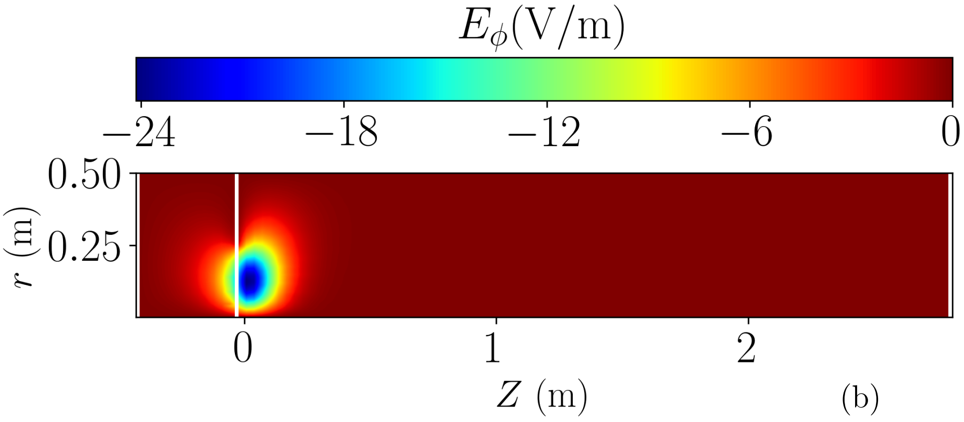

Figure 6.3: Helium ICP contour maps for the electric field; (a) $|E|$, (b) E_θ

electromagnetic field are set to 0. The contour maps of the electric field are plotted in fig. 6.3 for the 180 W RF power, 1.8 Pa case. The wave electric field has been set to have only an azimuthal component since the currents that are generating it are defined with only an azimuthal component, which is a close approximation to a spiral antenna or even the solenoid around a plasma torch. The magnitude of the complex valued electric field is plotted in fig. 6.3(a) and shows a peak at the antenna windings where the AC is flowing, since the field is completely azimuthal there is a null in the centre, which is a well known feature of these antennas. This can be seen by considering a test charge placed at this point, which will experience a balance of forces from either side of the z-axis since the induced E-fields on opposite parts of the winding are of equal magnitude with opposite sign. The E_θ plot in fig. 6.3(b) shows the real part only, pointing in the direction opposite to the current, which in this view is defined to be positive out of the page. The density and temperature thus far have been investigated by comparing how the decay of these parameters evolves according to the scaling of the skin depth, since the skin depth really describes the decay constant for the electric field it is pertinent to attempt a quantitative comparison. The skin depth of an RF plasma, in the collisional regime can be given as [40]:

$$\alpha = -\frac{\omega_{RF}}{c} \operatorname{Im} \sqrt{\kappa} = \delta^{-1}, \tag{6.2}$$

where α is the decay constant of the field and

κ is the plasma dielectric constant.

With the dielectric constant expressed as

$$\kappa = \frac{\omega_{pe}^2}{\omega_{RF}\left(\omega_{RF} - i\nu\right)}, \tag{6.3}$$

where ν is the collision frequency for the electrons.

With the volume averages of n_e and ν_e taken to be 9.9×10^{15} m^{-3} and 31 MHz respectively. This gives a value for the skin depth as 0.05 m. To compare with the calculation, the quantity:

$$\frac{|E|}{\frac{d|E|}{dz}} \tag{6.4}$$

is evaluated; assuming exponential decay this should provide an estimate of the average value of the folding distance. For the present calculation this average value is also found to be 0.05 m. The magnetic field profiles, plotted in

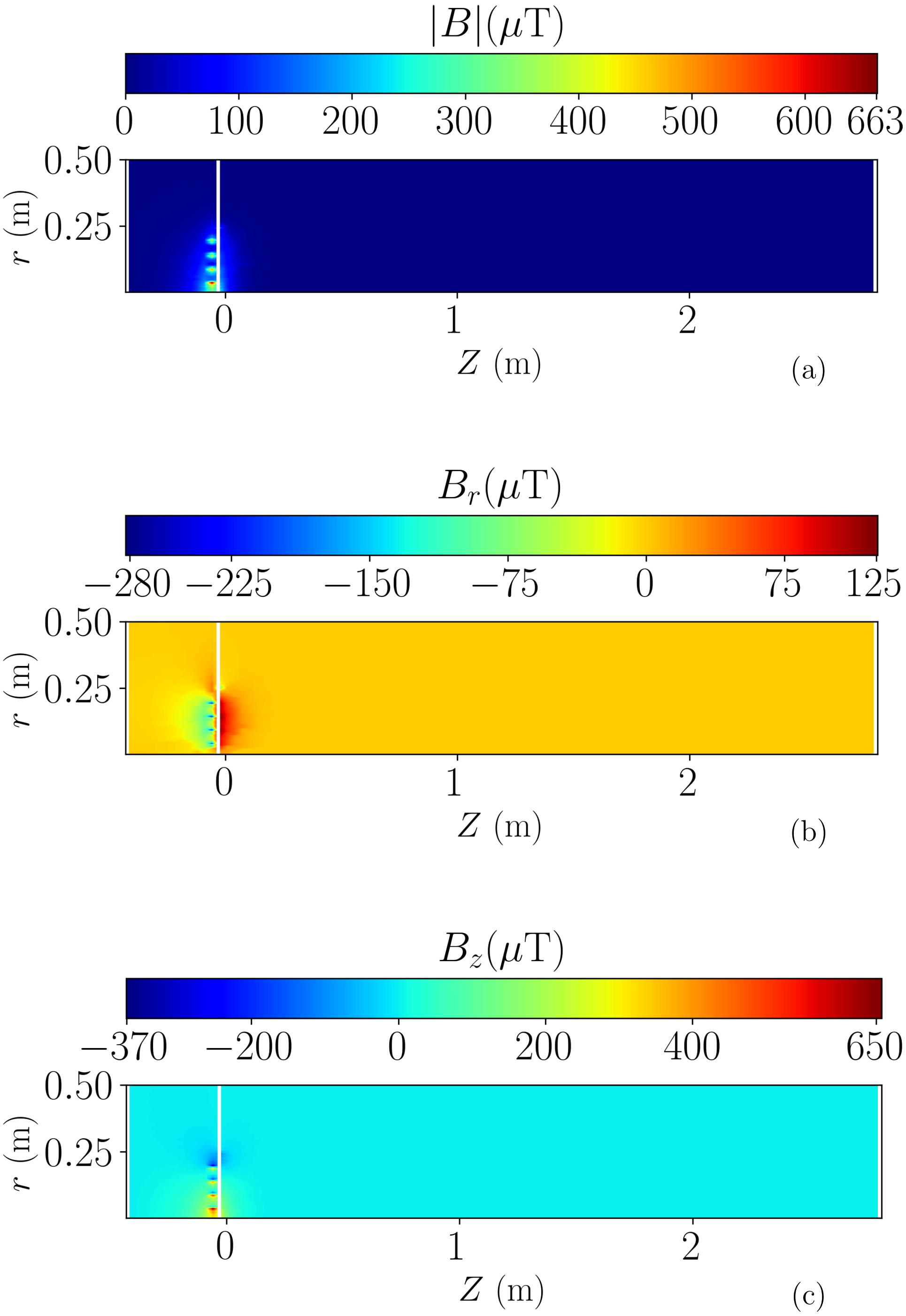

Figure 6.4: Helium ICP contour maps for B; (a) $|B|$, (b) B_r, (c) B_z.

fig. 6.4 show the expected structure for this antenna, with the wave magnetic field strength in the few 100s of μT. The field strength is peaked on axis since the currents flowing in the windings of the antenna have the same sign on the z component of induced magnetic fields circulating around the conductor. Conversely, the on axis radial components have opposite signs and thus cancel.

Lineouts of the electron density are shown in fig. 6.5 and fig. 6.7, demonstrating that the profile does not meaningfully change along the length of the system. Note the logarithmic density scale; on a linear scale the profiles are parabolic in a similar fashion to the experimental results (see appendix C). The axial plot in fig. 6.5(b) shows the density varies in an exponential fashion along the axis. The sharp drop off in density at the walls is the density drop across the plasma sheath and is of the order of a few cm, typical for the tenuous edge of RF plasmas in this parameter space[3]. The electron temperatures in fig. 6.6 also show a continuous variation in the electron temperature with peaks no greater than 6 eV on the window. An important discrepancy here is the difference in radial profile compared to experiments as the temperature falls towards the wall. It should be noted however that the densities and temperatures are overestimated by the numerical model and it may be that these profiles will manifest in the apparatus if the source is upgraded to provide more power and thus higher densities and temperatures.

Similar radial and axial lineouts are presented in fig. 6.7 showing the evolution of the discharge with applied RF power. The radial lineouts in fig. 6.7(a) and fig. 6.7(c) are at $z = 0.44$ m, to match with the microwave antenna location in the experiment, while the gas pressure is 1.8 Pa. Again the same profiles are seen and the profile is unaffected by the RF power in all but one case. At a low power of 3 W, the system suddenly drops in density and cannot be reasonably considered a plasma as the Debye length is reaching 10s of cm, a significant

---

[3] These sheaths have been known to be large enough to be visible on some experiments [40]

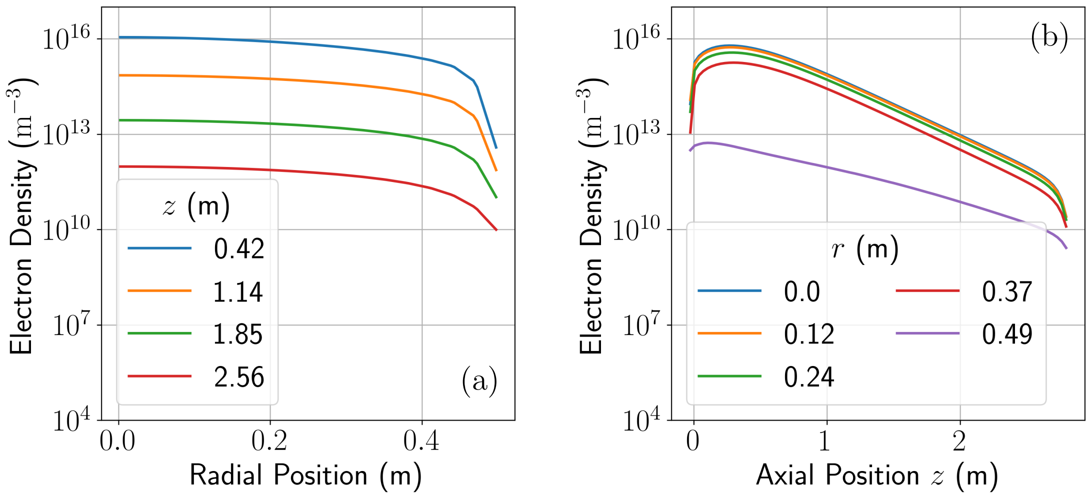

Figure 6.5: Helium axial and radial n_e profiles, P_{RF} = 180 W & p_{He} = 1.8 Pa

fraction of the vessel dimensions. The electron temperature also falls sharply in fig. 6.7. Lastly, a pressure scan in fig. 6.8 shows the same behaviour at low pressures, where the model moves outwith its limits of validity and the solver converges on a 'no plasma' steady state solution. This behaviour is thought to be a limit on the model validity as the profiles are entirely unaffected by these parameter scans until a critical point is reached where the solver throws no errors but simply returns a smooth profile of a very low density and temperature 'plasma'. Indeed, the convergence testing discussed in chapter 4 found these densities and temperatures to be a fundamental limit on the initial conditions Even when given a set of parameters for RF power, gas species, pressure etc. that are known to produce a reasonable estimate for the plasma profile, if the solver is started with the condition below $\approx 10^9$ m^{-3}, that initial condition will not evolve towards the anticipated steady state condition.

6.1.2 The limits on parameter space

These regime changes indicate the range of validity for the numerical model and knowing where the model can and cannot be applied is crucial for making further

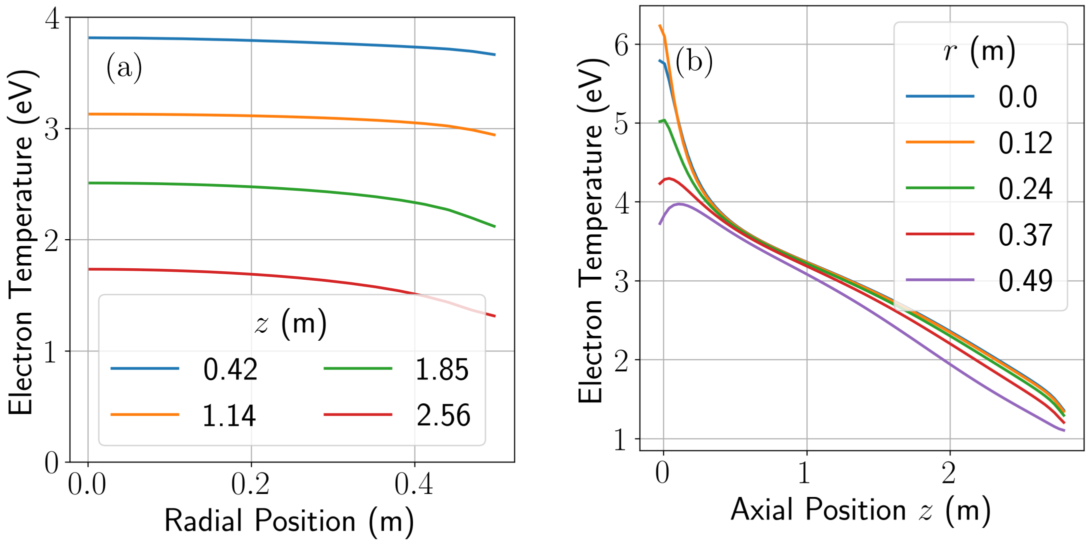

Figure 6.6: Helium axial and radial T_e profiles, $P_{RF} = 180$ W & $p_{He} = 1.8$ Pa

improvements and to inform comparisons to the experiment. A key benefit of this model is the ability to explore large areas of parameter space with relative ease. The underpinning theory makes many assumptions to make the problem more tractable, axial symmetry being an obvious one. However, not all assumptions are obvious and, even though COMSOL is a rather open and transparent commercial product that provides detailed information on how variables are defined and the expressions being solved for, the assumptions can be buried too far back in the derivation to reach the final help documents. However, one can probe for these by exploring parameter space, since the model should naturally start to diverge from reality where the underlying assumptions are broken. The difficulty is finding that parameter when it is coupled to many equations, themselves coupled to many other parameters.

The crash in density and temperature is seen when both the input RF power and the gas pressure are varied independently and so the underlying parameter that controls this condition may be something that couples these. The RF power and gas pressure both have a significant impact on the electron density while the

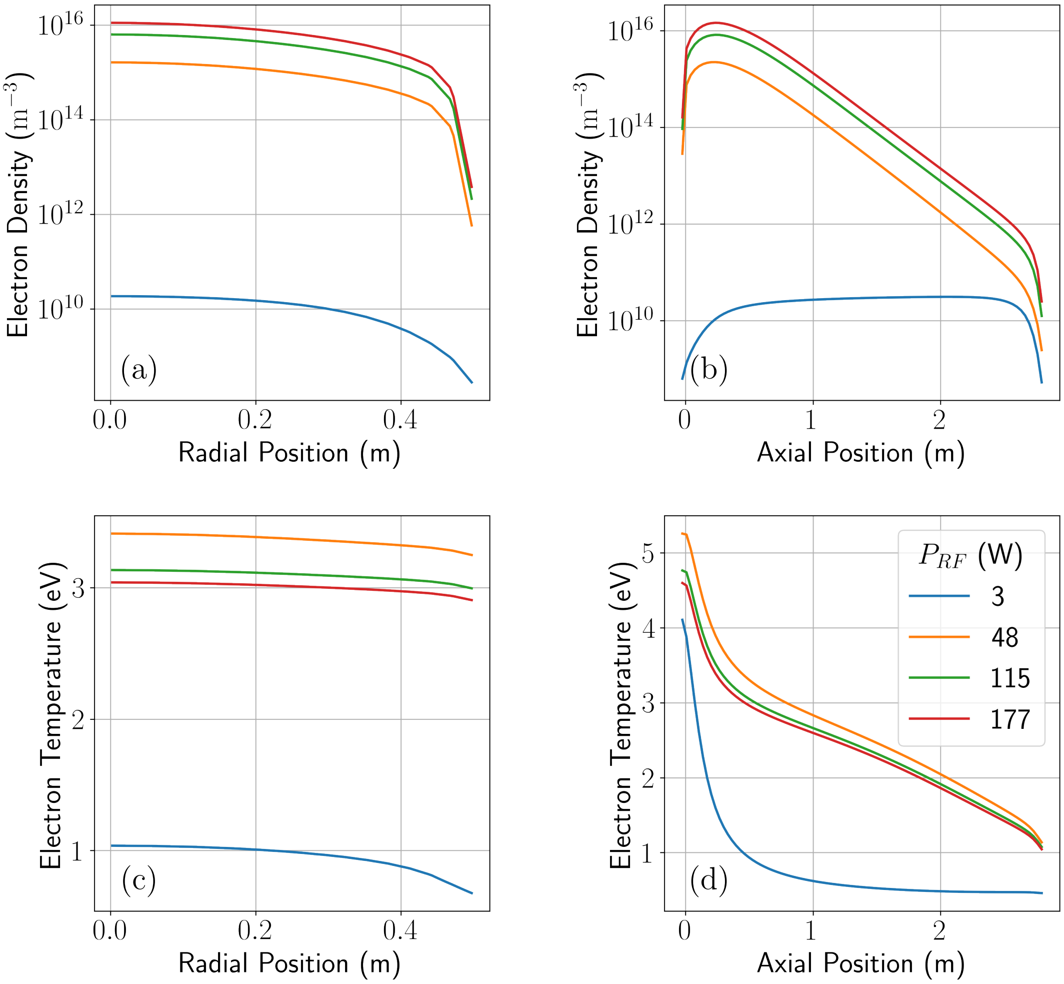

Figure 6.7: Helium profiles over a range of RF antenna powers

electron temperature is largely controlled by the behaviour of the sheaths and collisions with the gas. Thus, over a large range of input powers the density is expected to vary greatly while the temperature remains a few eV. The evolution of the volume averaged density and temperature are mapped in the parameter space contours shown in fig. 6.9, clearly marking the boundary where the model is no longer predicting a sustained plasma. In fig. 6.9(a) the density crash is clearly visible but is marked with a magenta line as a landmark for comparing to the other parameter plots presented in fig. 6.9(b) and fig. 6.10. In the high density,

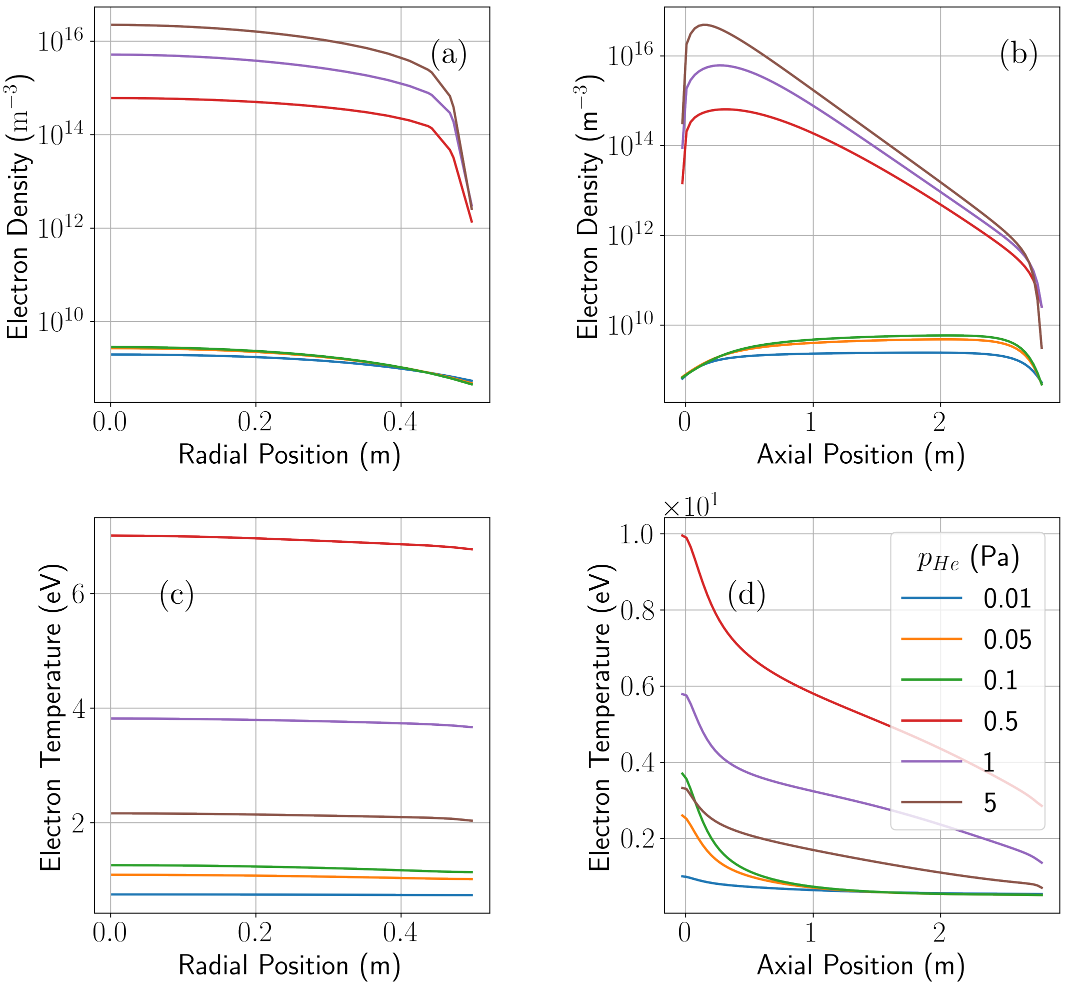

Figure 6.8: Helium profiles over a range of neutral gas pressures

high pressure and high RF power regime, the volume averaged density increases monotonically, with the RF power unsurprisingly having a greater influence than the gas pressure. In fig. 6.9 the critical boundary is close to the region in parameter space where the collision frequency is approximately the RF frequency, values of which are marked in black. At first this seems to imply the density crash may be caused by the transition from a collisional to a collisionless regime, where stochastic heating will be important.

Despite the appearance of fig. 6.9(b), the volume average T_e also crashes at the same parameter space boundary as the density. The discrepancy between the magenta line and the edge of the 'high' temperature is due to the linear colour scale and the sparse data grid. In this case the volume average does not reveal the electron heating that remains close to the antenna. This can be seen by comparing to fig. 6.7(d) where the bulk average has fallen significantly at 3 W but there is still a strong heating effect at the surface of the dielectric window. This is easily explained since, although there is no plasma because the regime is invalid, there is still a small residual density of $\approx 10^9$ m^{-3}. This will not screen the electric field from the antenna and thus strong localised heating can still take place. No wave pattern develops since, although the 'plasma frequency' is low enough (a few 100s of kHz) that the gas is transparent, the wave is still forbidden by the vessel geometry. While the electron density is a strong function of the RF power and a weak function of pressure, the temperature is a weak function of power and a strong function of pressure and this matches with the expected behaviour of an ICP, where drastically increasing the input power manifests as more ionising collisions. The gas pressure has a strong influence on the electron temperature as a lower mean free path implies a particle spends less time in the accelerating gradient of the fields. The gas can be thought of as a heat sink for the electron thermal energy and its heat capacity will increase with gas density.

To further explore the effects of the collision frequency another set of calculations were performed at $f_{RF} = 30$ MHz. This is plotted in fig. 6.10 and reveals the behaviour is unrelated to a transition to the collisionless regime. In fact the behaviour of the system is scarcely affected by the rise in the drive frequency as the density crash region does not move; the difference between the black lines marked on fig. 6.10(a) and fig. 6.10(b) is almost entirely due to the move in the RF frequency. This can be explained by comparing the thermal energy of the electron population to the drift speed from the antenna fields. Again, in an ICP it turns out the temperature is not strongly correlated to the drive power, thus

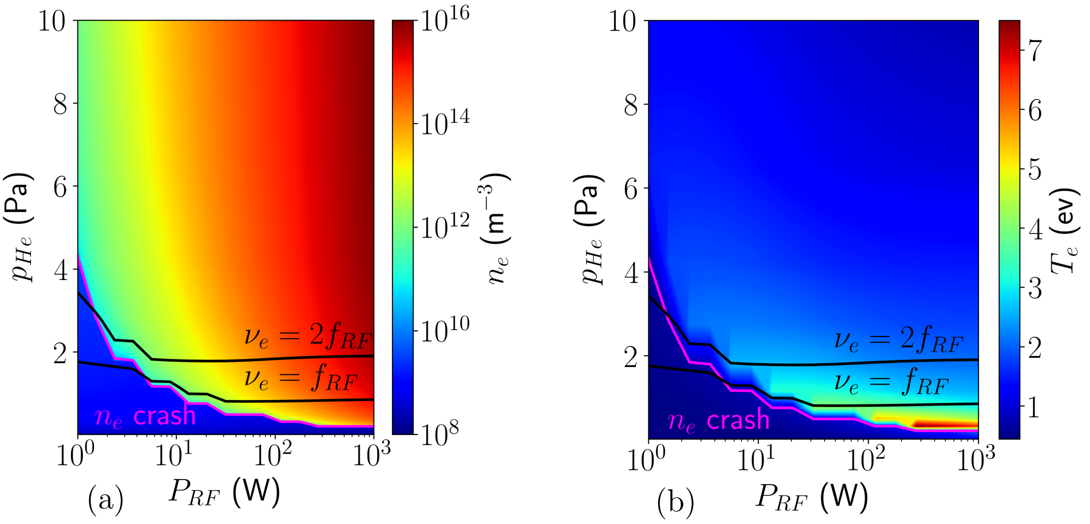

Figure 6.9: Pressure and power parameter space for n_e and T_e

most of the thermal energy for the electron population comes from the sheaths that form at the boundaries. As ions are pulled into the sheath at $v \geq v_B$, current continuity imposes an increase in the electron energy. The acceleration across the sheath is due to the plasma potential which is, to first order driven by the RF voltage on the spiral antenna, thus these energies remain fairly small over a large range of RF parameters. The electron temperatures are $\approx 3-10$ eV on the dielectric window (1×10^6 m/s $< v_{th} < 2 \times 10^6$ m/s), while typical drift velocities induced by the AC E-fields in this set of calculations range from 1×10^5 m/s $< u < 5 \times 10^5$ m/s. Thus the wave fields have little impact on the bulk energy of the electrons.

Another parameter that can signify a regime change for an ICP is the skin depth. Typical RF sources undergo a significant change in the way the RF power is coupled to the plasma when the skin depth becomes comparable to the dimensions of the vessel. The symptom of this transition is usually a sharp jump in density (sometimes an order of magnitude) and the low density mode where the skin depth is very large is a capacitively dominated regime while the high

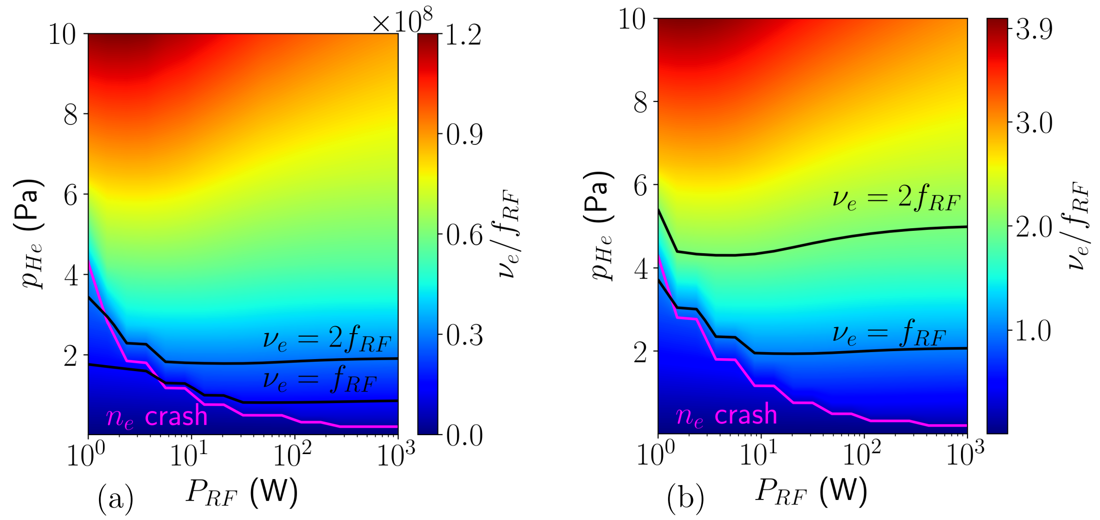

Figure 6.10: Pressure and power parameter space for ν at (a) 14 MHz drive frequency and (b) 30 MHz drive frequency

density, short skin depth mode is the inductive mode. These modes are discussed in chapter 1. Thus, the skin depth may evolve significantly over large areas of parameter space. The skin depth given by eq. (6.2) is averaged over a line segment in the bulk plasma, far from the walls and plotted over the pressure and power parameter space in fig. 6.11 beside the plot of the volume averaged electron density. In fig. 6.11(a) the scale has been altered to logarithmic for both the x and y axes and the underlying grid of parameter points is shown as a set of blue dots. The magenta line still indicates the point where the density crashes. In fig. 6.11(b) the skin depth is plotted, showing the same transition point as the density, marked in white. The lines are offset due to the nature of the contour grid. Starting in the bottom left corner of these plots and moving up in power and pressure, the magenta line connects the last set of calculations where the solution is ‘no plasma’, while the white line connects the set of calculations where the first plasma solutions occur. Thus these 2 parameters track each other exactly. The time behaviour of the skin depth follows one of two patterns: a) if the steady state solution shows a plasma, the skin depth starts off small (a few

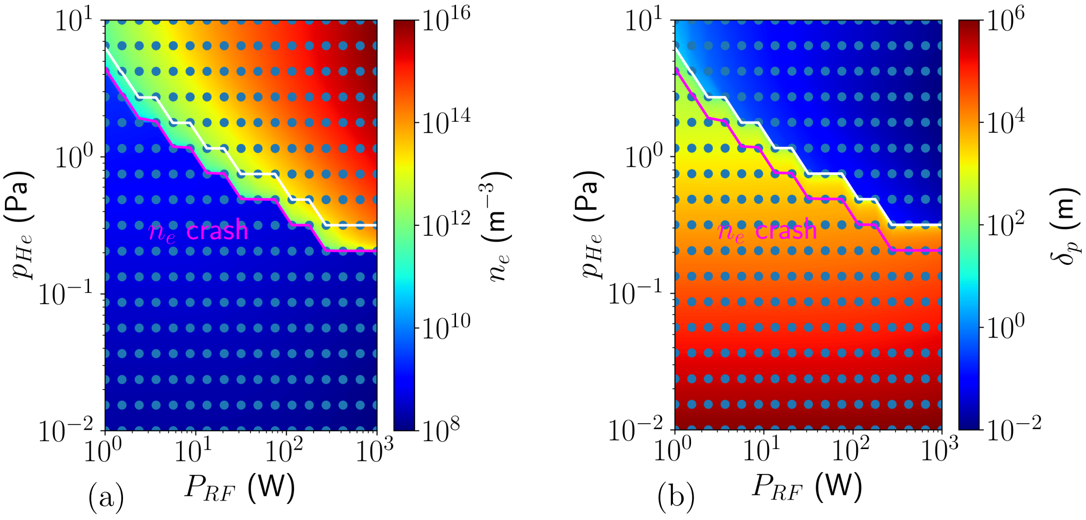

Figure 6.11: Comparsion of steady state (a) electron density and (b) skin depth at 14 MHz RF drive frequency.

cm) in the initial condition of $n_e = 10^{16}$ m^{-3} and evolves in a continuous manner, never reaching more than a few m in the plasma bulk; b) if the final solution is no plasma, the skin depth starts off evolving continuously and as the density falls below some critical value where the skin depth becomes more than a few m, the coupling efficiency plummets and the density crashes, resulting in a large jump in the skin depth to values on a scale of km. It may be that the model cannot self-consistently account for the capacitive coupling mechanism and the transition point cannot be modelled. As discussed in chapter 1, these coupling mechanisms are not mutually exclusive and both co-exist in a laboratory ICP. See chapter 7 for further discussion on this point.

6.2 Helicon mode

It is important for future experiments involving magnetised modes to have predictive capability for the helicon mode. Because of the confining magnetic field and enhanced ionisation due to damping of the helicon and TG waves, the densities are expected to be significantly higher, thus above the critical transition point shown in the field-free case. It is not immediately apparent that the present numerical model can accurately predict the helicon mode since the damping and absorption of the electrostatic wave may require a kinetic model if the distribution functions become significantly perturbed. This detail aside, the plasma dynamics seem well formulated, as do the electromagnetics, motivating a study of the parameter space. As a starting point the bias magnetic field is defined by simply imposing a constant bias field $\vec{B} = B_z$ at every point. Of course this is not representative of the experiment since the long solenoid approximation is not satisfied, but this is not a prerequisite for the existence of a helicon wave.

6.2.1 Profiles

The electron density profiles are plotted in fig. 6.12 for 3 cases of bias magnetic field in a helium plasma sustained by 200 W of 14 MHz RF power. In the field free case the usual plasma 'ball' localised to within a few skin depths of the antenna is shown. When the background magnetic field is set to 5 mT the peak density jumps by factor of 4 and the profile becomes confined to the axis, with the area of significant electron density now reaching the boundary at the far end of the vessel. This is a typical density jump and profile seen in helicons and strongly implies the helicon mode has been reached. However this trend does not hold as the magnetic field is further increased to 9 mT, where the calculation fails, producing a solution that shows very low densities. However in this case the lower hybrid frequency is reaching a few MHz and it is not surprising the model begins to fail as a resonance is approached. In each of the cases in fig. 6.12 the peak densities are (a) 5.2×10^{15} m^{-3}, (b) 2.3×10^{16} m^{-3} and (c) 4.3×10^{10} m^{-3} at the end of the calculation. However, the time evolution of each case reveals more. Each calculation begins its evolution in a similar manner, the initial plasma density evolves gradually, into a spheroid in the 0 mT case or a column in both the 5 mT

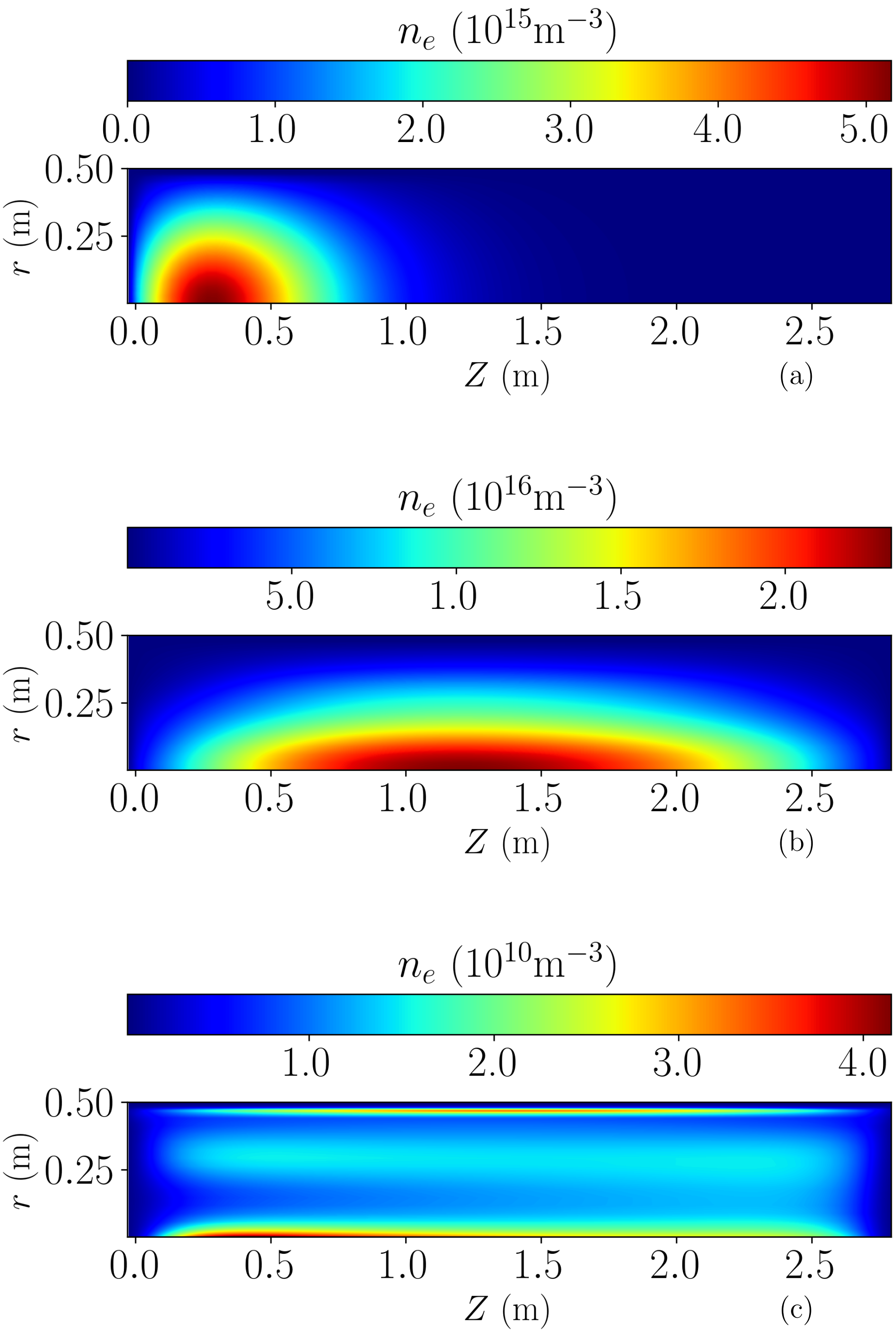

Figure 6.12: Electron density contour maps for various axial B-fields; (a) $B_z = 0$ mT, (b) $B_z = 5$ mT, (c) $B_z = 9$ mT.

and 9 mT case. At a critical point the density in the 9 mT case abruptly crashes. The lower hybrid frequency should, at the densities before the crash, not be a function of the electron density. This may indicate the solver fails, not because of a limitation in capturing resonant absorption of the waves, but some other physical mechanism that drives a density increase separately from a resonance condition.

The electron temperatures for these 3 cases are plotted in fig. 6.13 and show a similar behaviour. Of course, in the field-free case the heating is localised to within a few skin depths of the antenna. When the collimated plasma profile is present in the $B_z = 5$ mT case the electron temperature tracks the density profile, which is a typical result seen in helicon plasmas. The maximum temperature drops slightly since the energy is now deposited over a much longer scale length. In the case where the density has crashed there is still a small amount of heating confined to the antenna since there is still a tenuous electron population present, however the wave is cutoff in the geometry and so decays rapidly

6.2.2 Field structures

The most reliable indicator that the helicon mode has been predicted is a comparison of the electromagnetic fields to the established theory. The wave magnetic fields are plotted in fig. 6.14, clearly showing a wave pattern that is not present in the ICP case. These fields are plotted on a logarithmic scale as the antenna fields would otherwise dominate the contour maps. The radial structure can be compared to the theory for helicon waves (see chapter 2) by checking that they follow the correct Bessel functions. The z component of the magnetic field in fig. 6.14(c) should take the shape of a Bessel function of the first kind of zero order ($J_0(k_\perp r_v)$) where $k_\perp$ is the radial wavenumber and r is the radial coordinate. Of course it is clear that B_z is not simply a J_0 function. It does, however, at least satisfy the requirement that it be finite at $r = 0$. It can be shown that B_z is really

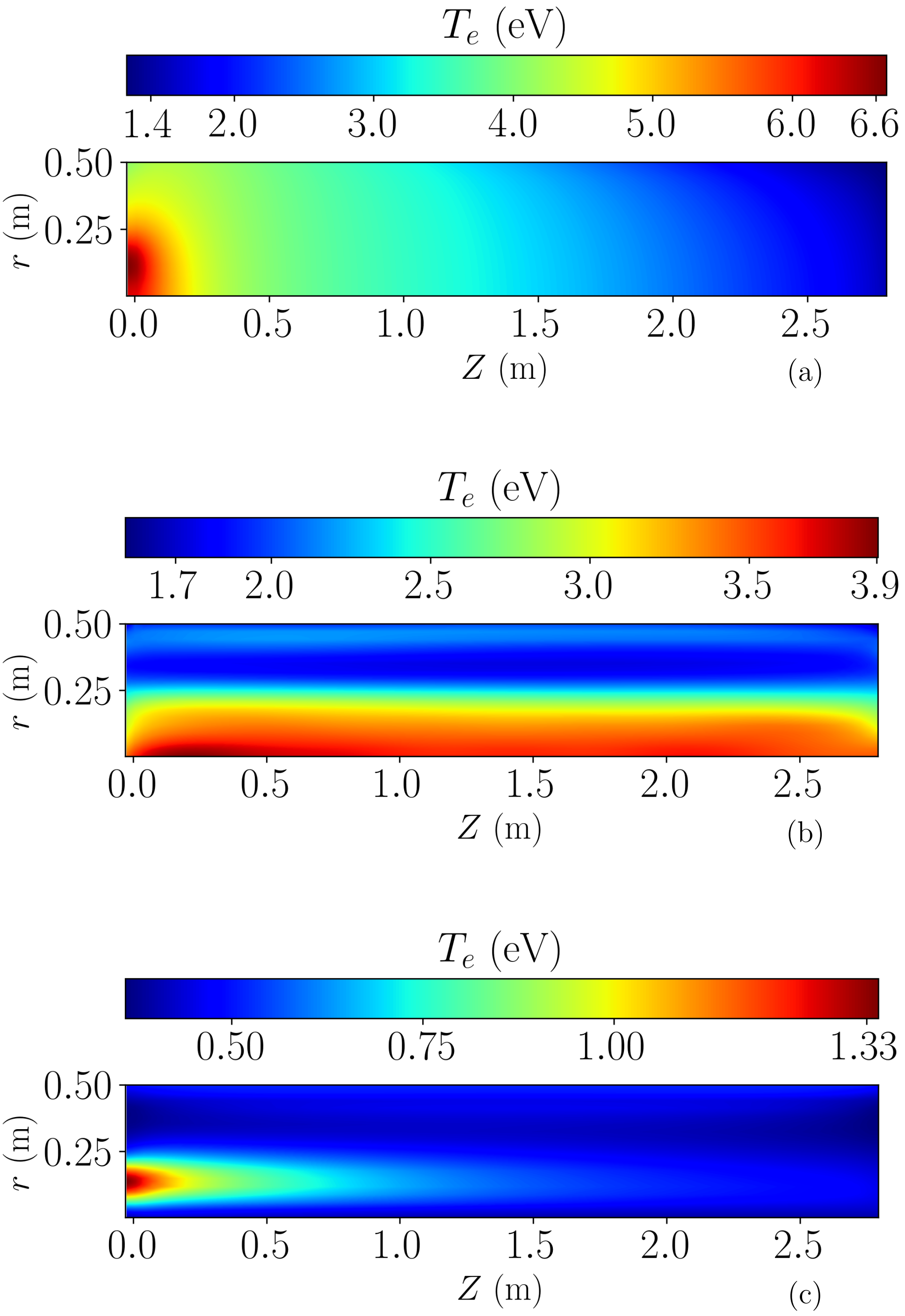

Figure 6.13: Electron temperature contour maps for various axial B-fields; (a) $B_z = 0$ mT, (b) $B_z = 5$ mT, (c) $B_z = 9$ mT.

a superposition of several radial modes, each having the shape of J_0. Each radial mode has a different T corresponding to the boundary condition given by [63]:

$$mkJ_m(k_\perp r_v) + k_z J_m'(k_\perp r_v) = 0, \tag{6.5}$$

where

m is the azimuthal mode number
k is the total wavenumber $k^2 \equiv k_z^2 + k_\perp^2$ and
R is the radius of the vessel.

Since the azimuthal mode excited by the spiral antenna should be $m = 0$, this reduces to:

$$\begin{aligned} k_z J_0'(k_\perp r_v) &= 0, \text{ where } k_z \text{ is obviously not 0 thus} \\ J_0'(k_\perp r_v) &= 0 \text{ and it is known that } J_0' = -J_1 \text{ and so} \\ J_1(k_\perp r_v) &= 0 \end{aligned}$$

This reveals that any wavenumber which gives the product of $k_\perp$ and R to be a root of the J_1 Bessel function will be an allowed mode. The first solution for $k_\perp$ is the trivial solution since the first root of J_1 is 0, thus $TR = 0 \implies k_\perp = 0$. The first order mode is given by $k_\perp r_v = 3.83 \implies 0.5k_\perp = 3.83 \implies k_\perp = 7.66\ \text{m}^{-1}$, the first 4 modes are given in table 6.1. With these wavenumbers known, the following relationship should hold:

$$B_z(r) \approx C_0 J_0(0) + C_1 J_0(7.66r) + C_2 J_0(14.02r) + C_3 J_0(20.34r) \tag{6.6}$$

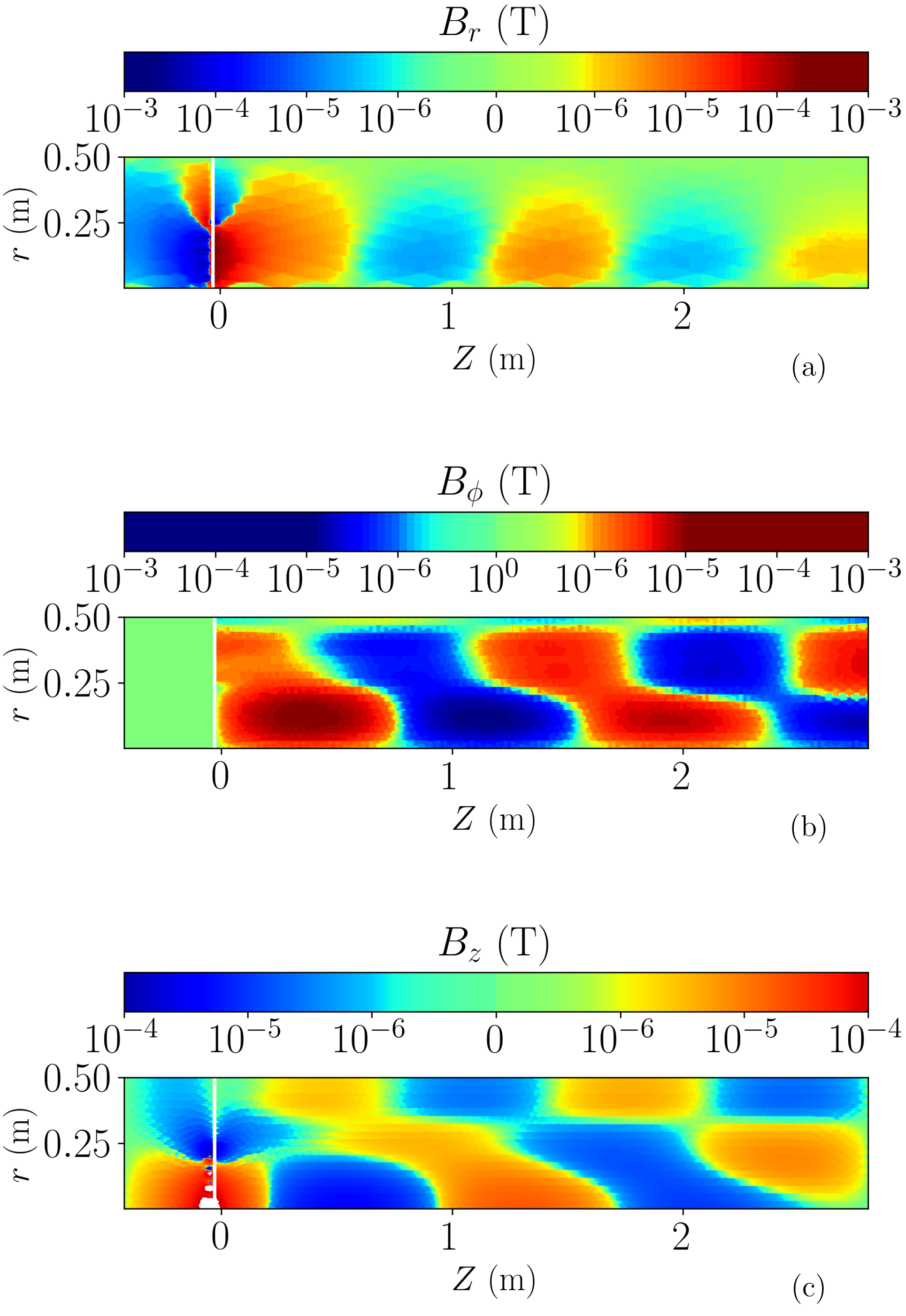

Figure 6.14: Wave magnetic fields in the 5 mT case; (a) B_r, (b) B_θ, (c) B_z.

Order	$k_\perp$
0	0
1	7.66
2	14.02
3	20.34

Table 6.1: Radial wavenumbers allowed in this system

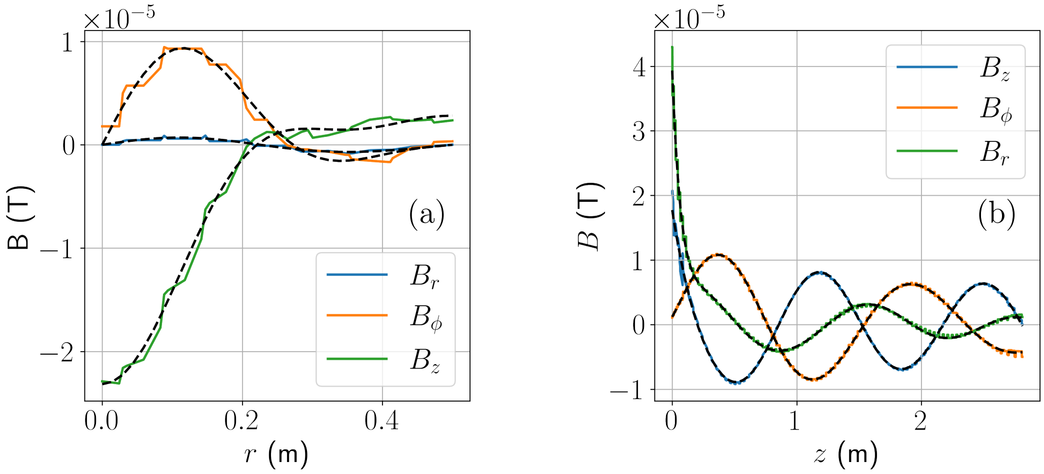

Figure 6.15: The helicon B fields and the resulting fits (dashed black line)

Passing this to a curve fitting algorithm yields the fit presented in fig. 6.15(a). The inclusion of the wavenumber $k_\perp = 0$ has a large impact on the accuracy of fitting to B_z. The fits to B_r and B_θ are carried out in a similar manner, although they follow J_1 functions and thus the $k_\perp = 0$ mode is truly trivial for those cases.

The wavelength can be determined by the dispersion relation for the helicon mode which (neglecting damping) is given by [40]:

$$kk_z = \frac{e\mu_0 n_0 \omega_{RF}}{B_0} \tag{6.7}$$

where k is the total wavenumber as before, this gives a 'quadratic' in k_z^2,

$$\left(k_z^2\right)^2 + k_\perp^2 k_z^2 - \left(\frac{en\mu_0\omega_{RF}}{B_0}\right)^2 = 0 \tag{6.8}$$

Order	k_z
0	5.96
1	4.09
2	2.49
3	1.7

Table 6.2: Radial wavenumbers allowed in this system

Solving for k_z given the values of $k_\perp$ in table 6.1 gives table 6.2. The axial variation is typically taken to be [63]:

$$B = Ae^{i(k_z z - \omega t + m\theta)} \tag{6.9}$$

Allowing for complex $k_z \rightarrow k_z + ik_d$ [63] on account of damping, this becomes

$$\begin{aligned}
B &= Ae^{i(k_z z - \omega t + m\theta)}, \\
B &= Ae^{ik_z z - k_d z - i\omega t + im\theta}, \\
B &= Ae^{k_d z} e^{i(k_z z - \omega t + m\theta)}, \\
B &= Ae^{k_d z} e^{i(k_z z + \phi)}.
\end{aligned} \tag{6.10}$$

Thus, the waveform for each mode should be a sinusoid with an exponentially decaying envelope, this should still be a superposition of each of the previously identified radial modes. The total waveform can now be approximated as:

$$\begin{aligned}
\mathrm{Re}(B(z)) \approx{}& e^{-k_{d0}z} A_0 \cos(5.96z + \phi_0) + e^{-k_{d1}z} A_1 \cos(4.09z + \phi_1) + \\
& e^{-k_{d2}z} A_2 \cos(2.49z + \phi_2) + e^{-k_{d3}z} A_3 \cos(1.7z + \phi_3)
\end{aligned} \tag{6.11}$$

and the result of this is plotted in fig. 6.15.

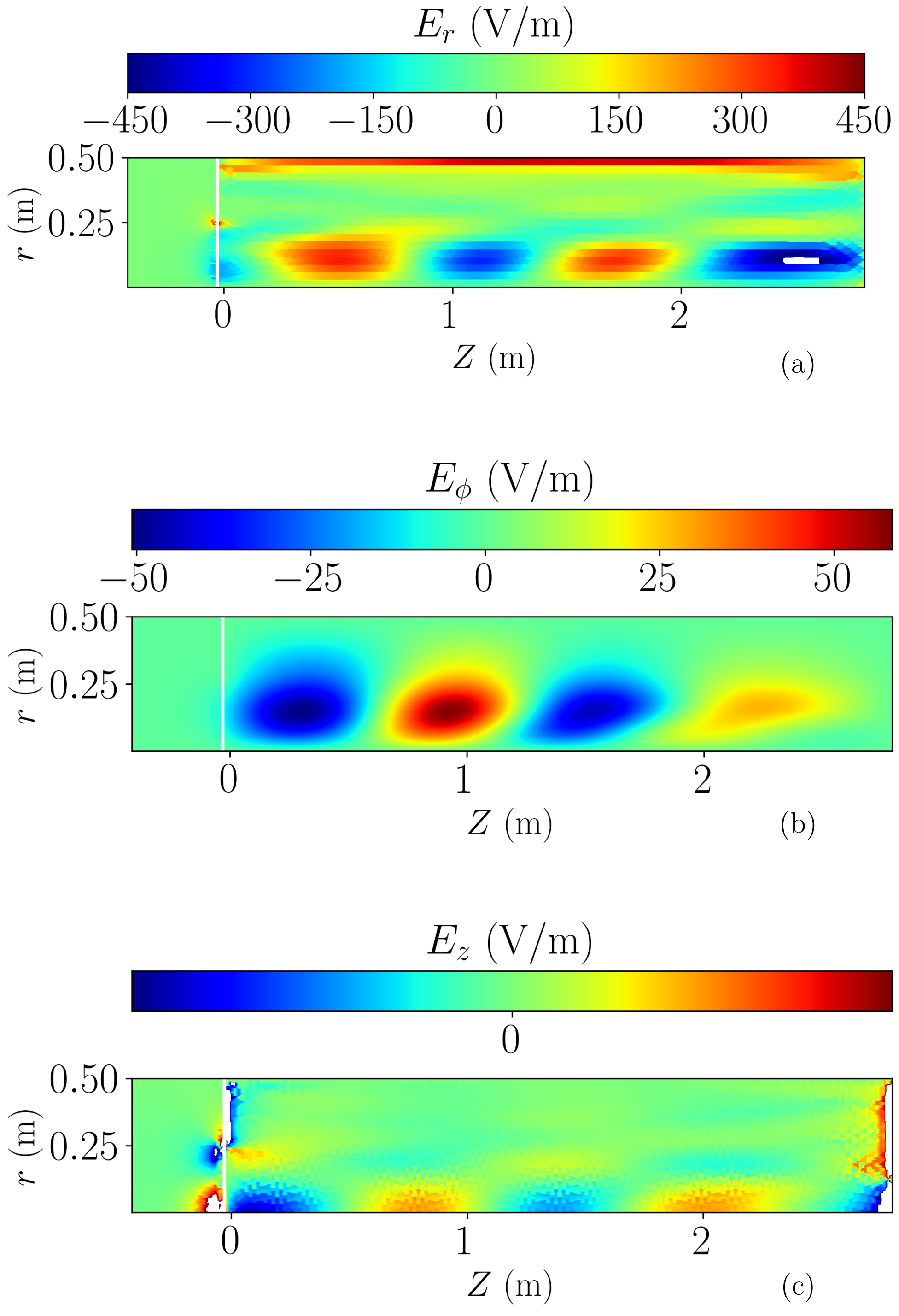

Figure 6.16: Electric fields in the 5 mT case; (a) E_r, (b) E_θ, (c) E_z

Chapter 7

Concluding remarks

7.1 Summary and discussion of key results

7.1.1 Plasma characterisation

The primary goal of this work is to design, build and commission a plasma source with a parameter space suitable for the study of parametric and other beat-wave type interactions in a magnetised plasma at microwave frequencies and this primary goal has been achieved. The parameter space required is governed by the available microwave sources and the thresholds and frequency requirements outlined in chapter 2. Since beat wave interactions involving electrostatic Langmuir waves are of interest, it is important that the densities provide plasma frequencies within the usable band of the microwave equipment. Both the magnetron oscillator and the TWT amplifier are operating at $f \approx 9.4$ GHz and thus all other equipment such as waveguides, isolators, filters, directional couplers etc. will be X-band (8 - 12.5 GHz). Therefore, any down-shifted or up-shifted signals resulting from instabilities must lie within this band. For down-shifted signals this means a maximum frequency shift $f_{\Delta} \approx 1.4$ GHz corresponding to an electron density of 2.4×10^{16} m^{-3} or for up-shifted signals up to 3.1 GHz or $n_e = 1.2 \times 10^{17}$ m^{-3}. The density, temperature and collision frequencies must also lie below certain

Device	Power	Frequency	a_0
TWT amplifier	9 kW	8 - 10 GHz	4×10^{-4}
Magnetron	25 kW	9 - 9.5 GHz	7×10^{-4}
Dispersive Pulse Compressor	200 kW	9 - 9.6 GHz	2×10^{-3}

Table 7.1: Microwave equipment available for wave mixing experiments

thresholds to ensure the onset of instabilities; taking Raman scattering as an example and using eq. (2.8), the threshold for an argon plasma at a density of 1 $\times$ 10^{16} m^{-3} and an electron temperature of 10 eV is 1.2 $\times 10^{-5}$ while for helium the threshold is 3.7 $\times 10^{-5}$. Available microwave equipment and their estimated intensities are listed in table 7.1.

It is clear that the parameter space of the plasma source is concordant with the needs of the planned non-linear wave mixing experiments. The flexibility of the source will be vital to these investigations. The most important control parameter of course will be the ability to vary the input RF power to modify the density. However, the ability to control the neutral gas pressure as well as easily change the gas species will be a useful control parameter when investigating the effects of collisions on these instabilities.

During this project the device has also been successfully operated in the helicon mode, which provides yet another method of controlling the density; the magnitude via the RF power and the profile via the magnetic field. The literature outlined in chapter 1 demonstrates this profiling ability. A particularly advantageous arrangement will be the ability to create 'flat-top' profiles which, while not proven in this thesis, are possible in principle. Indeed, the limited measurements of the helicon mode so far show a transition from a peaked profile to a hollowed profile. It would be safe to assume the plasma will take on flat-top profile at some point in between. This mode of operation will allow for a much richer variety of mode couplings to be explored; O and X mode when launching microwave beams perpendicular to the bias magnetic field or R and L modes launching parallel to the magnetic field.

7.1.2 Numerical model

The second goal of this project was to develop a numerical model of the plasma source to enhance understanding of the source and its dynamics as well as to provide predictive capability. This model over-predicts the electron density and electron temperature for the helicon discharge by factor of 3-4 at the operating pressure ≈ 1.8 Pa compared to the Langmuir probe results. The radial profiles are in agreement between experiment and measurement. Although the model does not predict the plasma parameters exactly, there are several factors that may influence this that provide scope for future improvements. The largest factor is the electrostatic vs. inductive coupling discussed in chapter 1. The numerical model developed by COMSOL was intended for plasma reactors operating in the purely inductively coupled regime, where this device may be operating in the capacitively coupled regime. This COMSOL solver does not calculate the electrostatic part of the electric field (assumes $\vec{E} = -d\vec{A}/dt$)[1]. The electrostatic part due to $-\nabla V$ is highly dependent on the antenna properties and geometry and any extension of the model to include electrostatic coupling would have to consider extending to 3D to calculate the electrostatic field of the spiral antenna. Another important aspect of the model is the plasma chemistry. If a reaction pathway is missing this can lead to an incorrect production rate of the charged particles. These are changes that can be implemented without significant cost to the computation times. This technique benefits from very low computation cost and therefore future work should attempt to extend this model over choosing a different technique.

Due to the hybrid frequency and time domain nature of this numerical model it was unclear if it could predict the helicon mode when a bias magnetic field was added. It has been shown that the addition of a bias magnetic field does

---

[1] The solver does keep track of this part of Maxwell's equations, but drops this term when calculating the work done on the plasma.

indeed alter the plasma profiles in the way one would expect for a helicon device. The electromagnetic fields also show a propagating wave structure indicating the presence of the helicon wave and not just enhanced confinement. It has also been shown the radial structure of the wave magnetic field follows the established theory using wavenumbers derived self consistently from the dispersion relation for a helicon wave.

7.1.3 Apparatus

The primary goal of this work was to develop and commission of a versatile and cost-effective plasma source that can serve as a platform for a variety of wave-plasma interaction experiments that can take advantage of the host institution's expertise in microwave technology. It is the intention that this source will serve as a facility for these kinds of investigation for many years to come. Therefore, it was important that the apparatus is flexible in adjusting experimental parameters and must provide easy access for diagnostics. A significant portion of this work therefore was tied up in building the vessel, designing and manufacturing equipment, commissioning the RF sources and developing diagnostics. An integral component of this work was developing the RF compensated Langmuir probe diagnostic; this includes design of the probe circuitry, the probe itself and the diagnostic software. The Langmuir probe diagnostic system performs well, with adequate rejection of RF signals across the HF band and provides local diagnostics of both the ion and electron densities as well as the electron temperatures. In future experiments on parametric instabilities these will provide invaluable insight into the density perturbations set up by the beat waves.

7.2 Future work

The apparatus is at the beginning of its service, therefore there are many avenues to explore, both in developing the source and its diagnostics as well as fundamental plasma physics research. In the remit of apparatus development, the next major upgrade will involve the installation of 4 more electromagnets. These will allow much finer control of the magnetic field profile and allow the helicon wave to propagate along the entire length of the vessel. The RF system will also shortly be upgraded to include a 4 kW valve amplifier that will further increase plasma densities, giving more experimental flexibility.

The Langmuir probe diagnostics will also be upgraded in due course to provide more flexible translation in the axial direction to allow for quicker scans of profiles. The ion temperatures have thus far not been measured since they are not important for the immediate studies relating to upper hybrid and Raman interactions. The ions in an RF discharge are usually considered to be at the gas temperature since they thermalise with this dominant species; since this dominant species is neutral its temperature does not depend on the EM fields. However, it is known that in some cases the ions can be significantly higher than room temperature (although still much cooler than the electrons), which could have an effect on the plasma source dynamics. This could be achieved by installing a retarding field energy analyser. Another important diagnostic to be added before further experiments in the helicon mode is the addition of a microwave interferometry system. When the bias magnetic field is present the collection area of a Langmuir probe is reduced as discussed in chapter 5. However, the probe's ability to measure the electron density profile is unaffected but its sensitivity is changed in a manner which is difficult to quantify. Therefore an interferometry diagnostic which provides a refractive index measurement across the vessel diameter can be used to determine the line integrated density. This value can be used to re-normalise the probe results in magnetised measurements.

The fluid model of the source should be extended to include the electrostatic coupling as it may be the case that the present apparatus is operating in the low density capacitive mode. This will require an increase in the order of shape function used in the model as the current linear shape function restricts any derived value to a first order differential. Because the partial differential equations are in terms of the magnetic vector potential $\vec{A}$, the magnetic flux density is given by $\vec{B} = \vec{\nabla} \times \vec{A}$. The electric field will then need to be calculated from Faraday's law, introducing a second differentiation with respect to position. In addition, the solver is capable of self consistently calculating the bias magnetic field for a given magnet geometry and current and future work should incorporate a self consistent magnetic field map for the helicon mode calculations.

Ongoing work by colleagues that is not part of the thesis involves particle-in-cell modelling of parametric scattering. These calculations use plasma parameters obtained from the Langmuir probe data and early results indicate that Raman scattering is feasible for the apparatus parameter space with microwave sources that are readily available. Further work by colleagues involves designing and commissioning a custom microwave horn antenna and lens system to focus the microwave beams and provide the intensities required to trigger the instabilities of interest to the wider project. The detail of this system and the non-linear wave mixing experiments will form a second thesis attached to the wider project.

Appendices

Appendix A

Dielectric tensor

$$\mathcal{S} = \frac{1}{2}\left(R + L\right) \tag{A.1}$$

$$\mathcal{D} = \frac{1}{2}\left(R - L\right) \tag{A.2}$$

$$\mathcal{R} = 1 - \sum_{s} \frac{\omega_{ps}^{2}}{\omega\left(\omega + \Omega_{s}\right)} \tag{A.3}$$

$$\mathcal{L} = 1 - \sum_{s} \frac{\omega_{ps}^{2}}{\omega\left(\omega - \Omega_{s}\right)} \tag{A.4}$$

$$\mathcal{P} = 1 - \sum_{s} \frac{\omega_{ps}^{2}}{\omega^{2}} \tag{A.5}$$

Where ω_{ps} is the plasma frequency of species s, Ω_s is the cyclotron frequency for species s and ω is the wave frequency.

Appendix B

The $v \times b$ term

Usually Ampère's law is presented as:

$$\vec{\nabla} \times \vec{B} = \mu_0 \vec{J} + \mu_0 \epsilon_0 \frac{\partial \vec{E}}{\partial t} \tag{B.1}$$

A slightly more compact form of Ampère's law is:

$$\vec{\nabla} \times \vec{B} = \mu_0 \vec{J} \tag{B.2}$$

Where the current density $\vec{J}$ includes both terms on the right hand side of B.1. A charge in free space under the action of an electric field experiences a force proportional to its charge and the strength of the electric field:

$$\vec{F} = q\vec{E} \tag{B.3}$$

This force underpins the derivation of the microscopic formulation of Ohm' law:

$$\vec{J} = \sigma \vec{E} \tag{B.4}$$

In free space, a charge can accelerate indefinitely, but in a collisional medium such as a solid conductor, the charges frequently suffer collisions with atoms in the lattice, leading to a periodic 'resetting' of the charge's momentum. These collisions mean the charge will not accelerate indefinitely but can be considered to reach an average velocity when taking into account that a charge does spend some time accelerating between collisions. Consider a charge immediately after a collision, assigning it a 'random' velocity $\vec{v}_0$ and thus a 'random' momentum $\vec{p}_0$:

$$\vec{p}_0 = m\vec{v}_0 \tag{B.5}$$

Where m is the mass of the charged particle. From this time until the next collision t_c, the charge q accelerates uniformly under the field:

$$\Delta\vec{p} = q\vec{E}t_c \tag{B.6}$$

Thus the total momentum just before the next collision is:

$$\vec{p} = m\vec{v}_0 + q\vec{E}t_c \tag{B.7}$$

Now consider an ensemble of charges, taking the average momentum:

$$\begin{aligned} <\vec{p}> &= m <\vec{u}> && \text{(B.8)} \\ &= \frac{1}{N}\Sigma_{i=1}^{N}\left(m\vec{v}_{0,i} + q\vec{E}t_{c,i}\right) && \text{(B.9)} \end{aligned}$$

Since the velocity after impact $\vec{u} + 0, i$ is completely random, their sum over a large population should be close to 0. The averaging over the particle collision time $t_{c,i}$ is not evaluated, just rewritten in terms of the collision frequency $1/\nu$:

$$\begin{aligned} <\vec{p}> &= m <\vec{u}> && \text{(B.10)} \\ &= \frac{q\vec{E}}{\nu} && \text{(B.11)} \\ \implies <\vec{u}> &= \frac{q\vec{E}}{m\nu} && \text{(B.12)} \end{aligned}$$

Noting that a current density is given by a flux of charge:

$$\begin{aligned}
\vec{J} &= nq\vec{u} && \text{(B.13)}\\
&= nq\frac{q\vec{E}}{m\nu} && \text{(B.14)}\\
&= \frac{nq^2}{m\nu}\vec{E} && \text{(B.15)}\\
&= \sigma\vec{E} && \text{(B.16)}
\end{aligned}$$

Where n is number density of the charged particles. This is the microscopic form of Ohm's law, an expression which modifies the acceleration under the action of a field by taking collisions into account. However, B.6 can be made a little more general, since really it is forces that moves the charge through the medium:

$$\vec{p} = \vec{F}_i t_c \tag{B.17}$$

Now including the magnetic field B via the Lorentz force law:

$$\vec{p} = q\left(\vec{E} + \vec{u}_\perp \times \vec{B}\right)t_c \tag{B.18}$$

The analysis of the ensemble average then results in:

$$< \vec{u} >= \frac{q}{m\nu}\left(\vec{E} + \vec{u}_{\perp,th} \times \vec{B}\right) \tag{B.19}$$

Where the averaging in the magnetic term has been done by using the thermal velocity. The current density from B.16 becomes:

$$\vec{J} = \sigma\vec{E} + \sigma\vec{u}_\perp \times \vec{B} \tag{B.20}$$

Then, upon substituting a conduction current into Ampère's law (B.1):

$$\vec{\nabla} \times \vec{B} = \mu_0 \sigma \vec{E} + \mu_0 \sigma \vec{u}_\perp \times \vec{B} + \mu_0 \epsilon_0 \frac{\partial \vec{E}}{\partial t} \tag{B.21}$$

Appendix C

Parabolic density profiles

Due to the multi-decade span of the electron density in the numerical results of chapter 6 a logarithmic scale was more appropriate. An important part of that discussion is the limits on the parameter space for the numerical model and being able to plot a profile at 10^{11} $\mathrm{m^{-3}}$ next to a profile at 10^{16} $\mathrm{m^{-3}}$ is a useful illustration. However, this obscures the similarity the profiles share with those measured by the Langmuir probes. Thus, the electron density as a function of radial position and axial position are presented here for the helium ICP at 1.8 Pa.

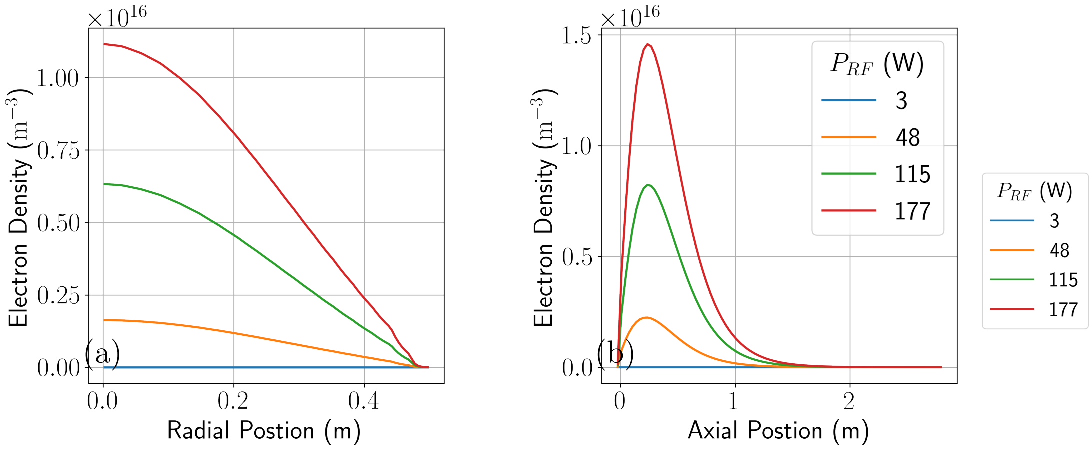

Figure C.1: Helium axial and radial n_e profiles, $P_{RF} = 180$ W & $p_{He} = 1.8$ Pa

Appendix D

Plasma potential uncertainty

When using a central difference scheme, 2 points are side of the point of interest must be used, this means the gradient is assigned to a group of three points, or a window of plus or minus the grid resolution. This effect cascades with growing orders of differentials. In the figure, a portion of a second derivative of a sin function is plotted in green. The points from the first differential which are assigning that gradient are mapped from the first derivative which is plotted in orange. Those points are then mapped back to the starting sin function in blue. It can be seen that the value of the second derivative is assigned across 5 points in a central difference scheme, thus the error moves from ± scale resolution for the function itself, to ± twice scale resolution for the first derivative and then three times the resolution for the second derivative.

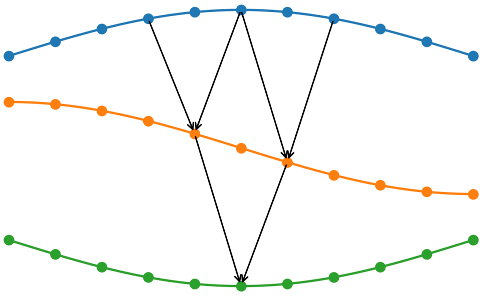

Figure D.1: The number of adjacent points informing the differential grows linearly with the order

References

[1] T. H. Stix, *Waves in plasmas.* American Institute of Physics, 1992.

[2] L. Landau, "On the vibrations of the electronic plasma," *Journal of Physics (USSR)*, vol. 10, p. 25, 1946.

[3] J. D. Lawson, "Some criteria for a power producing thermonuclear reactor," *Proceedings of the Physical Society. Section B*, vol. 70, pp. 6–10, Jan. 1957.

[4] J. Wesson, *Tokamaks.* Clarendon Press, 1987.

[5] P. McKenna, D. Neely, R. Bingham, and D. Jaroszynski, eds., *Laser-Plasma Interactions and Applications.* Springer International Publishing, 2013.

[6] E. Gibney, "Nuclear-fusion reactor smashes energy record," *Nature*, vol. 602, p. 371, Feb. 2022.

[7] E. Cartlidge, "National ignition facility's ignition milestone sparks fresh push for laser fusion." physicsworld.com, Jan. 2023. IOP Publishing.

[8] V. F. Shevchenko, E. Du Toit, A. Fokin, E. Tai, T. Bigelow, and J. B. Caughman, "2 mw ecrh system for st40 spherical tokamak," in *2021 46th International Conference on Infrared, Millimeter and Terahertz Waves (IRMMW-THz)*, pp. 1–2, 2021.

[9] D. Sweetman, J. G. Cordey, and T. Gren, "Heating and plasma interactions with beams of energetic neutral atoms," *Philosophical Transactions of the*

Royal Society of London. Series A, Mathematical and Physical Sciences, vol. 300, pp. 589–598, Apr. 1981.

[10] M. Porkolab, P. M. Ryan, and D. Rasmussen, "RF heating and current drive in magnetically confined plasma: a historical perspective," in *AIP Conference Proceedings*, AIP, 2007.

[11] W. M. Hooke, F. H. Tenney, M. H. Brennan, H. M. Hill, and T. H. Stix, "Experiments on ion cyclotron waves," *Physics of Fluids*, vol. 4, no. 9, p. 1131, 1961.

[12] J. Jacquinot, B. D. McVey, and J. E. Scharer, "Mode conversion of the fast magnetosonic wave in a deuterium-hydrogen tokamak plasma," *Physical Review Letters*, vol. 39, pp. 88–91, Jul. 1977.

[13] T. Stix, "Fast-wave heating of a two-component plasma," *Nuclear Fusion*, vol. 15, pp. 737–754, Oct. 1975.

[14] V. Golant, "Plasma penetration near the lower hybrid frequency," *Soviet Physics: Technical Physics*, vol. 16, p. 1980, 1972.

[15] M. Porkolab, "Parametric processes in magnetically confined CTR plasmas," *Nuclear Fusion*, vol. 18, pp. 367–413, Mar. 1978.

[16] N. J. Fisch, "Theory of current drive in plasmas," *Reviews of Modern Physics*, vol. 59, pp. 175–234, Jan. 1987.

[17] M. Porkolab, J. J. Schuss, B. Lloyd, Y. Takase, S. Texter, P. Bonoli, C. Fiore, R. Gandy, D. Gwinn, B. Lipschultz, E. Marmar, D. Pappas, R. Parker, and P. Pribyl, "Observation of lower-hybrid current drive at high densities in the alcator c tokamak," *Physical Review Letters*, vol. 53, pp. 450–453, Jul. 1984.

[18] F. Jobes, J. Stevens, R. Bell, S. Bernabei, A. Cavallo, T. K. Chu, S. Cohen, B. Denne, P. Efthimion, E. Hinnov, W. Hooke, J. Hosea, E. Mazzucato, R. McWilliams, R. Motley, S. Suckewer, G. Taylor, J. Timberlake, S. von Goeler, and R. Wilson, "Formation of a 100-kA tokamak discharge in the princeton large torus by lower hybrid waves," *Physical Review Letters*, vol. 52, pp. 1005–1008, Mar. 1984.

[19] R. A. Cairns and C. N. Lashmore-Davies, "The prospects for electron bernstein wave heating of spherical tokamaks," *Physics of Plasmas*, vol. 7, no. 10, p. 4126, 2000.

[20] M. Bornatici, R. Cano, O. D. Barbieri, and F. Engelmann, "Electron cyclotron emission and absorption in fusion plasmas," *Nuclear Fusion*, vol. 23, pp. 1153–1257, Sep. 1983.

[21] V. Alikaev, G. Bobrovskii, V. Poznyak, K. Razumova, V. Sannikov, Y. Sokolov, A., and A. Shmarin, "Ecr plasma heating in the tm-3 tokamak in magnetic fields up to 25koe," *Soviet Journal of Plasma Physics*, vol. 2, p. 212, 1976.

[22] W. L. Kruer, P. K. Kaw, J. M. Dawson, and C. Oberman, "Anomalous high-frequency resistivity and heating of a plasma," *Physical Review Letters*, vol. 24, pp. 987–990, May 1970.

[23] S. W. Mead, R. E. Kidder, J. E. Swain, F. Ranier, and J. Petruzzi, "Preliminary measurements of x-ray and neutron emission from laser-produced plasmas," *Applied Optics*, vol. 11, p. 345, Feb. 1972.

[24] R. Kidder, "Hot-electron preheat of laser-driven targets," *Nuclear Fusion*, vol. 21, no. 2, p. 145, 1981.

[25] N. B. Meezan, M. J. Edwards, O. A. Hurricane, P. K. Patel, D. A. Callahan, W. W. Hsing, R. P. J. Town, F. Albert, P. A. Amendt, L. F. B. Hopkins,

D. K. Bradley, D. T. Casey, D. S. Clark, E. L. Dewald, T. R. Dittrich, L. Divol, T. Döppner, J. E. Field, S. W. Haan, G. N. Hall, B. A. Hammel, D. E. Hinkel, D. D. Ho, M. Hohenberger, N. Izumi, O. S. Jones, S. F. Khan, J. L. Kline, A. L. Kritcher, O. L. Landen, S. LePape, T. Ma, A. J. MacKinnon, A. G. MacPhee, L. Masse, J. L. Milovich, A. Nikroo, A. Pak, H.-S. Park, J. L. Peterson, H. F. Robey, J. S. Ross, J. D. Salmonson, V. A. Smalyuk, B. K. Spears, M. Stadermann, L. J. Suter, C. A. Thomas, R. Tommasini, D. P. Turnbull, and C. R. Weber, "Indirect drive ignition at the national ignition facility," *Plasma Physics and Controlled Fusion*, vol. 59, p. 014021, Oct. 2016.

[26] R. S. Craxton, K. S. Anderson, T. R. Boehly, V. N. Goncharov, D. R. Harding, J. P. Knauer, R. L. McCrory, P. W. McKenty, D. D. Meyerhofer, J. F. Myatt, A. J. Schmitt, J. D. Sethian, R. W. Short, S. Skupsky, W. Theobald, W. L. Kruer, K. Tanaka, R. Betti, T. J. B. Collins, J. A. Delettrez, S. X. Hu, J. A. Marozas, A. V. Maximov, D. T. Michel, P. B. Radha, S. P. Regan, T. C. Sangster, W. Seka, A. A. Solodov, J. M. Soures, C. Stoeckl, and J. D. Zuegel, "Direct-drive inertial confinement fusion: A review," *Physics of Plasmas*, vol. 22, p. 110501, Nov. 2015.

[27] R. Betti and O. A. Hurricane, "Inertial-confinement fusion with lasers," *Nature Physics*, vol. 12, pp. 435–448, May 2016.

[28] R. Nora, R. Betti, K. S. Anderson, A. Shvydky, A. Bose, K. M. Woo, A. R. Christopherson, J. A. Marozas, T. J. B. Collins, P. B. Radha, S. X. Hu, R. Epstein, F. J. Marshall, R. L. McCrory, T. C. Sangster, and D. D. Meyerhofer, "Theory of hydro-equivalent ignition for inertial fusion and its applications to OMEGA and the national ignition facility," *Physics of Plasmas*, vol. 21, p. 056316, May 2014.

[29] W. Seka, D. H. Edgell, J. F. Myatt, A. V. Maximov, R. W. Short, V. N. Goncharov, and H. A. Baldis, "Two-plasmon-decay instability in direct-drive inertial confinement fusion experiments," *Physics of Plasmas*, vol. 16, p. 052701, May 2009.

[30] L. J. Perkins, R. Betti, K. N. LaFortune, and W. H. Williams, "Shock ignition: A new approach to high gain inertial confinement fusion on the national ignition facility," *Physical Review Letters*, vol. 103, p. 045004, Jul. 2009.

[31] S. Weber, C. Riconda, O. Klimo, A. Héron, and V. T. Tikhonchuk, "Fast saturation of the two-plasmon-decay instability for shock-ignition conditions," *Physical Review E*, vol. 85, p. 016403, Jan. 2012.

[32] W. Theobald, R. Nora, W. Seka, M. Lafon, K. S. Anderson, M. Hohenberger, F. J. Marshall, D. T. Michel, A. A. Solodov, C. Stoeckl, D. H. Edgell, B. Yaakobi, A. Casner, C. Reverdin, X. Ribeyre, A. Shvydky, A. Vallet, J. Peebles, F. N. Beg, M. S. Wei, and R. Betti, "Spherical strong-shock generation for shock-ignition inertial fusiona)," *Physics of Plasmas*, vol. 22, p. 056310, May 2015.

[33] P. Nicolaï, J.-L. Feugeas, M. Touati, X. Ribeyre, S. Gus'kov, and V. Tikhonchuk, "Deleterious effects of nonthermal electrons in shock ignition concept," *Physical Review E*, vol. 89, p. 033107, Mar. 2014.

[34] A. A. Offenberger, M. R. Cervenan, A. M. Yam, and A. W. Pasternak, "Stimulated brillouin scattering of CO2 laser radiation from underdense plasma," *Journal of Applied Physics*, vol. 47, pp. 1451–1458, Apr. 1976.

[35] W. L. Kruer, S. C. Wilks, B. B. Afeyan, and R. K. Kirkwood, "Energy transfer between crossing laser beams," *Physics of Plasmas*, vol. 3, pp. 382–385, Jan. 1996.

[36] R. K. Kirkwood, B. B. Afeyan, W. L. Kruer, B. J. MacGowan, J. D. Moody, D. S. Montgomery, D. M. Pennington, T. L. Weiland, and S. C. Wilks, "Observation of energy transfer between frequency-mismatched laser beams in a large-scale plasma," *Physical Review Letters*, vol. 76, pp. 2065–2068, Mar. 1996.

[37] P. Michel, L. Divol, E. A. Williams, S. Weber, C. A. Thomas, D. A. Callahan, S. W. Haan, J. D. Salmonson, S. Dixit, D. E. Hinkel, M. J. Edwards, B. J. MacGowan, J. D. Lindl, S. H. Glenzer, and L. J. Suter, "Tuning the implosion symmetry of ICF targets via controlled crossed-beam energy transfer," *Physical Review Letters*, vol. 102, p. 025004, Jan. 2009.

[38] T. Boehly, D. Brown, R. Craxton, R. Keck, J. Knauer, J. Kelly, T. Kessler, S. Kumpan, S. Loucks, S. Letzring, F. Marshall, R. McCrory, S. Morse, W. Seka, J. Soures, and C. Verdon, "Initial performance results of the OMEGA laser system," *Optics Communications*, vol. 133, pp. 495–506, Jan. 1997.

[39] I. V. Igumenshchev, W. Seka, D. H. Edgell, D. T. Michel, D. H. Froula, V. N. Goncharov, R. S. Craxton, L. Divol, R. Epstein, R. Follett, J. H. Kelly, T. Z. Kosc, A. V. Maximov, R. L. McCrory, D. D. Meyerhofer, P. Michel, J. F. Myatt, T. C. Sangster, A. Shvydky, S. Skupsky, and C. Stoeckl, "Crossed-beam energy transfer in direct-drive implosions," *Physics of Plasmas*, vol. 19, p. 056314, May 2012.

[40] M. A. Lieberman, *Principles of plasma discharges and materials processing.* Wiley-Interscience, 2005.

[41] J. Hopwood, "Review of inductively coupled plasmas for plasma processing," *Plasma Sources Science and Technology*, vol. 1, pp. 109–116, May 1992.

[42] B. Wu, A. Kumar, and S. Pamarthy, “High aspect ratio silicon etch: A review,” *Journal of Applied Physics*, vol. 108, p. 051101, Sep. 2010.

[43] S. Greenfield, I. L. Jones, and C. T. Berry, “High-pressure plasmas as spectroscopic emission sources,” *The Analyst*, vol. 89, no. 1064, p. 713, 1964.

[44] A. L. Gray, “Solid sample introduction by laser ablation for inductively coupled plasma source mass spectrometry,” *The Analyst*, vol. 110, no. 5, p. 551, 1985.

[45] W. Hittorf, “Ueber die electricitätsleitung der gase. vierte mittheilung,” *Annalen der Physik*, vol. 256, no. 12, pp. 705–755, 1883.

[46] K. Suzuki, K. Nakamura, H. Ohkubo, and H. Sugai, “Power transfer efficiency and mode jump in an inductive RF discharge,” *Plasma Sources Science and Technology*, vol. 7, pp. 13–20, Feb. 1998.

[47] C. B. Zarowin and C. K. Williams, “Quasi-cw, high numerical aperture, inductively excited ion laser,” *Applied Physics Letters*, vol. 11, pp. 47–48, Jul. 1967.

[48] J. Amorim, “High-density plasma mode of an inductively coupled radio frequency discharge,” *Journal of Vacuum Science Technology B: Microelectronics and Nanometer Structures*, vol. 9, p. 362, Mar. 1991.

[49] V. A. Godyak, R. B. Piejak, and B. M. Alexandrovich, “Experimental setup and electrical characteristics of an inductively coupled plasma,” *Journal of Applied Physics*, vol. 85, pp. 703–712, Jan. 1999.

[50] J. J. Thomson, “On the discharge of electricity through exhausted tubes without electrodes (part 1),” *The London, Edinburgh, and Dublin Philosophical Magazine and Journal of Science*, vol. 32, pp. 321–336, Oct. 1891.

[51] J. Thomson, "The electrodeless discharge through gases," *The London, Edinburgh, and Dublin Philosophical Magazine and Journal of Science*, vol. 4, pp. 1128–1160, Nov. 1927.

[52] J. Townsend and R. Donaldson, "Electrodeless discharges," *The London, Edinburgh, and Dublin Philosophical Magazine and Journal of Science*, vol. 5, pp. 178–191, Jan. 1928.

[53] K. MacKinnon, "On the origin of the electrodeless discharge," *The London, Edinburgh, and Dublin Philosophical Magazine and Journal of Science*, vol. 8, pp. 605–616, Nov. 1929.

[54] J. Kunz, "Theory of electromagnetic and electrostatic induction in electrodeless discharges," *The London, Edinburgh, and Dublin Philosophical Magazine and Journal of Science*, vol. 13, pp. 964–975, May 1932.

[55] J. Tykocinski-Tykociner, "Measurement of current in electrodeless discharges by means of frequency variations," *The London, Edinburgh, and Dublin Philosophical Magazine and Journal of Science*, vol. 13, pp. 953–964, May 1932.

[56] O. Strelko, Y. Berdnychenko, O. Pylypchuk, O. Pylypchuk, O. Sorochynska, and A. Horban, "Historical milestones in the development and creation of radio frequency inductively coupled plasma torches," in *2021 IEEE 3rd Ukraine Conference on Electrical and Computer Engineering (UKRCON)*, IEEE, Aug. 2021.

[57] M.-H. Lee and C.-W. Chung, "On the e to h and h to e transition mechanisms in inductively coupled plasma," *Physics of Plasmas*, vol. 13, p. 063510, Jun. 2006.

[58] U. Kortshagen, N. D. Gibson, and J. E. Lawler, "On the e - h mode transition in RF inductive discharges," *Journal of Physics D: Applied Physics*, vol. 29, pp. 1224–1236, May 1996.

[59] P. Aigrain, "Les 'helicons' dans les semiconducteurs," in *Proceedings of the International Conference on Semiconductor Physics, Prague, 1960*, 1960.

[60] F. F. Chen, "Helicon discharges and sources: a review," *Plasma Sources Science and Technology*, vol. 24, p. 014001, Jan. 2015.

[61] J. A. Lehane and P. C. Thonemann, "An experimental study of helicon wave propagation in a gaseous plasma," *Proceedings of the Physical Society*, vol. 85, pp. 301–316, Feb. 1965.

[62] J. P. Klozenberg, B. McNamara, and P. C. Thonemann, "The dispersion and attenuation of helicon waves in a uniform cylindrical plasma," *Journal of Fluid Mechanics*, vol. 21, pp. 545–563, Mar. 1965.

[63] F. F. Chen, "Plasma ionization by helicon waves," *Plasma Physics and Controlled Fusion*, vol. 33, pp. 339–364, Apr. 1991.

[64] K.-K. Chi, T. E. Sheridan, and R. W. Boswell, "Resonant cavity modes of a bounded helicon discharge," *Plasma Sources Science and Technology*, vol. 8, pp. 421–431, Jan. 1999.

[65] R. Boswell, "Dependence of helicon wave radial structure on electron inertia," *Australian Journal of Physics*, vol. 25, no. 4, p. 403, 1972.

[66] F. F. Chen and D. Arnush, "Generalized theory of helicon waves. i. normal modes," *Physics of Plasmas*, vol. 4, pp. 3411–3421, Sep. 1997.

[67] D. Arnush and F. F. Chen, "Generalized theory of helicon waves. ii. excitation and absorption," *Physics of Plasmas*, vol. 5, pp. 1239–1254, May 1998.

[68] S. S. S. Shinohara, S. T. S. Takechi, and Y. K. Y. Kawai, “Effects of axial magnetic field and faraday shield on characteristics of RF produced plasma using spiral antenna,” *Japanese Journal of Applied Physics*, vol. 35, p. 4503, Aug. 1996.

[69] Y. Sakawa, N. Koshikawa, and T. Shoji, “Characteristics of the high density plasma production by m-0 helicon wave,” *Applied Physics Letters*, vol. 69, pp. 1695–1697, Sep. 1996.

[70] T. Watari, T. Hatori, R. Kumazawa, S. Hidekuma, T. Aoki, T. Kawamoto, M. Inutake, S. Hiroe, A. Nishizawa, K. Adati, T. Sato, T. Watanabe, H. Obayashi, and K. Takayama, “Radio-frequency plugging of a high density plasma,” *Physics of Fluids*, vol. 21, no. 11, p. 2076, 1978.

[71] R. Boswell, “Plasma production using a standing helicon wave,” *Physics Letters A*, vol. 33, pp. 457–458, Dec. 1970.

[72] D. G. Miljak and F. F. Chen, “Helicon wave excitation with rotating antenna fields,” *Plasma Sources Science and Technology*, vol. 7, pp. 61–74, Feb. 1998.

[73] S. Shinohara, S. Takechi, N. Kaneda, and Y. Kawai, “Helicon m = 0 mode characteristics in large-diameter plasma produced by a planar spiral antenna,” *Plasma Physics and Controlled Fusion*, vol. 39, pp. 1479–1486, Sep. 1997.

[74] S. Shinohara and T. Soejima, “Trials of RF plasma production using different antenna geometries with magnetic field,” *Plasma Physics and Controlled Fusion*, vol. 40, pp. 2081–2095, Dec. 1998.

[75] S. Shinohara, H. Tsuji, T. Yoshinaka, and Y. Kawai, “Control of plasma profile by voltage biasing in large diameter RF produced plasma,” *Surface and Coatings Technology*, vol. 112, pp. 20–24, Feb. 1999.

[76] S. Shinohara, N. Matsuoka, and T. Yoshinaka, "Profile control and plasma rotation by biased electrodes in large diameter RF produced plasma," *Japanese Journal of Applied Physics*, vol. 38, p. 4321, Jul. 1999.

[77] S. Shinohara, K. P. Shamrai, and S. Shinohara, "Direct comparison of experimental and theoretical results on the antenna loading and density jumps in a high pressure helicon source," *Plasma Physics and Controlled Fusion*, vol. 42, pp. 865–880, Jul. 2000.

[78] S. Shinohara and T. Tanikawa, "Development of very large helicon plasma source," *Review of Scientific Instruments*, vol. 75, pp. 1941–1946, Jun. 2004.

[79] J. Scharer, A. Degeling, G. Borg, and R. Boswell, "Measurements of helicon wave propagation and arII emission," *Physics of Plasmas*, vol. 9, pp. 3734–3742, Sep. 2002.

[80] M. M. Balkey, R. Boivin, J. L. Kline, and E. E. Scime, "Ion heating and density production in helicon sources near the lower hybrid frequency," *Plasma Sources Science and Technology*, vol. 10, pp. 284–294, May 2001.

[81] G. R. Tynan, A. D. Bailey, G. A. Campbell, R. Charatan, A. de Chambrier, G. Gibson, D. J. Hemker, K. Jones, A. Kuthi, C. Lee, T. Shoji, and M. Wilcoxson, "Characterization of an azimuthally symmetric helicon wave high density plasma source," *Journal of Vacuum Science Technology A: Vacuum, Surfaces, and Films*, vol. 15, pp. 2885–2892, Nov. 1997.

[82] G. R. Tynan, M. J. Burin, C. Holland, G. Antar, N. Crocker, and P. H. Diamond, "Radially sheared azimuthal flows and turbulent transport in a cylindrical plasma," *Physics of Plasmas*, vol. 11, pp. 5195–5203, Nov. 2004.

[83] M. Yano and M. L. R. Walker, "Plasma ionization by annularly bounded helicon waves," *Physics of Plasmas*, vol. 13, p. 063501, Jun. 2006.

[84] J. P. Squire, F. R. Chang-Díaz, T. W. Glover, V. T. Jacobson, G. E. McCaskill, D. S. Winter, F. W. Baity, M. D. Carter, and R. H. Goulding, "High power light gas helicon plasma source for VASIMR," *Thin Solid Films*, vol. 506-507, pp. 579–582, May 2006.

[85] S. Shinohara, D. Kuwahara, Y. Ishigami, H. Horita, and S. Nakanishi, "Extremely small-diameter, high-density, radio frequency, plasma sources and central gas feeding for next-generation electrodeless plasma thrusters," *Review of Scientific Instruments*, vol. 91, p. 073507, Jul. 2020.

[86] D. Kuwahara, A. Mishio, T. Nakagawa, and S. Shinohara, "Development of very small-diameter, inductively coupled magnetized plasma device," *Review of Scientific Instruments*, vol. 84, p. 103502, Oct. 2013.

[87] J. Urban, J. Decker, Y. Peysson, J. Preinhaelter, V. Shevchenko, G. Taylor, L. Vahala, and G. Vahala, "A survey of electron bernstein wave heating and current drive potential for spherical tokamaks," *Nuclear Fusion*, vol. 51, p. 083050, Aug. 2011.

[88] W. Kruer, *The Physics of Laser Plasma Interactions.* Westview Press, 2001.

[89] H. Webster, S. Freethy, M. Henderson, J. Allen, O. Caretta, S. Desai, J. Holden, D. Maszczyk, E. Melidis, H. Meyer, E. Muir, A. Munasinghe, and S. Surendran, "Mast upgrade microwave heating and current drive system – engineering design overview," *EPJ Web of Conferences*, vol. 277, p. 04004, 2023.

[90] M. Amin and R. Cairns, "Two-dimensional analysis of beat wave current drive with intense microwave pulses," *Nuclear Fusion*, vol. 30, pp. 327–342, Feb. 1990.

[91] S. Shibaev, G. Naylor, R. Scannell, G. J. McArdle, and M. J. Walsh, “Real time operation of mast thomson scattering diagnostic,” in *2010 17th IEEE-NPSS Real Time Conference*, IEEE, May 2010.

[92] W. L. Kruer, “Laser-driven instabilities in long scalelength plasmas ii,” in *Laser Plasma Interactions 4* (B. M. Hooper, ed.), ch. 4, pp. 89–104, Edinburgh: SUSSP Publications, Department of Physics, University of Edinburgh, 1988.

[93] B. H. Ripin, F. C. Young, J. A. Stamper, C. M. Armstrong, R. Decoste, E. A. McLean, and S. E. Bodner, “Enhanced backscatter with a structured laser pulse,” *Physical Review Letters*, vol. 39, pp. 611–615, Sep. 1977.

[94] T. J. M. Boyd and J. J. Sanderson, *The Physics of Plasmas.* Cambridge University Press, 2003.

[95] D. D. Blackwell and F. F. Chen, “Two-dimensional imaging of a helicon discharge,” *Plasma Sources Science and Technology*, vol. 6, pp. 569–576, Nov. 1997.

[96] A. F. A. F. Harvey, *Microwave engineering.* New York: Academic Press, 1963. Includes bibliography.

[97] P. Debye, “On the theory of electrolytes,” *Phy. Z.*, vol. 24, pp. 305–325, 1923.

[98] D. Bohm, *Minimum Ionic Kinetic Energy for a Stable Sheath*, vol. 5 of *National Nuclear Energy Series (Manhattan Project Technical Section): Division 1*, ch. 3, pp. 77–86. Mcgraw-hill Book Company, Inc., 1949.

[99] D. H. Davis, “Monte carlo calculation of molecular flow rates through a cylindrical elbow and pipes of other shapes,” *Journal of Applied Physics*, vol. 31, pp. 1169–1176, Jul. 1960.

[100] P. H. Smith, “A transmission line calculator,” *Electronics*, pp. 29–31, Jan. 1939.

[101] P. H. Smith, “An improved transmission line calculator,” *Electronics*, p. 130, Jan. 1944.

[102] M. Steer, *Microwave and RF Design: Radio Systems, Volume 1.* NC State University, Jul. 2019.

[103] H. M. Mott-Smith and I. Langmuir, “The theory of collectors in gaseous discharges,” *Physical Review*, vol. 28, pp. 727–763, Oct. 1926.

[104] L. Tonks and I. Langmuir, “A general theory of the plasma of an arc,” *Phys. Rev.*, vol. 34, pp. 876–922, Sep 1929.

[105] A. Garscadden and K. G. Emeleus, “Notes on the effect of noise on langmuir probe characteristics,” *Proceedings of the Physical Society*, vol. 79, pp. 535–541, Mar. 1962.

[106] N. Hershkowitz, “How langmuir probes work,” in *Plasma Diagnostics*, pp. 113–183, Elsevier, 1989.

[107] I. D. Sudit and F. F. Chen, “RF compensated probes for high-density discharges,” *Plasma Sources Science and Technology*, vol. 3, pp. 162–168, May 1994.

[108] P. Patnaik, *Handbook of Inorganic Chemicals.* McGraw-Hill Professional, 2002.

[109] F. F. Chen, “Langmuir probe diagnostics,” in *Mini-Course on Plasma Diagnostics, IEEE ICOPS meeting, Jeju, Korea*, pp. 20–111, 2003.

[110] R. L. Merlino, “Understanding langmuir probe current-voltage characteristics,” *American Journal of Physics*, vol. 75, no. 12, pp. 1078–1085, 2007.

[111] A. Hrennikoff, “Solution of problems of elasticity by the framework method,” *Journal of Applied Mechanics*, vol. 8, pp. A169–A175, Dec. 1941.

[112] G. J. M. Hagelaar and L. C. Pitchford, “Solving the boltzmann equation to obtain electron transport coefficients and rate coefficients for fluid models,” *Plasma Sources Science and Technology*, vol. 14, pp. 722–733, Oct. 2005.

[113] K. Takahashi, C. Charles, R. Boswell, W. Cox, and R. Hatakeyama, “Transport of energetic electrons in a magnetically expanding helicon double layer plasma,” *Applied Physics Letters*, vol. 94, p. 191503, May 2009.

[114] S. Isayama, S. Shinohara, and T. Hada, “Review of helicon high-density plasma: Production mechanism and plasma/wave characteristics,” *Plasma and Fusion Research*, vol. 13, pp. 1101014–1101014, Mar. 2018.